Coupling geodynamic with thermodynamic modeling to investigate compositional evolution in magmatic systems

Dissertation
zur Erlangung des Grades
Doktor der Naturwissenschaften
im Promotionsfach Mineralogie
am Fachbereich Chemie, Pharmazie und Geowissenschaften der Johannes Gutenberg-Universität Mainz

von
Lisa Rummel
geboren in Soest

JOHANNES GUTENBERG UNIVERSITÄT MAINZ

Mainz, 2019

CONTENTS

0.1 Abstract xi
0.2 Zusammenfassung xiii

1 Introduction **1**
1.1 Melt generation 2
1.2 Non-linearity of crystal-melt ratio with decreasing temperature 3
1.3 Thesis structure 4

2 Coupled petrological-geodynamical modeling of a compositionally heterogeneous mantle plume **9**
2.1 Introduction 10
2.2 Thermodynamic and geodynamic modeling approaches 11
2.2.1 Thermodynamic modeling 12
2.2.2 Geodynamic modeling 19
2.3 Results 26
2.3.1 Factors controlling plume ascent and magma formation 27
2.3.2 Effect of mantle source chemistry on melting 30
2.3.3 Melt extraction depth and temperature 32
2.3.4 Effect of a decreasing M_{crit} 33
2.3.5 Evolution of simulated magma compositions 35
2.4 Discussion 37
2.4.1 Developed method 37
2.4.2 Model limitations 38
2.4.3 Potential application to the West Eifel (Germany) 38

2.5 Conclusion . . . 48
2.6 Acknowledgements . . . 49
2.7 Appendix . . . 50
2.A Methods . . . 50
2.B Executed geodynamic simulations . . . 59
2.C Comparison of modeled melts with Eifel rocks . . . 65
2.D West Eifel volcanism and the thermal and compositional structure of the mantle . . . 69

3 Resolution of phase diagrams and computational cost 81

4 An autonomous phase diagram database for geodynamic simulations of magmatic systems 91
4.1 Introduction . . . 92
4.2 Methods . . . 94
4.2.1 Modeling magmatic systems with petro-thermomechanical models . 94
4.2.2 Establishing the database . . . 97
4.2.3 Extending the database . . . 98
4.3 Results . . . 106
4.3.1 BRC forecasting based on unfractionated initial bulk rock compositions . . . 106
4.3.2 BRC forecasting based on clustered initial bulk rock compositions . 108
4.3.3 Evaluation of new BRCs . . . 110
4.4 Discussion . . . 113
4.4.1 Predictive power of the sampling techniques . . . 113
4.4.2 Evolution of requested BRCs with an increasing number of available phase diagrams . . . 116
4.4.3 Requested rock compositions and their correlation to melt extraction conditions . . . 118
4.4.4 Correlation between clustering, chemistry and melt extraction conditions . . . 120
4.4.5 Applicability of the phase diagram database . . . 122
4.5 Conclusion . . . 123
4.6 Acknowledgements . . . 124
4.7 Appendix . . . 125

5 Insights into the compositional evolution of crustal magmatic systems from coupled petrological-geodynamical models 141

5.1 Introduction . . . 142
5.2 Thermodynamic and geodynamic modeling approaches . . . 144
5.2.1 Thermodynamic modeling . . . 145
5.2.2 Geodynamic modeling . . . 147
5.2.3 Model setup . . . 158
5.3 Results . . . 160
5.3.1 Reference simulation . . . 160
5.3.2 Dike generation and propagation and longevity of partially molten/crystallized regions . . . 163
5.3.3 Chemical evolution of the magmatic system . . . 166
5.3.4 Mineralogical evolution of the magmatic system . . . 169
5.3.5 Effect of magma mixing on fracture formation and chemistry . . . 171
5.3.6 Influence of water content on melting, host rock assimilation and dike formation . . . 171
5.3.7 Number of employed phase diagrams . . . 176
5.4 Discussion . . . 176
5.4.1 Model limitations and assumptions . . . 176
5.4.2 Applicability of model results . . . 179
5.5 Conclusion . . . 188
5.6 Acknowledgements . . . 189
5.7 Appendix . . . 190
5.A Models . . . 190
5.B Modeling parameters . . . 191

6 Employed phase diagrams and their bulk rock compositions 207

7 Final remarks and outlook 213

LIST OF FIGURES

1.1 Melting of peridotites through different melting mechanisms 2
1.2 Schematic binary phase diagram showing the non-linear evolution of the solid-liquid ratio with decreasing temperature 4

2.1 Evolving thermodynamic modeling approach 15
2.2 Identifying representative oxide compositions of the initial phase diagram from the pyrolitic mantle using SOMs 18
2.3 Initial 2D numerical model configuration 25
2.4 Plume evolution and physical properties 28
2.5 Effect of T_{excess}, M_{crit} and LAB depth on model evolution 29
2.6 Temporal evolution of K_2O/Na_2O of modeled compositions of extracted melts, with a constant employed critical melt fraction (M_{crit}) 31
2.7 Temporal evolution of the average melt extraction depth and temperature 33
2.8 Temporal evolution of K_2O/Na_2O of modeled compositions of extracted melts, with a decreasing critical melt fraction (M_{crit}) 34
2.9 Evolution of average magma compositions with time of a representative simulation with decreasing M_{crit} 36
2.10 Evolution of magma compositions with time (M_{crit} = constant) and the effect of a second mantle plume 37
2.11 Simplified geological map of the West Eifel volcanic field (West-Germany) 40
2.12 TAS diagram for modeled melts 43
2.13 Employment of different phase diagrams for the metasomatized mantle and their relationship to melt extraction events 44

2.14 Illustration of the development of a step-like-profile in K_2O/Na_2O of the extracted melts from a heterogeneous mantle source 47
2.A1 Pseudosections for the upper and lower crust 51
2.A2 Main initial mineral distribution in the mantle 52
2.A3 Learning process of the SOM 53
2.A4 U-matrix and oxide concentrations of the prototype vectors, solid compositions are provided from the initial phase diagram of the metasomatized mantle 54
2.A5 SOM and k-means applied to solid compositions from the initial phase diagram of the metasomatized mantle 55
2.A6 Identifying representative solid compositions of the initial phase diagram from the metasomatized mantle using SOMs 56
2.B1 Overview of the temporal evolution of K_2O/Na_2O of modeled compositions of extracted melts (M_{crit} = const.) (part 1) 62
2.B2 Overview of the temporal evolution of K_2O/Na_2O of modeled compositions of extracted melts (M_{crit} = const.) (part 2) 63
2.B3 Overview of the temporal evolution of K_2O/Na_2O of modeled compositions of extracted melts (with decreasing M_{crit}) 64
2.B4 Total addition of extracted magmas with time 65
2.C1 Comparison of modeled melt chemistries with magmatic rocks from the West Eifel and from reference volcanic fields 67

3.1 Pseudosections, with different employed $final\_resolution$ values 83
3.2 Change in melt fraction and CaO concentrations with P and T depending on the resolution of the phase diagram 84
3.3 Pseudosections, with different grid resolutions 86

4.1 Different ways to sample the parameter space 99
4.2 Example of a BRC distribution in a 2D representation of the Barnes-Hut t-SNE projection 101
4.3 Finding new BRCs using principal component analysis 103
4.4 Finding new BRCs within manually pre-defined boundaries 105
4.5 New BRCs generated with different sampling methods, without clustering 107
4.6 New BRCs generated with different sampling methods, shown for two different clusters 109

4.7 New BRCs generated with different sampling methods using the clustering algorithm . . . 110
4.8 Minimal Euclidean distances computed between new BRCs and initial BRCs . . . 112
4.9 Minimal Euclidean distances computed between new BRCs and requested BRCs . . . 115
4.10 Requested BRCs and their melt extraction conditions for the oxide combination, CaO vs. SiO_2 . . . 119
4.11 Clustering algorithm applied to requested BRCs from geodynamic simulations . . . 121
4.12 Requested, forecasted and database BRCs shown on a TAS diagram for plutonic rocks . . . 123
4.A1 New BRCs created with M-CS, without clustering . . . 126
4.A2 New BRCs created with uniform PCA-CS, without clustering . . . 127
4.A3 New BRCs created with normal PCA-CS, without clustering . . . 128
4.A4 New BRCs created with normal-centering PCA-CS, without clustering . . . 129
4.A5 New BRCs created with M-CS, with clustering . . . 130
4.A6 New BRCs created with uniform PCA-CS, with clustering . . . 131
4.A7 New BRCs created with normal PCA-CS, with clustering . . . 132
4.A8 New BRCs created with normal-centering PCA-CS, with clustering . . . 133
4.A9 Requested BRCs are shown for two sets of geodynamic simulations . . . 134
4.A10 Melt extraction conditions of requested BRCs from geodynamic simulations, for all SiO_2 oxide combinations . . . 135

5.1 Methodological procedure of melt extraction . . . 151
5.2 Rock failure for tensile fracturing and shear banding . . . 153
5.3 Scheme describing the evolution of chemistry and melt fraction . . . 157
5.4 Initial 2D numerical model configuration . . . 159
5.5 Evolution of the reference simulation . . . 162
5.6 Orientation of dikes . . . 164
5.7 Melt retention as a function of rock cohesion and injection depth . . . 165
5.8 Compositional evolution of the magmatic system . . . 168
5.9 Snapshot of the magmatic system and corresponding mineral assemblages 170
5.10 Influence of water content on melting and fracture formation . . . 172
5.11 Influence of a higher crustal water content on melting and composition . . . 174
5.12 Assimilation of hydrated crustal host rocks . . . 175

5.13 Liquid lines of descent, modeled rock compositions and the change of SiO_2 concentration with melting degree . . . 180
5.14 Model results and rhyolites from the Snake River Plain . . . 181
5.15 Volume of different crust contributions, densities and mineral assemblages 185
5.16 Comparison of modeled igneous rocks with exposed rocks from the Famatinian and Kohistan arc . . . 187
5.A1 Higher basaltic intrusion temperature and its influence on rock compositions . . . 190
5.A2 Volume of different crust contributions, densities and mineral assemblages, for different intrusion conditions (temperature and basalt composition) . . . 191

6.1 Requested rock compositions and bulk rock compositions used in the phase diagram database . . . 208
6.2 Bulk rock compositions of employed phase diagrams (part 1) . . . 209
6.3 Bulk rock compositions of employed phase diagrams (part 2) . . . 210

LIST OF TABLES

2.1 Initial rock compositions used in pMELTS and Perple_X 13
2.A1 Activity-composition models used in the Perple_X calculations 50
2.A2 Rheology parameters used for the dislocation creep 57
2.A3 Rheology parameters used for the diffusion creep in the mantle 58
2.A4 Fixed parameters used in the geodynamic models 58
2.A5 Melt extraction parameters 59
2.A6 Temperature distribution in the initial model setup and in the newly-generated-crust 59
2.B1 Executed numerical experiments (part 1) 60
2.B2 Executed numerical experiments (part 2) 61
2.C1 Comparison of the chemical composition of "primary" lavas of both West Eifel suites with average model compositions of extracted melts from the pyrolitic and metasomatized mantle 68

4.1 Average and maximal D_{min} between initial BRCs and newly requested BRCs from geodynamic simulations 118

5.1 Initial rock compositions used in Perple_X 146
5.2 Parameters used to compute P_{crit} for the four different failure modes . . 153
5.3 Employed parameters used in the presented models 161
5.B1 Excluded and solution phases used in Perple_X 192
5.B2 Rheology parameters used for the dislocation creep 193
5.B3 Diffusion creep rheology parameters 194
5.B4 Constant parameters used in the geodynamic models 194

0.1 Abstract

Understanding the generation and stagnation of melt inside the lithosphere or asthenosphere is crucial to understand eruption processes on Earth. Recent advances in developing new thermodynamic melting models allow us to model realistic rock compositions and to investigate their properties (density, melt fraction, chemistry and mineralogy) with pressure (P) and temperature (T). Incorporating such thermodynamic data into a thermomechanical code is required to better understand the temporal and spatial evolution of magmatic systems. In this thesis, we develop different approaches that couple geodynamic with thermodynamic modeling to investigate the compositional evolution of magmatic systems, focusing on intraplate magmatism triggered by a rising mantle plume and on arc-related crustal magmatism.

The mantle plume consists of a heterogeneous source composed of pyrolitic and metasomatized mantle. Decompression and the occurrence of hydrous mantle rocks cause melting in the rising plume at different stages. The generated melt is extracted, as a critical melt fraction is exceeded, and is emplaced within or on top of the crust. Compositional trends of the extracted melts (consisting of up to twelve oxides) are used to describe melting related processes by focusing on the K_2O/Na_2O ratio as an indicator for the rock type that has been molten. The results are compared with magmatic rocks of the West Eifel volcanic field (Germany) to propose a possible scenario to explain the observation that features a trend of high-enriched to less-enriched rocks with time. The computation of mantle phase diagrams is executed with pMELTS, under consideration of several rock depletion degrees at different P–T conditions. To decrease the number of precomputed phase diagrams, a Self-organizing Map (SOM) is used to define P–T ranges of similar bulk rock compositions.

The chemical and the mineralogical evolution of the crust during arc magmatism are studied by incorporating a semi-analytical fracture algorithm into a geodynamic code to simulate dike/sill formation. Sill intrusion triggers the formation of dikes which propagate in the direction of the maximum principal stress. Each melt extraction event is leaving behind a depleted source with locally changeable rock compositions (10 oxides are considered) that is enhanced in case magma mixing is involved. To track this change in rock composition on each individual marker, tens of thousands of phase diagrams are precomputed using Perple_X. As the longevity of magma reservoirs is decisive for magma differentiation's efficiency, we investigate the conditions that keep regions of accumulated sills in a partially crystallized state (e.g., lower rock cohesion or deeper sill injection zone). Produced rocks are compared with igneous rocks from different arcs and the relevance of

the different rock types for crust genesis is evaluated.

Furthermore, we present an autonomous forecast approach to extend the phase diagram database with possible rock composition requests from geodynamic simulations. For this, new bulk rock compositions are determined within boundaries that are constrained manually or through principal components. A reduction of the sampling space is considered by applying a clustering algorithm to the database entries.

The developed petro-thermo-mechanical code can be applied to a wide range of geological settings to study magmatic processes that result in the formation of different igneous rock types.

0.2 Zusammenfassung

Um Vulkanausbrüche und deren Ursprung besser verstehen zu können, ist die Untersuchung der Generierung sowie der Stagnierung der Schmelze in der Lithosphäre oder Asthenosphäre von zentraler Bedeutung. Neueste Fortschritte in der Entwicklung thermodynamischer Schmelzmodelle erlauben uns die Gesteine und deren Eigenschaften (Dichte, Schmelzanteil, Chemie und Mineralogie) über Druck (P) und Temperatur (T) genauer zu bestimmen. Die Integrierung dieser thermodynamischen Daten in einen geodynamischen Code ist notwendig, um die zeitliche sowie räumliche Entwicklung von magmatischen Systemen besser nachvollziehen zu können. In dieser Arbeit haben wir verschiedene Verfahren entwickelt, zur Kopplung geodynamischer mit thermodynamischer Modellierung, um die Entwicklung der chemischen Zusammensetzung in magmatischen Systemen zu ermitteln. Hierbei liegt der Fokus einerseits auf Intraplattenmagmatismus ausgelöst durch einen aufsteigenden Mantelplume und andererseits auf krustale Magmareservoire in einem kontinentalen magmatischen Bogen.

Der Mantelplume besteht aus einer heterogenen Quelle, die aus pyrolitischen und metasomatisierten Mantel zusammengesetzt ist. Auf Grund von Druckentlastung sowie dem Vorkommen wasserreicher Gesteine, kommt es während des Aufstieges zur Schmelzbildung. Die Schmelze wird jeweils extrahiert, sobald der kritische Schmelzanteil erreicht ist, und entweder innerhalb der Kruste oder an der Oberfläche platziert. Zusammensetzungstrends der extrahierten Schmelze (bestehend aus bis zu 12 Oxiden), hier vor allem das K_2O/Na_2O Verhältnis, werden verwendet, um aufschmelzungsbezogene Prozesse zu ermitteln. Die hieraus gewonnenen Ergebnisse sind mit magmatischen Gesteinen aus der West Eifel verglichen worden, um ein mögliches Modell zu deren Entstehung herzuleiten. Die Berechnung der Phasendiagramme wird für verschiedene Verarmungsgrade des Mantels mit dem Programm pMELTS durchgeführt. Um die Anzahl der Phasendiagramme zu reduzieren, werden mit Hilfe einer sogenannten "Self-organizing Map"(SOM) P–T Bereiche bestimmt, in denen ähnliche Gesteinszusammensetzungen vorliegen.

Die chemische und mineralogische Entwicklung des kontinentalen magmatischen Bogens sind untersucht worden, unter Einbeziehung eines semi-analytischen Algorithmus zur Bildung von Dikes und Sills. Intrudierte Sills führen zur Bildung von Dikes, deren Entstehung und Ausbreitung durch das Spannungsfeld kontrolliert werden. Jeder dieser Schmelzextrahierungsevents hinterlässt eine abgereicherte Quelle, dessen Zusammensetzung (bestehend aus 10 Oxiden) stark lokal variiert, insbesondere wenn Magmamischung involviert ist. Um diese Änderung auf jedem einzelnen Marker zu verfolgen, sind zehntausende Phasendiagramme berechnet worden, unter Verwendung des Programmes Perple_X.

Da die Langlebigkeit von Magmareservoiren ausschlaggebend für die Differentiation des Magmas ist, haben wir unseren Schwerpunkt darauf gelegt, unter welchen Bedingungen eine vollständige Kristallisation verzögert werden kann (z.B. mit einer geringeren Gesteinskohäsion oder einer tieferen Zone der injizierten Sills). Die modellierten Gesteinszusammensetzungen sind mit natürlichen magmatischen Gesteinen verglichen und deren jeweiliger Beitrag zur Krustenbildung evaluiert worden.

Weiterhin präsentieren wir hier eine Strategie zum effizienten Aufbau und Erweiterung einer Phasendiagrammdatenbank. Hierzu werden neue Gesteinszusammensetzungen bestimmt, die kompositionell innerhalb manueller oder, durch Hauptkomponentenanalyse (PCA) definierter, Grenzen liegen. Der Parameterraum wird durch ältere Datenbankeinträge beschrieben, die in Gruppen ähnlicher Zusammensetzung unterteilt werden können.

Der entwickelte petrologische-thermomechanische Code kann auf verschiedenste geologische Bereiche angewendet werden, um magmatische Prozesse zu untersuchen, die zur Bildung unterschiedlichster magmatischer Gesteinstypen führen.

CHAPTER 1

INTRODUCTION

The chemical and mineralogical evolution of magmatic systems within the Earth are still incompletely understood, as most observations are limited by the temporal or spatial resolution. Geodynamic models focus mostly on mechanical problems, neglecting the chemical variety produced by melting related processes. Other models look into the chemical evolution of magma reservoirs but do not consider the large scale mechanical processes in the surrounding rocks. Therefore, we focus here on the coupling of geodynamics with thermodynamics to fill the gap between thermomechanical and chemical models. As the melting process is non-linear (see Section 1.2) and strongly changes with rock composition, a sufficiently large number of thermodynamic phase diagrams is required to take the variable chemistry of extracted melts and cumulates/residuum into account. This enables us to study the evolution of rock compositions in detail. As melting processes directly affect the dynamics in the models (e.g., density, melt fraction and thus viscosity), they have to be incorporated into lithosphere-scale models.

In this thesis, we analyze the compositional evolution of magmatic systems by incorporating thermodynamic phase diagrams for a wide range of bulk rock compositions into a 2D geodynamic finite element code. The results improve our knowledge about both crust formation and the chemical composition of potentially extracted melt that controls eruption processes on Earth.

1.1 MELT GENERATION

Magmatism is observed all over the world and can be triggered through different kinds of processes. At mid ocean ridges (MORs), mantle rises due to the diverging plates and creates an enormous amount of decompression melting. Intraplate magmatism is often triggered by a rising mantle plume that produces decompression melting as well. The reduced density that causes the buoyancy of mantle material, is attributed to an excess temperature of the plume towards the surrounding mantle, or to compositional anomalies. A further melting mechanism is the supply of fluids, which decreases the solidus temperature. This wet solidus plays especially in arc systems an important role. Here, melts are generated by the fluid release from the subducting oceanic plate into the mantle wedge. As soon as these melts stagnate within the mantle or crust, fractional crystallization, melt segregation, assimilation and other processes such as magma mixing or mingling may take place. In case the temperature of the intruded magma is sufficiently high compared to that of the host rocks, partial melting of crustal material may occur. On smaller scales, also mechanical processes can increase the temperature and thus trigger melting (e.g., Pseudotachylites in fault zones). The general mechanisms of melt generation through temperature increase, water supply, or pressure increase/decrease are summarized in Figure 1.1.

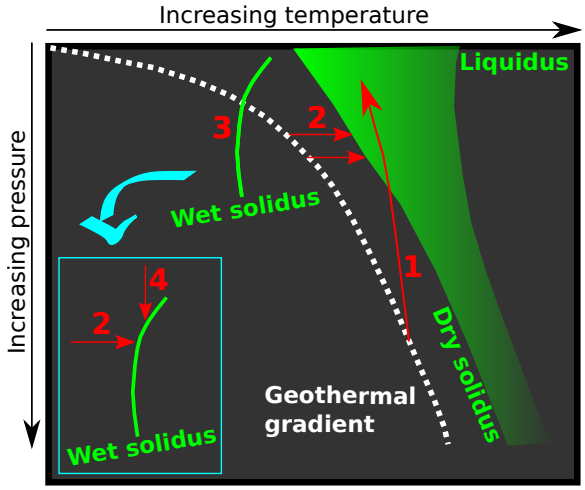

Figure 1.1: Melting of peridotites through 1: Adiabatic upwelling (decompression melting); 2: Temperature increase; 3: Supply of fluids that generates an opposite solidus curve; 4: Increase of pressure that results in melting for a wet solidus. Modified from Winter (2013).

1.2 NON-LINEARITY OF CRYSTAL-MELT RATIO WITH DECREASING TEMPERATURE

The melt solid proportions do not change linearly with decreasing temperature over the crystallization interval (between liquidus and solidus at constant pressure) and are therefore not easily describable with simple parameterizations. This can be illustrated on a binary eutectic system for two different liquid starting compositions (X1 and X2, Fig. 1.2). For composition X1, a solid proportion of 50% is already reached at a high temperature (T2), whereas an only slightly different starting composition (X2) requires a much lower temperature (T3) to reach the same amount of crystals in the cooling system, even though the liquidus temperatures for both compositions are quite similar. Consequently, for the same crystallization stage, the residual melt compositions and temperatures may be more distinct than at the beginning (see liquid compositions after 50% of crystallization, X1=A(65%)B(35%) and X2=A(55%)B(45%), Fig 1.2). This temperature difference between potentially extracted melts with an equivalent crystal proportion may even influence the melt properties, e.g. viscosity. Moreover, changing the starting composition in such a way that it evolves towards the eutectic (e) from the other side (X3, Fig. 1.2), leads to the crystallization of phase B at the beginning instead of phase A. Thus, especially for two similar starting compositions, which are located on different sides of the eutectic, the crystallization phases may be very different. At the eutectic (e) both phases crystallize simultaneously at a constant temperature until all melt is gone. Changing the pressure for the cooling system additionally influences each binary system. The observed non-linearity between melt crystal proportions and the effect of small variations in starting compositions become even larger in more complex natural systems, with eutectic, peritectic and cotectic reactions (Caricchi and Blundy, 2015). Therefore, simplified parameterizations do not even approximate the complexity observed in natural melting or freezing processes. Thus, phase diagrams describing the melting behavior over the whole melting interval for different starting compositions are required.

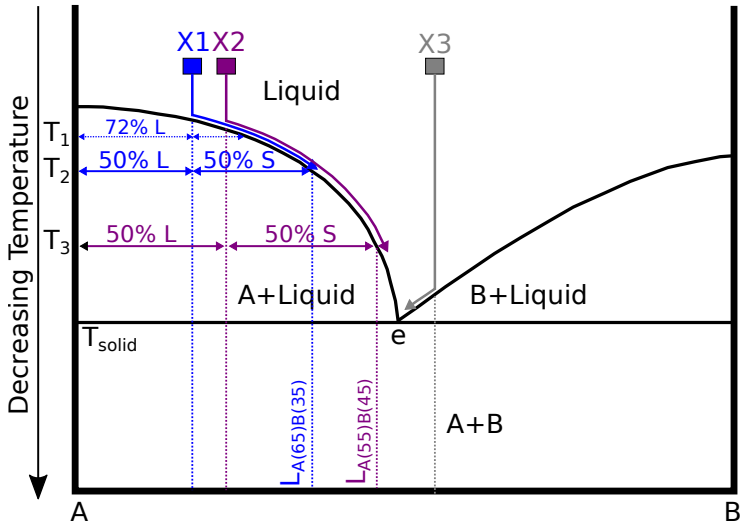

Figure 1.2: Schematic binary phase diagram showing the non-linear evolution of the solid (S)-liquid (L) ratio with decreasing temperature. Shown here for three different starting compositions (X1, X2 and X3). A and B are the crystallizing solid phases. Shifting only slightly the starting compositions (from X1 to X2) has already a significant effect on both the crystallization (solid-liquid ratio with decreasing temperature) and the liquid compositions.

1.3 THESIS STRUCTURE

The thesis contains five main chapters (Chapters 2–6) describing the coupling between geodynamic and thermodynamic modeling for two application fields, intracontinental magmatism caused by a rising mantle plume, and crustal magmatic reservoirs in an arc-like system. For the mantle plume study (Chapter 2), phase diagrams are computed mainly with pMELTS (Ghiorso et al., 2002). For studying crustal magma reservoirs, Perple_X (Connolly, 2005, 2009) is exclusively used (Chapters 3–6).

Chapter 2: Coupled petrological-geodynamical modeling of a compositionally heterogeneous mantle plume

This chapter deals with a rising mantle plume composed of pyrolitic and metasomatized mantle. The composition of the extracted melt is tracked in time and space via 12 oxides. The depth of the lithosphere-asthenosphere boundary, the extractable melt fraction and the plume temperature are systematically varied to investigate their influence on melt chemistry and plume dynamics. The rock depletion degree and the stable melt fraction play an essential role. Melt compositional trends are used to determine melting related processes using the K_2O/Na_2O ratio as an indicator for the rock type that has been molten. The chemistry of extracted melts is compared with magmatic rocks from the West Eifel.

Precomputed phase diagrams are incorporated into the 2D geodynamic finite element code (MVEP2), in which melt is extracted and emplaced instantaneously within or on top of the crust. Mantle phase diagrams (> 600 in total) are computed for different rock depletion degrees using pMELTS. To reduce the number of precomputed phase diagrams, a SOM (Self-organizing Map) is applied to find P–T fields of similar bulk rock compositions.

Chapter 3: Resolution of phase diagrams and computational cost
This chapter is about optimizing the computational cost for phase diagram calculations using Perple_X. We systematically vary option parameters in Perple_X to get an acceptable phase resolution by reducing the computation time to a minimum.

Chapter 4: An autonomous phase diagram database for geodynamic simulations of magmatic systems
This chapter presents an autonomous forecast approach that uses the entries of the existing (initial) phase diagram database to predict possible requests of chemical composition from geodynamic simulations. The bulk rock compositions of this initial database are requested compositions from previously performed geodynamic simulations with numerical model configurations described in Chapter 5. With our forecast approach, new bulk rock compositions are determined within boundaries that are constrained manually or through principal components. A possible reduction of the sampling space is considered by applying a clustering algorithm to the entries of the initial database. Using these new bulk rock compositions massively accelerates the extension of the database, as they can be used to create new phase diagrams using Perple_X. The repetition of geodynamic simulations is not necessarily needed anymore to collect new bulk rock compositions to extend the database in such a way that almost all requested phase diagrams are provided.

Chapter 5: Insights into the compositional evolution of crustal magmatic systems from coupled petrological-geodynamical models
This chapter deals with the chemical/mineralogical and dynamical evolution of crustal plutonic systems in an arc-like environment. The 2D geodynamic code MVEP2 is extended by a semi-analytical fracture opening algorithm that generates dikes and sills depending on the local stress field. Magma mixing is considered in a simplified manner. Melt is extracted from injected sills to form dikes while depleting the source region. Accumulated sills are turning into long-lived mush chambers by using a lower rock cohesion or due to high intrusion depths. High silica rocks (e.g. granites) are generated by partial melting of host rocks, melt segregation within dikes, and from high-degree fractional crystallization

of basalts. For the genesis of arc continental crust are these highly in silica enriched rocks only of minor relevance, as mafic to intermediate rocks dominate. The chemical evolution of extracted melts and related cumulates/residuum is tracked in detail via 10 main oxides by using up to thousands of phase diagrams within a single geodynamic simulation. In total ∼58,000 phase diagrams are available in the database constructed using Perple_X. The establishment and the extension of this database (up to 27,049 phase diagrams) are presented in Chapter 4. The additional database extension (from ∼27,000 to ∼50,000 phase diagrams) is mainly caused by partial melting of host rocks that required additional phase diagrams. The bulk rock compositions of all available phase diagrams are described in Chapter 6.

Chapter 6: Employed phase diagrams and their bulk rock compositions
In this chapter, bulk rock compositions of all computed phase diagrams of the database used in Chapter 5 are evaluated in the oxide parameter space. It is shown that the bulk rock compositions of employed phase diagrams are distinct for different rock phases and follow magma differentiation trends.

Chapter 7: Final remarks and outlook
Here, final remarks on the model results and methods are presented and an outlook is given.

REFERENCES

Caricchi, L., Blundy, J., 2015. The temporal evolution of chemical and physical properties of magmatic systems. Geological Society, London, Special Publications 422, SP422–11.

Connolly, J., 2009. The geodynamic equation of state: what and how. Geochemistry, Geophysics, Geosystems 10 (10).

Connolly, J. A., 2005. Computation of phase equilibria by linear programming: a tool for geodynamic modeling and its application to subduction zone decarbonation. Earth and Planetary Science Letters 236 (1), 524–541.

Ghiorso, M. S., Hirschmann, M. M., Reiners, P. W., Kress, V. C., 2002. The pMELTS: A revision of MELTS for improved calculation of phase relations and major element partitioning related to partial melting of the mantle to 3 GPa. Geochemistry, Geophysics, Geosystems 3 (5), 1–35.

Winter, J. D., 2013. Principles of igneous and metamorphic petrology. Pearson Education.

CHAPTER 2

COUPLED PETROLOGICAL-GEODYNAMICAL MODELING OF A COMPOSITIONALLY HETEROGENEOUS MANTLE PLUME

This chapter has been published in:

Rummel, L., Kaus, B.J.P., White, R. W., Mertz, D.F., Yang, J., Baumann, T.S. (2018). Coupled petrological-geodynamical modeling of a compositionally heterogeneous mantle plume. Tectonophysics, 723, 242-260. The appendix is extended.

Abstract Self-consistent geodynamic modeling that includes melting is challenging as the chemistry of the source rocks continuously changes as a result of melt extraction. Here, we describe a new method to study the interaction between physical and chemical processes in an uprising heterogeneous mantle plume by combining a geodynamic code with a thermodynamic modeling approach for magma generation and evolution. We precomputed hundreds of phase diagrams, each of them for a different chemical system. After melt is extracted, the phase diagram with the closest bulk rock chemistry to the depleted source rock is updated locally. The petrological evolution of rocks is tracked via evolving chemical compositions of source rocks and extracted melts using twelve oxide compositional parameters. As a result, a wide variety of newly generated magmatic rocks can in principle be produced from mantle rocks with different degrees of depletion. The results show that a variable geothermal gradient, the amount of extracted melt and plume excess temperature affect the magma production and chemistry by influencing decompression melting and the depletion of rocks. Decompression melting is facilitated by a shallower

lithosphere-asthenosphere boundary and an increase in the amount of extracted magma is induced by a lower critical melt fraction for melt extraction and/or higher plume temperatures. Increasing critical melt fractions activates the extraction of melts triggered by decompression at a later stage and slows down the depletion process from the metasomatized mantle. Melt compositional trends are used to determine melting related processes by focusing on K_2O/Na_2O ratio as an indicator for the rock type that has been molten. Thus, a step-like-profile in K_2O/Na_2O might be explained by a transition between melting metasomatized and pyrolitic mantle components reproducible through numerical modeling of a heterogeneous asthenospheric mantle source. A potential application of the developed method is shown for the West Eifel volcanic field.

2.1 INTRODUCTION

Understanding the mechanisms that trigger intracontinental volcanism is a critical step in understanding eruption processes on continents. However, as there are substantial complexity and chemical variability both within volcanic fields and between them, the interactions between physical and chemical processes are incompletely understood. Coupling geodynamic simulations with thermodynamic models allows making testable model predictions, which can be compared with petrological constraints and is thus a crucial step in understanding magmatic systems developing above mantle plumes. Such studies should in principle allow for a heterogeneous melting source within a plume, which is one of the typical endmember models proposed for plume-related magmatism (e.g. Phipps Morgan, 2000; Ito and Mahoney, 2005).

Many previous modeling studies focus on mantle plume dynamics and its interaction with the lithosphere. Yet, they typically do not take the chemical evolution of melts and source rocks into account (e.g. Gerya, 2014), and neglect continuous source rock depletion by fractional melting (e.g. Ribe and Christensen, 1999; Koptev et al., 2015). Other models have focused on the deep structure, origin and dynamics of plumes (e.g. Dannberg and Sobolev, 2015) and possible melt triggering mechanisms (e.g. Motoki and Ballmer, 2015). Many existing numerical models on melting processes employ a fixed chemistry for the source rocks and thus produced only a limited range of melt compositions (e.g. Gerya and Meilick, 2011; Vogt et al., 2012, 2013; Gorczyk et al., 2017). Others focus on the slab dehydration and induced melting processes in subduction zones by including thermodynamic modeling (Hebert et al., 2009; Gerya and Meilick, 2011; Bouilhol et al., 2015; Yang et al., 2017). Numerical simulations that are used to better constrain geochemical signa-

tures in crystallized plume-related magmas exist but are often simplified (e.g. Sossi et al., 2016). Combining geochemical signatures from erupted magmas with physically consistent geodynamic models might help to better understand how the chemical evolution of intracontinental magmas is connected to mantle plume dynamics.

From a thermodynamic point of view, quite realistic melting models have been developed, such as pMELTS for mantle melting (Ghiorso et al., 2002), and melting models for pelitic crustal rocks (White et al., 2001, 2014). Yet, coupling these models with geodynamic simulations is challenging as it, in principle, requires a new thermodynamic computation as soon as a small amount of melt has been extracted from the source rock. Depending on the complexity of the source rocks and the mantle models, computing a phase diagram may last a few hours, which may quickly become computationally infeasible if this calculation is done on the fly. To circumvent this problem, parameterizations have been developed for mantle melting (Katz et al., 2003), or more recently, mantle melting models that take the effect of CO_2 and H_2O on mantle melting into account (Keller and Katz, 2016). Whereas such models allow for a self-consistent coupling between reactions and deformation, they have the disadvantage that making petrological and geochemical predictions from them can only be done in an indirect manner, which complicates comparing the results with constraints.

In this work, we describe a different approach that takes thermodynamic melting models into account, but that reduces the computational requirements by using a method that combines diagrams with a similar chemical composition which allows precomputing the phase diagrams. In this manner, we can track the evolution of the source rocks and ascending melts and track quantities such as evolving major element composition of melt and continuous changes in the mantle source compositions from melt extraction. We apply the coupled geodynamic and thermodynamic models to the West Eifel volcanic field.

2.2 THERMODYNAMIC AND GEODYNAMIC MODELING APPROACHES

The mechanical and thermal evolutions within the continental lithosphere and asthenosphere are strongly affected by melt-related processes. Magma emplacement may heat up the crust and previously partially molten mantle sources become depleted (which results in a higher solidus temperature and hence an increase in density), which influences the buoyancy of mantle material. The loss of melt increases the viscosity, decreases the strain rate and thus influences the convective vigor in the mantle. On the other hand, these pro-

cesses that occurred in the mantle leave their fingerprints in the extracted melts. In our work, we focus on the connection between mechanical and thermal processes and melting related compositional trends found in extracted magmas, by modeling the dynamic and chemical evolution of a heterogeneous mantle plume. The plume consists of two different mantle sources, a pyrolitic and a metasomatized composition, respectively. For this, we combine a geodynamic code MVEP2 (Kaus, 2010; Thielmann and Kaus, 2012) with a petrological model. As petrological model, we use the Gibbs free energy minimization approach pMELTS (Ghiorso et al., 2002) and Perple_X (Connolly, 2009). Phase diagrams based on specific bulk rock compositions are computed using pMELTS and Perple_X to produce thermodynamic-dependent parameters (density, melt fraction, chemistry of melt and residuum) over a given P–T range. The information from the phase diagrams is used in the geodynamic simulations to model the interaction between physical and chemical processes. During geodynamic simulations, the chemical system might change locally due to melt extraction and thus phase diagrams have to be continuously updated (e.g., with a higher density and solidus temperature). Each phase diagram is computed for a specific bulk rock composition. The computation of phase diagrams is described in Section 2.2.1 with the rock compositions used for the initial model setup outlined in Section 2.2.1.1. The general procedure describing the geodynamic modeling, the melt extraction algorithm and the incorporation of updated phase diagrams into the geodynamic code, is described in Section 2.2.2. We do not take melt extraction from the crust into account in this work, predominantly because this seems to be only of minor importance in our application area, the Eifel. The computed phase diagrams for the crust are used to track the density distribution and the latent heat of fusion for emplaced magmas originated from melting the mantle.

2.2.1 Thermodynamic modeling

2.2.1.1 Rock compositions

In the simulations, we assume the continental crust to consist of an upper and lower crust, using compositions after Taylor et al. (1981). For an enriched (metasomatized) mantle, a hydrous lherzolitic lithospheric mantle xenolith from the Eifel was used, and for the anhydrous, more primitive mantle, the pyrolitic mantle composition of McDonough and Sun (1995) was employed (Tab. 2.1). For the newly-generated magmatic rocks in the crust, generated by melt extraction, an average chemical composition of the total extracted melt is used (newly-generated-crust, Tab. 2.1). The rock compositions outlined above were used

to compute the initial phase diagrams employed at the onset of the numerical simulations.

Table 2.1: Initial rock compositions used in pMELTS and Perple_X. "Pyrolitic mantle" (pyrolite model, McDonough and Sun, 1995), where MnO, NiO and P_2O_5 are excluded from the database. As "Metasomatized mantle" a mica pargasite lherzolite mantle xenolith from the location Deudesfeld (Germany) is used (Menzies et al., 1987). A water concentration of 0.15 wt% is added to the xenolith composition. Composition of the "Upper crust" and "Lower crust" (Taylor et al., 1981) are extended by 1.0 and 0.1 wt% water content. The water has to be added, because the respective rock analyses are calculated on LOI (loss on ignition) free basis. Oxides are given in wt%. The FeO to Fe_2O_3 ratio is automatically calculated by pMELTS along the QFM buffer. The "Newly-generated-crust" is based on the average chemistry of extracted melts of one exemplary executed simulation.

Oxide	**Mantle** **(pyrolitic)**	**Mantle** **(metasomatized)**	**Upper crust** **(0–10 km depth)**	**Lower crust** **(10–30 km depth)**	**Crust** **(newly-generated)**
SiO_2	45.00	41.10	66.00	54.00	42.03
TiO_2	0.20	0.42	0.60	0.90	2.65
Al_2O_3	4.45	2.48	16.00	19.00	11.55
Fe_2O_3	-	10.03	-	-	-
Cr_2O_3	0.38	-	-	-	-
FeO	8.05	-	4.50	9.00	10.94
MgO	37.80	41.02	2.30	4.10	16.35
CaO	3.55	3.36	3.50	9.50	5.64
Na_2O	0.36	0.60	3.80	3.43	6.98
K_2O	0.03	0.54	3.30	0.60	3.23
P_2O_5	-	0.07	-	-	-
H_2O	-	0.15	1.00	0.10	0.94

2.2.1.2 pMELTS

The AlphaMELTS 1.4 software package (Smith and Asimow, 2005) was used as a text-menu based front-end to the pMELTS software (Ghiorso et al., 2002) to facilitate thermodynamic modeling of phase equilibria in magmatic systems. The pMELTS algorithm allows phase equilibria calculations by Gibbs free energy minimization along a given P–T path and for a specified oxygen buffer (e.g., the quartz–fayalite–magnetite (QFM) oxygen buffer in our calculations).

The solid and liquid oxide compositions as well as densities and melt fractions for a given mantle rock composition were computed by pMELTS along a given P–T path (determined every 0.03 GPa and 5 °C) in a batch melting mode. The chemical system used is: SiO_2–TiO_2–Al_2O_3–Fe_2O_3–Cr_2O_3–FeO–MgO–CaO–Na_2O–K_2O–P_2O_5–H_2O.

Computing such phase diagrams simultaneously with a geodynamic simulation is computationally infeasible with pMELTS, as the provided binary code frequently fails to converge, and existing melt parameterizations (e.g. Katz et al., 2003) are only valid for limited compositional ranges. As the source code of pMELTS is not made available, we were

not able to fix the bugs that cause the numerical issues. Therefore, a different strategy was employed in which a large number of phase diagrams for different melting and melt extraction scenarios were precomputed. This method is general as long as sufficient thermodynamic data exist to predict the solidus and liquidus as well as the melt and depleted rock chemistry.

Starting from an initial phase diagram (for a pyrolitic or metasomatized composition, Tab. 2.1), solid compositions that are in equilibrium with small amount of melt fractions and thus near the solidus P–T field, are used as starting rock compositions in pMELTS for depleted rocks affected by a potential melt extraction scenario. Thus, before starting the geodynamic simulations, all relevant phase diagrams are already precomputed, which are valid for selected bulk rock chemistries. Which phase diagrams will effectively be used in the respective geodynamic simulation depends on the mechanical, thermal and compositional evolutions and is thus controlled by melt extraction conditions (P, T, melt percentage). The P–T conditions control the melt fraction that influences the solid chemistry on the marker and thus the choice of updated phase diagram (see Section 2.2.2.2).

Two different methods, dependent on the initial rock type (pyrolitic or metasomatized mantle), were used to take progressive source rock depletion with melt extraction events into account:

1. Pyrolitic mantle:

Starting from the initial phase diagram of the pyrolitic mantle, solid compositions as bulk rock compositions for future pMELTS computations are taken and stored in a separate file. The solid compositions are taken from the near solidus P–T field of the initial phase diagram at certain fixed pressure steps (every ∼0.65 GPa of a predefined pressure interval) and for specified melt fractions (1, 2, 4, 6 and 8 vol%). By using the respective solid compositions as residual depleted bulk composition as input, we compute thermodynamic-dependent properties (density, melt fraction and composition) using pMELTS for rocks that were affected by previous melt extraction events. The method is repeated to take subsequent melt depletion into account. In this way, phase diagrams for possible fractional melting processes that may occur in the geodynamic simulations, are precomputed by discrete melt extraction events at different P–T conditions along different liquid isolines (Fig. 2.1). 25 phase diagrams were computed for a possible first depletion event and starting from these 25 phase diagrams, additional 625 phase diagrams (25 for each previous one) were computed based on selected solid chemistries from the depleted phase diagrams. To cross-check whether the residual rock compositions we used covered all chemically relevant

fields between the solidus and ∼10 vol% of melt, a neural network approach was applied (Fig. 2.2, described in more detail in Section 2.2.1.3).

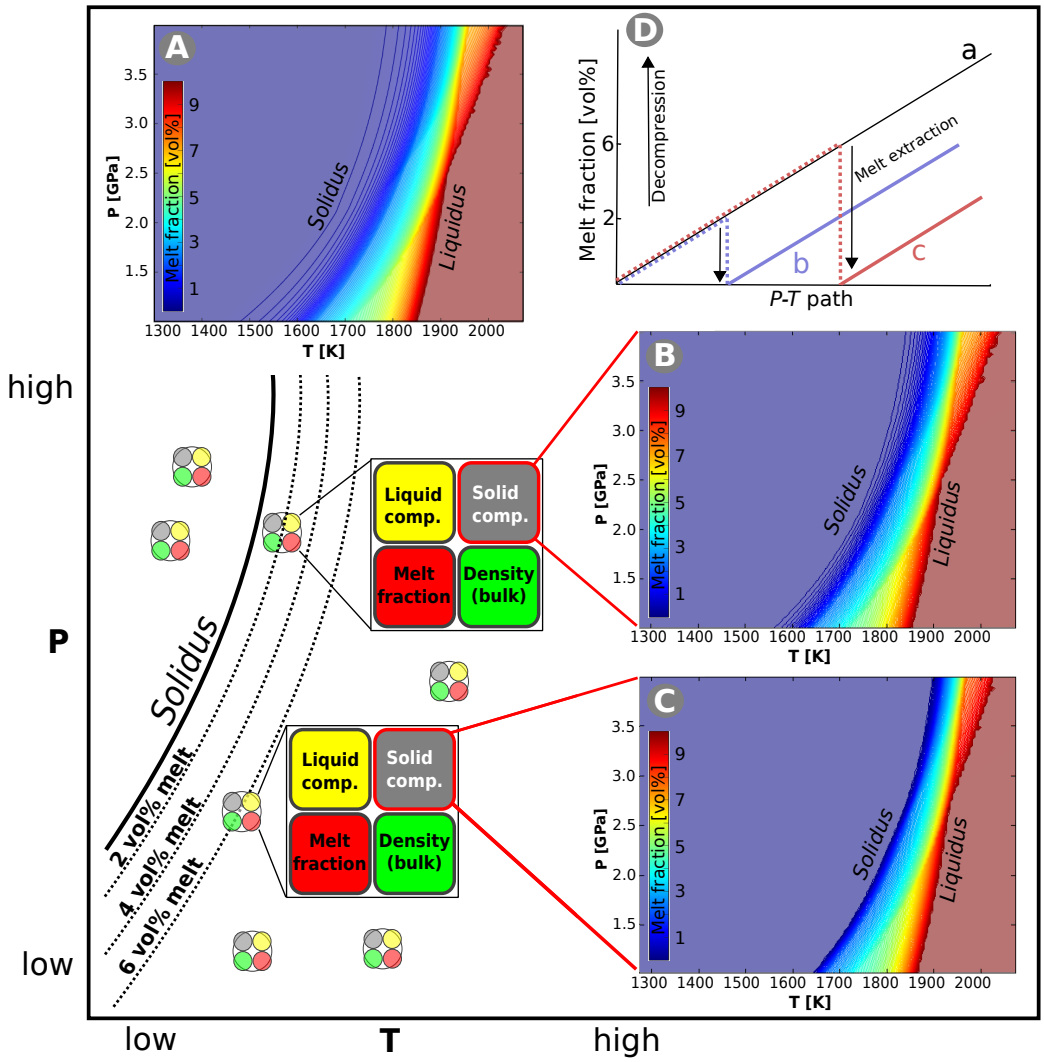

Figure 2.1: Evolving thermodynamic modeling approach employed here. The schematic is shown on three exemplary phase diagrams of the pyrolitic mantle (A, B, C). At each P–T condition, melt fraction (red boxes), density (green boxes) and oxide composition of the liquid (yellow boxes) and solid phase (grey boxes) are computed on a regular grid (every 0.03 GPa and 5 °C) using pMELTS. The change in the melt fraction with P and T for the initial (A) and depleted (B and C) rock compositions. Each of the three phase diagrams has a specific bulk rock chemistry. For the depleted phase diagrams (B, C) this bulk chemistry is defined by the solid composition at P–T condition where the melt is extracted. Using a solid rock composition equilibrated with a lower melt fraction (B), a lower solidus temperature is computed than for the residual solid composition stable with a higher percentage of melt (C). The interval between the liquid isolines in A, B and C is 1 vol% in melt fraction. D: Schematic describing how melt will increase in the geodynamic simulation due to decompression of mantle material until it exceeds a critical melt fraction (2 or 6 vol% here) for melt extraction. After melt extraction from the initial rock (a), the melt can be built up again in the more depleted rocks (b and c).

2. Metasomatized mantle:

For the metasomatized mantle, we use a neural network approach (see Section 2.2.1.3) to find representative solid residue compositions from the initial phase diagram, focusing on the near solidus P–T field (0–10 vol% melt). A representative solid residue composition is a composition that is representative for the solid chemistry in a certain P–T range and distinguishable to other representative solid compositions from neighboring P–T fields (Fig. 2.2). By using the representative solid compositions as input compositions in pMELTS, rock depletion after potential melt extraction events is considered. The total number of computed phase diagrams was 56. 7 based on solid residual compositions remained after a potential first melt extraction event (Fig. 2.A6, see Appendix) and additional 49 phase diagrams for a second melt extraction event from the already depleted phase diagrams. For each of the 7 depleted phase diagrams, a neural network approach is applied again in the same way as described for the initial phase diagram (Fig. 2.A6, see Appendix). The advantage of this method is that it greatly reduces the number of phase diagrams that have to be computed. This was particularly important for the hydrated metasomatized mantle compositions, for which pMELTS calculations were numerically more unstable.

The implementation of multiple melt extraction events takes into account the change in source rock chemistry over time until the solidus is shifted to such high temperatures that melting no longer occurs under typical upper mantle conditions (Fig. 2.1). To stabilize the pMELTS calculations in general and to minimize random crashes and hangups of the distributed binary program, a minimum value of incompatible elements (order of few ppm) in all depleted and multiply-depleted hydrous and anhydrous rock compositions were incorporated.

The choice of phase diagrams used in each geodynamic simulation after melt extractions is limited by the number of precomputed ones (several hundreds in our study). The phase diagram with the closest bulk rock composition to the solid chemistry on the marker replaces the previous one after melt extraction in the geodynamic simulation (see Section 2.2.2.2). Ideally, a future version of our algorithm would cover the full range of compositions required in the simulations, but this will require a massively parallel computational framework to precompute such phase diagrams, and likely involve 10's to 100's of thousands of precomputed diagrams.

2.2.1.3 Finding representative chemical compositions using Self-organizing Maps

Precomputing phase diagrams for all residual (solid) compositions that remain after melt extraction in the geodynamic models, is currently computationally infeasible. Instead, our strategy is to identify representative depleted rock compositions that are used as input for the thermodynamic models (pMELTS). Classifying all compositions that may result from our geodynamic model into groups of similar models and finding representative models for each group is non-trivial. One possibility is to employ a neural network approach, which seems appropriate because the compositions are multidimensional (we have a total of 10 or 11 compositional dimensions, with 10 oxides for the pyrolitic and 11 oxides for the metasomatized mantle). We use a method called "Self-organizing Maps" (SOM, Kohonen, 2001), which is available as a MATLAB toolbox (Vesanto et al., 2000), in combination with k-means clustering (e.g. Jain and Dubes, 1988). An illustrative example and a more detailed description of how the SOM works including a code example can be found in Baumann (2016).

In our study, the SOM is used to find representative depleted rock compositions that may be produced by any kind of melt extraction scenario in the executed geodynamic simulations. A graphic example of how such a classification procedure works is given in Figure 2.2 and in Figure 2.A6 (see Appendix). The data set to which the SOM was applied here, consists of 2325 combinations of rock compositions. Each of the rock composition consists of 10 or 11 oxides that correspond to a pressure and temperature condition and thus to a specific melt fraction. The number is coming from the resolution of each phase diagram which has ∼100 pressure and ∼100 temperature values producing a grid of 100×100 P–T points. However, the P–T range used in the SOM is reduced to near solidus P–T conditions, which decreases the number from 10,000 to 2325. The only information that is provided to the SOM, are the oxide concentrations (Fig. 2.2C and Fig. 2.A6C, see Appendix). The SOM analysis of solid compositions (2325 combinations) of the near-solidus P–T field (0–10 vol% melt and 1.0–4.0 GPa) yielded seven groups that are compositionally distinguishable on the basis of variations in the major oxides (Fig. 2.2C and Fig. 2.A6C, see Appendix). Based on the distribution in the parameter space that is spanned by the axes of oxide concentration, the SOM identifies parts of the diagram that have similar compositions in terms of the various oxide contents. The classes are color coded, and in Figure 2.2A–B and Figure 2.A6A–B (see Appendix), the classification result is illustrated in terms of pressure, melt fraction and temperature. At least one representative solid composition from each class is used within pMELTS to compute density, melt fraction as

well as liquid and solid composition of depleted rocks from pyrolitic mantle (Fig. 2.2) and metasomatized mantle (Fig. 2.A6, see Appendix).

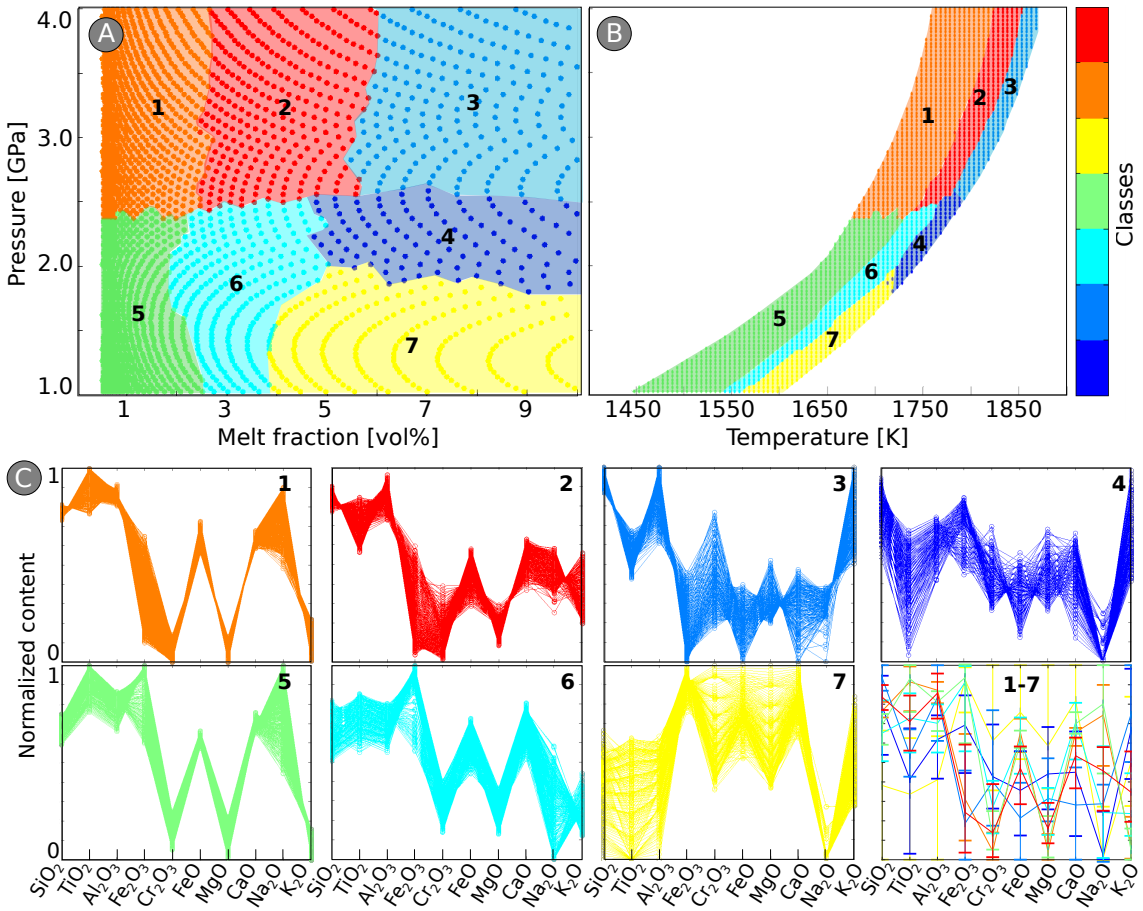

Figure 2.2: Identifying representative oxide compositions of the initial phase diagram from the pyrolitic mantle using SOMs. The data set is given by solid oxide compositions with 10 different oxides from the near-solidus P–T field (0–10 vol% melt and 1.0–4.0 GPa). Classified compositions are illustrated in terms of pressure and melt fraction (A) and pressure and temperature (B). Colors represent 7 classes determined by SOM analysis. C: Each class has a characteristic distribution pattern of solid oxide compositions. The average compositions (colored lines) and the respective minimum and maximum value (horizontal thick lines) of the normalized oxides are plotted together from all classes (bottom right).

2.2.1.4 Perple_X

The density distribution for the upper and lower crust is calculated in the chemical system: SiO_2–TiO_2–Al_2O_3–FeO–MgO–CaO–Na_2O–K_2O–H_2O using Perple_X 6.7.0 (Connolly, 2009), with internally-consistent thermodynamic data for endmembers and activity-composition models for solid-solution phases. The thermodynamic data file used "hp02ver" is based on Holland and Powell (1998). The activity-composition models used in the cal-

culations are listed in Table 2.A1 (see Appendix). Silica liquid was suppressed in the Perple_X calculations to exclude the presence of metastable melt in the subsolidus region. As we do not consider melt extraction from crustal rocks in this work, one diagram suffices for each crustal rock type (Tab. 2.1).

2.2.2 Geodynamic modeling

2.2.2.1 General method

The geodynamic modeling utilised the finite element code MVEP2[1] (Kaus, 2010; Thielmann and Kaus, 2012), within which the density was incorporated with a parameterized melting and melt extraction algorithm in 2D visco-elasto-plastic thermo-mechanical models, in which markers (marker-in-cell-technique) are used to track rock properties. The parameterized 2D code solves the governing conservation equations of mass, momentum and energy of slowly creeping fluids on geological timescales (Kaus, 2010; Thielmann and Kaus, 2012). The code employs realistic densities and solid/liquid compositions consisting of up to 12 oxides, and laboratory-constrained creep laws. The weakening effect of water and melt on the effective viscosity in the mantle, is considered in the experimentally determined diffusion and dislocation creep flow laws ("dry" and "wet" olivine rheologies, Hirth and Kohlstedt, 2003) (Tabs. 2.A2–2.A3, see Appendix). If H_2O is removed from the source rock by melt extraction (< 0.01 wt% H_2O in the solid rock), the creep law switches to that for the dry mantle. The upper crust (0–10 km depth) is assumed to have a quartzite rheology (Ranalli, 1995) and the lower crust (10–30 km depth) as well as the newly-generated crust from crystallized mantle melts, to have a plagioclase$_{An75}$ (Ranalli, 1995) dislocation creep rheology. Our melt extraction algorithm removes the melt phase from the partially molten mantle and emplaces it above or within the crust as plutons. The melt fraction, which is in equilibrium with the surrounding source rock, is removed from the mantle once a critical melt fraction M_{crit} is exceeded. The chemical evolution of the partially molten source rock is included by using individually-changeable phase diagrams for each affected marker, for the conditions at which melt extraction occurred. In order to find the most appropriate melt-depleted phase diagram to replace the previous undepleted one, the composition of the residuum at the marker is compared with the bulk chemistries of all precomputed phase diagrams using a nearest neighborhood algorithm. The numerical code employed here has been described in detail elsewhere (Kaus, 2010; Thielmann and Kaus, 2012; Johnson et al., 2014), and is only briefly summarized here.

[1] code is provided at: https://bitbucket.org/bkaus/mvep2

In the following section, new model features, such as a new melt extraction and evolution method are described in more detail.

2.2.2.1.1 Governing equations:

The conservation of mass and momentum for slowly creeping incompressible rocks are described by:

$$\frac{\partial v_i}{\partial x_i} = 0 \tag{2.1}$$

$$-\frac{\partial P}{\partial x_i} + \frac{\partial \tau_{ij}}{\partial x_j} = -\rho g_i, \tag{2.2}$$

where v is the velocity, $P = -0.5(\sigma_{xx} + \sigma_{zz})$ is the pressure, τ is the deviatoric stress tensor, g is the gravitational acceleration, ρ is the density and $i = (x, z)$ denotes spatial directions, and we employ a Boussinesq approximation.

The rheology is Maxwell visco-elasto-plastic:

$$\dot{\varepsilon}_{ij} = \dot{\varepsilon}_{ij}^{elastic} + \dot{\varepsilon}_{ij}^{viscous} + \dot{\varepsilon}_{ij}^{plastic} = \frac{1}{2G}\frac{D\tau_{ij}}{Dt} + \frac{1}{2\eta_{eff}}\tau_{ij} + \dot{\lambda}\frac{\partial Q}{\partial \sigma_{ij}}, \tag{2.3}$$

where $\dot{\varepsilon}_{ij}$ is the (deviatoric) strain rate tensor, G the elastic shear modulus, $\frac{D\tau_{ij}}{Dt}$ the Jaumann objective derivative, $\dot{\lambda}$ the plastic multiplier and Q the plastic flow potential. η_{eff} is the effective creep viscosity, which is computed from dislocation and diffusion creep laws:

$$\eta_{eff}^{dis} = FA^{-\frac{1}{n}}((C_{OH})^r)^{-\frac{1}{n}}\ \dot{\varepsilon}_{II}^{\frac{1}{n}-1}\exp\left(\tfrac{E+PV}{nRT}\right)\exp\left(-\tfrac{\beta}{n}M\right) \tag{2.4}$$

$$\eta_{eff}^{diff} = FA^{-1}d^p((C_{OH})^r)^{-1}\exp\left(\tfrac{E+PV}{RT}\right)\exp(-\beta M), \tag{2.5}$$

with F as prefactor for tensorial form, prefactor A, powerlaw exponent n, water fugacity in $H/10^6 Si$ (C_{OH}), exponent of C_{OH}-term r, grain size d, exponent of the grain size p, second invariant of the strain rate tensor $\dot{\varepsilon}_{II}$, activation energy E, pressure P, activation volume V, gas constant R, temperature T, melt fraction prefactor β and M as current melt fraction. To avoid numerical instabilities, a lower and upper viscosity cutoff of 10^{17} and 10^{25} Pas is used.

The solved energy equation is given by:

$$\rho c_p\left(\frac{\partial T}{\partial t} + v_i\frac{\partial T}{\partial x_i}\right) = \frac{\partial}{\partial x_i}\left(k\frac{\partial T}{\partial x_i}\right) + H_r + H_a + H_d + H_l, \tag{2.6}$$

where ρ is the density, c_p heat capacity, $v_i\frac{\partial T}{\partial x_i}$ the advection term with v_i as spatial velocity

and k is the thermal conductivity. H_r, H_a and H_d are the heat sources with radioactive (H_r), adiabatic (H_a) and dissipative or shear heating (H_d). Additionally, latent heat (H_l) induced by melting (heat consumption) or crystallization (heat production) processes is taken into account, by increasing the effective heat capacity (C_{Peff}) and the effective thermal expansion (α_{eff}) of the partially molten rock, calculated following Burg and Gerya (2005) as:

$$C_{Peff} = C_P + Q_L \left(\frac{\partial M}{\partial T}\right)_{P=const.} \tag{2.7}$$

$$\alpha_{eff} = \alpha + \rho \frac{Q_L}{T} \left(\frac{\partial M}{\partial P}\right)_{T=const.}, \tag{2.8}$$

with Q_L as the latent heat of fusion. α_{eff} is considered in the adiabatic heating term H_a.

The density in the models is a function of rock composition (X), melt fraction (M), pressure (P) and temperature (T):

$$\rho = f(X, M, P, T). \tag{2.9}$$

The variations of crustal density as a function of P and T are computed with Perple_X. The parameters (ρ, $\left(\frac{\partial M}{\partial T}\right)_{P=const.}$ and $\left(\frac{\partial M}{\partial P}\right)_{T=const.}$) for the newly-generated plutonic and volcanic crust are calculated from an average extracted melt composition (Tab. 2.1). After each melt extraction event, the active mantle phase diagram is changed at the conditions of melt extraction and correspondingly also the density values in the P–T field.

The density of the partially molten mantle rock is computed as follows:

$$\rho = \rho_{liquid}\ M_{current} + \rho_{solid}(1 - M_{current}), \tag{2.10}$$

where $M_{current}$ is the current melt fraction and ρ_{liquid} and ρ_{solid} are the densities of the liquid and solid phases in equilibrium with the corresponding melt fraction. The values are used from the pMELTS precomputed phase diagrams.

2.2.2.2 Melt extraction and update of phase diagrams

Melting of crustal rocks is not taken into account in the geodynamic modeling and we assume that magmas ascended rapidly through dikes. The timescale of this process is significantly smaller (in an order of hours) than a typical time step employed in the geodynamic model (hundreds of years), which is why we assume it to occur quasi-instantaneously and emplace the magma directly above the crust to mimic extrusive and within the crust for intrusive rocks.

The melt extraction algorithm in the code including the update of phase diagrams is

done in several steps:

1. The melt fractions, as well as liquid and solid compositions and densities, calculated by pMELTS on a regular grid over mantle P–T conditions for a given rock prior to extraction, are interpolated from the phase diagram to the markers in the geodynamic code.

2. For each mantle rock, melt extraction conditions (M_{min} and M_{crit}) are separately defined and so the amount of extractable melt can be variable between different mantle rocks and change with time. Once the melt exceeds a critical fraction (M_{crit}), melt is extracted. We considered two possible scenarios, i) M_{crit} is constant during the whole simulation and ii) M_{crit} decreases step-wise by 1 vol% after a certain number of melt extraction events occurred (e.g., every 5 melt extraction events, such that after 20 melt extraction events M_{crit} is lowered by 4 vol%). The maximal and minimal M_{crit} values that might be reached in ii) are specified at the beginning of each simulation. For the respective time steps, the M_{crit} value is applied for the whole model domain homogeneously. A small amount of non-extractable melt (M_{min} = 0.5 vol%) remains in the rock such that the actual extracted amount of melt is:

$$M_{extract} = M_{current} - M_{min}. \tag{2.11}$$

   The total amount of extracted magma can be computed as well as its spatial distribution, which results in compositionally-distinct volcanic sequences (see Section 2.3.1, Fig. 2.4A). Moreover, we keep track of how much melt was extracted from a certain patch of rock, and specify a maximum cumulative total extractable melt (M_{max}) of 50 vol% above which melt is no longer extracted. As a result of continuing rock depletion, melting mantle rocks under given P–T conditions becomes increasingly difficult. Consequently, the amount of extracted melt from a patch of rock is normally below M_{max} (see Section 2.3.1, Fig. 2.4C) and the extracted melt per time step is never higher than ∼15 vol%.

3. New markers are randomly inserted in the region of newly generated crust to represent freshly generated crust. The corresponding melt extraction zone will decrease in volume by the same amount and we mimic the resulting compaction process by moving markers in between downwards accordingly, in a volume-conservative manner. This is a numerically simple manner to mimic volumetric processes within a Boussinesq model approximation. Other approaches are possible, which involve adding sink/source terms in the conservation of mass equation (e.g. Gerya and Yuen,

2007; Vogt et al., 2012; Schmeling and Arndt, 2017). The newly injected markers track both the rock type that correlates with the mantle source of extracted melts, and the temperature of intrusion by setting the temperature of the newly-formed volcanic and plutonic crust to 90% of the average melting temperature of the extracted melts. 10% is assumed to be lost during the ascent that is not modeled here. Furthermore, latent heat of fusion added in the simulations takes into account the required or consumed energy during the melting/crystallization process.

4. The transient weakening effect caused by ascending melts is implemented by decreasing the yield strength of the rocks between the area of melt generation and emplacement (e.g. Gerya and Meilick, 2011; Vogt et al., 2012) during a melt extraction event. The width of the weakened zone depends on the lateral extension of the partially molten region from which melt is extracted. The weakening process limits the creep viscosity:

$$\eta_{creep} \leq \sigma_{yield}/(2\dot{\varepsilon}_{II}). \tag{2.12}$$

The weakening factor λ lowers the yield stress (σ_{yield}) by reducing the effective friction angle due to melt pressure in the plasticity equation:

$$\sigma_{yield} = c\ \cos(\phi) + \sin(\phi)P\lambda, \tag{2.13}$$

with P denoting dynamic pressure, c the cohesion, ϕ the internal friction angle and λ the melt weakening or pore melt pressure factor:

$$\lambda = 1 - P_{melt}/P_{solid}, \tag{2.14}$$

with P_{melt} as melt pressure (assumed to be lithostatic) and $P_{solid} = P$ (dynamic pressure). For simplification, we use a constant λ value of 0.5.

5. Plutons are formed in the continental crust in areas of the highest possible intrusion emplacement rate (i.e., highest possible local crustal divergence rate, div_{crust}). The depth of intrusive rock emplacement is thus determined by the maximum ratio of effective melt overpressure to effective viscosity above the melt extraction region (e.g. Vogt et al., 2012):

$$div_{crust} = |(dP_{solid} - dP_{melt})/\eta_{eff}|. \tag{2.15}$$

As we use an incompressible formulation, the real melt overpressure, as a result of elastic bulk deformation, is not computed. Instead, the effective overpressure in

div_{crust} is approximated as the difference in the change in dynamic (dP_{solid}) and lithostatic pressure (dP_{melt}).

6. Each phase diagram computed using pMELTS or Perple_X describes how melt fraction, chemistry and the density change over a predefined P–T range (defined on a regular P–T grid). It is based on a bulk rock chemistry and is valid for one specific chemical system. As long as the bulk rock chemistry does not change on a specific marker, the phase diagram from which the melt fraction, chemistry and density are used and interpolated to the markers does not change. In a closed system, the bulk chemistry only changes as a result of extraction of material, in our case melt. When melt is extracted from a marker, the total chemistry (described by solid and liquid chemistry) is changed by extracting the liquid composition from the source. The employed phase diagram on the affected marker thus has to be updated based on the remaining residuum chemistry, in order to model the rock behavior after a melt extraction event. Thus, the chemical evolution of the partially molten source rock is included in the model by using individually-changeable phase diagrams for each affected marker, for the conditions at which melt extraction occurred. In order to find the most appropriate melt-depleted phase diagram after melt extraction, the composition of the residuum (equivalent to the solid chemistry) from the respective marker is compared with the bulk chemistries of all precomputed phase diagrams using a nearest neighbor searching algorithm (in our case a Kd-tree algorithm). The phase diagram, whose bulk chemistry is the closest to the residual solid rock chemistry, is updated on the marker by interpolating the density, melt fraction and composition from the phase diagram to the marker P–T condition.

The employed parameters for the geodynamic modeling are given in the Appendix, Tables 2.A2–2.A6.

2.2.2.3 Model setup

We consider a crust-to-upper mantle 2D model of a rising thermo-mechanical-chemical plume in a 400 km wide and 125 km deep box over a 2 Ma time span. The uppermost part of the 2D model box (Fig. 2.3A) consists of an upper (0–10 km depth) and a lower crust (10–30 km depth). The crust is underlain by a pyrolitic mantle to a depth of 125 km. Small compositional anomalies are inserted in the central part of the mantle representing a compositional anomaly (Fig. 2.3A). Furthermore, we tested in one simulation the effect of an additional material influx of metasomatized material by injecting metasomatized

components within a thermal anomaly at the position where the components were located initially, 500 ka after the model has been started. Due to the missing basal influx of metasomatized material, the term heterogeneous plume used here is referred to a rising compositional anomaly within a thermal plume.

The geodynamic model employs a computational mesh of 450×250 nodes with a resolution of ∼0.9 km horizontal and ∼0.5 km vertical. The compositions are tracked on markers of which there are initially ∼ 2.5 million. The number of markers increases during the simulations as new crust is generated.

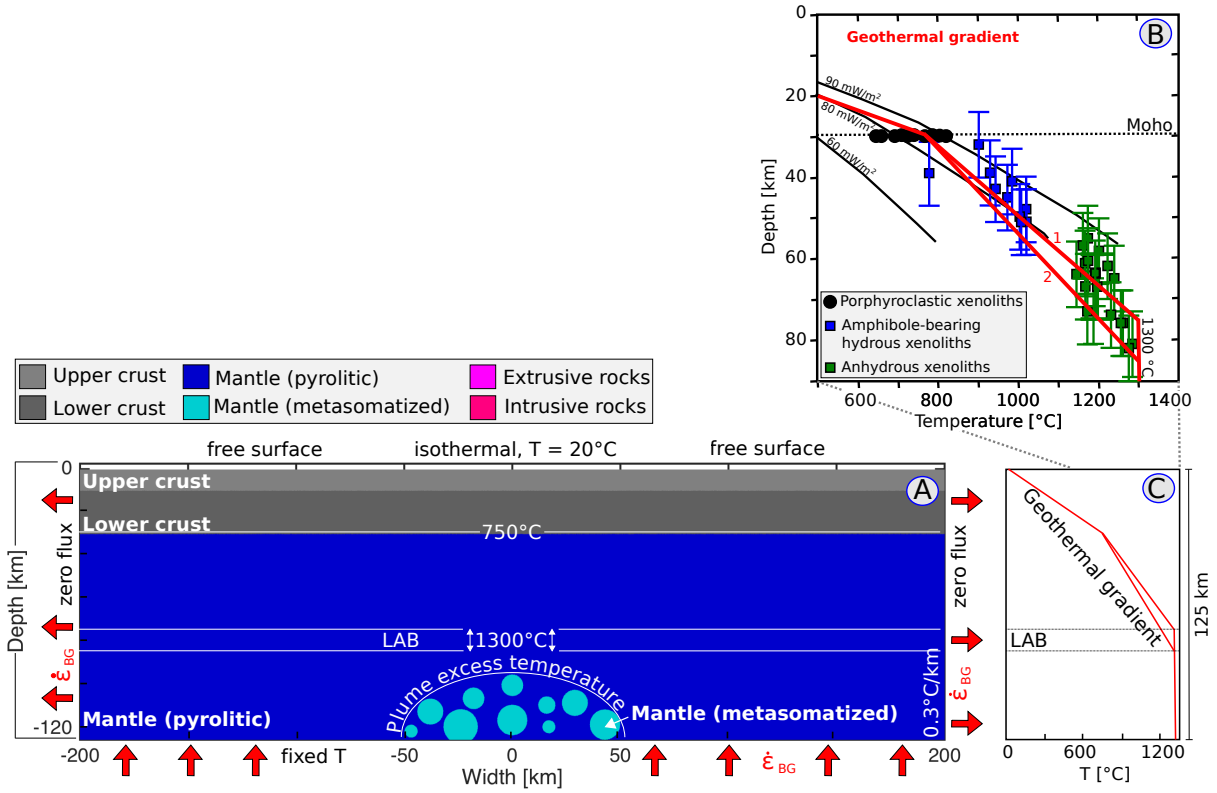

Figure 2.3: A: Initial 2D numerical model configuration. The thermal and mechanical boundary conditions used are outlined in the main text. The laterally central area of excess temperature to the surrounding mantle adiabat is indicated by a half circle. B: P–T estimations for equilibrated West Eifel xenoliths modified after Witt-Eickschen (2007). Blue symbols are hydrous and green symbols are anhydrous lithospheric mantle xenoliths. Temperatures of recrystallization in porphyroclastic Eifel xenoliths are shown with black circles. Red lines characterize the possible geothermal gradient used in the initial model setup. C: The initial geothermal gradients for a thermal asthenosphere (LAB) at 75 and at 85 km depth.

Mechanical boundary conditions are kinematic prescribed velocities on both model sides and on the bottom where the velocity is chosen such that a background strain rate of 10^{-16} 1/s is employed throughout the model. The top boundary is a free surface (stress-free). This thus simulates an extensional environment over the whole model domain

that facilitates the plume rise. Thermal boundary conditions are zero flux at the side boundaries.

The temperature is prescribed at the top and bottom boundary. At the top we employ isothermal conditions, meanwhile, the bottom temperature profile features an excess temperature zone in the central domain, defined by the plume excess temperature.

The initial geotherm has a surface temperature of 20 °C and increases linearly until 750 °C at the Moho. In the lithospheric mantle, the geothermal gradient is determined from mantle xenoliths and increases linearly to 75–85 km depth, where the temperature converges to the adiabatic upwelling curve (∼1300 °C) of the asthenosphere (Fig. 2.3B/C). Beneath the lithosphere, an adiabatic gradient (0.3 °C/km) is used to allow a modest increase in temperature with depth. A positive thermal anomaly, between 150 and 220 °C (T_{excess}) on top of the geothermal gradient mentioned before, is inserted into the central lower part of the mantle to initiate the thermal plume.

We calibrated the geothermal gradient with P–T conditions of equilibrated xenoliths, inspired by the West Eifel volcanic field, Germany (Fig. 2.3B), as a typical example of an intracontinental volcanic field.

2.3 RESULTS

The change in magma composition generated in an uprising heterogeneous mantle plume over time is analyzed via coupled geodynamic petrological models. We show how plume-related thermal and mechanical processes interact with chemical processes, such as rock depletion through melt extraction. The models also illustrate how the onset of melt extraction, melt compositions and P–T conditions for melt extraction, are linked to thermal and mechanical processes inside the mantle (e.g., plume rising time affects decompression melting). We test the effect of several parameters on magma chemistry, in particular on the K_2O/Na_2O, in a systematic manner (Tabs. 2.B1–2.B2, see Appendix), with the main focus on varying initial plume excess temperatures, the depth of the thermal lithosphere-asthenosphere boundary (LAB) and variations in extracted melt fraction with critical melt fractions (M_{crit}) of 1–8 vol%. We focused on the K_2O/Na_2O ratio to compare our modeling results with volcanic rocks from the West Eifel (Germany). There, rock compositions indicate that a step-like profile in K_2O/Na_2O results from melting two different types of mantle rocks (e.g. Mertes and Schmincke, 1985; Schmincke, 2007; Mertz et al., 2015). For the critical melt fraction, a possible decrease during plume ascent is considered as well. The term “critical melt fraction” defines the percentage of melt that has to be exceeded

in a partially molten rock in order to be extracted.

The melt chemistry and its melting P–T conditions are only analyzed and visualized when the melt is extracted from the partially molten source region. Our melt chemistry thus represents melt compositions that form volcanics or plutonics and not how melt evolves in the partially molten mantle region without being extracted. The term "melt extraction episode" is used here to indicate the merging of successive melt extraction events that occur without considerable temporal breaks in between. Different melt extraction episodes are separated by a larger temporal break.

2.3.1 Factors controlling plume ascent and magma formation

The plume ascent in all models is controlled by thermal-, mechanical- and compositional processes. The low density material (e.g. Fig. 2.4E/F) induces ascent of the mantle plume in the center of the domain (Fig. 2.4, Fig. 2.5). The density is reduced either directly by its chemistry (caused by previous metasomatic enrichment processes) and/or by a higher excess temperature with respect to the surrounding mantle (e.g. Fig. 2.4G/H). Within the plume domain, higher temperatures and the presence of fluids and/or melt increase the strain rate (e.g. Fig. 2.4I/J) and decrease the viscosity (e.g. Fig. 2.4K/L). At the lithosphere-asthenosphere boundary (LAB), the increase of viscosity prevents further plume ascent and causes the plume head to impinge and spread out beneath the lithosphere (Fig. 2.4K/L). When the melt is extracted, it is emplaced within the continental crust above and produces volcanic rocks with a laterally varying composition, reflecting that of the source region (e.g. Fig. 2.4A). The compaction of markers below the melt emplacement area produces a wavy topography, as can be seen at the Moho (e.g. Fig. 2.4A/B). During plume ascent, melting behavior and rising velocities of the plume may change due to the depletion of plume material caused by melt extraction. Once melt is extracted, the system chemistry changes on the respective marker (as liquid chemistry is removed) and the phase diagram is updated (e.g. Fig. 2.4C). The total number of melt extraction events can be more than 300 for one simulation, which corresponds with a melt extraction event nearly every second time step.

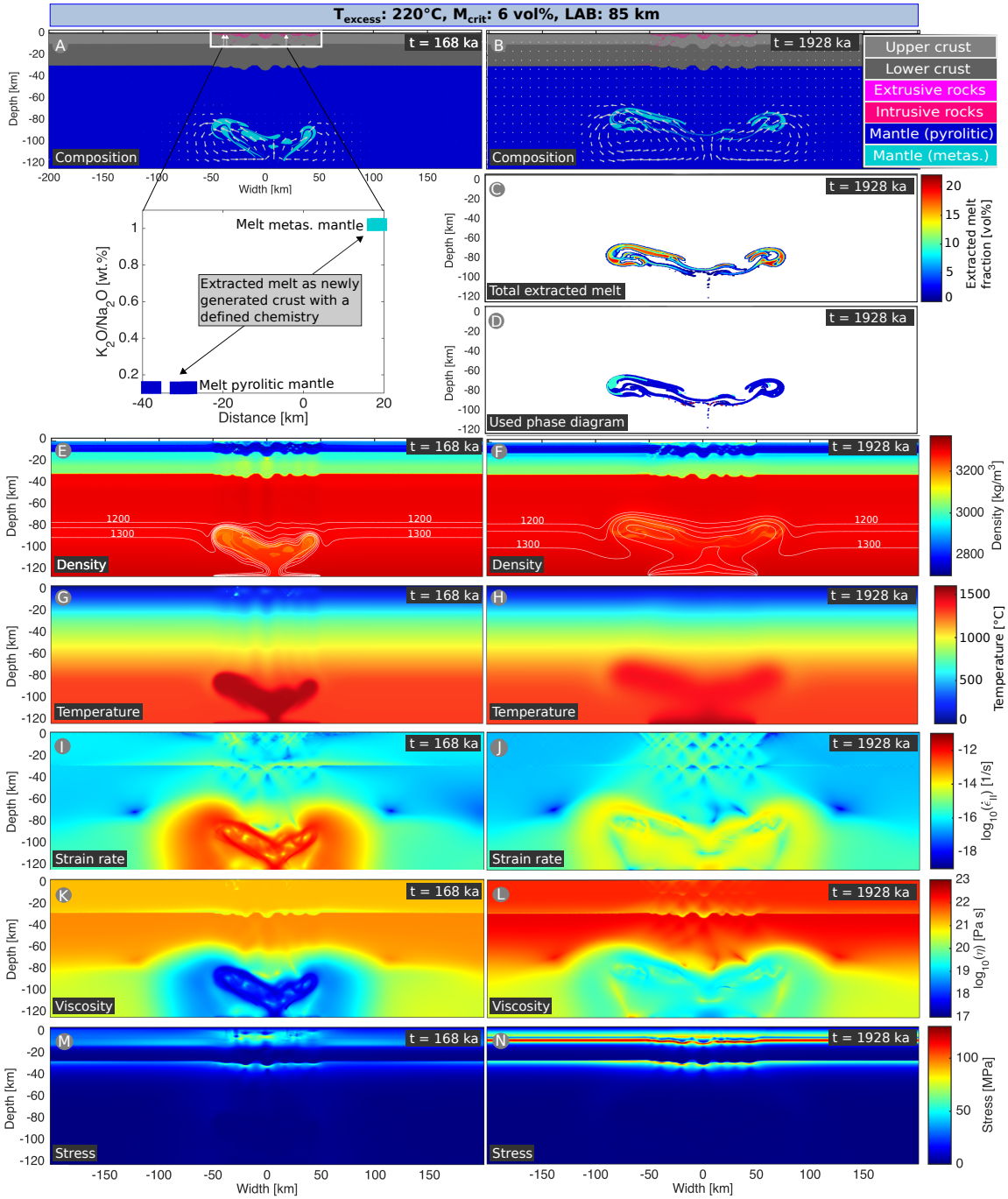

Figure 2.4: Plume evolution with an initial +220 °C plume excess temperature (T_{excess}), a constant critical melt fraction (M_{crit}) of 6 vol% and LAB at 85 km depth. A/B: Composition and the velocity field (white arrows). The newly-generated-crust contains information about the melt chemistry originating from melting of mantle material. The chemistry can change laterally depending on the location where mantle melting occurred. C: Amount of total extracted melt and D: used phase diagrams, where each color represents a different employed phase diagram (white=initial phase diagram used). E/F: Density including isotherms (every 50 °C from 1200 °C upward), G/H: temperature, I/J: strain rate invariant, K/L: viscosity and M/N: stress invariant. The decrease in density is caused by a higher plume temperature and metasomatized material. The effect of a higher temperature and the possible presence of melt and/or water in the plume is seen in both strain rate (increasing) and viscosity (decreasing).

The systematic variation of parameters (M_{crit}, T_{excess} and LAB depth) in the numerical experiments shows that plume ascent velocities are strongly dependent on the plume temperature with a higher temperature resulting in faster plume ascent rates (Fig. 2.5E–L) by decreasing viscosity and density (higher positive buoyancy). By contrast, a deeper LAB has the opposite effect and reduces plume ascent rates (e.g. Fig. 2.5C–D compared to Fig. 2.5A–B). A change in critical melt fraction does not significantly alter the ascent of the plume.

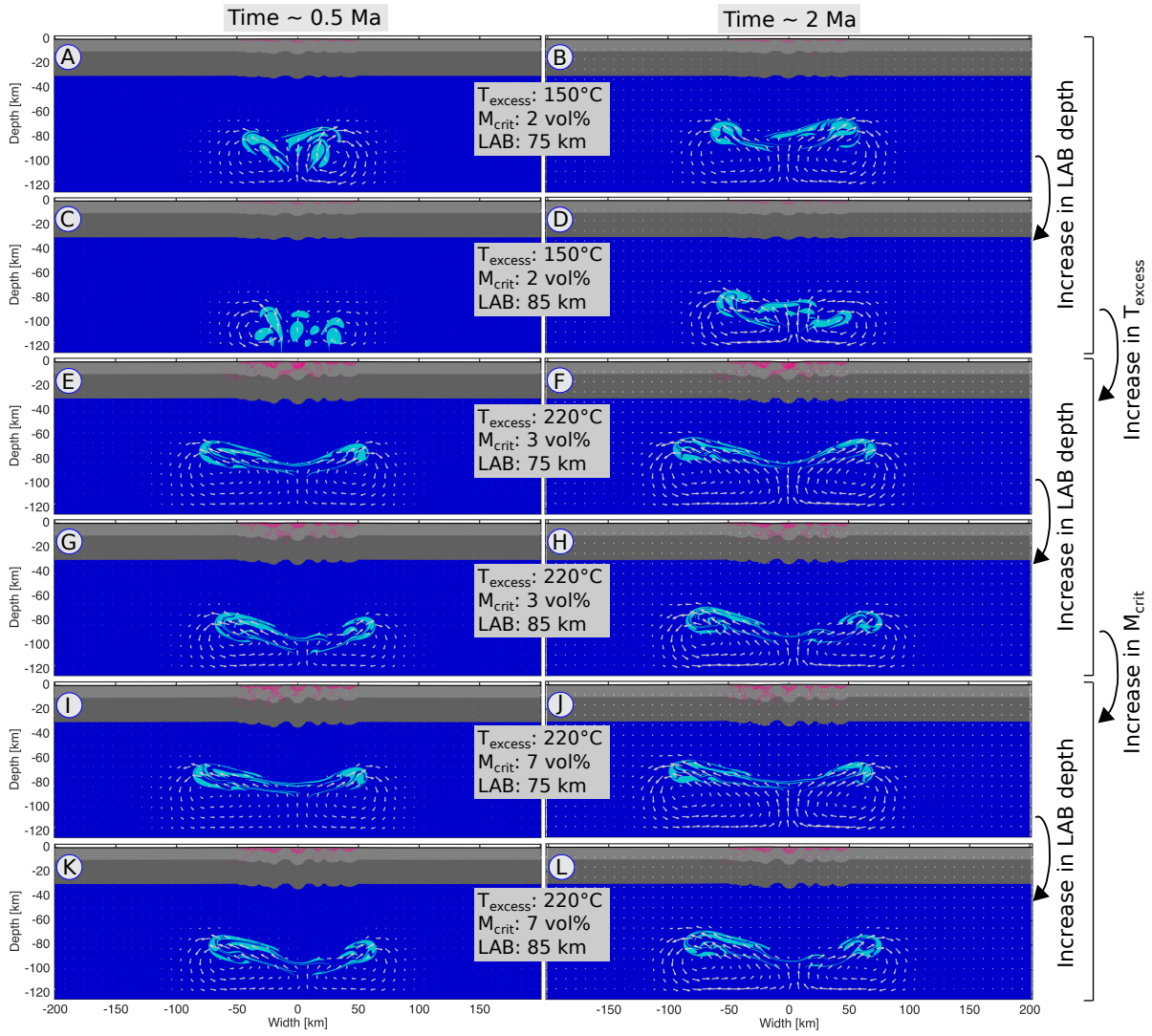

Figure 2.5: Effect of plume excess temperature (T_{excess}), critical melt fraction (M_{crit}) and LAB depth on model evolution. A–B: Lower plume excess temperature, which slows down plume rise compared to model E–F with a higher employed plume temperature. C–D/G–H: LAB at greater depth slows down plume ascent and induces a smaller convective cell in the velocity field (white arrows) compared to models with a shallower LAB (A–B/E–F). I–J/K–L: Increase in M_{crit} does not significantly change the physical behavior of plume evolution compared to models E–F/G–H with a smaller employed M_{crit} value.

Partial melting of mantle material can occur during plume ascent but is limited by the loss of plume excess temperature due to thermal diffusion. Furthermore, the amount of H_2O and more incompatible elements in the source rock can affect melt fertility and induce melting at greater depth. With each melt extraction event, decompression melting becomes increasingly important for the metasomatized mantle as well, where melting was initially caused by having a lower solidus.

2.3.2 Effect of mantle source chemistry on melting

The composition of melt is commonly used to deduce mantle processes, which is why we analyze the effect of different sources on the K_2O/Na_2O ratio in the extracted melt. Melting anhydrous mantle material is usually induced by decompression (decrease of the pressure by nearly constant temperature). The plume rises driven by its positive buoyancy and transports heat into shallower mantle levels. Due to heat diffusion, the plume loses heat successively from its interior and heats up more or less effectively the surrounding colder mantle depending on the time scale over which this process takes place. Consequently, in order to trigger decompression melting, the initial plume temperature has to be sufficiently high to not lose all the necessary heat for melting already during decompression. Melt extraction from the pyrolitic mantle at any stage during the simulation, requires a minimum initial plume excess temperature of +150 °C, for a critical melt fraction of 1 vol%. The high initial plume temperatures (between +150 °C and +220 °C) in all our simulations result from the required temperatures to melt anhydrous pyrolitic mantle.

The first episode of partial melting of pyrolitic rocks occurs at the onset of the simulation as the highest temperatures occur during these stages. A second melt extraction episode is triggered by decompression melting after heat is transported to shallower depths during plume ascent. The degree of decompression melting is strongly dependent on the LAB depth, with a shallower LAB of 75 km favoring higher melt fractions (Fig. 2.6A compared to Fig. 2.6B). A lower critical melt fraction and/or higher plume excess temperatures encourage melt extraction (Fig. 2.6C compared to Fig. 2.6D).

High melt fractions occur in the metasomatized mantle at the beginning of the simulations, as the fluid-rich mantle has a lower solidus temperature. After the first melt extraction event, the residuum is typically highly depleted such that subsequent melt generation only occurs as a result of decompression. The resulting melts from the second melt extraction episode show a strong increase in K_2O/Na_2O content (Fig. 2.6A–C).

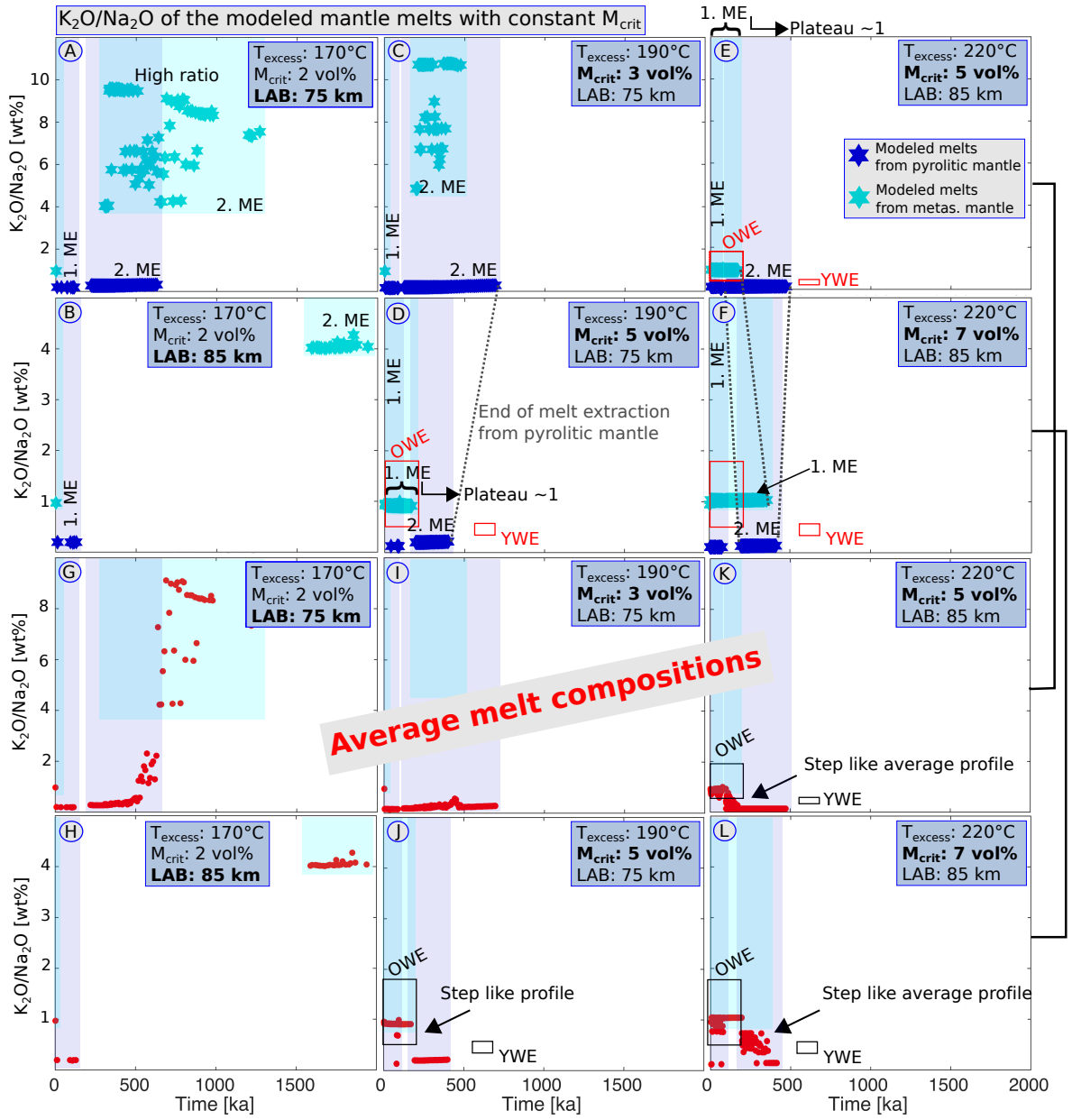

Figure 2.6: Temporal evolution of K_2O/Na_2O (in wt%) of modeled compositions of extracted melts, with a constant employed critical melt fraction (M_{crit}) during one simulation. Dark blue stars show average compositions of magmas extracted from the pyrolitic mantle and turquoise stars from the metasomatized mantle. Red dots represent the average composition of extracted magma after magma mixing, considering different portions of the respective melt phase. ME = Melt extraction episode. The main melt extraction episodes (ME) for the respective mantle sources are deposited with turquoise and bluish boxes. A–F: The change of T_{excess}, M_{crit} and LAB depth influence the occurrence of melt extraction episodes, melt chemistry and the mantle source of extracted melts. Dotted black lines illustrate the influence of a higher M_{crit} value. The models G–L show the average compositions of extracted magmas associated with the extracted melts in the respective models A–F. Red and black rectangles show the compositional range for the West Eifel volcanic rocks (OWE=Old West Eifel (> 480 ka), YWE=Young West Eifel (< 80 ka), after Mertz et al. (2015)).

An increase in temperature of the thermal anomaly results in larger melt fractions at greater depths and, as a result, in faster plume ascent velocities as long as the melt fraction does not exceed the critical fraction for extraction. The melt fraction in the rock decreases the viscosity and density. Thus, because of higher plume rising velocities, decompression melting may occur earlier in time. An increase in critical melt fraction, on the other hand, has the opposite effect and shifts the occurrence of a second melt extraction episode to a later stage in the simulations. Here, more decompression is needed to create a higher percentage of melt that is able to be extracted from the partially molten mantle.

If relatively high critical melt fractions are employed ($\geq$ 5 vol%), a plateau in K_2O/Na_2O (at $\sim$1) forms at the beginning of the plume ascent due to a longer lasting melt extraction episode from the metasomatized mantle. An increase in critical melt fraction (if $M_{crit} \geq$ 5 vol%) encourages a step-like-profile (high to low values) of the average K_2O/Na_2O of extracted melt (Fig. 2.6J–L). This effect is induced by the second melt extraction episode from pyrolitic mantle material that starts later, in combination with a longer lasting first magmatic episode from the metasomatized mantle (Fig. 2.6D). Despite an overlap of both magmatic activities from metasomatized and pyrolitic mantle rocks, the average magma chemistry of one time step still follows a step-like-profile in K_2O/Na_2O, depending on the relative proportions of metasomatized and pyrolitic melts (Fig. 2.6K–L). A deeper LAB (at 85 km) further encourages the development of a step-like-profile, as it results in the later onset of the second melt extraction episode from pyrolitic rocks and a reduction in its total magma production. This process is reduced to the lower plume rising time (e.g. Fig. 2.5C), that slows the decompression process accompanied by a heat loss over a longer time. A double step-like-profile in K_2O/Na_2O of the extracted melt is produced if a second thermal-chemical mantle plume follows the first one $\sim$500 ka after its initialization (see Section 2.3.5, Fig. 2.10B).

2.3.3 Melt extraction depth and temperature

The melting depth and temperatures of the extracted magmas generally decrease with time in all simulations (Fig. 2.7), which implies a shorter pathway for magma ascent. Furthermore, previously formed melt pathways may create weak zones that facilitate the ascend of subsequent melt pulses. Therefore, the possible effect of a decreasing M_{crit} on melt chemistry during the plume ascent has to be tested in our simulations.

The melts in the metasomatized mantle exceed the critical melt fraction at lower temperatures and at greater depths than those in the pyrolitic (more primitive) mantle (Fig. 2.7). Already depleted metasomatized mantle (second melt extraction episode)

requires higher temperatures to exceed the critical melt fraction (Fig. 2.7A).

The largest difference in melt temperatures of both types of extracted melts occurs if the critical melt fraction is sufficiently high to provoke a longer magmatic activity in the first melt extraction episode in the metasomatized mantle (e.g. Fig. 2.7B). Due to the high critical melt fraction, the metasomatized mantle is not depleted everywhere at the onset of the simulation and thus relatively low temperatures are only needed to reach the critical melt fraction of mantle rocks with a low solidus temperature.

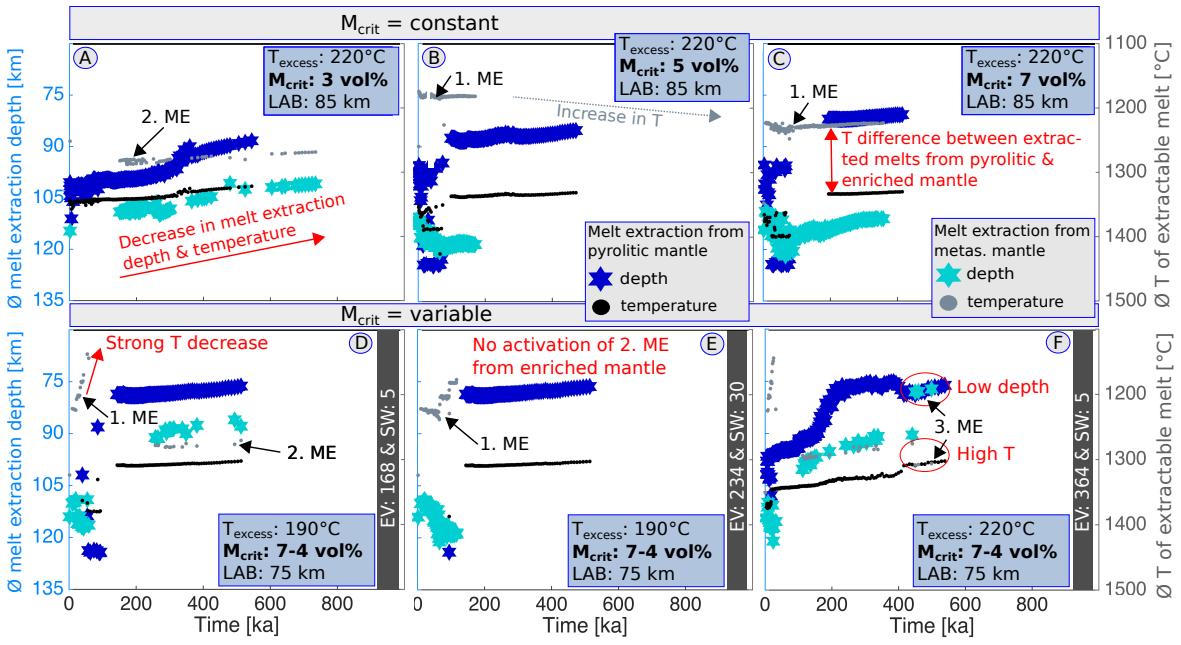

Figure 2.7: Temporal evolution of the average (⌀) melt extraction depth and temperature. ME: Melt extraction episode. Dark blue stars show average melt extraction depths (in km) from the pyrolitic mantle and turquoise stars from the metasomatized mantle (left axis). Average magma formation temperatures of extracted melts (in °C) are shown by black dots for magma originating from the pyrolitic mantle and grey dots for magma from the metasomatized mantle (right axis). The average is calculated from all affected markers where melt extraction is active for the respective time step. A–C: M_{crit} is constant within one simulation. The melting depth and the temperature of extracted magmas decrease during plume ascent, the metasomatized mantle melts exceed the critical melt fractions at lower temperatures and mostly in higher depths compared to pyrolitic mantle melts. D–F: Magma temperatures and melt extraction depths for a sequentially decreasing critical melt fraction within one simulation. EV: total melt extraction events, SW (step width): after a specified number of melt extraction events (here after 5 or 30 respectively) the critical melt fraction is decreased by 1 vol%.

2.3.4 Effect of a decreasing M_{crit}

Smaller melt fractions may reach the surface via decreasing melt formation depth with time in the uprising mantle plume (Section 2.3.3), which implies a shorter pathway for magma ascent. Based on this, we considered the effect of a decreasing critical melt fraction

on magma composition and performed systematic simulations in which we decrease M_{crit} from 7 to 1 vol%. The M_{crit} value is decreased by 1 vol% step-wise after a certain number of melt extraction events is reached.

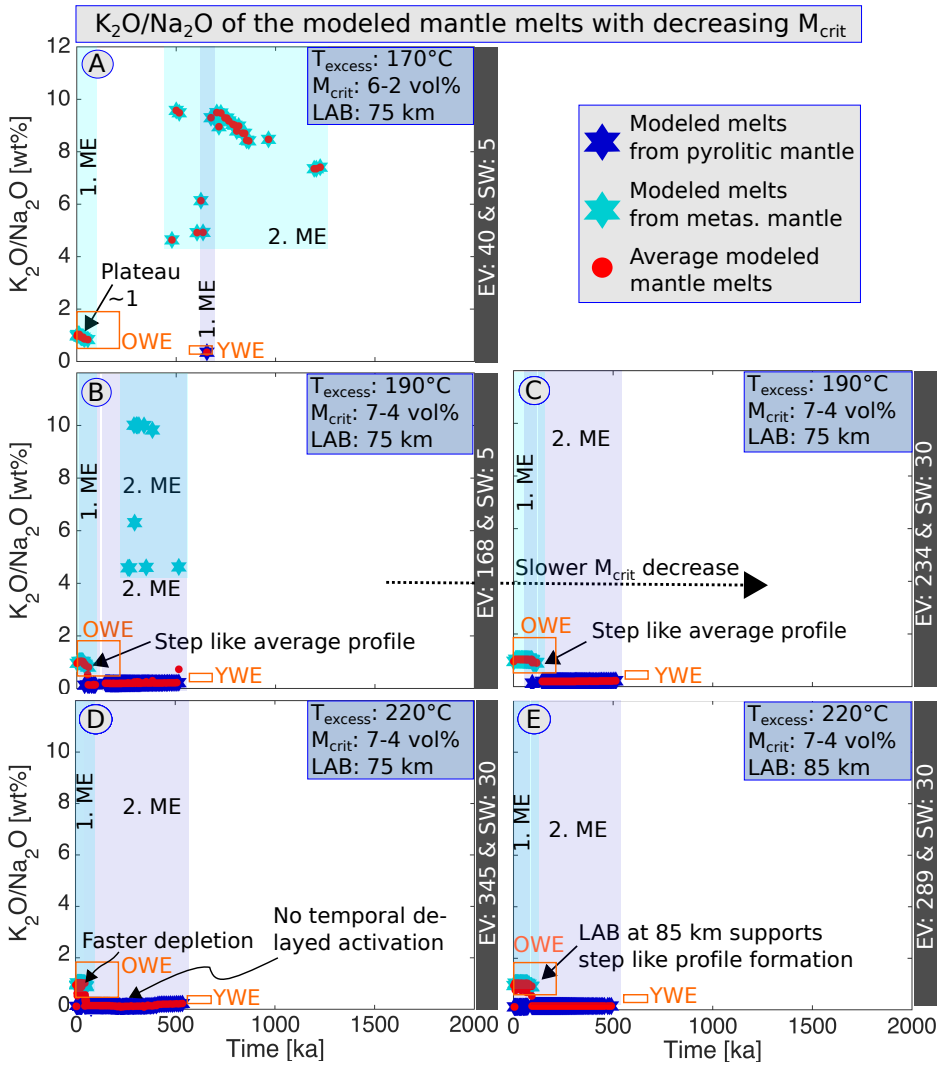

Figure 2.8: Temporal evolution of K_2O/Na_2O (in wt%) of modeled compositions of extracted melts, with a decreasing critical melt fraction (M_{crit}) during one simulation. Stars show average magma compositions from the respective mantle sources, whereas red dots represent the average compositions after magma mixing. The main melt extraction episodes (ME) for the respective mantle sources are deposited with turquoise and bluish boxes. EV: total melt extraction events, SW (step width): after a specified number of melt extraction events (here after 5 or 30 respectively) the critical melt fraction is decreased by 1 vol%. Orange rectangles show the compositional range for the West Eifel volcanic rocks (OWE=Old West Eifel (> 480 ka), YWE=Young West Eifel (< 80 ka), after Mertz et al. (2015)).

The results show that a high initial M_{crit} (≥ 5 vol%) stabilizes melt extraction from the metasomatized mantle during the first tens of thousands of years. This first melt extraction episode is accompanied by a rapid temperature drop with time in the extracted melts (Fig.

2.7D–F). With decreasing values of M_{crit}, melt extraction from pyrolitic mantle becomes increasingly likely, despite relatively low plume excess temperatures. However, not only the critical melt fraction but also the temperature is reduced due to heat diffusion during plume ascent and thus melt production may be hindered (comparison between Fig. 2.6A and Fig. 2.8A). If the initial plume excess temperature is high (+220 °C), decreasing the critical melt fraction is counterproductive in forming a step-like-profile in K_2O/Na_2O of extracted melt (Fig. 2.6F/L compared to Fig. 2.8E). Here, melt extraction from pyrolitic mantle occurs immediately due to high temperatures, whereas melt production from the metasomatized mantle is completed earlier due to faster rates of melt depletion.

Changing the interval after which the critical melt fraction will decrease by 1 vol%, from every 5 to every 30 melt extraction events, helps to build the step-like K_2O/Na_2O profile from high to low ratios. This supports a longer lasting first melt extraction episode from the metasomatized mantle and a larger temporal delay of melt extraction from pyrolitic material (Fig. 2.8C). Another effect is the suppression of the second melt extraction episode of highly enriched magmas (high K_2O/Na_2O) from the metasomatized mantle. Furthermore, with a high initial plume temperature, a third melt extraction episode is triggered by decompression melting of the metasomatized mantle. It is characterized by a shallower and depleted melting source, whose melt extraction depth and magma temperature are equivalent to those from pyrolitic mantle (Fig. 2.7F). Moreover, the step-like-profile is more distinct in simulations with a deeper LAB (Fig. 2.8E)

We thus conclude that a decrease in the critical melt fraction with time favors a magma chemistry with high K_2O/Na_2O at the beginning (first melt extraction episode of metasomatized material) followed by low ratios (pyrolitic mantle melting) in a relatively cold plume-related environment (Fig. 2.8).

2.3.5 Evolution of simulated magma compositions

The average magma chemistry changes significantly during plume ascent depending on the mantle source of the extracted melts (Fig. 2.9, Fig. 2.10). The first longer melt extraction episode from metasomatized mantle (E2, Fig. 2.9) is characterized by initially low SiO_2, Al_2O_3, Na_2O, K_2O and H_2O concentrations which subsequently increase and initially high FeO, MgO, CaO, TiO_2, P_2O_5 and Fe_2O_3 concentrations that subsequently decrease with time during lowering the critical melt fraction. Whereas magmas originating from the pyrolitic mantle have generally higher SiO_2, MgO, FeO and CaO concentrations, for identical critical melt fractions, but lower Na_2O, K_2O, Al_2O_3, TiO_2 contents and H_2O is completely absent (Fig. 2.9). The last magmatic episode (E4, Fig. 2.9), which is

characterized by the lowest critical melt fraction, predominantly consists of melts from the pyrolitic mantle. Compared to the previous melt extraction episode (E3, Fig. 2.9), which has a higher critical melt fraction and thus higher melting temperatures, the magmas are less primitive. MgO and FeO contents decrease, whereas SiO_2, Al_2O_3, Na_2O and K_2O contents increase from magmatic episode 3 to 4. Within the last melt extraction episode (E4, Fig. 2.9), which has a constant critical melt fraction, the temporal change in magma chemistry is minor. SiO_2, Al_2O_3, Na_2O as well as K_2O contents slightly increase and MgO, FeO and CaO contents slightly decrease in the extracted magma with time. This trend of the respective oxides is recognizable in magmas from the metasomatized mantle with an employed constant critical melt fraction also (Fig. 2.10A) and is attributed to decreasing pressures at which melt formation occurs during plume ascent (Fig. 2.10C). Chemical deviations to the general trend in E4 are caused by reactivation of melt extraction from the metasomatized mantle (seen in the increase in water content, Fig. 2.9).

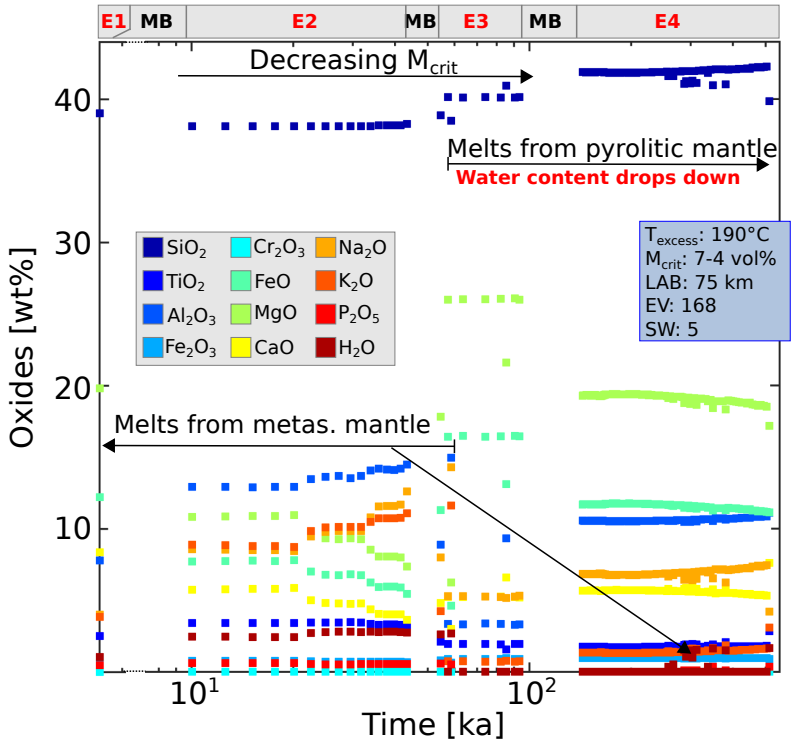

Figure 2.9: Evolution of average magma compositions with time of a representative simulation with a decreasing critical melt fraction (M_{crit}). During plume ascent, melt extraction occurs from different mantle sources and thus several magmatic episodes (E=magmatic episode) and breaks (MB=magmatic break) take place. Each magmatic episode is characterized by a specific chemical pattern of extracted melts and changes by a decreasing critical melt fraction (M_{crit}, e.g., along E2 or between E3 and E4) or slightly with time (slope of the respective oxide, e.g. E4). EV: total melt extraction events, SW (step width): after a specified number of melt extraction events (here after 5) the critical melt fraction is decreased by 1 vol%.

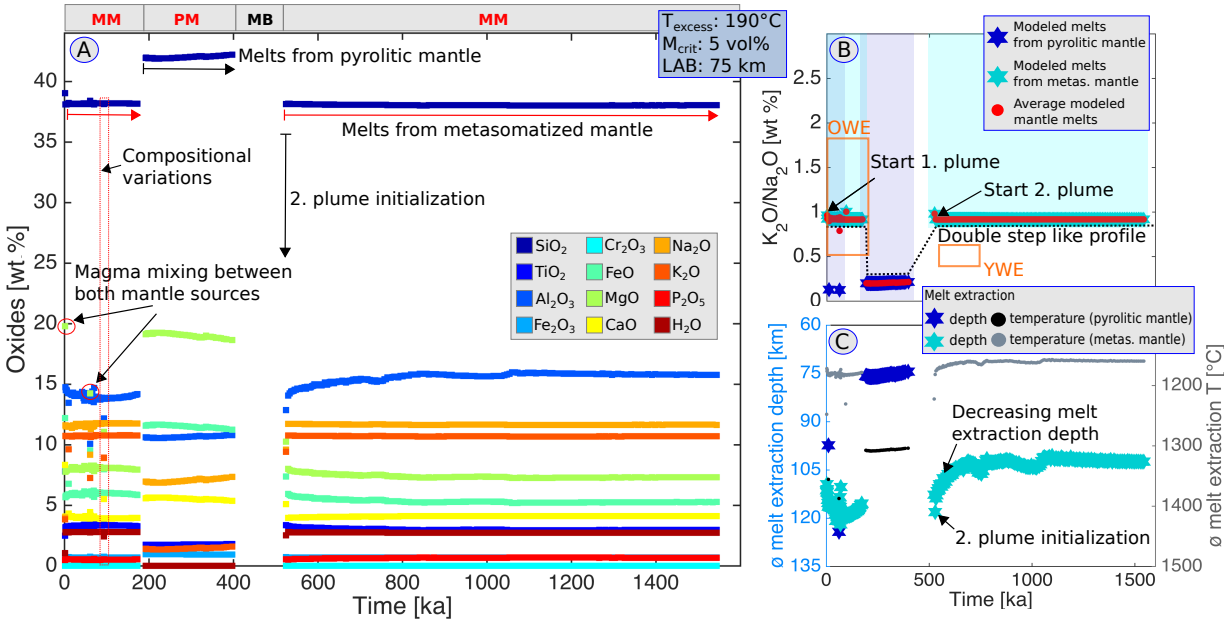

Figure 2.10: Evolution of magma compositions with time (M_{crit} = constant) and the effect of a second mantle plume initialized ~500 ka after the first one (new metasomatized components are emplaced in a hot mantle region in the central lower model domain). A: Temporal evolution of average extracted magma compositions. Extracted melts from the metasomatized mantle (MM) and the pyrolitic mantle (PM). MB=magmatic break. B: Temporal evolution of K_2O/Na_2O (in wt%) of modeled magma compositions, with a constant employed critical melt fraction during one simulation. Dark blue stars show average compositions of magmas extracted from the pyrolitic mantle and turquoise stars from the metasomatized mantle. Red dots represent the average composition of extracted magma after magma mixing, considering different portions of the respective melt phase. The main melt extraction episodes for the respective mantle sources are deposited with turquoise and bluish boxes. The second plume initialization causes a double step-like-profile in K_2O/Na_2O. Orange rectangles show the compositional range for the West Eifel volcanic rocks (OWE=Old West Eifel (> 480 ka), YWE=Young West Eifel (< 80 ka), after Mertz et al. (2015)). C: Dark blue stars show average (⌀) melt extraction depth (in km) from the pyrolitic mantle and turquoise stars from the metasomatized mantle (left axis). Average (⌀) magma formation temperatures of extracted melts (in °C) are represented in black dots for magma originating from pyrolitic mantle and grey dots for magma from metasomatized mantle (right axis). The average is calculated from all affected markers where melt extraction is active for the respective time step.

2.4 DISCUSSION

2.4.1 Developed method

Our newly developed method combines geodynamic with thermodynamic modeling and represents an important link between petrology and geophysics for understanding magmatic systems from the melting source to the point of magma emplacement. The method is applicable to most magmatic systems, but thermodynamic phase diagrams have to be tuned to the respective chemical systems to which the model is applied. In addition, new thermodynamic models that cover a wider compositional range, need to be developed,

particularly to better understand intracontinental magmatism or arc magmatism. Our methodology uses a neural network approach to limit the number of diagrams that need to be computed, and we employ the diagrams that are compositionally closest to the required chemistry. An alternative approach is to discretize the chemical composition and to compute new diagrams for all required compositions. For this to be practically feasible, a new massively parallel framework to precompute the required thermodynamic phase diagrams is needed.

2.4.2 Model limitations

While comparing the chemical results of thermodynamically modeled melts with real rock compositions, one has to consider small discrepancies occurring within the thermodynamic pMELTS model. MgO can be overestimated (by up to 4 wt%) in the liquid and required temperatures for a specific melt fraction are up to ∼60 °C higher in pMELTS compared to experiments, particularly for larger melt fractions (Ghiorso et al., 2002). The plume excess temperature creating the characteristic chemical signal may thus be overestimated in our models. Furthermore, the limited number of minerals and oxides considered in pMELTS and the employed oxygen buffer may have an influence on the magma formation and its composition as well.

2.4.3 Potential application to the West Eifel (Germany)

The temporal change in modeled melt chemistry is compared with that of natural West Eifel magmatic rocks to test the effect of a potentially heterogeneous asthenospheric mantle source on magma chemistry. We tested our model with extreme compositional endmembers (anhydrous pyrolitic mantle and metasomatized mantle from a lithospheric mantle xenolith) to show the potential range in magma compositions produced in a compositionally heterogeneous uprising mantle plume. Therefore, the modeled magma sources are simplified and less complex than those beneath the West Eifel region, where larger chemical variations within the mantle source are to be expected. Because of (i) unknown exact mantle source composition, (ii) the limited chemical composition in the thermodynamic modeling approach and (iii) the simplified mantle chemistry, our results show compositional trends rather than the exact compositions expected for the West Eifel magmatic rocks. Nevertheless, it is interesting to see to what extent we can reproduce observed first-order chemical trends.

The intraplate West Eifel volcanic field (WEVF) is of specific magmatic and geody-

namic relevance because it is physically related to a seismological low-velocity anomaly in the upper mantle (e.g. Ritter et al., 2001; Keyser et al., 2002) and it is geochemically and geochronologically well-studied (e.g. Mertes and Schmincke, 1985; Schmincke, 2007; Mertz et al., 2015). Results from this study may additionally be of global relevance since the West Eifel represents an example of common intraplate volcanic activity in an orogenic foreland setting which is genetically related to a small-scale plume type in the continental environment (Ritter et al., 2001).

2.4.3.1 Geological setting of the West Eifel volcanic field

2.4.3.1.1 Eifel volcanism

The Eifel volcanism is subdivided into the Pleistocene East and West Eifel as well as the Eocene Hocheifel activity and is located within the Hercynian Rhenish Massif (West-Germany), constrained between the Upper Rhine and Lower Rhine-Roer Graben (Fig. 2.11). The West Eifel volcanic field (WEVF) covers an SE-striking area of approximately 600 km^2 (Fig. 2.11) and includes the youngest volcanism of the Central European Volcanic Province (at ca. 11 ka, Zolitschka et al., 1995).

2.4.3.1.2 West Eifel lavas

The West Eifel low-SiO_2 lavas were classified compositionally as ONB-suite (olivine-nephelinites and basanites) and F-suite (foidites) (Mertes and Schmincke, 1985). Further evidences (chemical, isotopic, geochronological and petrological) suggest distinct petrogenetic evolution and mantle sources for the ONB- and F-suite rocks (e.g. Mertz et al., 2015). Over a period of ca. 0.7 Ma, the magmatic activity started in the north-western part of the WEVF and migrated to the southeast at a lateral motion rate of 4–5 cm/year. Two major magmatic episodes of $>$ 480 ka and $<$ 80 ka age have been identified (Fig. 2.11), which are characterized by distinct elemental and isotopic compositions (Mertz et al., 2015): e.g., volcanism $>$ 480 ka in the NW shows consistent higher radiogenic Sr and higher K_2O/Na_2O compared to $<$ 80 ka activity in the SE of the WEVF (Fig. 2.11). Here, for terminological simplification, these products will be referred to either high-K_2O/Na_2O or low-K_2O/Na_2O group, respectively.

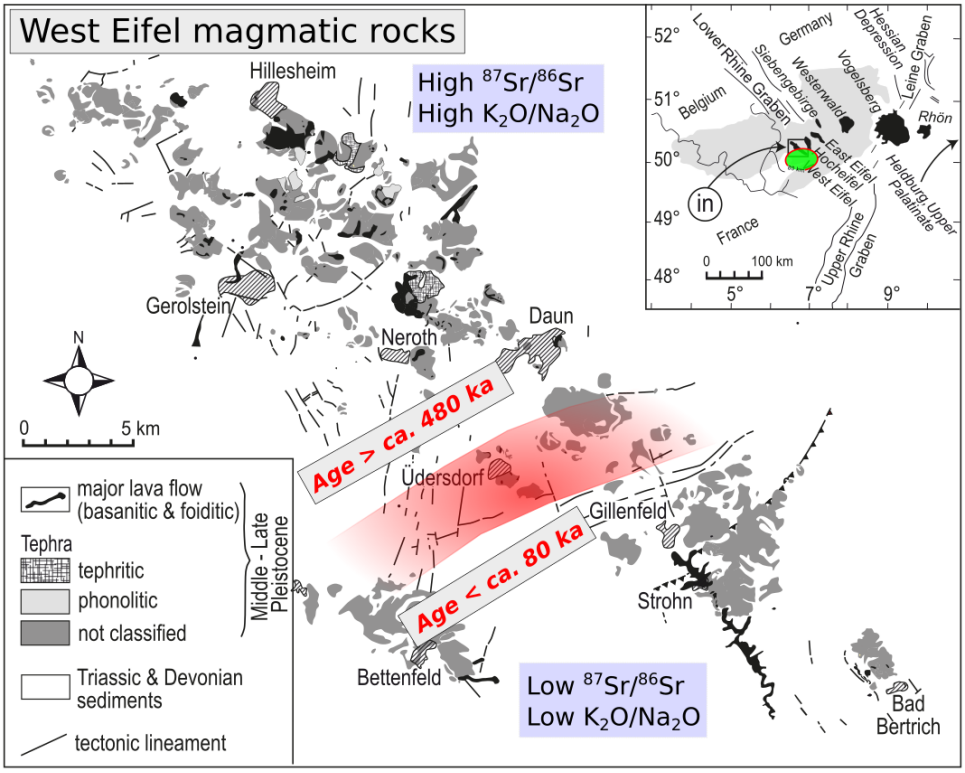

Figure 2.11: Simplified geological map of the West Eifel volcanic field (West-Germany) modified after Mertz et al. (2015). The red shaded area separates activity > 480 ka characterized by high-radiogenic Sr, low-radiogenic Nd and high K_2O/Na_2O in the NW from activity < 80 ka having low-radiogenic Sr, high-radiogenic Nd and low K_2O/Na_2O in the SE. Inset (in) shows the setting of the West Eifel volcanic field within the Cenozoic Central European Volcanic Province. The greyish layer indicates the Hercynian Rhenish Massif. The filled green circle shows the surface-projected lateral extension of the mantle plume at ∼80 km depth after Ritter et al. (2001).

2.4.3.1.3 West Eifel magma sources

Pleistocene Eifel volcanism resulted from the interaction of melts derived from a depleted and enriched mantle source, with the depleted mantle as dominant source for lavas from the low-K_2O/Na_2O group (< 80 ka) (Schmincke, 2007). The origin of all West Eifel magmas is suggested in the garnet-spinel peridotite field at depth of > 70 km (Mertz et al., 2015). The depleted source is interpreted as corresponding to asthenospheric material (e.g. Witt-Eickschen et al., 2003; Mertz et al., 2014). By contrast, the enriched source is suggested as: (1) phlogopite or amphibole-bearing lithospheric mantle metasomatized by multi-stage magmatic processes prior to the eruption (e.g. Witt-Eickschen et al., 2003; Mertz et al., 2015), or alternatively as: (2) part of an uprising mantle plume (e.g. Witt-Eickschen et al., 2003; Shaw et al., 2005); asthenospheric phlogopite-garnet-spinel peridotite (Shaw and Woodland, 2012).

Significant modification of low-SiO_2 magmas by contamination through country rocks

might be unlikely, because of high magma ascent velocities, inferred from the size (e.g. Mertes and Schmincke, 1985; Shaw, 2004) and diffusion profiles (Shaw, 2004) of mantle xenoliths, as well as from isotope analyses which exclude significant crustal contamination (e.g. Wörner et al., 1986). Furthermore, extensive interaction of magma with the country rocks require pervasive flow. However, magma flow along fractures is expected to be much more efficient to transport small magma volumes and mantle xenoliths to the surface. Even the fact that hydrated mantle xenoliths, which are only restricted to the shallower lithospheric mantle < 45 km depth (e.g. Witt-Eickschen et al., 2003), were transported in both young and old West Eifel magmatic rocks (Shaw et al., 2005), suggest that both suites of lavas might pass through a similar enriched lithospheric mantle.

2.4.3.1.4 Pleistocene Eifel plume

The formation of magma in the West Eifel appears to be genetically linked to a seismological low-velocity anomaly (mantle plume), which has been interpreted to have formed via a thermally upwelling upper mantle, with an excess temperature of 150–200 °C (Ritter et al., 2001), or a mantle compositional anomaly (Wilson, 2008; Seiberlich et al., 2013; Prelević et al., 2015). Moreover, a compositional anomaly may even stabilize a small scale cylindrical plume over a longer time span (Dannberg and Sobolev, 2015).

The Eifel plume extends from the mantle transition zone into the lithospheric mantle generally with a diameter of around 100 km (Ritter et al., 2001; Seiberlich et al., 2013). A minor temperature anomaly in the plume is consistent with the lowering of the 410 km discontinuity underneath the Eifel region studied by receiver functions (Grunewald et al., 2001). The surface-projected P-wave-anomaly of the Eifel plume overlaps at $\sim$70 km depth with the geographical position of the < 80 ka volcanism in the WEVF (Mertz et al., 2015), consistent with the numerical simulations indicating that younger pyrolitic magmas were generated at shallower depth during late-stage plume ascent.

The enriched melting source of West Eifel magmas may be directly related to enriched plume material or may be enriched by plume-related processes such as melt or fluid production. Enrichment of the Eifel plume may occur by Alpine or Hercynian subducted material (e.g. fertile eclogite) rising up from the mantle transition zone (e.g. Motoki and Ballmer, 2015). This may support melt generation under relatively cold plume conditions and could be responsible, as a highly reactive agent, for enrichment processes in the overlying mantle.

In our simulations we focus, based on the literature, on the alternative model that the chemical variability (indicated by, e.g., varying K_2O/Na_2O) in West Eifel low-SiO_2

volcanic rocks is related directly to a heterogeneous primary mantle source (including a "metasomatized" asthenospheric plume component) rather than being caused by the interaction of asthenospheric melts with the shallow enriched lithospheric mantle. To test the assimilation of the lithospheric mantle within our modeling approach, two-phase flow including reaction kinetics would be required. However, this is beyond the scope of this work. An involvement of the lithospheric continental mantle cannot be fully excluded.

2.4.3.2 Comparison of the West Eifel magmatic rocks with model magma compositions

2.4.3.2.1 Generation of different magmatic rock compositions

Adaption of numerical model compositions to potentially chemical mantle compositions represented by low-SiO_2 West Eifel lavas is considered to provide geologically significant results of the numerical modeling, i.e., sources of low- and high-K_2O/Na_2O groups correspond to pyrolitic and metasomatized mantle rocks (Tab. 2.1), respectively. Geological significance of the modeling approach is also supported by preserved near-primary compositions of the low-SiO_2 West Eifel lavas, which have not been modified by magma chamber processes (e.g. Wörner et al., 1986), although, slight chemical variations between source and lava compositions may be due to variations in partial melting conditions, high-pressure fractionation or magma mixing. The crystallized magmas, which form the modeled new crust, are foidites forming a trend to basanitic compositions for magmas originating from the model pyrolitic mantle (Fig. 2.12). With increasing critical melt fraction, extracted magmas are depleted in alkali elements (Fig. 2.12B). Rocks with high K_2O+Na_2O (up to 26 wt% for M_{crit} = 4 vol% and up to 18 wt% for M_{crit} = 7 vol%) and K_2O/Na_2O of ∼1 are formed via modeling by melting of primary metasomatized mantle, which has not experienced a previous episode of melt extraction (Fig. 2.12C–E). Late extracted melts from the pyrolitic mantle are higher enriched in silicon and total alkalis (Fig. 2.12A).

Because of the extreme compositional endmembers used in the modeling approach, the results may only represent a trend rather than the exact composition assumed for the West Eifel volcanic rocks. Thus, a combination of both mantle sources employed in different proportions or magma mixing may result in mantle sources that reproduce Eifel-like mantle melts.

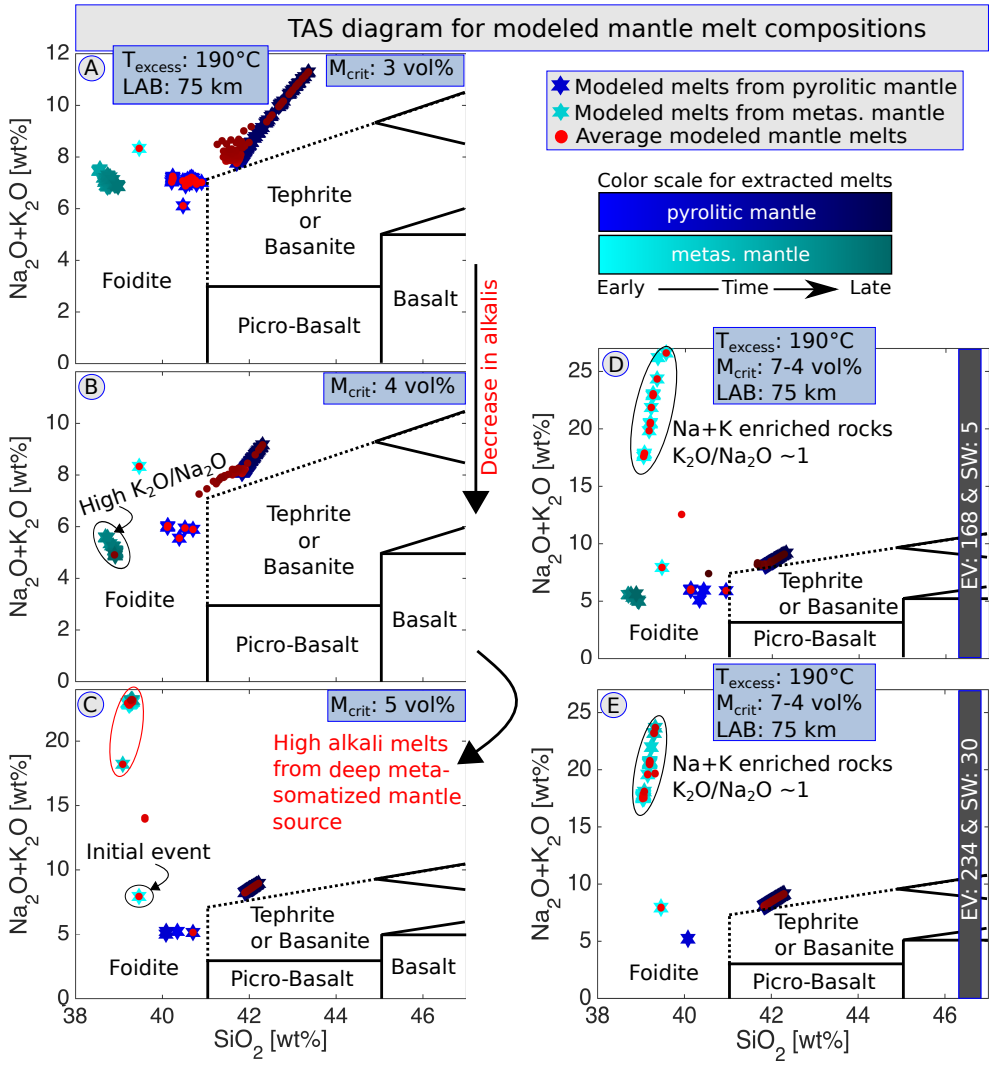

Figure 2.12: Total alkali vs. silica diagram with IUGS classification of aphanitic and glassy volcanic rock types. Melt compositions are recalculated to 100% on a LOI (loss on ignition) free basis. Stars show average compositions of extracted melts from the respective mantle sources, whereas red dots represent the average compositions after magma mixing. The respective colors getting darker with time. EV: total melt extraction events, SW (step width): after a specified number of melt extraction events (here after 5 or 30 respectively) the critical melt fraction is decreased by 1 vol%. The resulting rocks from the extracted melts are foidites. Rocks originating from pyrolitic mantle magmas forming a trend to basanitic compositions.

2.4.3.2.2 Melts from metasomatized mantle

A small critical melt fraction (< 5 vol%) induces a significant amount of extracted melt (100–200 km^2) from the partially molten metasomatized mantle during the first melt extraction event in the simulations. Using a higher critical melt fraction, an elevated plume temperature is required to extract melt from the entire metasomatized mantle. Since temperature decreases from the center to the boundary of the plume, the initial

rock composition is preserved longer at the boundary (Fig. 2.13). This results in a longer lasting melt extraction episode from the metasomatized mantle producing a stable plateau in K_2O/Na_2O (at ~1) (Fig. 2.6D–F) as well as alkali-rich melts with $Na_2O+K_2O > 16$ wt% (Fig. 2.12C).

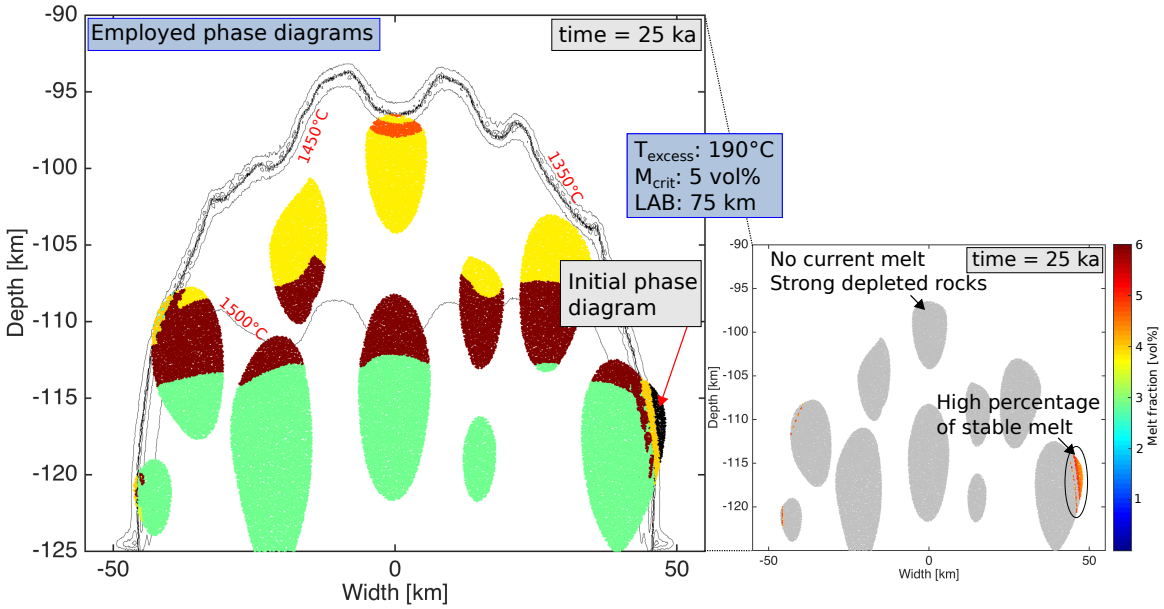

Figure 2.13: Left: Different phase diagrams used for metasomatized mantle components in the uprising mantle plume after 25 ka. Each color represents a different phase diagram. Isotherms (every 50 °C) show the propagation of the thermal plume. For a high employed critical melt fraction (M_{crit} = 5 vol%), the initial phase diagram does not change everywhere to a more depleted phase diagram during the first kyrs of plume ascent. Colder areas along the peripheral thermal mantle plume can still use the initial phase diagram (black), whereas in the central plume melt extraction has already depleted the rocks preventing further melting. The colder metasomatized mantle is characterized by a high stable melt fraction (right) that successively exceeds the critical melt fraction with time and produces the plateau in K_2O/Na_2O (Fig. 2.6D/2.6J).

The melt extracted from the metasomatized mantle represents the magma composition stable at P–T conditions that are reasonable to present the melting source of West Eifel volcanic rocks. Even if the metasomatized mantle would be partially molten at deeper levels than the maximum depth of the model domain, it may equilibrate during its ascent until it is decoupled from the source region by melt extraction which, in our study, takes place in the uppermost mantle (120–70 km).

However, in order to generate volcanic rocks similar to the high-K_2O/Na_2O group, a mantle source more enriched in Ca and more depleted in K and Na compared to our metasomatized mantle here is required, based on the composition of West Eifel volcanic rocks (Mertes and Schmincke, 1985) that may actually reflect the composition of the source. Lower Na_2O+K_2O values of ≈5 wt% can be produced by remelting previously

melt-depleted metasomatized mantle (Fig. 2.12A–B). However, these modeled melts are characterized by high K_2O/Na_2O as well (e.g., Fig. 2.6C), inconsistent with the observed chemical compositions of the high-K_2O/Na_2O group of the West Eifel (Mertes and Schmincke, 1985).

2.4.3.2.3 Mantle sources potentially responsible for the chemical signal of West Eifel rocks

Low-K_2O/Na_2O group:

The most primitive extracted melts (highest MgO and FeO and lowest Al_2O_3, Na_2O and K_2O concentrations) form during the earliest stage of the plume ascent (E3, Fig. 2.9) at deep levels of the pyrolitic mantle with high melting temperatures. Thus, a decrease in the plume temperature may decrease the Mg-concentration in the extracted melt. This process may be important for the formation of the low-K_2O/Na_2O group of the West Eifel. They are less primitive (lower MgO contents in the low-K_2O/Na_2O group, Mertes and Schmincke, 1985) than our modeled melts from the pyrolitic mantle and may thus be better explained by magmas generated at shallower depths and lower temperatures than in our simulations.

High-K_2O/Na_2O group:

The most primitive melt composition of the metasomatized mantle is formed during the first melt extraction event and is characterized by much higher MgO, FeO and CaO as well as lower Al_2O_3, Na_2O, K_2O and H_2O contents due to a higher partial melt fraction at the beginning (Fig. 2.9). Despite the similar K_2O and Na_2O values between the extracted melt and the high-K_2O/Na_2O group (Mertes and Schmincke, 1985), the high MgO concentration shows that magmas generated from higher melt fractions cannot simply form rocks from the high-K_2O/Na_2O group. However, lower Al_2O_3, K_2O, Na_2O and H_2O as well as higher MgO, FeO and CaO concentrations are formed after the initial melt extraction event too (red dotted rectangle, Fig. 2.10). The generated magma fits in Al_2O_3, FeO and MgO concentration the magma compositions from the high-K_2O/Na_2O group, but still contains too high K_2O and Na_2O values and too low CaO concentrations (Mertes and Schmincke, 1985).

Mantle source mixing:

A combination of both mantle sources in different percentages may lead to average mantle sources that are able to produce Eifel-like mantle melts. Such a mixed source would slightly increase the K_2O/Na_2O in extracted melts, resulting in better agreement with the low-K_2O/Na_2O group of the "Young West Eifel" (e.g. Fig. 2.6D). For the enriched

magmas, especially the late generated magmas formed by decompression melting, the model magmas are too strongly depleted in Na_2O compared to K_2O (high K_2O/Na_2O, e.g. Fig. 2.6A) compared to the high-K_2O/Na_2O group. Potentially, magma mixing between both sources in different percentages may produce similar magma compositions to those found in the West Eifel volcanic field. Magma mixing may explain small variations within one rock suite in the West Eifel as well (Shaw and Woodland, 2012), where melt was simultaneously extracted from both the more primitive anhydrous and the metasomatized hydrous mantle sources.

Temporal activation of different mantle sources:
The onset of melt extraction from pyrolitic mantle and occurrence of magmatic breaks between different magmatic episodes, are influenced by several parameters. Higher plume excess temperature results in earlier melt generation and increases the mantle plume ascent velocity and thus the rate of decompression melting. Furthermore, a small enriched component in the pyrolitic mantle source, which is absent in our models, would likely decrease the plume excess temperature required to exceed the critical melt fraction and hence the rate at which the plume rises. All these affect the difference between the temporal onset of the younger West Eifel volcanism (< 80 ka) and the onset of melt extraction from pyrolitic mantle in our simulations. Changing the composition of the metasomatized mantle components to a less enriched one will decrease the stable melt fraction at the beginning of the simulation and slow the mantle depletion process. Consequently, a more enriched pyrolitic mantle lowers the required plume melting temperature. A less enriched metasomatized mantle delays full chemical depletion and thus melt extraction is active over a longer period of time. Furthermore, mechanical boundary conditions employed in the models (e.g. background strain rate) may affect the plume rising time. At the employed extensional background strain rate (10^{-16} 1/s) in our simulations, there are no significant differences between numerical experiments with free slip and constant strain rate mechanical boundary conditions. Thus, the buoyancy force induced by the low-density material as well as the high strain rates have a larger effect on the plume rising time.

Final remarks:
Our modeling results show that extracted melts from a metasomatized asthenospheric mantle generate magma compositions that are consistent with the chemical signature observed in the high-K_2O/Na_2O group of the West Eifel. Together with decompression melting of more fertile components in the uprising mantle plume, a chemical magma evolution from high to low K_2O/Na_2O is observed. Thus, a decrease in K_2O/Na_2O (step-like-profile) found in the West Eifel lavas is reproducible through numerical modeling of a

heterogeneous asthenospheric mantle source in a rising plume, consistent with a transition between melting metasomatized and pyrolitic mantle components (Fig. 2.14).

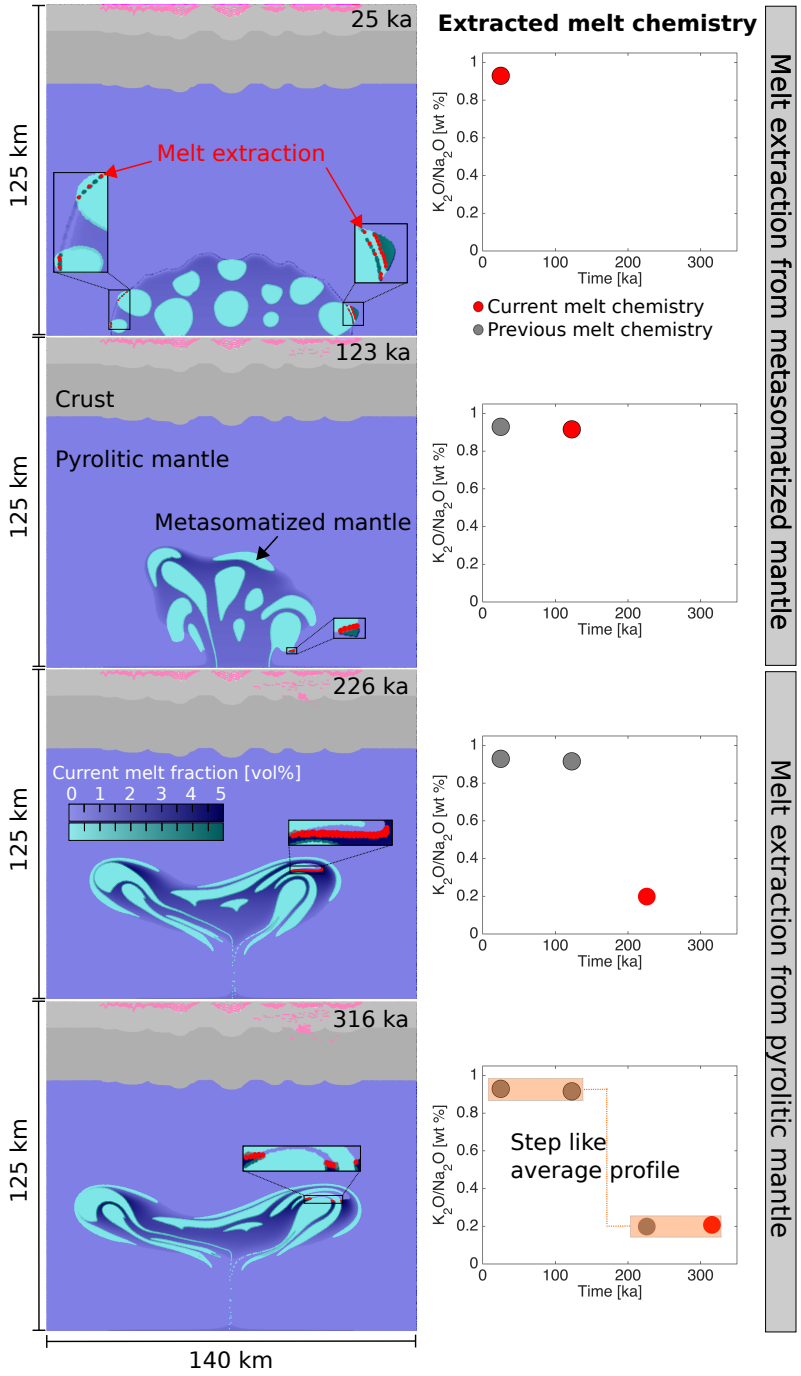

Figure 2.14: Illustration of the development of a step-like-profile in K_2O/Na_2O of the extracted melts from a heterogeneous mantle source. The transition from high to low K_2O/Na_2O is concomitant with the transition of melt from metasomatized to pyrolitic mantle. The plume and melt extraction evolution are shown for a simulation with +190 °C plume excess temperature and a LAB at 75 km depth. The melt is extracted as soon as the critical fraction of 5 vol% is exceeded (in red is shown where melt extraction occurred in the plume).

The decrease in M_{crit} during one simulation causes a more distinct step-like-profile in K_2O/Na_2O. By decreasing the M_{crit} value, we assume that an ever smaller amount of melt is extracted from the partially molten source and that can reach the surface to form volcanic rocks. This assumption is based on REE ratios that suggest a potential decrease of melt fraction from the older (> 480 ka) to the younger (< 80 ka) group of the West Eifel magmatic rocks (Mertz et al., 2015). Furthermore, previous melt pathways may weak the crust by creating vertically oriented structures (such as crystallized dikes, oriented crystals in the dike or chilled margins) that might help melts to localize in ascent zones and to follow previous pathways. Very small melt fractions would not reach the surface if the rock is fully intact or if horizontally oriented structures form a barrier. To break these rocks much higher magma pressures are required and the magma ascent rates will be much slower, which is likely to result in crystallization before the melts reach the surface.

A table that compares the composition of the high- and low-K_2O/Na_2O group with the modeled magma compositions is given in the Appendix (Tab. 2.C1).

2.5 CONCLUSION

A new method was developed that tracks the evolving chemistry of source and magmatic rocks by combining a geodynamic code with a thermodynamic modeling approach.

Coupled petro-thermo-mechanical simulations have been performed to understand the interaction between physical and chemical processes that influence magma formation and chemical evolution in an uprising heterogeneous mantle plume. The main results can be summarized as follows:

- A first episode of partial melting occurs at the onset of the simulation, followed by a second one, which is triggered by decompression.
  - The occurrence of the second melt extraction episode is favored by a shallower LAB at 75 km.
  - A lower critical melt fraction and/or higher plume excess temperature facilitates melt extraction.
  - The resulting melts from the second melt extraction episode of the metasomatized mantle show a strongly increased K_2O/Na_2O ratio.
- A step-like-profile in the K_2O/Na_2O ratio (high to low values seen in extracted melts), occurs by melting a heterogeneous mantle source in an uprising mantle plume (Fig. 2.14).

  - Relatively high critical melt fractions ($\geq$ 5 vol%) that prevent the metasomatized mantle source from rapid depletion, are required to form a step-like-profile.
  - Despite a temporal overlap between both magmatic activities, the average magma chemistry of one time step still follows a step-like-profile in K_2O/Na_2O, depending on the relative proportions of extracted melts from the metasomatized and pyrolitic mantle rocks.
  - A deeper lithosphere-asthenosphere boundary facilitates the development of a step-like-profile, as it results in a later onset of the second melt extraction episode from pyrolitic mantle which melt productivity is reduced.
  - The decrease of the critical melt fraction during plume ascent favors under cool plume conditions the formation of a step-like-profile. Here, the first melt extraction episode from the metasomatized mantle is more stabilized at the beginning and melt extraction from the more primitive pyrolitic mantle is activated later.

- The average melting depth and temperature decreases during plume ascent. The magma temperature is higher and the melt formation occurs at shallower depth for extracted melts originating from a pyrolitic mantle source. The lowest magma temperatures occur for strongly enriched metasomatized mantle that did not undergo melt extraction yet.

- Our results are consistent with first order trends observed in the plume-related intracontinental West Eifel volcanism, where a change in magma compositions from high to low K_2O/Na_2O ratios, suggests that subsequent melt pulses tap compositionally different mantle source regions.

2.6 ACKNOWLEDGEMENTS

Funding was provided by the VAMOS Research Center, University of Mainz (Germany). We would like to thank the editor Rob Govers and the reviewers Jeroen van Hunen and Harro Schmeling for the useful comments.

2.7 APPENDIX

2.A Methods

2.A.1 Crustal phase diagrams

The computation of crustal phase diagrams is executed with Perple_X 6.7.0 (Connolly, 2005, 2009). Input scripts are provided in the electronic supplementary materials. The main equilibrium mineral assemblages of the employed upper and lower crust are shown in the pseudosections, Figure 2.A1. The activity-composition models used in Perple_X are listed in Table 2.A1.

Table 2.A1: The activity-composition models used in the Perple_X calculations.

Mineral	**Activity-composition model**	**Reference**
Garnet	Gt(HP)	Holland and Powell (1998)
Chloritoid	Ctd(SGH)	Smye et al. (2010)
Chlorite	Chl(HP)	Holland et al. (1998)
Biotite	Bio(TCC)	Tajčmanová et al. (2009)
White mica	Mica(CHA)	Auzanneau et al. (2010)
		Coggon and Holland (2002)
Feldspar	Pl(I1,HP)	Holland and Powell (2003)
Clinoamphibole	cAmph(DP)	Diener et al. (2007)
Ilmenite	Ilm(WPH)	White et al. (2000)
Clinopyroxene	Cpx(HP)	Holland and Powell (1996)
Orthopyroxene	Opx(HP)	Holland and Powell (1996)
Olivine*	O(HP)	Holland and Powell (1998)
Liquid model*	melt(HP)	Holland and Powell (2001)
		White et al. (2001)

*) Added for the “Newly-generated-crust”

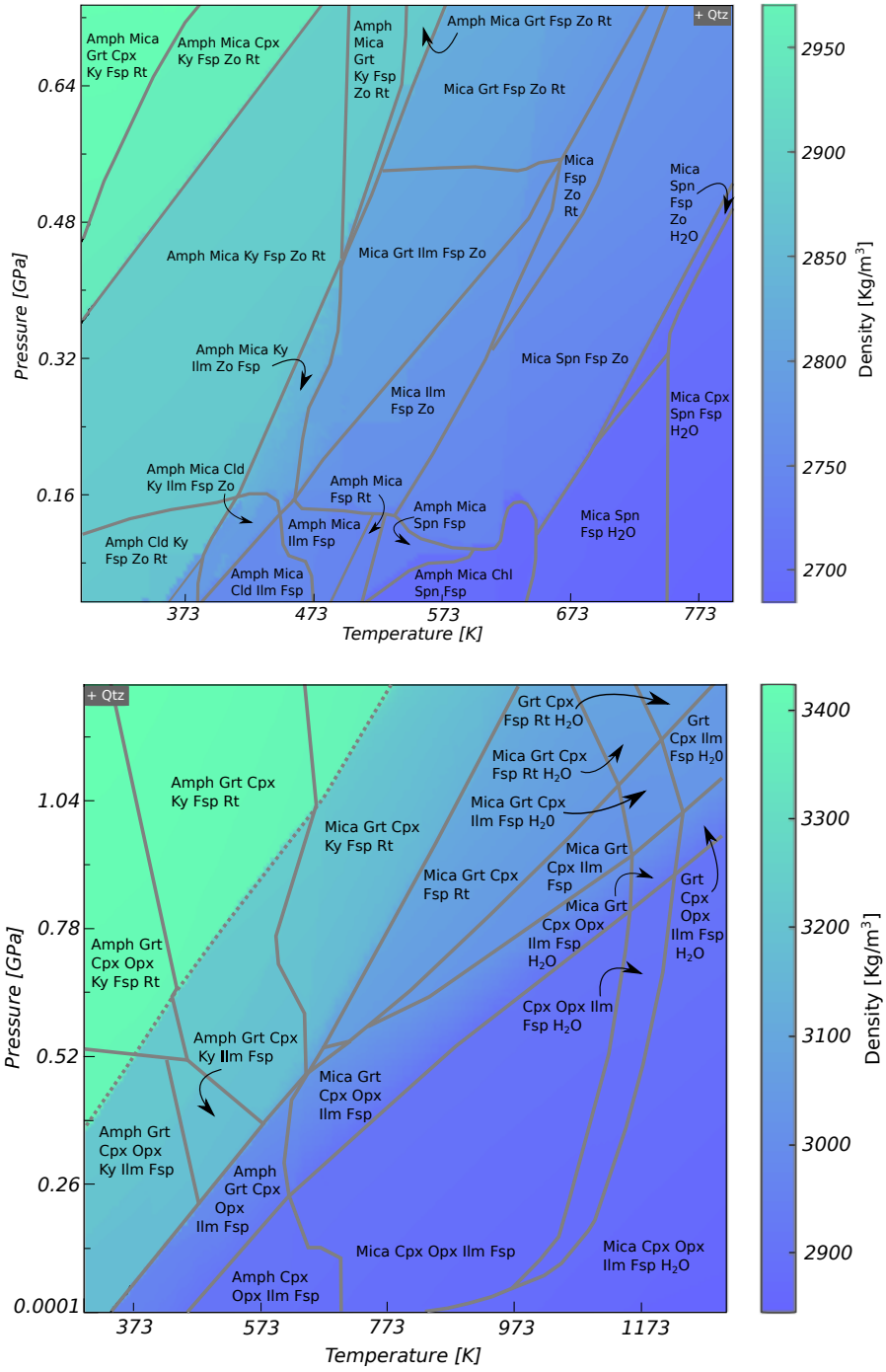

Figure 2.A1: Pseudosections and density distributions calculated with Perple_X 6.7.0 for the upper (top) and lower crust (bottom). The used mineral abbreviations are: Amph = amphibole (glaucophane, actinolite, cAmph(DP), pargasite); Mica = mica (Mica(CHA), Bio(TCC)); Grt = garnet (Gt(HP)); Cpx = clinopyroxene (Cpx(HP)); Opx = orthopyroxene (Opx(HP)); Ky = kyanite; Fsp = feldspar (microcline, albite, sanidine, Pl(I1,HP)); Rt = rutile ; Zo = zoisite (zoisite, clinozoisite); Spn = sphene; H_2O = H_2O; Chl = chlorite (Chl(HP)); Ilm = ilmenite (Ilm(WPH)) and Cld = chloritoid (Ctd(SGH)). Only the main phase stability fields are presented.

2.A.2 Computation of pyrolitic phase diagrams

The computation of mantle phase diagrams is executed using AlphaMELTS 1.4 (software package, Smith and Asimow, 2005) as a text-menu based front-end to the pMELTS software (Ghiorso et al., 2002). The phase diagrams of the pyrolitic mantle are computed with pMELTS in an automatized way starting with the initial phase diagram to create phase diagrams for depleted and double depleted rock compositions (scripts for the calculation are provided in the electronic supplementary materials). An automated routine is used to restart the thermodynamic simulation as soon as the executed pMELTS computation fails which frequently occurs. Starting conditions are slightly changed (initial pressure and pressure interval) for the restart. The mineral assemblages from both initial phase diagrams (pyrolitic and metasomatized mantle) are shown together along a middle cross-section through our model domain in Figure 2.A2.

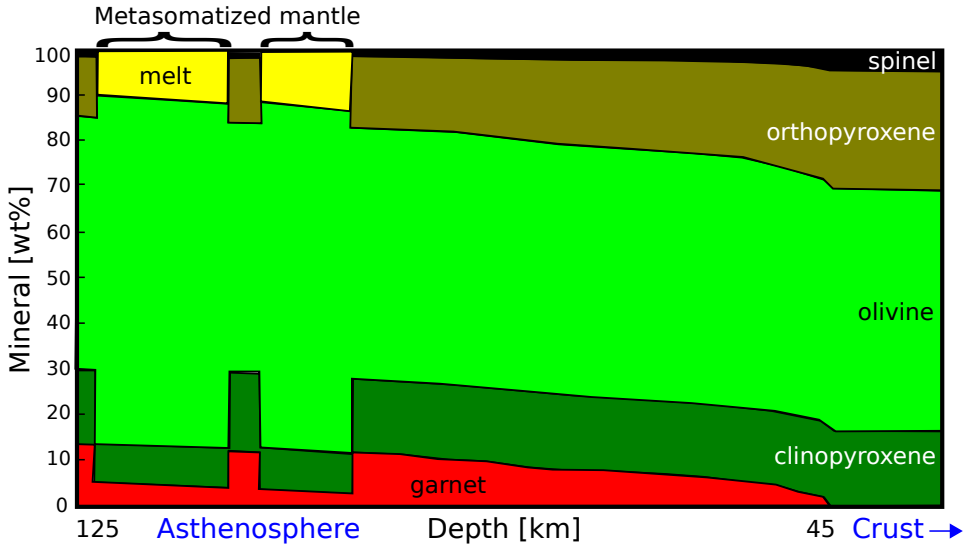

Figure 2.A2: Main initial mineral distribution in the mantle (30–125 km depth) along a middle cross-section through our model domain (Fig. 2.3). The used model is characterized by an initial plume excess temperature of 150 °C forming melts in the metasomatized mantle and by a LAB at 75 km depth. Further information about the mineral assemblages over mantle P–T conditions are provided in the respective phase diagrams of the initial metasomatized and pyrolitic mantle found in the electronic supplementary materials.

In general, the chemical evolution of extracted melts is strongly affected by the choice of bulk rock compositions used for computing the initial phase diagrams. These initial phase diagrams control the rock evolution in the geodynamic simulations, as all phase diagrams for depleted and double depleted rocks are constructed from them. Moreover, the limited number of available phase diagrams has an influence on the rock type that can be formed.

2.A.3 Self-organizing Maps

We apply a neural network approach to identify representative solid compositions (see Section 2.2.1). As neural network approach (machine learning algorithm), a Self-organizing Map (SOM, Kohonen, 2001) is used in combination with a vector quantization algorithm, k-means (e.g. Jain and Dubes, 1988). The SOM consists of a set of notes ("neurons") forming a hexagonal arranged two-dimensional regular grid (each neuron has six neighbors, if not located at the boundary). Each of the neurons is represented by a "prototype vector" in the input space. Consequently, the prototype vectors have the same dimension as the input data (here 10D or 11D, depending on the number of oxides).

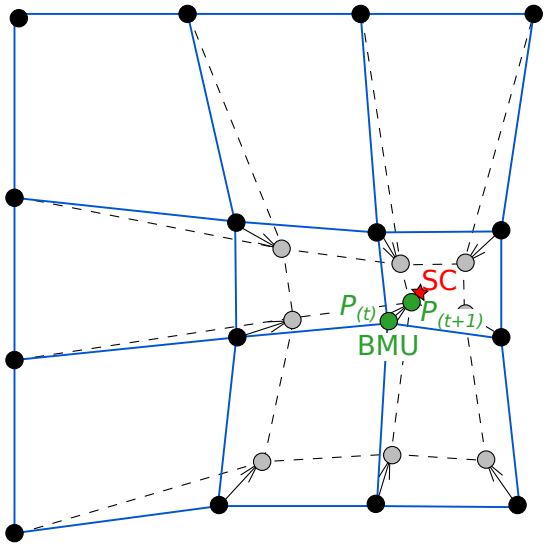

Figure 2.A3: Learning process of the SOM after Vesanto et al. (2000). The best-matching unit (BMU), which represents the neuron closest to the data point, moves together with neighboring neurons towards the data point (here described by one solid composition (SC), indicated as a red star). Grey notes correspond to the adjusted SOM after a training step t. The displacement of the closest prototype vector (BMU) within one training step is shown in green.

During the training, the SOM behaves like an elastic net that folds onto the input data. After the prototype vectors are initialized, the training of the SOM starts by selecting a random input data point and its distance to the surrounding prototype vectors. The closest prototype vector is the best-matching unit (BMU). The BMU and the prototype vectors in the near surrounding move towards the current data point and the lattice deforms (Fig. 2.A3).

For the clustering results presented in this section, solid compositions are used from the near solidus P–T field (0–10 vol% melt) of the initial phase diagram from the meta-somatized mantle (Figs. 2.A4–2.A6). The adjusted prototype vectors represent the input data (solid compositions) on the SOM (Fig. 2.A4) and are used for further clustering.

A cluster formation can already be visualized on the SOM, as large distances between neighboring prototype vectors indicate a significant change in chemistry (Fig. 2.A4).

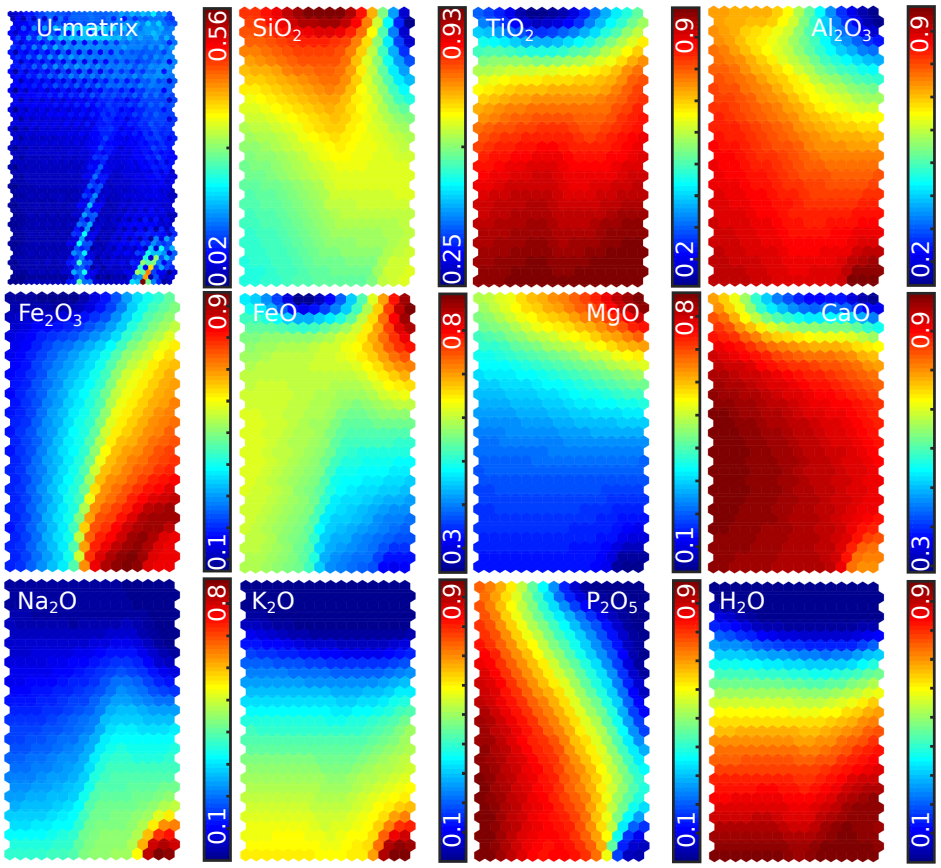

Figure 2.A4: U-matrix and oxide concentrations of the prototype vectors. The solid compositions used as input data for the SOM are provided from the initial phase diagram of the metasomatized mantle. The Unified distance matrix (U-matrix) shows the distances between neighboring prototype vectors in a color-coded representation. Normalized oxide concentrations are shown on the prototype vectors of the SOM.

However, to really classify the different clusters, a vector quantization algorithm, k-means, must be applied to group similar prototype vectors (Fig. 2.A5B). To estimate a suitable number of clusters, we compute a validity index by determining the ratio between the sum of intracluster and intercluster distances, called Davies–Bouldin (DB) index (Davies and Bouldin, 1979). For the phase diagram of the initial metasomatized mantle, the most suitable number of clusters is 7. The solid compositions used for the SOM as input data are assignable to the clusters. Thus, each of the seven clusters combines solid compositions with similar oxide concentrations (Fig. 2.A5C), which derive from specific P–T and thus melt fraction conditions (Fig. 2.A5A–B). From each cluster, at least one of the solid compositions is used as bulk rock composition to compute a new phase diagram

for depleted mantle rocks using pMELTS.

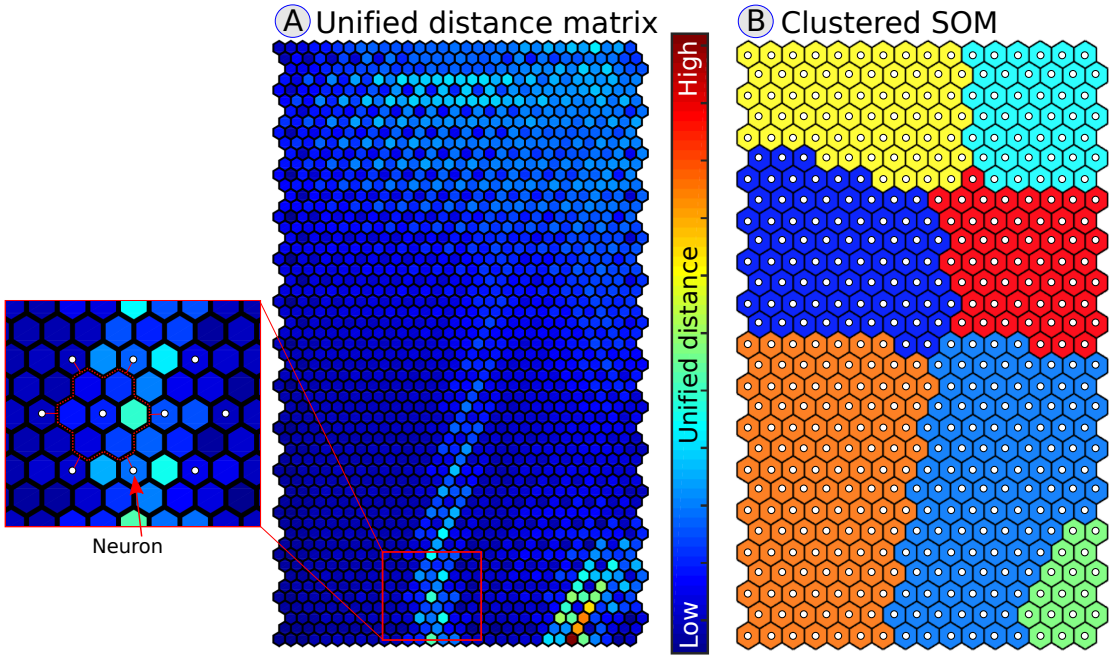

Figure 2.A5: SOM and k-means applied to solid compositions from the initial phase diagram of the metasomatized mantle. A: The Unified distance matrix (U-matrix) shows the distances between neighboring prototype vectors. Warm colors represent large and cold colors short distances. Each neuron (white circle) is surrounded by six other ones producing a hexagonal lattice. The color of the central neuron indicates the average distance to the surrounding ones. The color of the hexagonal fields between the neurons is scaled according to the internode distances. B: Clustered SOM after k-means is applied to the prototype vectors. Classification result is shown on the SOM and is directly related to the U-matrix. The colors of the seven clusters are referred to the colors in Figure 2.A6. Each white circle represents a neuron.

A code example of the clustering algorithm (SOM with k-means and DB-index) is given in the electronic supplementary materials (SOM.m) applied to the initial phase diagram of the metasomatized mantle. The MATLAB library is downloadable at: http://www.cis.hut.fi/somtoolbox/ (Vesanto et al., 2000).

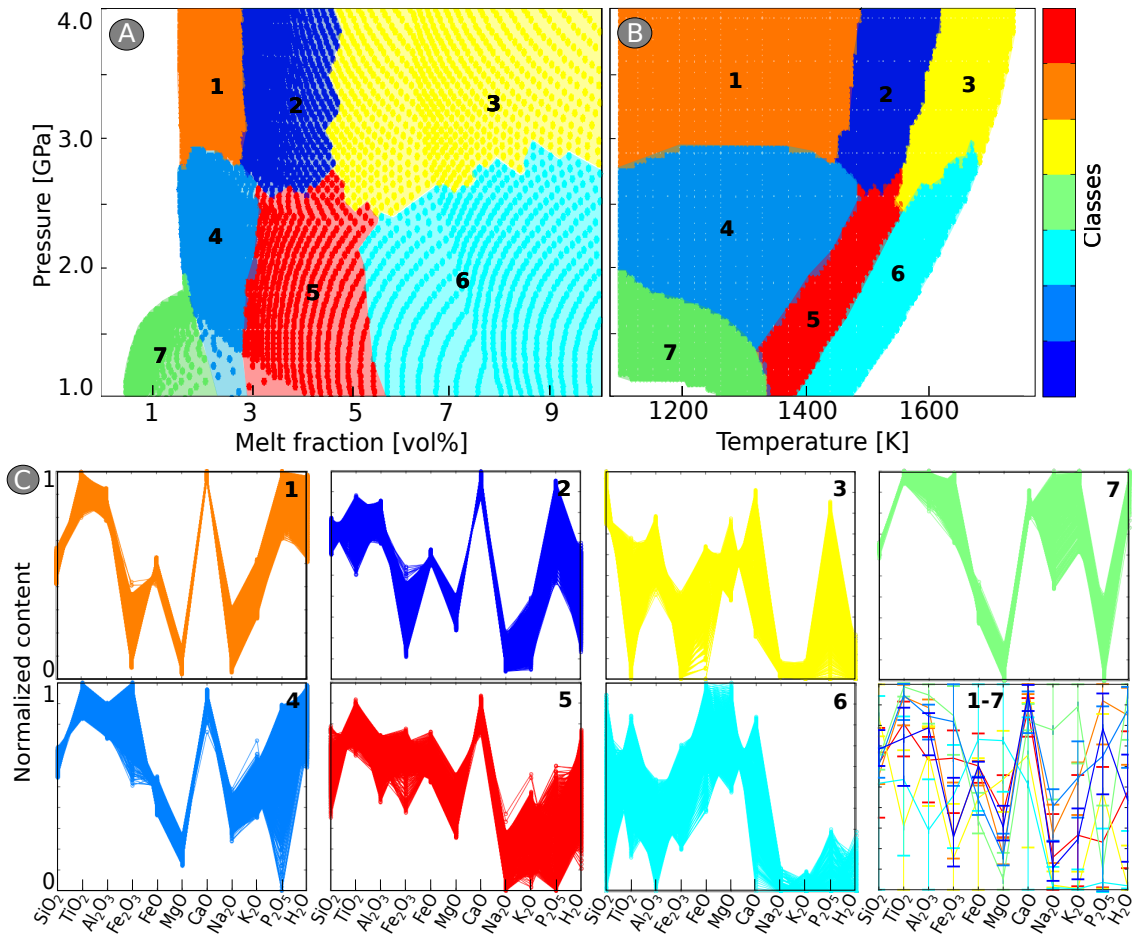

Figure 2.A6: Identifying representative solid compositions of the initial phase diagram from the metasomatized mantle using SOMs. The input data are solid compositions (consisting of 11 different oxides) from the near-solidus P–T field (0–10 vol% melt and 1.0–4.0 GPa). Classified compositions are illustrated in terms of pressure and melt fraction (A) and pressure and temperature (B). Colors represent 7 classes determined by SOM analysis. C: Each class has a characteristic distribution pattern of solid oxide compositions. The average compositions (colored lines) and the respective minimum and maximum value (horizontal thick lines) of the normalized oxides are plotted together from all classes (bottom right).

2.A.4 Modeling parameters

Rheology parameters used for dislocation and diffusion creep laws are provided in Tables 2.A2 and 2.A3. Other applied parameters for the geodynamic modeling are described in Tables 2.A4–2.A6.

Table 2.A2: Rheology parameters used for the dislocation creep. Dry and wet olivine creep law parameters are from Hirth and Kohlstedt (2003). β parameter is only valid if melt fraction $M \lesssim 12$ vol% (Hirth and Kohlstedt, 2003). Quartzite and plagioclase$_{An75}$ dislocation creep parameters are from Ranalli (1995).

			Upper crust	**Lower crust**	**Rock$_{extrusive}$ (new crust)**	**Rock$_{intrusive}$ (new crust)**	**Mantle (pyrolitic)**	**Mantle (metasomatized)**
Symbol	**Meaning**	**Unit**	Quartzite	Plagioclase$_{An75}$	Plagioclase$_{An75}$	Plagioclase$_{An75}$	Dry Olivine	Dry Olivine Wet Olivine
A	Prefactor	$\mathrm{Pa}^{-n}s^{-1}$	$2.6673{\cdot}10^{-20}$	$2.0822{\cdot}10^{-23}$	$2.0822{\cdot}10^{-23}$	$2.0822{\cdot}10^{-23}$	$1.1000{\cdot}10^{-16}$	$1.1000{\cdot}10^{-16}$ $9.0000{\cdot}10^{-20}$
n	Stress exponent		2.4	3.2	3.2	3.2	3.5	3.5 3.5
E	Activation energy	kJ/mol	156	238	238	238	530	530 480
V	Activation volume	m^3/mol	0	0	0	0	$1.5{\cdot}10^{-5}$	$1.5{\cdot}10^{-5}$ $1.1{\cdot}10^{-5}$
F	Prefactor for tensorial form		0.3065	0.3019	0.3019	0.3019	0.3048	0.3048 0.3048
C_{OH}	Water fugacity	$H/10^6 Si$	1	1	1	1	1	1 1000
r	C_{OH}-exponent		0	0	0	0	0	0 1.2
β	Melt fraction prefactor		0	0	0	0	40	40 40

Table 2.A3: Rheology parameters used for the diffusion creep in the mantle. Dry and wet olivine creep law parameters are from Hirth and Kohlstedt (2003). β parameter is only valid if melt fraction $M \lesssim 12$ vol% (Hirth and Kohlstedt, 2003).

			Mantle (pyrolitic)	**Mantle (metasomatized)**
Symbol	**Meaning**	**Unit**	Dry Olivine	Dry Olivine
				Wet Olivine
A	Prefactor	$Pa^{-1}s^{-1}$	1500	1500
				1
E	Activation energy	kJ/mol	375	375
				335
V	Activation volume	m^3/mol	$5{\cdot}10^{-6}$	$5{\cdot}10^{-6}$
				$4{\cdot}10^{-6}$
F	Prefactor for tensorial form		0.5	0.5
				0.5
d	Grain size	m	0.01	0.01
				0.01
p	Grain size exponent		3	3
				3
C_{OH}	Water fugacity	$H/10^6Si$	1	1
				1000
r	C_{OH}-exponent		0	0
				1
β	Melt fraction prefactor		30	30
				30

Table 2.A4: Fixed parameters used in the geodynamic models.

Symbol	**Meaning**	**Unit**	**Value**
η_{LC}	Viscosity lower cutoff	Pas	10^{17}
η_{UC}	Viscosity upper cutoff	Pas	10^{25}
g	Gravity value	m/s^2	9.8
	Gravity angle	°	90
$\dot{\varepsilon}_{BG}$	Background strain rate	1/s	10^{-16}
α	Thermal expansivity	K^{-1}	$3{\cdot}10^{-5}$
k	Thermal conductivity	W/(mK)	3
C_p	Heat capacity	J/(kgK)	1050
	Radioactive heat	$\mu W/m^3$	1 for crust
			0.022 for mantle
Q_L	Latent heat of fusion	kJ/kg	400
ϕ	Friction angle	°	30
c	Cohesion	Pa	$10{\cdot}10^6$
G	Shear modulus	Pa	$3.6{\cdot}10^{10}$ for crust
			$7.4{\cdot}10^{10}$ for mantle

Table 2.A5: Melt extraction parameters. M_{min} = non-extractable melt fraction, M_{max} = maximum of total extractable melt and M_{crit} = melt threshold (melt extraction takes place if the critical melt fraction is exceeded), in vol%. $\text{rock}_{intrusive}/\text{rock}_{extrusive}$ = ratio between volcanic and plutonic rock generation and λ = factor that weakens the lithosphere/asthenosphere between melt extraction and emplacement, with values defined between 0 and 1.

Parameter	**Mantle (pyrolitic)**	**Mantle (metasomatized)**
M_{min}	0.5	0.5
M_{max}	50	50
M_{crit}	1–8	1–8
$\text{rock}_{intrusive}/\text{rock}_{extrusive}$	0.95	0.95
Melt weakening plasticity factor (λ)	0.5	0.5

Table 2.A6: Temperature distribution in the initial model setup and in the newly-generated-crust.

	Depth [km]	**Temperature [°C]**
Surface	0	20
$\text{Rock}_{extrusive}$	∼0	90% of melting T
Upper crust	0–10	linear increase
Lower crust	20–30	linear increase
$\text{Rock}_{intrusive}$	< 30	90% of melting T
Moho	30	750
Pyrolitic mantle	30–125	linear increase
	75 or 85	1300
Adiabatic gradient	75–125 or 85–125	0.3 °C/km
Metasomatized mantle	∼95–125	+150 – +220
	(radius ∼50)	plume excess T

2.B Executed geodynamic simulations

2.B.1 General overview

The depth of the thermal lithosphere-asthenosphere boundary (LAB), the extractable melt fraction and the initial plume excess temperature are systematically varied in coupled geodynamical petrological models (Tabs. 2.B1–2.B2) to investigate their influence on melt chemistry and plume dynamics. An exemplary input script for the geodynamic simulation (Plume.m) is given in the electronic supplementary materials.

Table 2.B1: Part 1: Executed numerical experiments. Changed parameters are: initial plume excess temperature (T_{excess}), critical melt fraction (M_{crit} in vol%), the step width (after a specified number of melt extraction events the critical melt fraction is decreased by 1 vol%) and the depth of the thermal LAB. X: melt extraction from the pyrolitic mantle occurs. $^{ref)}$ Pure thermal plume; $^{*)}$ A second plume is initialized ∼500 ka after the model has been started.

Experiment	**T$_{excess}$ [°C]**	**M$_{crit}$**	**Step width**	**LAB [km]**	**Melting pyrolitic mantle**
1	150	1	-	75	X
2	150	1	-	85	X
3	150	2	-	75	
4	150	2	-	85	
5	150	5–1	5	75	X
6	150	5–1	2	85	
7a	170	2	-	75	X
7b^{ref}	170	2	-	75	X
8a	170	2	-	85	X
8b^{ref}	170	2	-	85	X
9	170	3	-	75	X
10	170	3	-	85	X
11	170	4	-	75	
12	170	4	-	85	
13	170	6–2	5	75	X
14	170	6–2	2	85	X
15	170	7–3	5	75	
16	170	7–3	5	85	
17	190	3	-	75	X
18	190	3	-	85	X
19	190	4	-	75	X
20	190	4	-	85	X
21a	190	5	-	75	X
21b*	190	5	-	75	X
22	190	5	-	85	X
23	190	6	-	75	X

Table 2.B2: Part 2: Executed numerical experiments. Changed parameters are: initial plume excess temperature (T_{excess}), critical melt fraction (M_{crit} in vol%), the step width (after a specified number of melt extraction events the critical melt fraction is decreased by 1 vol%) and the depth of the thermal LAB. X: melt extraction from the pyrolitic mantle occurs.

Experiment	**T$_{excess}$ [°C]**	**M$_{crit}$**	**Step width**	**LAB [km]**	**Melting pyrolitic mantle**
24	190	6	-	85	
25	190	7–3	5	75	X
26	190	7–3	30	75	X
27	190	7–3	5	85	X
28	190	7–4	5	75	X
29	190	7–4	30	75	X
30	190	7–4	5	85	X
31	220	3	-	75	X
32	220	3	-	85	X
33	220	4	-	75	X
34	220	4	-	85	X
35	220	5	-	75	X
36	220	5	-	85	X
37	220	6	-	75	X
38	220	6	-	85	X
39	220	7	-	75	X
40	220	7	-	85	X
41	220	7–3	5	75	X
42	220	7–3	30	75	X
43	220	7–3	5	85	X
44	220	7–3	30	85	X
45	220	7–4	5	75	X
46	220	7–4	30	75	X
47	220	7–4	5	85	X
48	220	7–4	30	85	X

2.B.2 K_2O to Na_2O ratio in the extracted melts of all executed simulations

The temporal evolution of the K_2O/Na_2O ratio in the extracted melts is presented in the Figures 2.B1–2.B3 for all executed geodynamic simulations. The K_2O/Na_2O ratio is affected by the critical melt fraction (M_{crit}), the initial plume temperature (T_{excess} to the surrounding mantle) and the LAB depth.

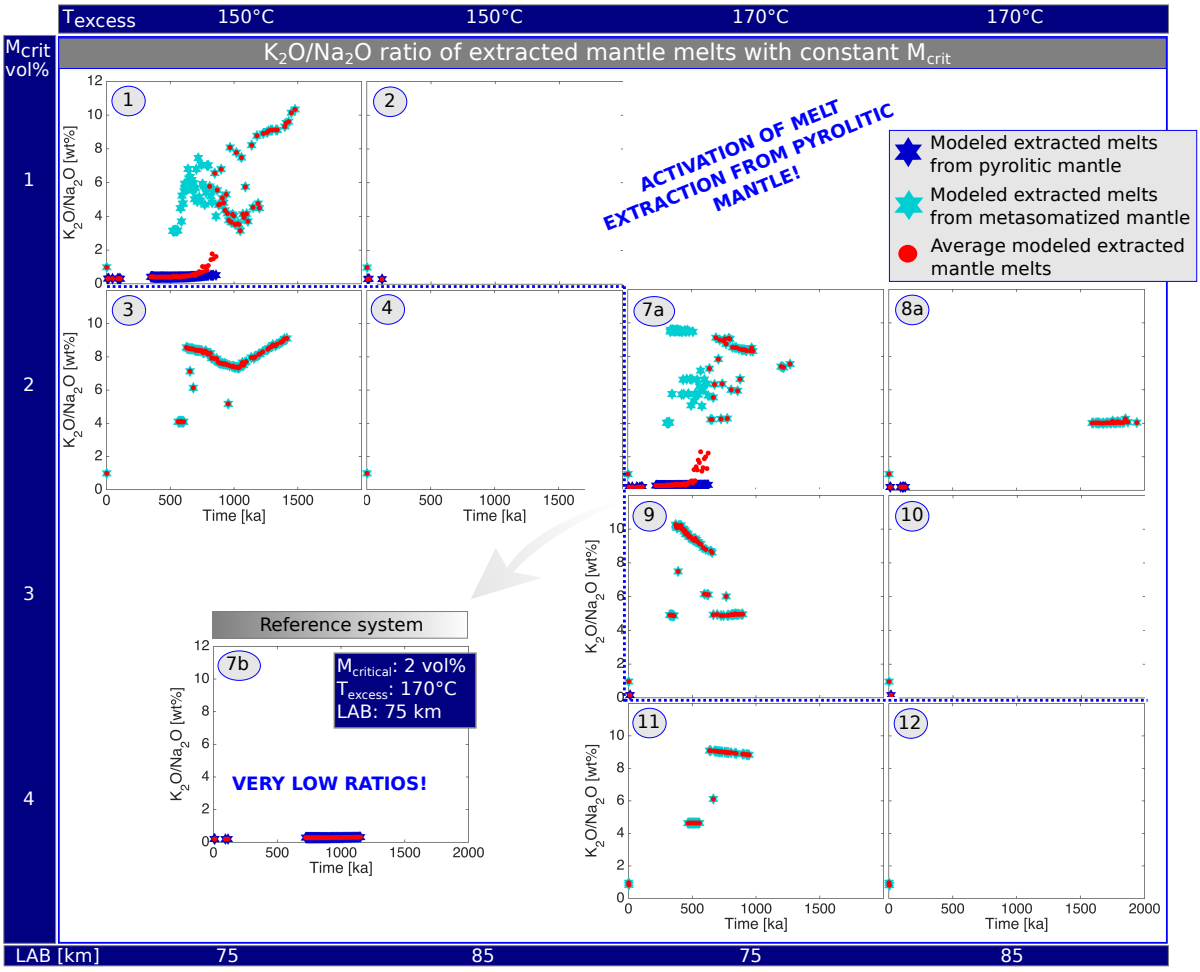

Figure 2.B1: Temporal evolution of K_2O/Na_2O (in wt%) of modeled compositions of extracted melts, with a constant employed critical melt fraction during one simulation. Dark blue stars show average compositions of magmas extracted from the pyrolitic mantle and turquoise stars from the metasomatized mantle. Red dots represent the average compositions of extracted magmas after magma mixing, considering different portions of the respective melt phase. Blue dotted line indicates the boundary above which melt extraction from the pyrolitic mantle is active. Model 7b is a reference simulation of a pure thermal plume, without metasomatic enriched components in the mantle. The numbers are referred to the executed simulations listed in Tables 2.B1–2.B2.

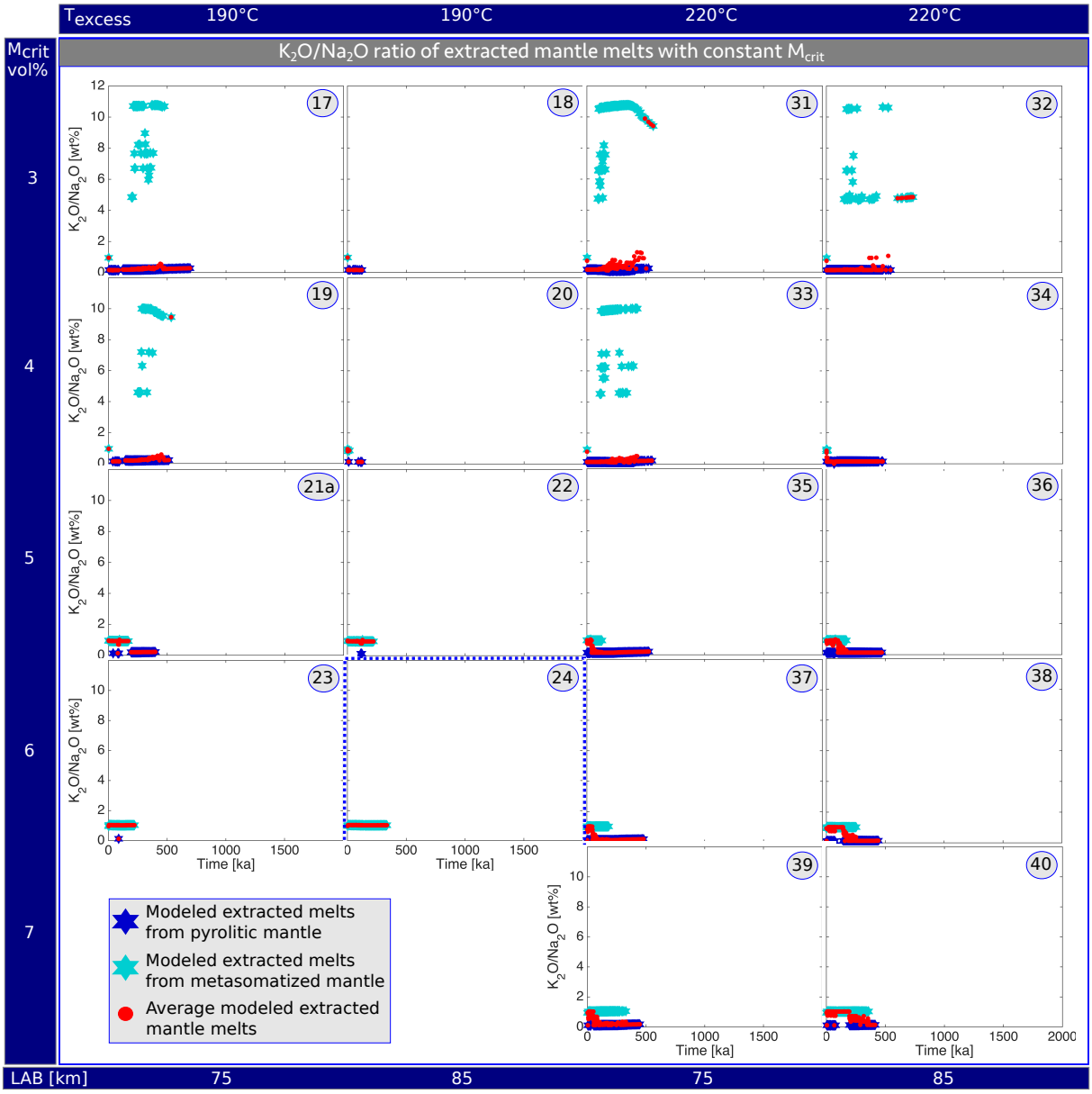

Figure 2.B2: Continuation of Figure 2.B1.

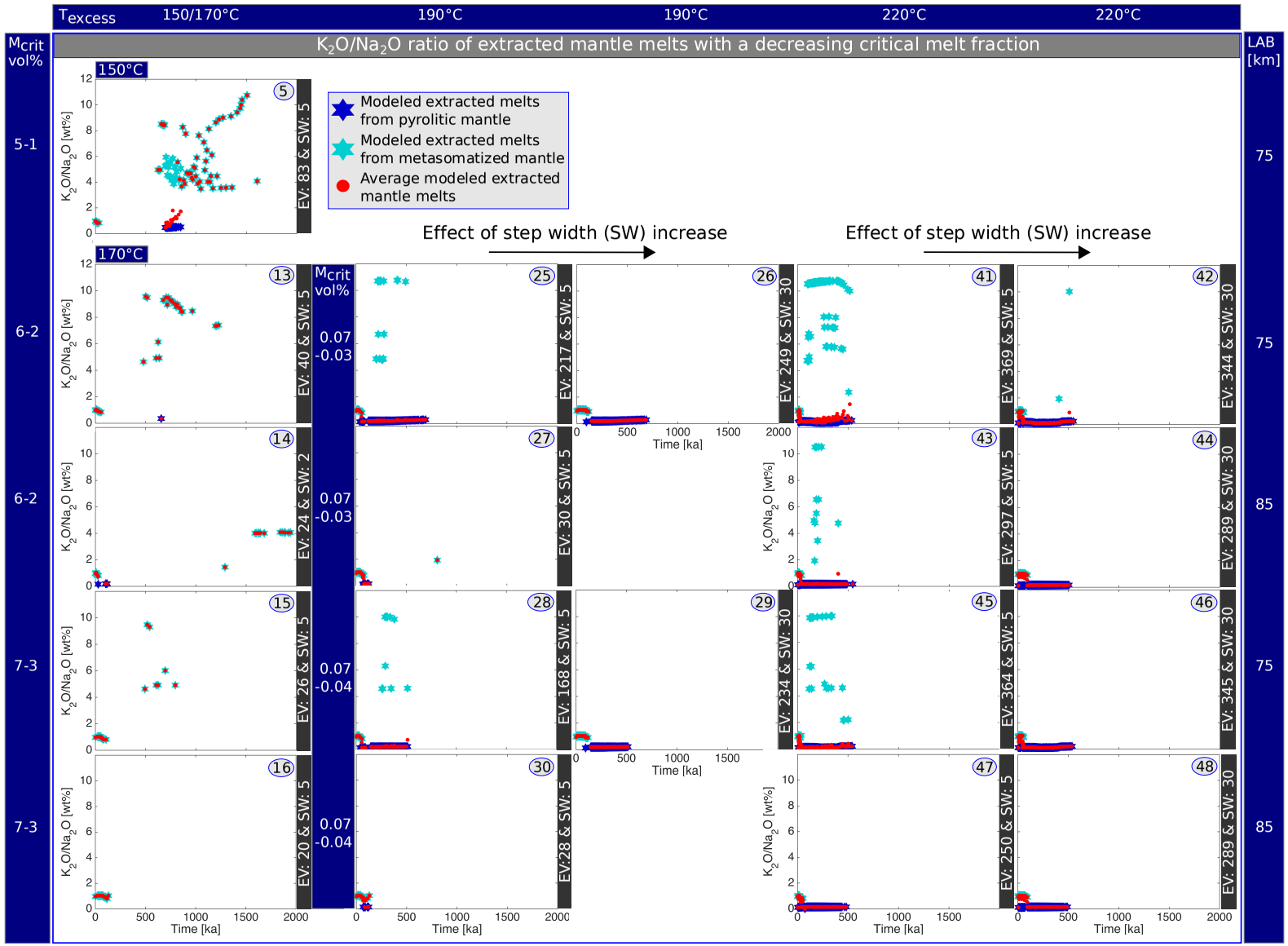

Figure 2.B3: Temporal evolution of K_2O/Na_2O (in wt%) of modeled compositions of extracted melts, with a decreasing critical melt fraction (M_{crit}) during one simulation. Stars show average magma compositions from the respective mantle sources, in dark blue for extracted melts from the pyrolitic and in turquoise from the metasomatized mantle. Red dots represent the average compositions after magma mixing. EV: total melt extraction events, SW (step width): after a specified number of melt extraction events (here after 5 or 30) the critical melt fraction is decreased by 1 vol%. The numbers are referred to the executed simulations listed in Tables 2.B1–2.B2.

2.B.3 Magma addition

The extracted melts during the ongoing geodynamic simulation are mostly dominated by those from the pyrolitic mantle and especially a lower LAB at 75 km depth supports the melting of rising pyrolitic material through decompression. However, if the LAB is located at 85 km depth and the critical melt fraction (M_{crit}) is $\geq$ 5 vol%, the volume fraction of extracted magma from both mantle sources can be equal (Fig. 2.B4C). Under these conditions, the first melt extraction episode (1. ME) from the metasomatized mantle is extended. Using a smaller critical melt fraction instead ($<$ 5 vol%), depletes the entire metasomatized mantle through the first melt extraction event while supporting melt extraction from the pyrolitic mantle (Fig. 2.B4A). The first melt extraction event from the metasomatized mantle is not considered in the magma addition rates presented in Figure 2.B4. From the depleted metasomatized mantle only a limited amount of melt can be generated, which is insignificant for the total magma addition (2. ME, Fig. 2.B4A).

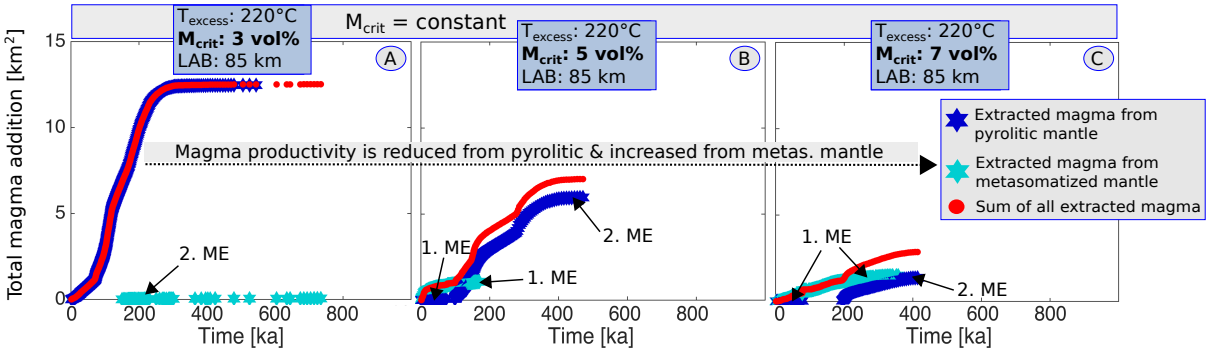

Figure 2.B4: Total addition of extracted magmas with time in km^2. ME: Melt extraction episode. Dark blue stars show total magma addition from the pyrolitic mantle and turquoise stars from the metasomatized mantle. Filled red circles represent the total addition of extracted melts from both pyrolitic and metasomatized mantle. Each star represents a new melt extraction event. M_{crit} is constant within the simulations. The first melt extraction event of the metasomatized mantle is excluded from the graph. With an increasing critical melt fraction (M_{crit}), magma productivity decreases for the pyrolitic mantle and increases for the metasomatized mantle.

2.C Comparison of modeled melts with Eifel rocks

Magmatic rocks generated either through our numerical simulations or above the WEVF, show differences in terms of their chemistries illustrated by the Na_2O/K_2O ratio and Na_2O+K_2O concentrations (Fig. 2.C1). The West Eifel magmatic rocks are chemically located between the extracted melts from the metasomatized mantle and the Na_2O-enriched modeled melts from the pyrolitic mantle (Fig. 2.C1). Due to the link between source rock chemistry and magma composition, it is likely that differences in magma chemistry reflect

differences in source rock compositions between simulation and nature. The complexity of the mantle source(s) beneath the WEVF can be illustrated by the isotopic signature found in West Eifel volcanic rocks and in embedded mantle xenoliths. Isotopic data indicate that West Eifel volcanic rocks were derived from a long-term depleted and subsequently metasomatically enriched source, which overlaps in their isotope ratios with hydrous Eifel mantle xenoliths (Shaw and Woodland, 2012). Especially magmatic rocks formed < 80 ka ago are isotopically close to the Common Mantle Reservoir (CMR) for an asthenospheric mantle source (Shaw and Woodland, 2012). Starting with these observations, we choose two endmember compositions for the mantle of our model. The metasomatically enriched source is described by a hydrous mantle xenolith, and for the more primitive mantle source an anhydrous pyrolitic composition is used (Tab. 2.1). However, the modeling results indicate that these extreme endmembers are not suitable alone to describe the observations in the WEVF. Thus, using a metasomatized mantle source equivalent in chemistry to a hydrous mantle xenolith produces extracted melts in our model, which are more enriched in K_2O (light turquoise, Fig. 2.C1B) than natural Eifel rocks. Whereas, the chosen pyrolitic mantle composition neglects a small enrichment component supposed to be present in the source of young (< 80 ka) West Eifel magmas (Mertes and Schmincke, 1985). This may affect the melting behavior and the melt compositions from the pyrolitic mantle. Thus, a combination of both employed mantle sources in different percentages may result in mantle sources that reproduce Eifel-like mantle melts, assuming that the amount of alkali elements (K, Na) in the melts is directly related to the source. Having a less Na_2O or more K_2O enriched mantle source would shift the composition of extracted melts from pyrolitic mantle towards the Eifel basanites (for late and at shallower depth generated magmas), or towards the Eifel olivine-nephelinite field for earlier and at greater depth generated magmas (Fig. 2.C1A). Modeled magmas from the metasomatized mantle, especially the late extracted ones formed through decompression (dark turquoise, Fig. 2.C1), are strongly enriched in K_2O (moderate Na_2O+K_2O values but low Na_2O/K_2O) compared to the Eifel rocks. The highest alkali concentrations are found in early extracted magmas from the metasomatized mantle, which are much higher than of any volcanic field (Fig. 2.C1B). All other modeled melt compositions have less variations in the Na_2O+K_2O concentration and show a nearly horizontal trend in Figure 2.C1B, producing an enrichment in SiO_2 concentration from late extracted melts of the metasomatized mantle, over early at great depth extracted melts from pyrolitic mantle, to late at shallow depth extracted melts from pyrolitic mantle.

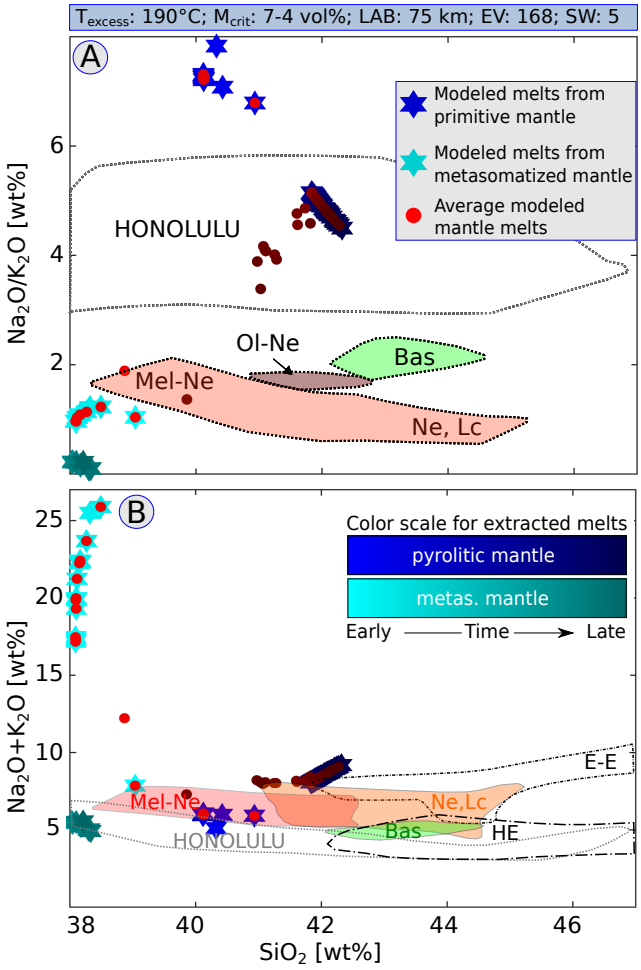

Figure 2.C1: Comparison of modeled melt chemistries of one exemplary simulation with magmatic rocks from the West Eifel and from reference volcanic fields (modified after Mertes and Schmincke, 1985). A: Na_2O/K_2O vs. SiO_2 and B: Na_2O+K_2O vs. SiO_2. Mel=melilitites, Ne=nephelinites, Ol=olivine, Bas = basanites, Lc=leucitites. E-E=East Eifel and HE=Hocheifel. West Eifel magmatic rocks are shown with colored fields. Dark blue stars show average compositions of extracted melts from the pyrolitic mantle and turquoise stars from the metasomatized mantle. Red dots represent the average compositions after magma mixing, considering different portions of the respective melt phase. Light colors represent early in time and dark colors late in time extracted magmas. EV: total melt extraction events, SW (step width): after a specified number of melt extraction events (here after 5) the critical melt fraction is decreased by 1 vol%.

Furthermore, mixing between extracted melts from both mantle sources in different percentages (red dots, Fig. 2.C1) may produce similar magma compositions as those observed in the West Eifel volcanic field. Magma mixing is assumed to be responsible for compositional variations within one or neighboring volcanic centers in the West Eifel as well, where the chemical variations in the volcanic rocks are suggested to result from different source rock compositions in combination with magma mixing (Shaw and Woodland, 2012). Their preferred model involves 1–5% partial melting of a LREE-enriched anhy-

Table 2.C1: Comparison of the chemical composition of "primary" lavas of both West Eifel suites (Mertes and Schmincke, 1985) with average model compositions of extracted melts from the pyrolitic and metasomatized mantle of a representative simulation. The employed parameters are: T_{excess} = 190 °C, M_{crit} = 5 vol% and LAB at 75 km, second plume initialization after ∼500 ka. Melt compositions are recalculated to 100% on a LOI (loss on ignition) free basis. *) with 1^{st} standard deviation.

Oxides [wt%]	**M= mean*** **R= range**	**high-K_2O/Na_2O group (field study)**	**low-K_2O/Na_2O group (field study)**	**Magma metasomatized mantle (numerical experiment)**	**Magma pyrolitic mantle (numerical experiment)**
SiO_2	M	42.2 ±1.5	42.4 ±0.7	39.20 ±0.08	41.93 ±0.30
	R	38.7–45.0	40.9–43.6	39.09–39.46	40.08–42.21
TiO_2	M	2.6 ±0.2	2.6 ±0.1	3.25 ±0.18	1.76 ±0.03
	R	2.3–3.1	2.4–2.8	2.54–3.60	1.58–1.80
Al_2O_3	M	11.6 ±0.7	12.1 ±0.4	15.25 ±0.96	10.47 ±0.98
	R	10.4–12.8	11.3–12.7	7.89–16.43	3.15–10.81
Fe_2O_3	M	6.1 ±1.6	4.4 ±1.1	0.72 ±0.01	0.96 ±0.01
	R	3.4–11.1	2.2–6.1	0.72–0.84	0.88–0.96
FeO	M	4.3 ±1.4	6.5 ±1.5	5.82 ±0.51	11.68 ±0.70
	R	0.3–6.5	3.7–8.7	5.36–12.35	11.26–16.63
MgO	M	11.2 ±1.0	12.8 ±1.0	7.97 ±0.78	19.28 ±1.07
	R	9.5–13.6	11.1–14.6	7.46–20.03	18.64–26.72
CaO	M	14.5 ±1.0	12.4 ±0.6	4.17 ±0.27	5.60 ±0.14
	R	12.5–16.5	11.3–13.2	4.03–8.45	5.39–6.60
Na_2O	M	2.94 ±0.54	3.47 ±0.57	11.99 ±0.48	6.93 ±0.42
	R	1.67–4.03	2.88–4.69	4.05–12.12	4.55–7.35
K_2O	M	3.08 ±0.45	1.85 ±0.43	11.01 ±0.41	1.39 ±0.15
	R	1.98–3.92	1.32–2.66	3.90–11.10	0.58–1.59
P_2O_5	M	0.80 ±0.23	0.88 ±0.10	0.62 ±0.07	0
	R	0.51–1.50	0.72–1.09	0.50–0.72	0

drous mantle in the garnet stability field, which were mixed with variable degrees (2–4%) of partial melts from the phlogopite-spinel/-garnet peridotite field.

Average compositions of West Eifel magmatic rocks and modeled compositions of extracted melts are provided in Table 2.C1 for comparison. Even though the modeling results might not explain the chemical composition of natural rocks in detail, they are important to improve our understanding about the formation of the chemical trend found in rocks of the WEVF.

2.D West Eifel volcanism and the thermal and compositional structure of the mantle

In the following sections (2.D.1–2.D.3), additional information is given about the Eifel volcanism, volcanic products and their relationship to the mantle underneath. The provided information helps to better understand the differences between the modeling results and the observations in the WEVF. It is shown that even if magmas reached the surface relatively unmodified, their origin and ascent are controversially discussed, as described already in the discussion section (Section 2.4.3).

2.D.1 West Eifel volcanism

In the WEVF a total of ca. 2.7 km^3 of magma (Mertes and Schmincke, 1985) has erupted from ∼240 eruption centers (Schmincke, 2013) during both volcanic episodes. This number of eruption centers is in agreement with the modeled melt extraction events, which is up to a few hundreds, but might be influenced by the computational time step. Speculative estimations of the total amount of magma produced beneath the WEVF are around 50 km^3 or higher suggesting that a significant amount of magma crystallized already within the crust (Schmincke, 2007). The compositional variations in the West Eifel volcanic rocks are only minor due to their mostly primitive character, common peridotite inclusions and the small average magma volume (about 80 m^3) of each eruption center (Mertes and Schmincke, 1985). Mantle magmas are suggested to have ascended rapidly through dikes, consistent with magma velocities of up to 15 km/h (Shaw, 2004). The timescale of this process is significantly smaller (in an order of hours) than a typical time step employed in the geodynamic model (hundreds of years), which is why we assume it to occur quasi-instantaneously and emplace the magma directly above the crust to mimic extrusive and within the crust for intrusive rocks.

The West Eifel volcanic rocks are classified in ONB-suite (olivine-nephelinites and

basanites) and F-suite (foidites) (Mertes and Schmincke, 1985). The highly enriched F-suite lavas (here defined as high-K_2O/Na_2O group) are distinguishable from the mafic sodic ONB-suite (here defined as low-K_2O/Na_2O group) by higher K_2O/Na_2O, CaO/Al_2O_3 and $^{87}Sr/^{86}Sr$ ratios as well as higher Rb, Ba, H_2O, CO_2, LREE concentrations and lower $^{143}Nd/^{144}Nd$ ratios (Mertes and Schmincke, 1985). The low-K_2O/Na_2O group lavas, which are only slightly enriched in LILE, present the most primitive suite of all Quaternary volcanic Eifel rocks (Schmincke, 2007). The basanites of the low-K_2O/Na_2O group, which occur in the eastern/southeastern margin of the WEVF, have compositionally the closest chemistry to the Eocene alkali basalts and thus to an asthenospheric mantle source (Schmincke, 2007). In these rocks, the chemical signature of the Quaternary magma suites is still maintained by preserving low Al_2O_3 concentrations, a relatively high CaO content and higher amount of incompatible elements (Schmincke, 2007). In our simulations, these primitive magmatic rocks are generated late during plume ascent. However, the missing enrichment component in CaO and incompatible elements in the employed pyrolitic mantle causes differences in composition between modeled melts and West Eifel magmatic rocks. Therefore, only magma mixing is leading to comparable results. Moreover, especially CO_2 but also other incompatible elements, which are missing in our source rocks due to pMELTS limitations, may affect the melting behavior, the stability of minerals and the magma compositions.

The formation of magma in the West Eifel appears to be genetically linked to a seismological low-velocity anomaly (Ritter et al., 2001). Beneath Europe, it is suggested that small upper mantle plumes can be fed from a large scale low-velocity anomaly in the lower mantle (Goes et al., 1999). Moreover, these authors assume that the relatively weak volcanism, compared to other regions with plume associated volcanism, can be explained by the subduction under southern Europe. The thin European lithosphere with preexisting weak zones and the existing stress field produced by the Alpine collision may allow the relatively weak plumes to ascent. A connection between the Eifel plume and old subducted slabs may also be reasonable due to the fact that the Pannonian and western Mediterranean basins are underlain by high-velocity anomalies in the mantle transition zone, which are associated with subducted material lying on the 660-km discontinuity (Goes et al., 1999). The small mantle plumes in the upper mantle are connected and skirt around the flat-lying slabs under these areas (Goes et al., 1999). Compositional mantle plumes are expected all over the world, e.g. the continental Yellowstone hotspot, which shows similarities to the Eifel plume (Smith et al., 2009).

2.D.2 Lithosphere beneath the West Eifel volcanic field

In the following section, we describe the compositional structure of the lithospheric mantle beneath the West Eifel region in more detail. The initial phase diagram used to describe the behavior of our metasomatized mantle is based on a bulk rock composition corresponding to a lithospheric mantle xenolith transported to the surface by West Eifel magmas. The choice of the rock composition influences the melting process, as it controls the solid and liquid fractions and their compositions in the phase diagram. The depleted rocks are constructed from solid compositions of the initial metasomatized mantle phase diagram and are thus influenced by its chosen bulk rock composition. In order to understand, why this xenolithic composition can show only limited the composition of the source region, we provide the information below.

Xenoliths from the Eifel show evidence for multistage enrichment processes, which produced a very compositionally and isotopically heterogeneous lithospheric mantle (Witt-Eickschen et al., 2003). The xenoliths consist of mainly anhydrous and hydrous spinel peridotites from fertile lherzolite through harzburgite to dunite (Witt-Eickschen, 2007). Garnet is completely absent in the xenoliths (Witt-Eickschen, 2007), but present in the melting source (e.g. Mertes and Schmincke, 1985; Shaw and Woodland, 2012; Mertz et al., 2015). Thus, only including magma mixing may allow a lithospheric mantle xenolith to represent the enriched mantle source, assuming that magmas from a deep garnet-bearing source are mixed with magmas generated in a shallower garnet absent metasomatized mantle source. The depth interval from which both the lherzolites and harzburgites came from is between 30 and 70 km (Witt-Eickschen, 2007). Whereby the pargasitic amphibole carrying hydrous xenoliths (and/or its breakdown products), which are used to describe the modeled metasomatized mantle (Tab. 2.1), are restricted to the shallowest lithospheric mantle ($<$ 50 km depth) (Witt-Eickschen, 2007). In some locations (Gees, Baarley, Rockeskyller Kopf; Shaw et al., 2005) of the WEVF, phlogopite-bearing wehrlites, dunites or clinopyroxenites can be found, whose origin has been attributed to metasomatic alteration processes (Witt-Eickschen, 2007). Wehrlite production is the result of a large amount of potassic penetrative magma flow along grain boundaries in the lherzolite-harzburgite mantle and is associated with a high magmatic activity (Shaw et al., 2005). However, even if hydrous mantle xenoliths dominate in those erupted magmas, they do not have to necessarily represent the partially molten region (e.g., hydrous mantle xenoliths are even found in the low-K_2O/Na_2O group; Shaw et al., 2005). The erupted magma could be fully decoupled from the magma that stagnates in the mantle and metasomatized it, possibly much earlier in time. The fact that all xenoliths were from shallower depth as expected

for the partially molten mantle source(s), or at least for one of the sources, supports the assumption that the area of melt generation is likely located below the zone of rapid uprise in which mantle fragments become incorporated into the magma.

2.D.3 Models for the origin of the high- and low-K_2O/Na_2O group

The origin of the high- and low-K_2O/Na_2O group is still under debate and different models suggest different formation processes. We here present two different models and demonstrate their weaknesses. Mertes and Schmincke (1985) assume in their model that a garnet lherzolite is enriched in fluids and LILE and produced two different magma types originating from different depths. F-suite lavas (high-K_2O/Na_2O group) from a phlogopite-bearing, CO_2 enriched, metasomatized mantle source at about 100 km and ONB-suite lavas (low-K_2O/Na_2O group) from an amphibole-bearing, CO_2-poorer melting source at about 60–75 km depth. Whereas, Schmincke (2007) suggests that the enriched magmas are generated by decompression melting of a fusible metasomatized base of the lithosphere that is uplifted by the impinging mantle plume. The abrupt appearance of the chemically different ONB-suite magmas reflects, in that case, the limited productive lifetime of finger-like peridotite melting domains with much smaller dimensions than the plume anomaly (Schmincke, 2007). The smaller domains (few km to tens of km size) within the thermal plume with distinguishable composition and/or variable ascent rates, interact with the lithosphere at different times or stages (Schmincke, 2007).

Whereas the first model does not consider the mantle plume, the second model neglects the origin of the mantle xenoliths embedded in the erupted magmas. Those mantle xenoliths indicate a restriction of the enriched hydrous lithospheric mantle to < 50 km depth and the thermal LAB at ~ 75 km depth (Witt-Eickschen, 2007). Therefore, the mantle plume would spread around this depth (~ 75 km) due to the viscosity contrast, at a much greater depth than expected for the hydrous metasomatized lithospheric mantle. To melt the hydrated mantle, deep originating melts (from a depth $>$ LAB) have to stagnate in the shallowest mantle (< 50 km depth). However, embedded xenoliths, the relatively primitive composition of the melts and the amount of erupted magma in the WEVF indicate a fast magma ascent, which implies limited heat transfer to the surrounded host rocks.

REFERENCES

Auzanneau, E., Schmidt, M., Vielzeuf, D., Connolly, J. D., 2010. Titanium in phengite: a geobarometer for high temperature eclogites. Contributions to Mineralogy and Petrology 159 (1), 1–24.

Baumann, T., 2016. Appraisal of geodynamic inversion results: a data mining approach. Geophysical Journal International 207 (2), 667–679.

Bouilhol, P., Magni, V., van Hunen, J., Kaislaniemi, L., 2015. A numerical approach to melting in warm subduction zones. Earth and Planetary Science Letters 411, 37–44.

Burg, J.-P., Gerya, T., 2005. The role of viscous heating in Barrovian metamorphism of collisional orogens: thermomechanical models and application to the Lepontine Dome in the Central Alps. Journal of Metamorphic Geology 23 (2), 75–95.

Coggon, R., Holland, T., 2002. Mixing properties of phengitic micas and revised garnet-phengite thermobarometers. Journal of Metamorphic Geology 20 (7), 683–696.

Connolly, J., 2009. The geodynamic equation of state: what and how. Geochemistry, Geophysics, Geosystems 10 (10).

Connolly, J. A., 2005. Computation of phase equilibria by linear programming: a tool for geodynamic modeling and its application to subduction zone decarbonation. Earth and Planetary Science Letters 236 (1), 524–541.

Dannberg, J., Sobolev, S. V., 2015. Low-buoyancy thermochemical plumes resolve controversy of classical mantle plume concept. Nature communications 6.

Davies, D. L., Bouldin, D. W., 1979. A cluster separation measure. IEEE transactions on pattern analysis and machine intelligence (2), 224–227.

Diener, J., Powell, R., White, R., Holland, T., 2007. A new thermodynamic model for clino-and orthoamphiboles in the system Na2O–CaO–FeO–MgO–Al2O3–SiO2–H2O–O. Journal of Metamorphic Geology 25 (6), 631–656.

Gerya, T., 2014. Plume-induced crustal convection: 3D thermomechanical model and implications for the origin of novae and coronae on Venus. Earth and Planetary Science Letters 391, 183–192.

Gerya, T., Meilick, F., 2011. Geodynamic regimes of subduction under an active margin: effects of rheological weakening by fluids and melts. Journal of Metamorphic Geology 29 (1), 7–31.

Gerya, T. V., Yuen, D. A., 2007. Robust characteristics method for modelling multiphase visco-elasto-plastic thermo-mechanical problems. Physics of the Earth and Planetary Interiors 163 (1), 83–105.

Ghiorso, M. S., Hirschmann, M. M., Reiners, P. W., Kress, V. C., 2002. The pMELTS: A revision of MELTS for improved calculation of phase relations and major element partitioning related to partial melting of the mantle to 3 GPa. Geochemistry, Geophysics, Geosystems 3 (5), 1–35.

Goes, S., Spakman, W., Bijwaard, H., 1999. A lower mantle source for central European volcanism. Science 286 (5446), 1928–1931.

Gorczyk, W., Mole, D., Barnes, S., 2017. Plume-lithosphere interaction at craton margins throughout Earth history. Tectonophysics.

Grunewald, S., Weber, M., Kind, R., 2001. The upper mantle under Central Europe: Indications for the Eifel plume. Geophysical Journal International 147 (3), 590–601.

Hebert, L. B., Antoshechkina, P., Asimow, P., Gurnis, M., 2009. Emergence of a low-viscosity channel in subduction zones through the coupling of mantle flow and thermodynamics. Earth and Planetary Science Letters 278 (3), 243–256.

Hirth, G., Kohlstedt, D., 2003. Rheology of the upper mantle and the mantle wedge: A view from the experimentalists. Inside the subduction Factory, 83–105.

Holland, T., Baker, J., Powell, R., 1998. Mixing properties and activity-composition relationships of chlorites in the system MgO-FeO-Al2O3-SiO2-H2O. European Journal of Mineralogy, 395–406.

Holland, T., Powell, R., 1996. Thermodynamics of order-disorder in minerals: II. Symmetric formalism applied to solid solutions. American Mineralogist 81 (11-12), 1425–1437.

Holland, T., Powell, R., 1998. An internally consistent thermodynamic data set for phases of petrological interest. Journal of metamorphic Geology 16 (3), 309–343.

Holland, T., Powell, R., 2001. Calculation of phase relations involving haplogranitic melts using an internally consistent thermodynamic dataset. Journal of Petrology 42 (4), 673–683.

Holland, T., Powell, R., 2003. Activity–composition relations for phases in petrological calculations: an asymmetric multicomponent formulation. Contributions to Mineralogy and Petrology 145 (4), 492–501.

Ito, G., Mahoney, J. J., 2005. Flow and melting of a heterogeneous mantle: 1. Method and importance to the geochemistry of ocean island and mid-ocean ridge basalts. Earth and Planetary Science Letters 230 (1), 29–46.

Jain, A. K., Dubes, R. C., 1988. Algorithms for clustering data. Prentice-Hall, Inc.

Johnson, T. E., Brown, M., Kaus, B. J., VanTongeren, J. A., 2014. Delamination and recycling of Archaean crust caused by gravitational instabilities. Nature Geoscience 7 (1), 47–52.

Katz, R. F., Spiegelman, M., Langmuir, C. H., 2003. A new parameterization of hydrous mantle melting. Geochemistry, Geophysics, Geosystems 4 (9).

Kaus, B. J., 2010. Factors that control the angle of shear bands in geodynamic numerical models of brittle deformation. Tectonophysics 484 (1), 36–47.

Keller, T., Katz, R. F., 2016. The role of volatiles in reactive melt transport in the asthenosphere. Journal of Petrology, egw030.

Keyser, M., Ritter, J. R., Jordan, M., 2002. 3D shear-wave velocity structure of the Eifel plume, Germany. Earth and Planetary Science Letters 203 (1), 59–82.

Kohonen, T., 2001. Self-organizing maps, vol. 30 of Springer Series in Information Sciences.

Koptev, A., Calais, E., Burov, E., Leroy, S., Gerya, T., 2015. Dual continental rift systems generated by plume-lithosphere interaction. Nature Geoscience 8 (5), 388–392.

McDonough, W. F., Sun, S.-S., 1995. The composition of the Earth. Chemical geology 120 (3), 223–253.

Menzies, M., Rogers, N., Tindle, A., Hawkesworth, C., 1987. Metasomatic and enrichment processes in lithospheric peridotites, an effect of asthenosphere-lithosphere interaction.

Mertes, H., Schmincke, H.-U., 1985. Mafic potassic lavas of the Quaternary West Eifel volcanic field. Contributions to Mineralogy and Petrology 89 (4), 330–345.

Mertz, D. F., Budsky, A., Chauvel, C., Prelević, D., Regelous, M., 2014. Zonation of the Pleistocene West Eifel volcanism (Germany): Relating isotopic, geochemical and geochronological evidence to the seismic low-velocity anomaly in the asthenosphere. In: GeoFrankfurt 2014- Dynamik des Systems Erde/ Earth System Dynamics- Abstract Volume. Vol. 85. Schriftenr. Dt. Gesellsch. Geowiss. SDGG, p. 427.

Mertz, D. F., Löhnertz, W., Nomade, S., Pereira, A., Prelević, D., Renne, P. R., 2015. Temporal–spatial evolution of low-SiO_2 volcanism in the Pleistocene West Eifel volcanic field (West Germany) and relationship to upwelling asthenosphere. Journal of Geodynamics 88, 59–79.

Motoki, M. H., Ballmer, M. D., 2015. Intraplate volcanism due to convective instability of stagnant slabs in the mantle transition zone. Geochemistry, Geophysics, Geosystems 16 (2), 538–551.

Phipps Morgan, J., 2000. Isotope topology of individual hotspot basalt arrays: Mixing curves or melt extraction trajectories? Geochemistry, Geophysics, Geosystems 1 (12).

Prelević, D., Mertz-Kraus, R., Buhre, S., Mertz, D., 2015. Petrological characterization of the seismic low-velocity anomaly beneath the Eifel volcanic field (West Germany) using major and trace element compositions of olivine macrocrysts. In: GeoBerlin2015 - Dynamic Earth from Alfred Wegener to today and beyond - Abstracts. GFZ German Research Centre for Geosciences, p. 300.

Ranalli, G., 1995. Rheology of the Earth. Springer Science & Business Media.

Ribe, N., Christensen, U., 1999. The dynamical origin of Hawaiian volcanism. Earth and Planetary Science Letters 171 (4), 517–531.

Ritter, J. R., Jordan, M., Christensen, U. R., Achauer, U., 2001. A mantle plume below the Eifel volcanic fields, Germany. Earth and Planetary Science Letters 186 (1), 7–14.

Schmeling, H., Arndt, N., 2017. Modelling komatiitic melt accumulation and segregation in the transition zone. Earth and Planetary Science Letters 472, 95–106.

Schmincke, H.-U., 2007. The Quaternary volcanic fields of the east and west Eifel (Germany). In: Mantle Plumes. Springer, pp. 241–322.

Schmincke, H.-U., 2013. Vulkane der Eifel: Aufbau, Entstehung und heutige Bedeutung. Springer-Verlag.

Seiberlich, C., Ritter, J., Wawerzinek, B., 2013. Topography of the lithosphere–asthenosphere boundary below the Upper Rhine Graben Rift and the volcanic Eifel region, Central Europe. Tectonophysics 603, 222–236.

Shaw, C. S., 2004. The temporal evolution of three magmatic systems in the West Eifel volcanic field, Germany. Journal of Volcanology and Geothermal Research 131 (3), 213–240.

Shaw, C. S., Eyzaguirre, J., Fryer, B., Gagnon, J., 2005. Regional variations in the mineralogy of metasomatic assemblages in mantle xenoliths from the West Eifel Volcanic Field, Germany. Journal of Petrology 46 (5), 945–972.

Shaw, C. S., Woodland, A. B., 2012. The role of magma mixing in the petrogenesis of mafic alkaline lavas, Rockeskyllerkopf Volcanic Complex, West Eifel, Germany. Bulletin of volcanology 74 (2), 359–376.

Smith, P. M., Asimow, P. D., 2005. Adiabat_1ph: A new public front-end to the MELTS, pMELTS, and pHMELTS models. Geochemistry, Geophysics, Geosystems 6 (2).

Smith, R. B., Jordan, M., Steinberger, B., Puskas, C. M., Farrell, J., Waite, G. P., Husen, S., Chang, W.-L., O'Connell, R., 2009. Geodynamics of the Yellowstone hotspot and mantle plume: Seismic and GPS imaging, kinematics, and mantle flow. Journal of Volcanology and Geothermal Research 188 (1), 26–56.

Smye, A., Greenwood, L., Holland, T., 2010. Garnet–chloritoid–kyanite assemblages: eclogite facies indicators of subduction constraints in orogenic belts. Journal of Metamorphic Geology 28 (7), 753–768.

Sossi, P. A., Eggins, S. M., Nesbitt, R. W., Nebel, O., Hergt, J. M., Campbell, I. H., ONeill, H. S. C., Van Kranendonk, M., Davies, D. R., 2016. Petrogenesis and geochemistry of Archean komatiites. Journal of Petrology 57 (1), 147–184.

Tajčmanová, L., Connolly, J., Cesare, B., 2009. A thermodynamic model for titanium and ferric iron solution in biotite. Journal of Metamorphic Geology 27 (2), 153–165.

Taylor, S., McLennan, S., Armstrong, R., Tarney, J., 1981. The composition and evolution of the continental crust: rare earth element evidence from sedimentary rocks [and discussion]. Philosophical Transactions of the Royal Society of London A: Mathematical, Physical and Engineering Sciences 301 (1461), 381–399.

Thielmann, M., Kaus, B. J., 2012. Shear heating induced lithospheric-scale localization: Does it result in subduction? Earth and Planetary Science Letters 359, 1–13.

Vesanto, J., Himberg, J., Alhoniemi, E., Parhankangas, J., 2000. SOM toolbox for Matlab 5. Helsinki University of Technology, Finland.

Vogt, K., Castro, A., Gerya, T., 2013. Numerical modeling of geochemical variations caused by crustal relamination. Geochemistry, Geophysics, Geosystems 14 (2), 470–487.

Vogt, K., Gerya, T. V., Castro, A., 2012. Crustal growth at active continental margins: numerical modeling. Physics of the Earth and Planetary Interiors 192, 1–20.

White, R., Powell, R., Holland, T., 2001. Calculation of partial melting equilibria in the system Na2O–CaO–K2O–FeO–MgO–Al2O3–SiO2–H2O (NCKFMASH). Journal of Metamorphic Geology 19 (2), 139–153.

White, R., Powell, R., Holland, T., Johnson, T., Green, E., 2014. New mineral activity–composition relations for thermodynamic calculations in metapelitic systems. Journal of Metamorphic Geology 32 (3), 261–286.

White, R., Powell, R., Holland, T., Worley, B., 2000. The effect of TiO2 and Fe2O3 on metapelitic assemblages at greenschist and amphibolite facies conditions: mineral equilibria calculations in the system K2O-FeO-MgO-Al2O3-SiO2-H2O-TiO2-Fe2O3. Journal of Metamorphic Geology 18 (5), 497–511.

Wilson, M., 2008. Fluid streaming from the Transition Zone as a trigger for within-plate magmatism. In: Geophysical Research Abstracts. Vol. 10.

Witt-Eickschen, G., 2007. Thermal and geochemical evolution of the shallow subcontinental lithospheric mantle beneath the Eifel: constraints from mantle xenoliths, a review. In: Mantle Plumes. Springer, pp. 323–337.

Witt-Eickschen, G., Seck, H., Mezger, K., Eggins, S., Altherr, R., 2003. Lithospheric mantle evolution beneath the Eifel (Germany): constraints from Sr–Nd–Pb isotopes and trace element abundances in spinel peridotite and pyroxenite xenoliths. Journal of Petrology 44 (6), 1077–1095.

Wörner, G., Zindler, A., Staudigel, H., Schmincke, H.-U., 1986. Sr, Nd, and Pb isotope geochemistry of Tertiary and Quaternary alkaline volcanics from West Germany. Earth and Planetary Science Letters 79 (1-2), 107–119.

Yang, J., Zhao, L., Kaus, B. J., Lu, G., Wang, K., Zhu, R., 2017. Slab-triggered wet upwellings produce large volumes of melt: Insights into the destruction of the North China Craton. Tectonophysics.

Zolitschka, B., Negendank, J., Lottermoser, B., 1995. Sedimentological proof and dating of the early Holocene volcanic eruption of Ulmener Maar (Vulkaneifel, Germany). Geologische Rundschau 84 (1), 213–219.

CHAPTER 3

RESOLUTION OF PHASE DIAGRAMS AND COMPUTATIONAL COST

The computation of phase diagrams over a large numerical grid (257×257 P–T points in our case) is very time-consuming. How good stable mineral assemblages are resolved with Perple_X (using version 6.7.9, Connolly, 2005, 2009) is dependent on two groups of keywords specified in the perplex_option.dat file. The adaptive minimization keyword group (*iteration*, *initial_resolution*, $final\_resolution$, $auto\_refine\_factor\_I$, *reach_increment*, *global_reach_increment*, *solvus_tolerance* and $solvus\_tolerance\_II$) determines the accuracy and precision with which Perple_X computes phase relations at an individual grid point. The other keyword group is related to the grid (*grid_levels*, *x_nodes*, *y_nodes* and *linear_model*) and determines the number of grid points used to map the phase relations of a phase diagram section. Thus, to run Perple_X efficiently, we have to find values under which high-quality results can be produced at minimal computational cost. For this, we systematically vary the values of the $auto\_refine\_factor\_I$, the *initial_resolution* and the $final\_resolution$ to get the highest possible accuracy and precision within the phase diagram while reducing the computation time. Additional reduction of the computation time can be obtained by decreasing the numerical grid to 257×257 P–T points (every 11.7 MPa and 6.3 K for our employed P–T space).

The computation of stable phase assemblages through Gibbs free energy minimization is executed on a 2D multilevel grid in Perple_X (Connolly, 2005). For gridded minimization, a multilevel grid refinement strategy is used in which phase relations are mapped on an initial course grid spanned by x- and y-nodes, followed by a refinement stage (the grid is refined *grid_levels* - 1 times by bisection). The effective resolution of a multilevel grid is described by (*x_nodes* - 1) · $2^{(grid\_levels-1)}$ + 1 in the x-direction and by (*y_nodes* - 1) ·

$2^{(grid\_levels-1)} + 1$ nodes in the y-direction. For the *grid_levels*, we use the default values 1 and 4. *x_nodes*, *y_nodes* and *grid_levels* are composed of two values, the first one for the exploratory stage of the gridded minimization calculations and the second value is used for the auto-refinement stage.

The meanings of the relevant adaptive minimization keywords are described in the following section. The $auto\_refine\_factor\_I$ describes the increase in compositional resolution between the exploratory and auto-refinement stage of the gridded minimization calculations. This keyword permits a finer effective initial resolution ($initial\_resolution/auto\_refine\_factor\_I$) during the auto-refinement stage. The *initial_resolution* determines the initial (molar) compositional resolution used for solution models during the exploratory stage of a calculation. The final precision is specified by the $final\_resolution$ keyword. The $final\_resolution$ describes the (molar) precision with which phase compositions are calculated. During adaptive minimization, compositions are iteratively refined (Connolly, 2009) until their precision is better than the specified value of the $final\_resolution$. The first value is used during the exploratory stage and the second value in the final (auto-refined) stage of the calculation. For the *iteration* keyword, we use the two default values 3 and 4. The first value defines a factor by which compositional precision increases in each iteration, the second value controls Perple_X's ability to distinguish stable phases from nearly stable phases, and represents the number of metastable phases considered during the adaptive minimization. The *solvus_tolerance* specifies the minimal distance between two compositions of a solution phase at which the compositions are considered to represent distinct (immiscible) phases of the solution. Compositions that are separated by a distance less than the *solvus_tolerance* are considered to represent a single phase whose composition is computed as the weighted average of the different compositions of the solution. We set the *solvus_tolerance* to 1 and thus neglect immiscible phases because immiscible liquids have caused problems in our automatized computations. This may average separated phases into a single phase with a composition that might be thermodynamically unstable. Due to the fact, that we are only interested in the chemical evolution of the system (melt and solid compositions and main mineral phases) and not in individual phase compositions, suppressing the occurrence of immiscible phases seems to be acceptable. The meanings of the keywords defined in the perplex_option.dat file are taken from the Web-based Documentation of the Perple_X software [http://www.perplex.ethz.ch/perplex_documentation.html] and from Connolly (2005, 2009).

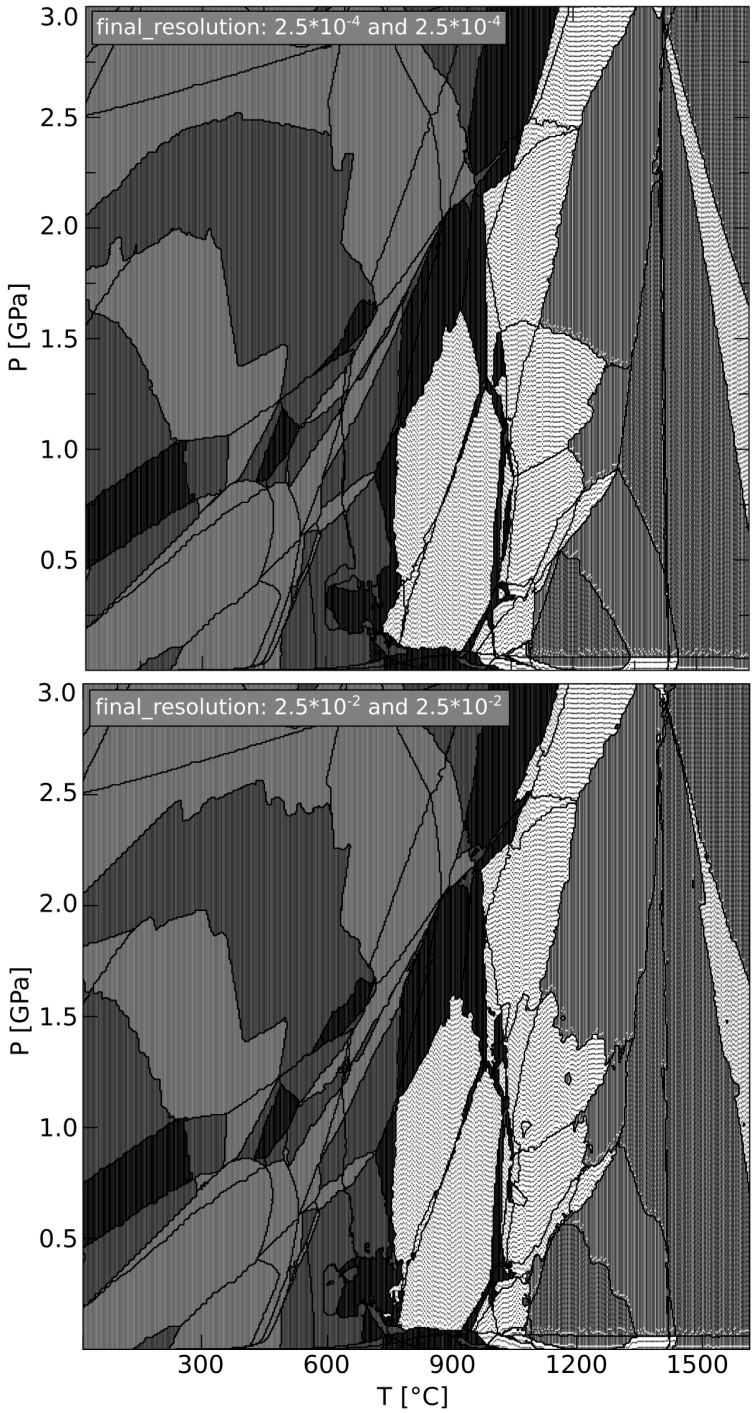

Figure 3.1: Pseudosections, showing fields of different stable phase assemblages. O_2 is set as saturated component. $auto\_refine\_factor\_I = 2$, $initial\_resolution = 0.2$ mol and x_nodes and y_nodes are 40 for the exploratory stage and 60 for the auto-refinement stage, with an effective resolution of 473 nodes in x- and y-direction. The $final\_resolution$ is set to $2.5{\cdot}10^{-4}$ (top) and to $2.5{\cdot}10^{-2}$ (bottom) for both the exploratory and the auto-refinement stage. The computation time is $\sim$ 72 h for the phase diagram on top and $\sim$ 13 h for the phase diagram on the bottom. Increasing the final compositional resolutions (smaller values) massively increases the computation time.

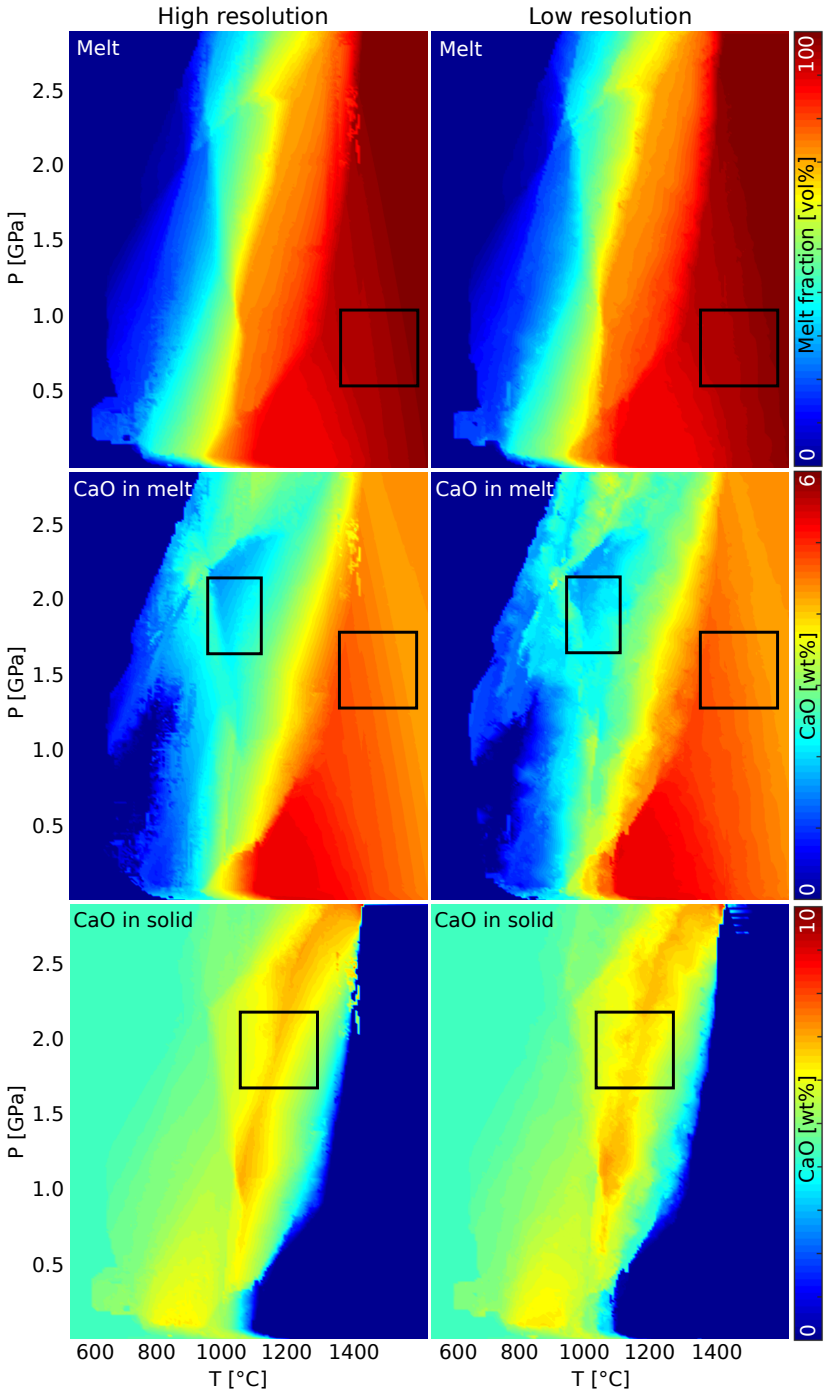

Figure 3.2: Change in melt fraction and CaO concentrations with P and T. Left: on a higher numerical grid (x_nodes and y_nodes values are 40 for the exploratory stage and 60 for the auto-refinement stage) and with a higher compositional resolution ($final\_resolution = 2.5{\cdot}10^{-4}$ mol for both exploratory and auto-refinement stage). Right: $final\_resolution$ of $2.5{\cdot}10^{-2}$ mol each and x_nodes and y_nodes are defined with 22 for the exploratory stage and 33 for the auto-refinement stage. $auto\_refine\_factor\_I = 2$ and $initial\_resolution = 0.2$ mol. O_2 is set as saturated component. With a lower compositional resolution (larger $final\_resolution$ values), the change in concentrations becomes more diffuse (examples are shown in the black rectangles).

We systematically vary the $auto\_refine\_factor\_I$ (between 1 and 4), the $initial\_resolution$ (0.3 – 0.1 mol) and the $final\_resolution$ ($2.5{\cdot}10^{-1}$ – $2.5{\cdot}10^{-4}$ mol) in 44 experiments. The employed default values not changed here, are provided in the perplex_option.dat file in the electronic supplementary materials. Here, also the input script including the employed bulk rock composition and the solution models is provided. Preceding test experiments suggest that using values for the keyword group far beyond our systematically varied ranges (e.g., $auto\_refine\_factor\_I \gg 4$ or $initial\_resolution \ll 0.1$ mol), causes the failure of the Perple_X software due to memory limitation. Our results show that using intermediate values for all three parameters mentioned before produces the best result in terms of data quality and computation time. Generally, the longer the computation time, the better the phase boundaries are resolved, e.g. Figure 3.1 (top) and Figure 3.2 (left) show that with increasing compositional resolution the data quality increases at the expense of the computation time. Consequently, decreasing the final compositional resolution from $2.5{\cdot}10^{-4}$ to $2.5{\cdot}10^{-2}$ mol (for exploratory and auto-refinement stage), makes phase transitions more diffuse (e.g., black rectangles, Fig. 3.2), but still resolves all relevant properties. Changing the $final\_resolution$ values by one power of ten (e.g., from $2.5{\cdot}10^{-2}$ to $2.5{\cdot}10^{-3}$ mol) using constant values for both the $auto\_refine\_factor\_I$ and the $initial\_resolution$, doubles the computation time. The same effect has the increase of the $auto\_refine\_factor\_I$. Increasing both the $auto\_refine\_factor\_I$ by 1 and the $initial\_resolution$ by 0.1 mol preserves the quality of the results and the computation time.

We chose our optimal model with an $auto\_refine\_factor\_I = 2$, an $initial\_resolution$ = 0.2 mol and a $final\_resolution = 2.5{\cdot}10^{-2}$ mol for both the exploratory and the auto-refinement stage. To further decrease the computation time, we tested in additional 10 experiments how the grid resolution influences the quality of the phase diagrams. For the x_nodes and the y_nodes we use values between 10 and 35 for the exploratory stage and between 15 and 52 for the auto-refinement stage. The optimal grid resolution appears to be 22 (for the exploratory stage) and 33 (for the auto-refinement stage), creating an effective resolution of 257 points in x- and y-direction. Using these values, all phase boundaries observed in the high resolution performances are resolved (comparison between Fig. 3.1 (bottom) and Fig. 3.3 (bottom)) and the computation time is reduced to a minimum (in this case to $\sim$ 6 h). Using a much coarser computational grid may not resolve all phase stability fields (Fig. 3.3 (top)).

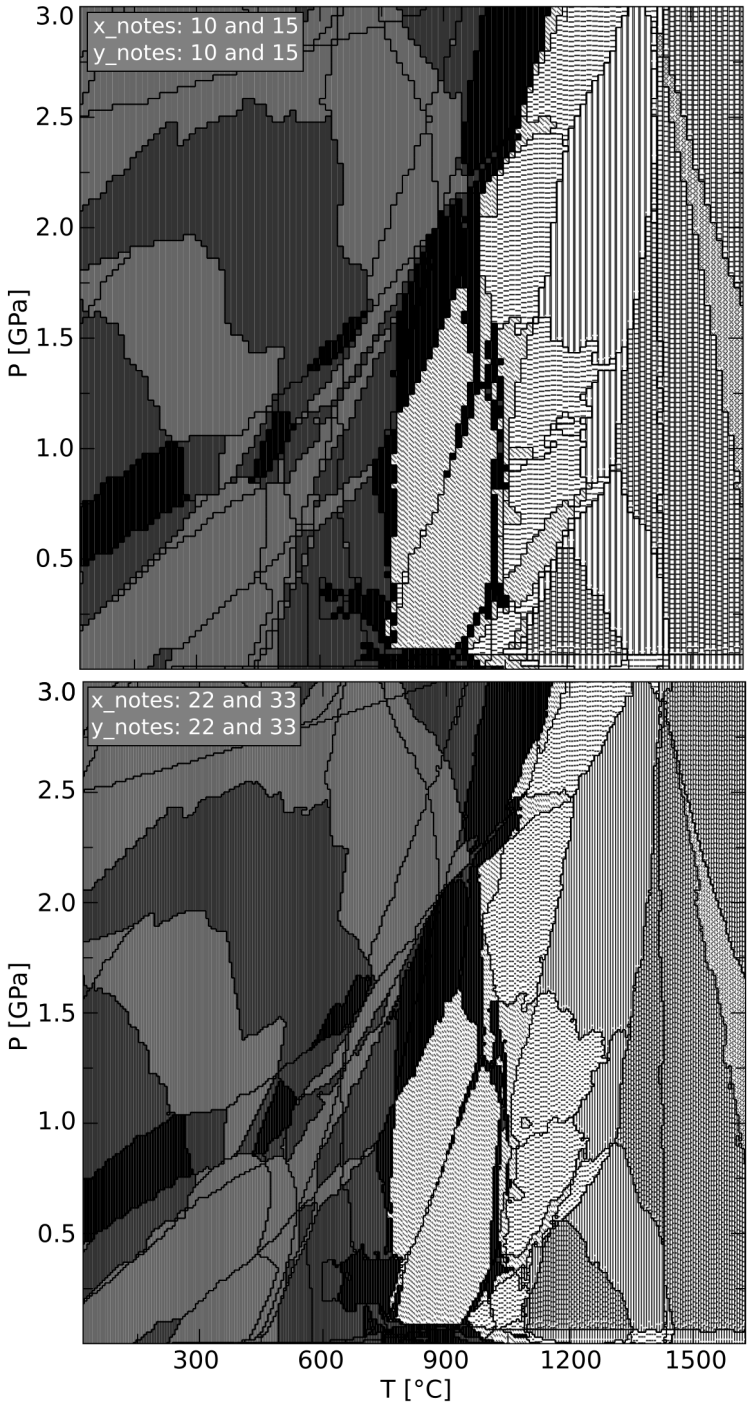

Figure 3.3: Pseudosections, showing fields of different stable phase assemblages. O_2 is set as saturated component. $auto\_refine\_factor\_I = 2$, $final\_resolution = 2.5{\cdot}10^{-2}$ mol for both the exploratory and the auto-refinement stage, and $initial\_resolution = 0.2$ mol. x_nodes and y_nodes values are 10 for the exploratory stage and 15 for the auto-refinement stage, resulting in an effective resolution of 113 nodes in x- and y-direction (top). For the bottom phase diagram, x_nodes and y_nodes are defined with 22 and 33 for the respective stages, producing an effective resolution of 257 nodes in x- and y-direction. Increasing the grid resolution, increases the computation time from $\sim$ 2:30 h (top) to $\sim$ 6 h (bottom).

However, in these calculations, the O_2 concentration is not buffered in the system (only set as a saturated component). Using a QFM (quartz-fayalite-magnetite) buffer massively increases the computation time (four-fold in our case). Nevertheless, it is necessary to employ a QFM-buffer to compute more realistic phase stability fields, especially above the solidus.

This model configuration is optimal for this particular bulk rock composition. Investigating the pseudosections of other simulations with different bulk rock compositions suggests that this model configuration is appropriate to compute realistic phase properties (density, melt fraction, chemical and mineralogical compositions) with an average computation time of several hours. Therefore, we use this configuration for all phase diagram calculations to establish our database (Chapter 4).

The computation of the phase diagrams described in this chapter is executed on a machine with 4 processors (AMD Bulldozer), each with 8 cores. It has 512 GB RAM and uses a Linux operating system (Ubuntu 16.04 LTS).

REFERENCES

Connolly, J., 2009. The geodynamic equation of state: what and how. Geochemistry, Geophysics, Geosystems 10 (10).

Connolly, J. A., 2005. Computation of phase equilibria by linear programming: a tool for geodynamic modeling and its application to subduction zone decarbonation. Earth and Planetary Science Letters 236 (1), 524–541.

CHAPTER 4

AN AUTONOMOUS PHASE DIAGRAM DATABASE FOR GEODYNAMIC SIMULATIONS OF MAGMATIC SYSTEMS

Abstract Self-consistent modeling of magmatic systems is challenging as the melt continuously changes its chemical composition upon crystallizing, which may affect the mechanical behavior of the system. Melt extraction and subsequent crystallization creates new rocks while depleting the source region. As the chemistry of the source rocks changes locally as a result of melt extraction, new phase diagrams are required to track the future rock evolution for each chemical state. This will change density, solidus and liquidus as well as the mineralogical and chemical compositions of the rock. As a consequence, a large number of phase diagrams is required to study the evolution of magmatic systems in detail. As state of the art melting diagrams may depend on 10 oxides as well as pressure and temperature, this is a 12-dimensional computational problem. Since computing a single phase diagram for a fixed chemical composition (as a function of pressure and temperature) may take several hours, computing new phase diagrams during an ongoing numerical simulation is currently computationally intractable. One strategy to avoid this is to precompute diagrams and to create a comprehensive database, which contains all bulk rock compositions that may emerge during petro-thermo-mechanical simulations. Establishing such a database would require repeating geodynamic simulations many times while collecting all requested compositions that may occur during a typical simulation and continuously updating the database until no further new compositions are required. Here, we describe an alternative method that is better suited for implementation on large scale parallel computers. Our method uses a forecast method with which entries of an existing

database are employed to predict possibly required chemical compositions. They can be computed within boundaries that are defined manually or through principal component analysis (PCA) in a parameter space consisting of clustered database entries. We have implemented both methods within a massively parallel computational framework while using the Gibbs free energy minimization program Perple_X. Results show that our autonomous forecast approach has a very good predictive power. Our predicted models focus on physically realistic parts of the oxide parameter domain, which is spanned by the requested rock compositions of the forward models. This thus opens new perspectives in modeling magmatic systems.

4.1 INTRODUCTION

The chemical evolution of magmatic systems within the continental crust is complex as their compositions change locally upon melt extraction. Phase transitions caused by a change in pressure and/or temperature can be easily tracked by computing phase diagrams for specific bulk rock compositions over the entire possible P–T range. Yet, the effect of melt extraction on the local rock chemistry is more difficult to handle. Depending on the amount of extracted melt, the remaining residuum has different chemical and mineralogical compositions. For each of the modified chemical systems, new rock properties (density, solid and liquid fractions and their compositions) must be calculated by minimizing the Gibbs free energy. Thermodynamic melting models have evolved massively in recent years such that it has now become feasible to realistically simulate melting and crystallization processes.

Thermodynamic processes can be integrated into a thermomechanical model in different ways. Phase diagrams can be precomputed for relevant bulk rock compositions and P–T ranges (e.g. Rüpke et al., 2004; Kaus et al., 2005; Yamato et al., 2007; Gerya and Meilick, 2011; Magni et al., 2014; Rummel et al., 2018), or phase relations can be determined on the fly during an ongoing geodynamic simulation (e.g. Tirone et al., 2009; Hebert et al., 2009; Duesterhoeft et al., 2014; Oliveira et al., 2017; Riel et al., 2018). In case the phase diagrams are precomputed, they are normally limited by their compositional ranges, as they are often only designed to estimate density changes and seismic velocities (e.g. Nakagawa et al., 2009; Faccenda and Dal Zilio, 2017) or to investigate the influence of water release in subduction zones (e.g. Rüpke et al., 2004; Magni et al., 2014). However, to fully understand magmatic processes, including the feedback between chemistry and thermomechanics is crucial. This requires a detailed consideration of the compositional

evolution, which can be modeled with a large thermodynamic database that contains a few thousand up to several ten-thousands of phase diagrams. Recently, Rummel et al. (2018) showed that physical processes such as the melting source of a mantle plume can be better understood when the chemistry of extracted melt is taken into account during a geodynamic simulation. This result also shows that it is possible to track the chemical evolution although a limited database consisting of 625 phase diagrams was used.

Recent advances in extending melting models from metapelitic rocks (White et al., 2001, 2014) to mantle rocks (Jennings and Holland, 2015), metabasic rocks (Green et al., 2016), or even for the whole range (Holland et al., 2018), allow phase diagram calculations for a very broad compositional range. Yet, so far these thermodynamic models have only been used in a simplified manner. Implementing them as part of a thermomechanical simulation of a magmatic system is an important future step towards creating predictive models of magmatic systems. Several software packages exist to compute such phase diagrams, e.g. MELTS/pMELTS/rhyolite-MELTS (Ghiorso and Sack, 1995; Ghiorso et al., 2002; Gualda et al., 2012), THERMOCALC (Powell and Holland, 1988), THERIAK-DOMINO (de Capitani and Petrakakis, 2010), or Perple_X (Connolly, 2005, 2009). We use Perple_X in this study, which is a sequential software. This means that the computation of the phase diagram is performed on a single CPU, which may require a couple of hours up to a few days. Here, we created a MPI-parallel (Gropp et al., 1999) framework that invokes multiple Perple_X sessions simultaneously. In this manner, many thousands of phase diagrams can be computed within a few days depending on the size of the parallel computer available.

The phase diagram database is always established with an ensemble of requested rock compositions of previous geodynamic simulations. To forecast possibly requested rock compositions, we have to investigate the multidimensional parameter space that is spanned by the existing database entries, in our case nine oxides. Here, we apply methods from machine learning for dimensionality reduction, which is crucial to understand trends and correlations in the oxide distribution. A very popular method for dimensionality reduction is the so-called "t-Distributed Stochastic Neighbor Embedding" (t-SNE) method (Maaten and Hinton, 2008; Van Der Maaten, 2014), which projects data on a lower dimensional manifold (usually 2D) and simultaneously groups together similar data samples. We combine this data reduction technique with a clustering algorithm (DBSCAN, Ester et al., 1996) to identify groups of similar bulk rock compositions based on their distributions on the two-dimensional projection. After these processing steps, we deal with subsets of the database that contain similar rock compositions without much variation. This allows us to

apply linear dimensionality reduction techniques such as for example principal component analysis (Hotelling, 1933) to locally estimate linear trends of the distribution. Having determined these local trends enables us to perform forecast modeling by focusing a sampling along these trends of various widths. The new rock compositions obtained from this are used to extend the phase diagram database. The suitability of those rock compositions to describe possible chemical processes in petro-thermo-mechanical models is affected by the sampling space in which they are computed. The volume of this sampling space is controlled by whether a clustering algorithm is applied or not.

In this paper, we present different sampling techniques to determine new bulk rock compositions for a phase diagram database. We validate their suitability to predict rock compositions that could emerge during geodynamic simulations. Differences between the required phase diagrams and available ones are investigated while extending the size of the database. To better understand the origin of required phase diagrams, their bulk rock compositions are presented together with their formation conditions at which they were produced (e.g., temperature, pressure and melt/crystal fraction).

4.2 METHODS

4.2.1 Modeling magmatic systems with petro-thermomechanical models

The chemical evolution of magmatic systems is a multifaceted process, which is associated with many melt extraction events that locally change the chemical composition of the respective rocks. This does not only change the chemical and mineralogical evolution but may also have a feedback on the thermomechanical behavior of the dynamic system. In the following sections, we briefly describe the thermomechanical model that we employ in this study and provide a detailed description of the coupling with petrological approximations to model the compositional evolution of magmatic systems.

The petrological modeling approach is integrated in a thermomechanical simulation code MVEP2[1] (Kaus, 2010; Thielmann and Kaus, 2012; Rummel et al., 2018). MVEP2 employs finite elements to discretise the model domain and solves the conservation equations of mass, momentum and energy of slowly creeping fluids on geological timescales. The rheology is handled with constitutive relationships that define the visco-elasto-plastic deformation behavior of rocks. To model diking, the numerical approach is combined with

[1]code is provided at: https://bitbucket.org/bkaus/mvep2

a semi-analytical fracture opening algorithm that will be described in an accompanying paper (Chapter 5) in which also the modeling results will be presented more in detail. The first dike formation is triggered by basaltic magma from the mantle that is injected as sills into the crust or uppermost mantle. We employ a marker-in-cell-technique to track rock properties during the geodynamic simulation. These markers play a central role in our approach as we also use them as tracers of the mineralogical and chemical evolution of the magmatic system. In our approximation, the chemical system is restricted to nine oxides, i.e. SiO_2–TiO_2–Al_2O_3–FeO–MgO–CaO–Na_2O–K_2O–H_2O, from which diverse mineral and melt compositions can be formed using the thermodynamic melting model of Green et al. (2016).

The information about the local compositional state is tracked by assigning an individual phase diagram to each marker employed in the geodynamic simulation. Our model has a lateral extent of 50 km and is 40 km deep, which is resolved with 400 and 350 finite elements, respectively. We start the simulation with ∼1.3 million markers, but the number increases during the simulations as new dikes/sills are generated, to ensure that the spatial evolution of rock and melt chemistry is tracked with sufficient accuracy. We neglect reaction kinetics and assume thermodynamic equilibrium. However, despite these simplifications, an immense thermodynamic database is required to cover all possible chemical states of liquid and residuum compositions generated in the evolving magmatic system. The high number of requested phase diagrams as a consequence of only one newly generated dike can be illustrated with the following example. As the local chemical system changes due to melt extraction, the chemistry of the system is split into a liquid part forming a dike and into a residuum part. The dike is described by only one phase diagram (average liquid chemistry), assuming homogeneous mixing of all generated melts. However, the remaining residuum chemistry changes strongly depending on the local amount and composition of extracted melt. Due to the different rock depletion stages, the number of phase diagrams with distinguishable bulk rock compositions can be very high. Our tests show that a few thousands of phase diagrams are required for a typical complete simulation.

The phase diagrams are computed with Perple_X (Perple_X 6.7.9, Connolly, 2005, 2009) and are evaluated for discrete P–T conditions (257×257 points) for the given ranges and describe how solid and liquid oxide compositions as well as densities, melt fractions and stable mineral assemblages will evolve. With a pressure range of 0.1-3000 MPa and a temperature range of 290-1900 K, thermodynamic properties are determined every 11.7 MPa and 6.3 K for a specific bulk rock composition. The thermodynamic data files used

are provided in electronic supplementary materials.

In general, there are two different strategies to combine geodynamic simulations of magma migration with thermodynamic phase diagrams. We call the first method the *dynamic* method (i), in which a new phase diagram is computed on the fly during an ongoing simulation. The geodynamic simulation pauses while thermodynamic calculations are performed. The alternative approach is the *static* method (ii), in which a look-up table with existing phase diagrams for different bulk rock compositions is used. Here, a phase diagram that is acceptably similar to the requested phase diagram is used to immediately continue with the geodynamic simulation after updating the marker with the incoming request.

i) In the *dynamic* method, the computation of phase diagrams is performed during an ongoing geodynamic simulation through which the number of required phase diagrams is reduced to a minimum. After each melt extraction event, the residuum or melt compositions can be directly used to compute new phase diagrams, provided they do not exist yet in a database. The phase diagram is directly updated on the marker, from which melt is extracted, and the chemical system develops based on this specifically updated phase diagram. The disadvantage of this method is that the respective geodynamic simulation has to pause until all necessary phase diagrams are computed. This massively increases the computation time for each geodynamical time step, as the computation of an individual phase diagram may take several hours. From a computational perspective, the process is a sequential task, which is hard to parallelize with a multitask architecture, because the workload can differ a lot due to a different number of newly requested compositions. For example, a single phase diagram request would force all other tasks to wait.

ii) For the *static* method, a database of existing phase diagrams is used to describe the future rock evolution after each melt extraction event. Here, the most similar phase diagram in terms of bulk rock chemistry is used and replaces the previously associated phase diagram of the marker. As a similarity measure, we use the Euclidean distance in the space spanned by the components of bulk rock chemistry. Clearly, the closer the query is to the existing database entries, the more accurate the model becomes. For this reason, we store all requested residuum and melt compositions during a simulation and compute new phase diagrams separately from the simulations. The advantage is that the job can efficiently be performed in parallel depending on the size of the computer available. In our case, we use 256 tasks in parallel and compute $\sim$1000 of phase diagrams in a 3-4 days although that could

be increased the more cores are used. However, it was initially unclear how many different phase diagrams are required for a typical simulation, as well as what the error is that is made by employing phase diagrams with the approximate, but not the exactly correct, chemical composition during the simulations. The obvious advantage of this approach is that the computation time for all phase diagrams is reduced to a minimum. The disadvantage, however, is that the respective geodynamic simulation has to be repeated many times until the differences between the requested and bulk rock compositions of the database become negligible. In principle, such a database can become very large, such that technical issues arise when loading the full database during a geodynamic simulation, as well as problems with storing the data. We note that there are techniques to compress the rock properties without losing much in accuracy (Afonso et al., 2015), which we have not explored here.

Here, we investigate the second strategy. In the following, we will make suggestions on how such a database can be established and efficiently extended with an autonomous forecast method.

4.2.2 Establishing the database

From a computer science point of view, we deal with a parameter space that is spanned by nine oxides, bounded by upper and lower limits, respectively. There is the additional requirement that the oxide concentrations of each bulk rock composition (BRC) must add up to exactly 100 wt%, effectively reducing the parameter space to a 9D manifold to which all BRCs in the database (called here as initial BRCs) are restricted. To facilitate the problem, it is assumed that the parameter space is discretized and only states with offsets of $\Delta_{\mathrm{Ox.}} = 0.1$ wt% can be realized. Although this dramatically reduces the possible number of states, it would be inefficient to establish the database by randomly creating new BRCs between the maximum and minimum concentrations of the respective oxides while respecting the constraints. Instead, we make use of expert knowledge, which provides good initial guesses about the interesting regions of the oxide-space, or about BRCs most likely being required by future simulations. As a starting point, we compute five initial phase diagrams as representative BRCs for the upper, middle and lower crust as well as for the mantle and the mafic basaltic intrusion. Using these initial diagrams, we perform a series of iterative geodynamic simulations. As soon as a melt extraction occurs, the existing phase diagrams can not sufficiently describe the future rock evolution and new phase diagrams are requested. We compute the requested phase diagrams and repeat

the simulation to produce additional composition requests from the evolving magmatic system. To further improve our initial guess, we vary the configurations of the simulations by changing tectonic boundary conditions, intrusion depths and temperatures of magma influx from the mantle, geothermal gradients, and other properties. With this strategy, we created an initial database with thousands of phase diagrams that ideally covers the possible oxide concentration limits of requested BRCs in our petro-thermo-mechanical models. Theoretically, one could further improve the database with more simulations and new requests that result from them. However, this requires significant manual interaction. In the following section, we describe our approach to extend the database in a more autonomous manner.

4.2.3 Extending the database

To further extend the database in an autonomous manner, we make use of our initial guesses and guide the sampling of new BRCs with the location of the initial BRCs. Visualizing the BRCs along different oxides illustrates that existing BRCs are correlated with each other, visible as they gather in smaller clouds or align along mostly non-linear pathways that usually split up in multiple branches (Fig. 4.1). This means that the approach of uniformly sampling the entire initial BRC space between their extreme concentrations (Fig. 4.1A) is unsuitable to create exclusively new BRCs that are similar in chemistry to the initial BRCs. From a data science perspective, we deal with high-dimensional, natural data that are correlated, i.e. 9D-BRCs that only locate on lower dimensional manifolds in the oxide space. A robust method for linearly correlated data is the principal component analysis (PCA, Hotelling, 1933). A large number of approaches exist for non-linear data, including manifold learning and non-linear PCA and kernel-PCA methods. By using PCA (PCA-CS, Section 4.2.3.2) or by constraining the oxide space manually (M-CS, Section 4.2.3.3), the sampling space for new BRCs is reduced (Fig. 4.1B). However, even though corners are already neglected, in which no initial BRCs are located, the sampling space is still relatively large and new BRCs can be created between compositional branches of initial BRCs. To further reduce the sampling space, a combination of robust dimensionality reduction techniques can be used by applying PCA or manually constrained boundaries to individual compositional clusters (Section 4.2.3.1) in the mapping space (Fig. 4.1C).

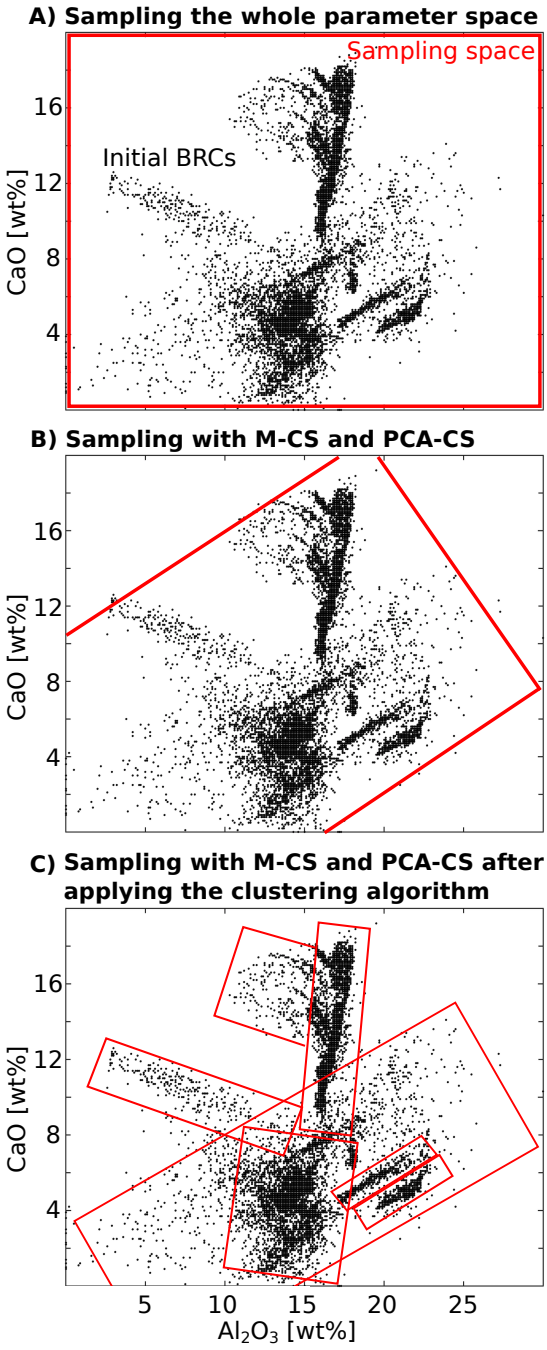

Figure 4.1: Three different ways to sample the parameter space of initial BRCs (black points; 17,088 in total), shown for the oxide combination Al_2O_3 vs. CaO. The sampling space is marked with the red lines. A) The rectangular sampling space is defined by the extreme oxide concentrations of initial BRCs. An oversampling of low probability regions (corners) would be the consequence. B) Manually constrained sampling (M-CS) and PCA-constrained sampling (PCA-CS) are used to reduce the sampling space. Larger deviations from the initial data set are allowed for new samples (BRCs). C) Applying M-CS and PCA-CS on smaller compositional subgroups (clusters) reduces further the sampling space, but also does not allow new BRCs to be chemically dissimilar to the initial BRCs.

Although we use nine oxides to describe the rock compositions, for some of these compositions, an oxide concentration can be zero. In this case, the nonexistent oxides are not required to describe the chemistry of the rock and can be neglected. We create groups of rock compositions for which the same oxides are relevant. This reduces the dimension for specific groups and thus less oxides have to be considered to determine a new BRC. Resulting groups, which are too small (< 10 BRCs), are not taken into account, and those that contain more than 100 BRCs, are used for further clustering (Section 4.2.3.1). For each compositional cluster and group of intermediate size (10–100 BRCs), we determine new BRCs using PCA- (PCA-CS, Section 4.2.3.2) or manually constrained sampling (M-CS, Section 4.2.3.3). If not all oxides were considered here for a specific group, the concentration of the missing oxide is subsequently set to zero such that each new BRC is finally described by all nine oxide compositional parameters.

4.2.3.1 Simplifying the parameter space with t-SNE and DBSCAN

In order to deal with the complex BRC relationships, we break down the distributions in smaller fractions of similar compositions using a combination of a dimensionality reduction technique and a clustering algorithm. We first apply the Barnes-Hut t-SNE (Van Der Maaten, 2014) to map the high-dimensional data to a lower dimensional manifold such that clusters of similar bulk rock compositions become visible. To quantitatively distinguish those clusters, it requires a method that utilizes the coordinates of the data points to find dense distributed regions and thus clusters. For this, the clustering technique DBSCAN (Density-Based Spatial Clustering of Applications with Noise, Ester et al., 1996) is applied. Both algorithms, Barnes-Hut t-SNE and DBSCAN, are briefly described below.

The Barnes-Hut t-SNE is based on the previously developed algorithms, SNE (Stochastic Neighbor Embedding, Hinton and Roweis, 2003) and t-SNE (t-Distributed Stochastic Neighbor Embedding, Maaten and Hinton, 2008). It is different compared to the previous t-SNE version, as it includes the Barnes-Hut algorithm (Barnes and Hut, 1986) that massively accelerates the t-SNE procedure (Van Der Maaten, 2014), which is necessary to analyze large data sets. In general, t-SNE projects high-dimensional data (in our case 9 dimensions) on a two-dimensional map (Fig. 4.2), such that each data point (BRC) has a 2D representation. Nearby points correspond to similar BRCs and distant points correspond to dissimilar BRCs. t-SNE reduces the dimensionality while preserving the essential structures (local and global ones such as clusters at multiple scales) of the high-dimensional data in the low-dimensional map (Maaten and Hinton, 2008). The Barnes-Hut t-SNE algorithm is available as MATLAB library (http://lvdmaaten.github.io/tsne/), that

we employ in this study with default values.

In a second step, we identify clusters (Fig. 4.2) by applying DBSCAN to the projected data of the 2D map space. Each cluster is characterized by specific BRCs that are chemically similar and distinguishable to those of other clusters. DBSCAN is a density-based data clustering algorithm where clusters are defined as dense regions that contain a certain number of core points. Core points are data points that have a minimum number of neighbors ($minPts = 15$) within a predefined 'neighbourhood' distance ($\epsilon = 3$). The clusters also contain points that are not defined as core points but locate within the neighborhood distance of a core point. All other points are classified as noise. In comparison to k-means (Steinhaus, 1956; MacQueen et al., 1967), DBSCAN has the big advantage that the number of clusters must not be defined in advance. In this study, we employ a MATLAB implementation of DBSCAN that is available at http://yarpiz.com/255/ypml110-dbscan-clustering.

As a result, we now deal with small fractions of the BRC ensemble that align on lower dimensional manifolds in a much less complex manner. This allows us to adapt simplified models of the local distribution and to make predictions about requested BRCs. We employ two different approaches in this study, to which we will refer to as PCA-constrained sampling (PCA-CS, Section 4.2.3.2), and manually constrained sampling (M-CS, Section 4.2.3.3).

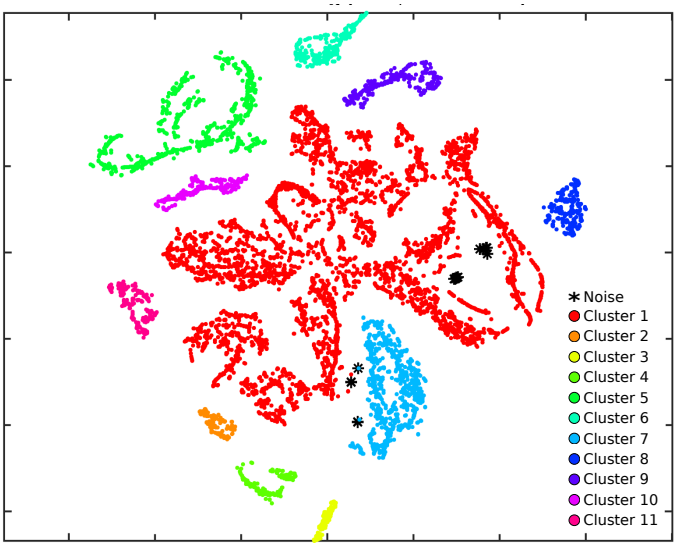

Figure 4.2: Example of a BRC distribution in a 2D representation of the Barnes-Hut t-SNE projection showing the relative coordinates of the data points. Colors show clustering results using DBSCAN applied to the ensemble in the projection space. Here, the ensemble contains 8457 BRCs, which can be summarized into 11 clusters, that gather BRCs with similar properties. 16 BRCs could not be included in particular clusters and are classified as noise.

4.2.3.2 PCA-constrained sampling (PCA-CS)

For each individual cluster, we determine the principal components and use them to parameterize the spatial distribution (Fig. 4.3). Based on the parameterisation with the eigenvectors, we perform a guided sampling, i.e. we focus the sampling on a region that is interesting in the sense that the predicted BRCs become relevant for future geodynamic simulations. In the following four steps, we explain the details of the algorithm.

1. Find the principal components, i.e. eigenvalues and eigenvectors, of the individual cluster distribution.

2. In the coordinate system of the principal components, we determine the center of mass and the extreme values along each component that define the ranges for each axis.

3. We draw new samples by selecting new BRCs

   (a) either from a uniform distribution between the defined ranges (uniform PCA-CS),

   (b) or, from a normal distribution that is centered in the center of mass and the standard deviation observed along the current dimension (normal PCA-CS),

   (c) or, from a normal distribution that is centered in the center of the range along the current dimension (normal-centering PCA-CS).

4. The samples are transformed back into the original BRC coordinate system. As the sum of all oxides has to be 100 wt% to represent a BRC, we repeat the sampling procedure until this requirement is fulfilled and a desired number of new BRCs is reached.

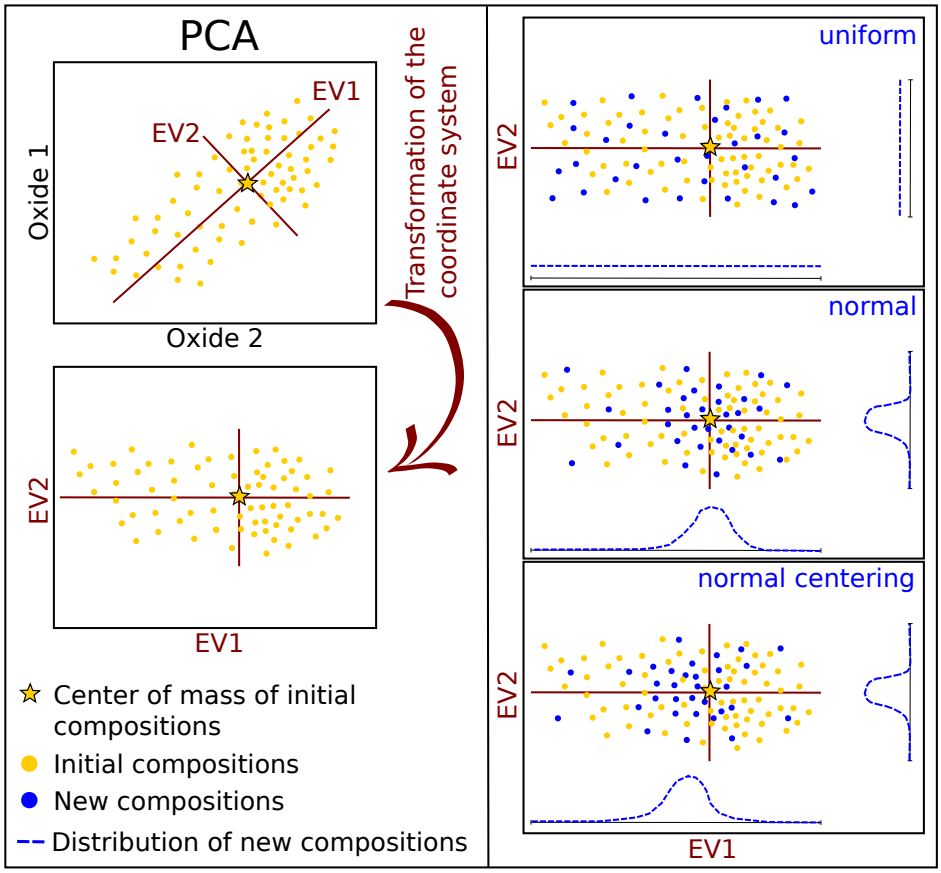

Figure 4.3: Finding new BRCs using principal component analysis (PCA). Shown on a 2D example, where red lines are the two eigenvectors (principal components), which are orthogonal to each other and cover the full parameter space of initial compositions. The eigenvectors form the axis of the new coordinate system, in which new compositions are determined and translated back later into the original coordinate system. New oxide concentrations are determined by using different random number generators (uniform, normal or normal centering) along the eigenvectors within their variances (eigenvalues).

4.2.3.3 Manually constrained sampling (M-CS)

Sometimes a linear description of the distribution within a cluster may not be appropriate and PCA might not be a good choice to parameterise the distribution. We, therefore, present an alternative approach that requires a less intuitive guidance but may result in a more accurate representation of the distribution. We consider the marginal distributions of all oxide combinations independently and determine polynomial fits and use them to define boundaries for a guided sampling. The exact procedure is presented below with Steps 1 – 3 and is illustrated in Figure 4.4. For simplicity, we use here “Ox1” and “Ox2” to describe the two components of an oxide combination.

1. For each oxide combination, polynomial regression is performed and depending on the coefficients of determination, a first- or a second-degree polynomial is used.

To set boundaries for the guided sampling, we translate this function along the coordinate axes until all BRCs are included in the interval (Fig. 4.4).

2. Starting from SiO_2 as Ox1, a second oxide (Ox2) is randomly chosen. The behavior of the fitting line is crucial to determine the oxide concentrations and two different cases must be considered.

Case 1: Both boundary lines have the same x-coordinates. Within their horizontal range, a concentration for Ox1 is randomly determined (x, Case 1, Fig. 4.4). The resulting range in the vertical direction, between both boundary lines ($y1$ and $y2$, Case 1, Fig. 4.4), is used to determine a random concentration for Ox2 (blue star, Case 1, Fig. 4.4).

Case 2: The boundary lines have different x-coordinates (e.g., for a banana-like shape, Case 2, Fig. 4.4). The axes are flipped to get the same x-coordinates for both boundary lines. Within their vertical range, a concentration for Ox1 is randomly determined (y, Case 2, Fig. 4.4). The resulting range in the horizontal direction, between both boundary lines ($x1$ and $x2$, Case 2, Fig. 4.4), is used to determine a random concentration for Ox2 (red star, Case 2, Fig. 4.4). For Case 2, several exception rules must be considered to determine the Ox2 concentration, examples are shown in Figure 4.4.

3. It is ensured that the newly determined oxide concentrations are within the boundaries of other oxide combinations that include one of these oxides. If other oxide concentrations were already determined before, they have to be considered as well in the determination of the new oxide concentrations. The sum of all oxides has to be 100 wt% to represent a BRC. The sampling procedure is repeated until this requirement is fulfilled and a desired number of new BRCs is reached.

A further reduction of the parameter space could be possible, if the upper and lower boundaries do not have to cover necessarily all initial BRCs and if the new oxide concentrations are determined along a normal rather than along a uniform distribution. This may avoid a possible oversampling of low probability regions (Afonso et al., 2013).

All rock compositions obtained from PCA- and manually constraint sampling, are rounded on one decimal place and are used as input compositions in Perple_X. Thus, phase diagrams in the database are distinguishable from each other in their BRCs at least

with 0.1 wt% (accuracy of an oxide concentration). A MATLAB implementation of the autonomous forecast approach is provided in the electronic supplementary materials.

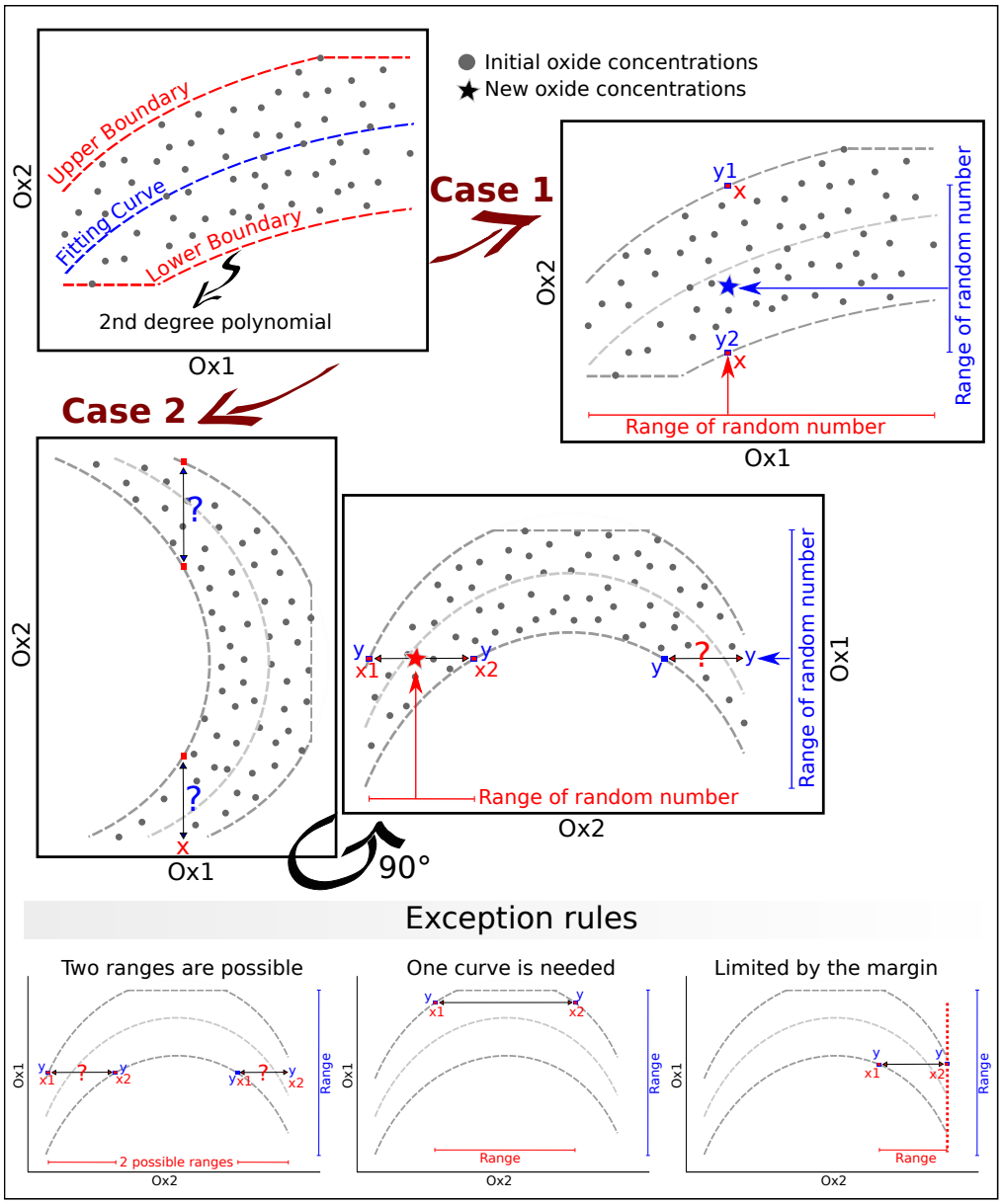

Figure 4.4: Finding new BRCs within manually pre-defined boundaries. A fitting line through the data is used to create the upper and lower boundaries of an oxide combination, within which new oxide concentrations can be determined. Case 1: Boundary lines have the same x-coordinates. The first oxide (Ox1) concentration is determined within the horizontal range of the boundaries (red section). The related range in the vertical direction (blue section) is used to determine the corresponding concentration for the second oxide (Ox2). Case 2: Boundary lines have different x-coordinates. The axes are flipped (90° rotation) so that the vertical range of the boundaries is used to determine the Ox1 concentration. In that special case shown here, two horizontal ranges are possible for the corresponding Ox2 concentration, one range has to be chosen. Different exception rules have to be considered to determine the Ox2 concentration for Case 2 and are presented at the bottom. Within the respective ranges, a uniform random number generator is used to specify the oxide concentrations.

4.3 RESULTS

In the following sections, we compare the sampling approaches. We first consider sampling based on the unfractionated initial BRCs (Section 4.3.1) and then apply all sampling techniques to individual clusters of the clustered initial BRC data set (Section 4.3.2).

4.3.1 BRC forecasting based on unfractionated initial bulk rock compositions

In the first approach, we determine new rock compositions (new BRCs) using the sampling techniques described in Sections 4.2.3.2 (PCA-CS) and 4.2.3.3 (M-CS), without performing clustering on the initial data set. The manually constrained boundaries include all initial BRCs (grey points, Fig. 4.5) without weighing the single compositions. Consequently, it results in a relatively large volume of the parameter space to emplace new BRCs ("M-CS", Fig. 4.5). We obtain similarly distributed scattering of new BRCs for uniform sampling along principal components using the uniform PCA-CS method ("Uniform PCA-CS", Fig. 4.5). In contrast, defining oxide concentrations with a normal (Gaussian) distribution along each principal component ("Normal PCA-CS", Fig. 4.5), concentrates new BRCs in the center of mass of the initial BRCs. Sampling with the normal-centering PCA-CS focuses the normal distribution in the center of the range between minimum and maximum concentrations of initial BRCs. Its sampling is therefore strongly affected by the outliers.

Thus, the choice of the most suitable sampling method to extend a phase diagram database with new BRCs used in Perple_X is strongly model dependent. In case new BRCs should be very similar to initial BRCs, a PCA-CS method, in which the concentrations are determined along a normal distribution, is the most suitable one. In this case, however, large parts of the parameter space are not well, or not at all, sampled with new BRCs, and the sampling is not explorative. In cases where all initial BRCs are considered to be equally important, weighted sampling is not appropriate. Here, M-CS or uniform PCA-CS are better choices, as they sample the parameter space without weighing but within ranges. Consequently, if we aim to create new BRCs with a chemistry that is very similar to that of the initial BRC ensemble, none of the sampling methods is fully suitable. Normal PCA-CS does not uniformly cover the compositional range of individual branches and focuses on the center of mass of the entire initial ensemble. M-CS and uniform PCA-CS sample new BRCs in all relevant oxide ranges, which may differ significantly from the initial BRCs of the database, such that these might never be requested by the geodynamic forward models. From these observations, we note that general sampling without prior

fractionation of the initial data set generally yields an exploratory result. New prediction models can show large chemical deviations from the initial models.

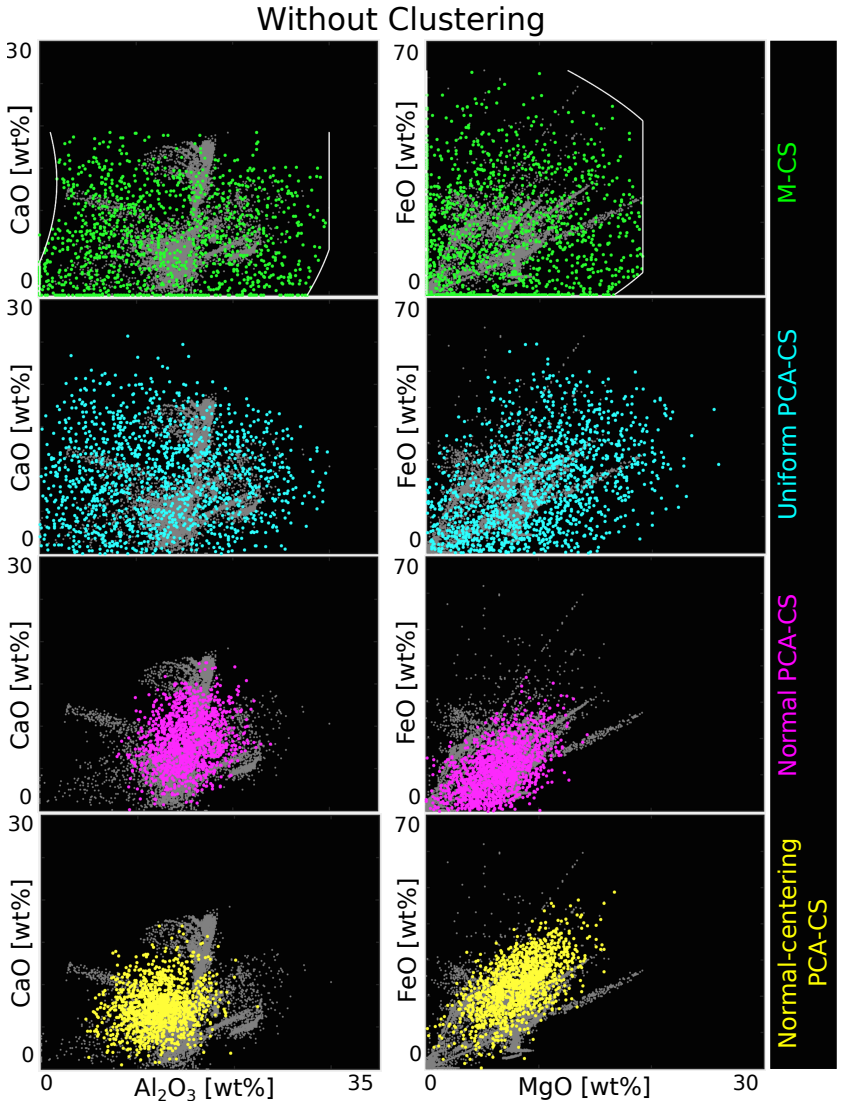

Figure 4.5: New BRCs generated with different sampling methods. The initial BRCs (grey points, 17,088 bulk rock compositions) are not clustered here. Within the manually constrained boundaries (white lines), new oxide concentrations are determined (green points). New BRCs created through one of the PCA-CS techniques are shown with the respective colors: turquoise for rock compositions determined uniformly along the principal components, pink for rock compositions determined with a normal distribution (centered in the mean) and yellow for new rock compositions determined with a normal distribution (centered between the maximum and minimum values) along the respective principal component. For each sampling method, ∼1350 new BRCs are computed. The compositions are shown for two oxide combinations (CaO vs. Al_2O_3 and FeO vs. MgO); for the whole oxide range, see Figures 4.A1–4.A4 in the Appendix.

4.3.2 BRC forecasting based on clustered initial bulk rock compositions

To focus the sampling on individual compositional branches of the initial BRC ensemble (Fig. 4.1C), the parameter space can be effectively reduced by applying a clustering algorithm to the initial BRCs (Section 4.2.3.1). For each cluster, M-CS and PCA-CS are separately applied to determine new BRCs. Results are shown in Figure 4.6 for two exemplary clusters.

Using the M-CS and the uniform PCA-CS methods (Fig. 4.6), we compute new oxide concentrations covering a large part of the parameter space. For a non-linear distribution of the initial BRCs, M-CS may cover more precisely the parameter space, as it allows non-linear boundaries (e.g., CaO vs. Al_2O_3, cluster 11, Fig 4.6). The M-CS method defines its ranges by shifting the fitting lines through the initial data up- and downwards by the same amount. This amount is determined by the maximum distance between the regression line and the extreme values. If far located data points only exist in one direction of the regression line (i.e., only above the parameterization, FeO vs. MgO, cluster 11, Fig. 4.6), the sampling space is large compared to other sampling methods and may include regions without the support of initial BRCs. Uniform PCA-CS constrains the sampling range of new BRCs to minimal and maximal initial concentrations. Thus, if only one outlier of an initial BRC exists (e.g., in FeO vs. MgO, cluster 11, Fig. 4.6), all new oxide concentrations are sampled uniformly between this outlier and the center of mass that limits the range towards the other extremum (Fig. 4.6). The influence of the outliers on the new BRCs is smaller for the normal PCA-CS. Here, we use a normal distribution along the respective principal component to sample a new BRC, which implies a low impact of distant samples. This is especially noticeable for cases in which only a few data points are located far away from the center of mass. This method may be the most suitable one to determine new BRCs in already existing compositions (initial BRCs). In comparison, the distribution of new BRCs that were created with normal-centering PCA-CS is shifted towards the location of outlier BRCs (FeO vs. MgO, cluster 11, Fig. 4.6).

Splitting the initial BRCs into groups of similar compositions using the clustering algorithm, allows the overall sampling to be almost the same for all applied methods (M-CS and PCA-CS) (Fig. 4.7), through which the disadvantages of the respective sampling methods become negligible. All newly computed BRCs are well located around the initial BRCs in the parameter space (Fig. 4.7) and thus existing branches of initial BRCs are covered and still maintained by the new BRCs.

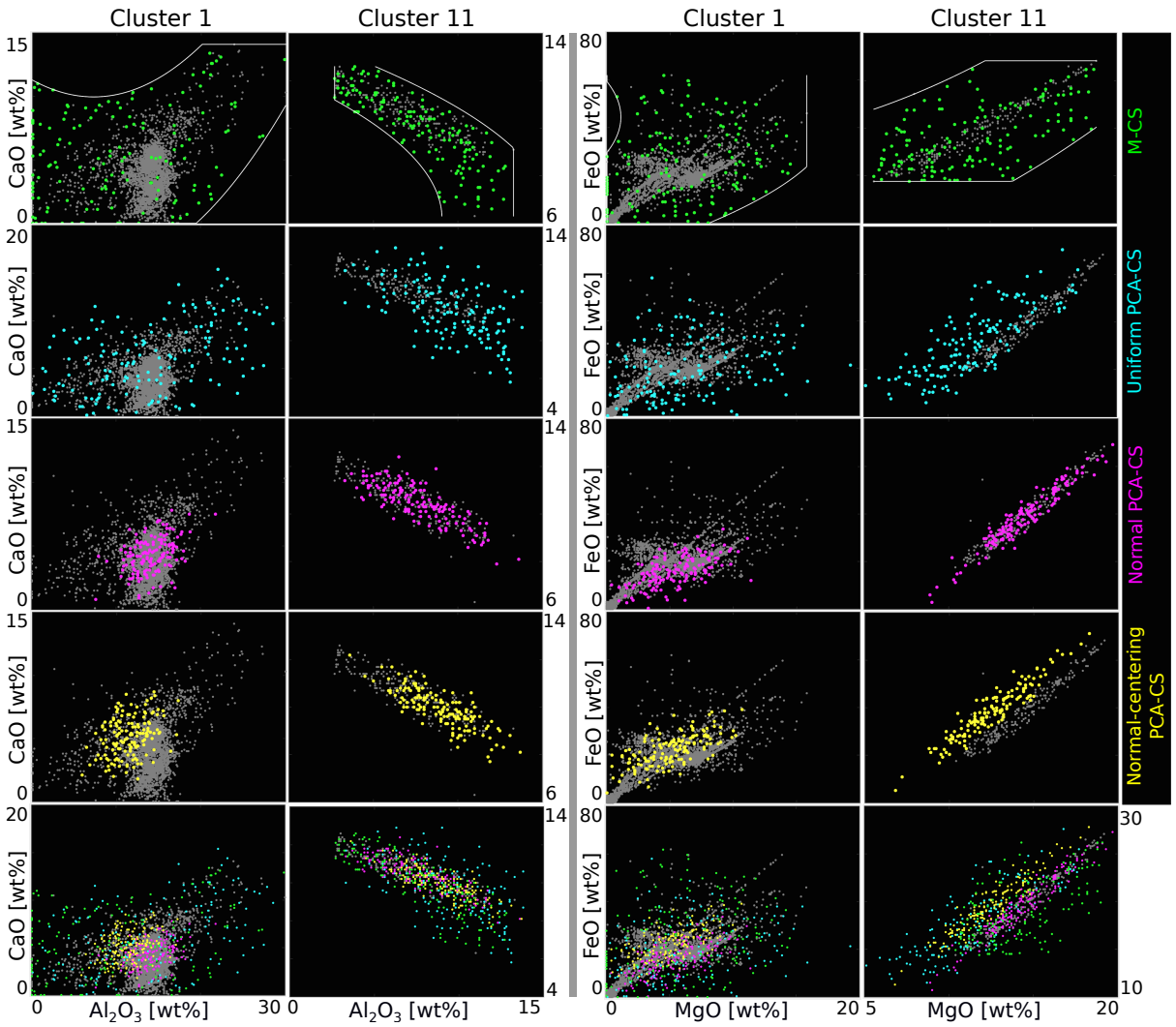

Figure 4.6: New BRCs generated with different sampling methods, shown for two different clusters (cluster 1 and cluster 11, Fig. 4.2). The initial BRCs of the respective clusters are shown as grey points. 8,457 initial BRCs are used for the clustering. 5,078 of them are in cluster 1 and 226 of them in cluster 11, the rest is allocated to the other clusters. New oxide concentrations are determined (green points) within the manually constrained boundaries (white lines). The lines are the respective shifted polynomial fitting line through the initial BRCs (here, 2nd-degree polynomial) and are limited to their maximum and minimum concentrations. New BRCs created with one of the PCA-CS methods, are shown with the respective colors: turquoise for rock compositions determined uniformly along each principal component, pink for those determined with a normal distribution (centered in the mean) and yellow for rock compositions determined with a normal distribution (centered between the maximum and minimum values) along the principal component. For each cluster and sampling method, ∼150 new BRCs are computed. The rock compositions are shown for two oxide combinations (CaO vs. Al_2O_3 and FeO vs. MgO). All BRCs are plotted together for comparison at the bottom.

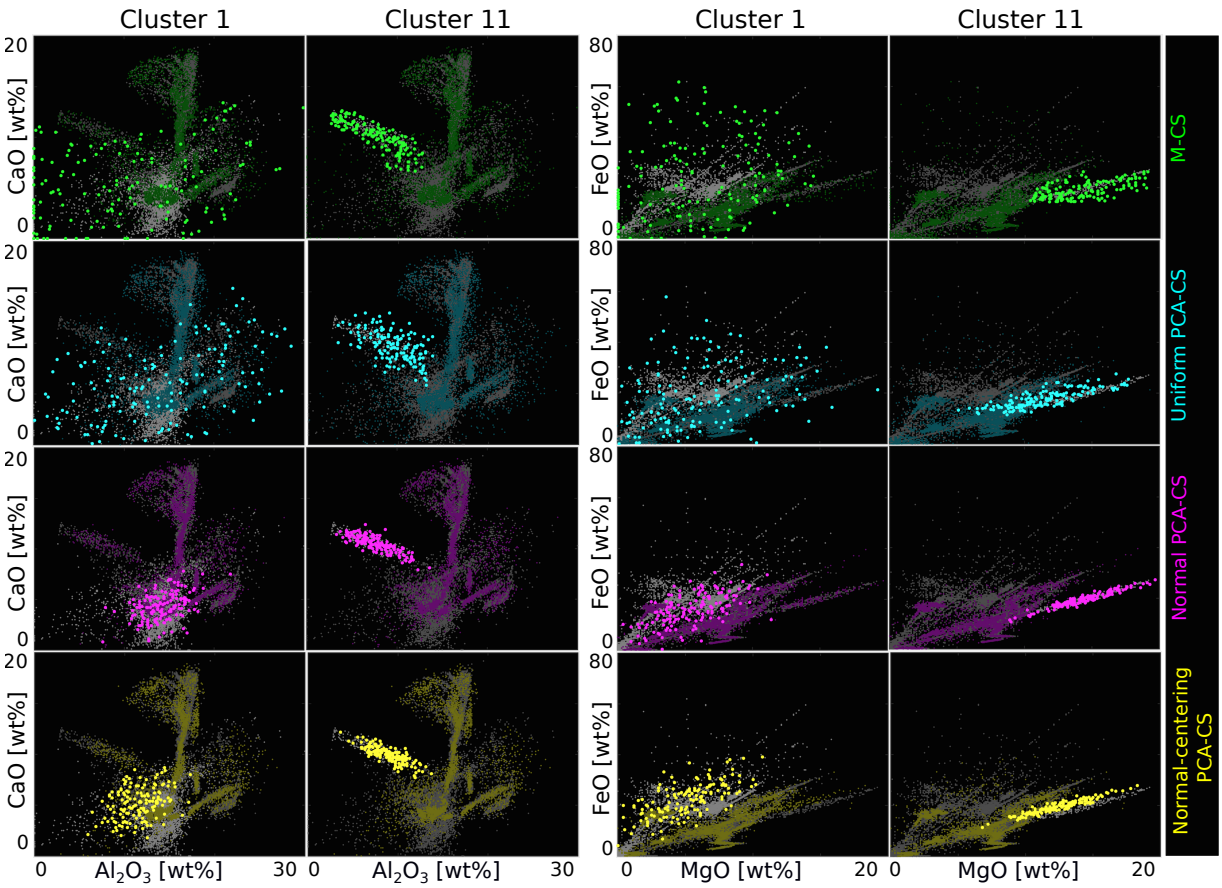

Figure 4.7: New BRCs generated with different sampling methods. Highlighted are new BRCs created in the two clusters 1 and 11 (Fig. 4.2 and Fig. 4.6). 17,088 initial BRCs are used for the clustering, shown as grey points. 5,078 of them are in cluster 1 and 226 of them in cluster 11, the rest is allocated to other clusters (not highlighted). Sampling results from the M-CS are shown with green points, from the uniform PCA-CS with turquoise, from normal PCA-CS with pink and new BRCs determined with the normal-centering PCA-CS are shown as yellow points. For each cluster and sampling method, ∼150 new BRCs are computed. The compositions are shown for two oxide combinations (CaO vs. Al_2O_3 and FeO vs. MgO); for the whole oxide range, see Figures 4.A5–4.A8 in the Appendix.

4.3.3 Evaluation of new BRCs

In the previous sections, we demonstrated several sampling approaches to predict BRCs that may be requested by future simulations. To quantitatively evaluate the success of various forecasting sampling methods, we now define a similarity index as follows:

$$D_{min,i} = \min_{j=1,\ldots,N_2} \left(\sqrt{\sum_{ox=1}^{9} (\mathrm{BRC1}_{i,ox} - \mathrm{BRC2}_{j,ox})^2} \right), i = 1, \ldots, N_1, \tag{4.1}$$

where ox represents the respective oxide and N_1,N_2 is the number of either initial BRCs from the database or new BRCs created with the sampling approaches.

Our similarity index D_{min} is a distance-based measure with units of wt% and denotes

the Euclidean distance between every new BRC and its closest neighbor among all initial BRCs. This calculation is executed in both directions by either starting from the new BRCs (Fig. 4.8A) or from the initial BRCs (Fig. 4.8B). In Figure 4.8, we compare the results of M-CS and PCA-CS applied to both the unfractionated and the clustered initial data set.

The minimal Euclidean distances (D_{min}) and the average D_{min} are computed for each sampling method. The average D_{min} (red numbers, Fig. 4.8) indicates the most suitable sampling technique to locate new BRCs close to initial BRCs in the parameter space, the smaller the average D_{min}, the more similar are new BRCs to already existing compositions. Additionally, we present the frequency distribution of the minimal Euclidean distances to visualize differences between the sampling techniques and to show the effect of applying the clustering algorithm to initial BRCs (Fig. 4.8).

In the following section, results are presented from the minimal-distance-calculations in which the minimal Euclidean distances are computed starting from the newly created BRCs (Fig. 4.8A). Without using the clustering algorithm, many of the new BRCs are located far from the neighboring initial BRCs, especially for the M-CS and the uniform PCA-CS (Fig. 4.8A). This is observed in the average D_{min} for each sampling method (red numbers, Fig. 4.8), but also in the frequency distribution of their minimal Euclidean distances. New BRCs produced with the uniform PCA-CS show the largest scattering, with the longest minimal Euclidean distance of all sampling methods (Fig. 4.8A). With all four sampling techniques, no or very few BRCs are produced that are close to the initial BRCs. Defining new compositions within clusters of the initial data ensemble, strongly improves the result, with the average D_{min} being reduced by at least a factor of four and the frequency distributions show that many of the newly generated BRCs have similar chemistries to those of the initial data set (Fig. 4.8A, left). Thus, with pre-clustering, all sampling methods produce almost equally well new BRCs that are similar in chemistry to the initial BRCs, with slightly better results for PCA-CS with a normal distribution. The same trend is observed for an extended database (extended from 17,088 to 27,049 initial BRCs), with a slightly lower average D_{min} for most of the applied sampling methods. The decrease of the average D_{min} may be caused by the increase of the number of initial BRCs while keeping the number of newly defined BRCs constant. This increases for each method the likelihood to create a new composition that is chemically more close to already existing ones. However, these results are based on minimal-distance-calculations in which the Euclidean distances are computed starting from each of the new BRCs (Fig. 4.8A). Thus, far away located initial BRCs are not considered, as long as closer ones exist in the

parameter space.

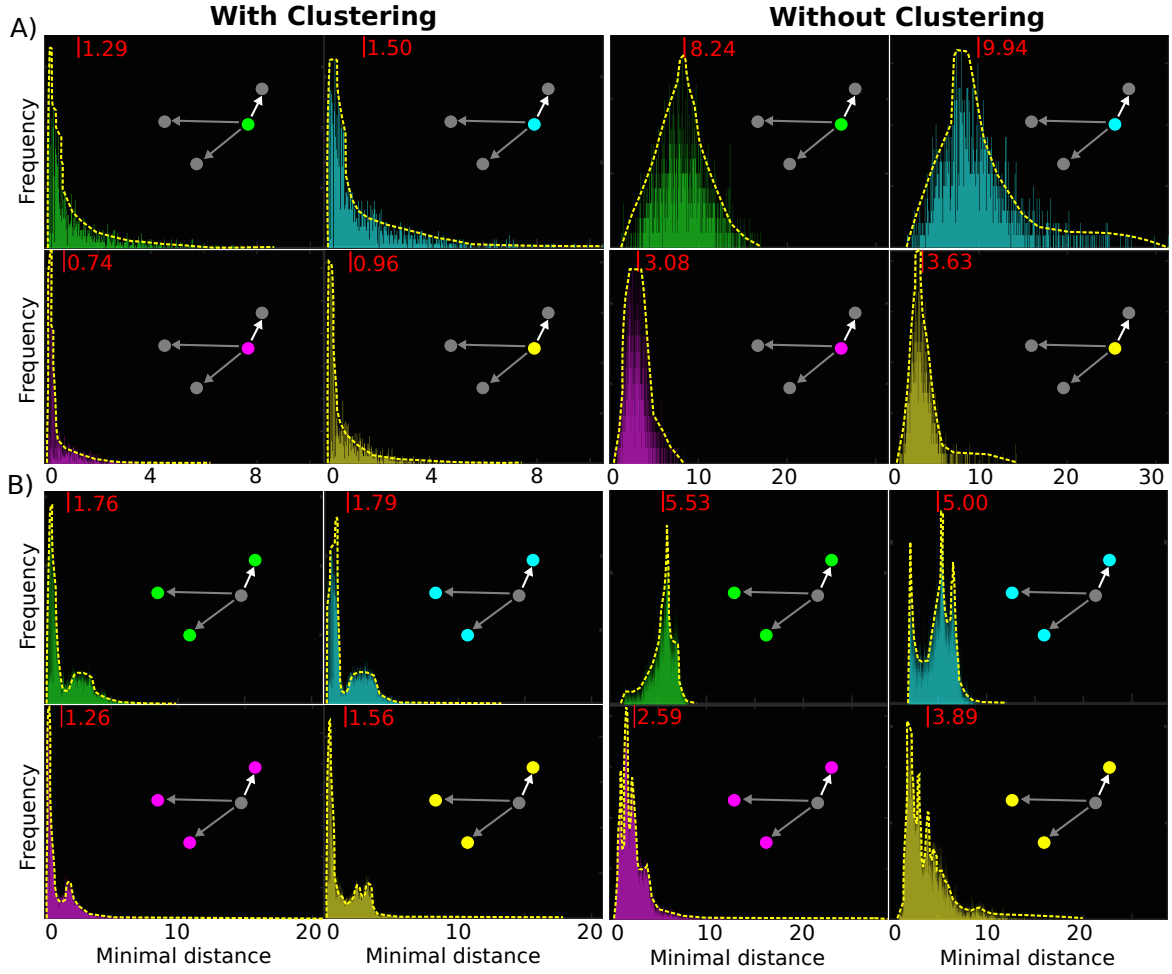

Figure 4.8: Minimal Euclidean distances computed between newly created and initial BRCs (eq. 4.1). Results are shown for initial BRCs that are either clustered (left) or unfractionated (right). A) the minimal Euclidean distances are computed starting from each of the new BRCs and B) starting from each of the initial BRCs. The direction is indicated by the small sketches, where grey balls represent the initial BRCs and the colored balls belong to the respective sampling methods. The minimal Euclidean distance (D_{min}) is shown with the white arrow. Red lines, with the corresponding numbers, specify the average D_{min} for each of the applied methods. The colors refer to the used sampling methods with which new rock compositions are determined: green for M-CS, turquoise for uniform PCA-CS, pink for normal PCA-CS and yellow for normal-centering PCA-CS. The results are shown as histogram plots. 1,350 new BRCs are used from each sampling method. The number of initial BRCs is 17,088.

To quantify the minimal Euclidean distances of the initial BRCs to the nearest newly created composition, we computed the minimal Euclidean distances starting from the initial BRCs (Fig. 4.8B). This decreases the average D_{min} for unfractionated initial BRCs, especially for the M-CS and the uniform PCA-CS methods. Consequently for these two sampling methods, new BRCs exist that are quite far from the initial BRCs (Fig. 4.8A) and which are not considered in the D_{min} if much closer data points exist (Fig. 4.8B).

All in all, the results from the minimal-distance-calculations (Fig. 4.8A,B) show that only by applying the clustering algorithm to the initial BRCs, new BRCs are created that are similar in chemistry to the initial ones independent of the sampling method. Normal PCA-CS produces the best result with the smallest average D_{min}. However, because of its location of new BRCs in the center of mass, some initial BRCs have here also the longest minimal Euclidean distance to a new BRC (length of the yellow dotted line, Fig. 4.8B). The determination of new BRCs within the extended sampling space of 27,049 initial BRCs produce nearly the same results. Only the average D_{min} increases slightly for each of the applied sampling approaches. With the increase of the number of initial BRCs (from 17,088 to 27,049), it increases the possibility that some of the initial BRCs are located more far away from the newly created BRCs in the parameter space.

4.4 DISCUSSION

Ideally, we would like to extend the database such that no additional phase diagrams are required to describe the chemical evolution of magmatic systems in geodynamic models. We have presented several approaches to create and extend a petrological database of phase diagrams for thermomechanical simulations. Whether or not a new phase diagram is required, is defined in the geodynamic model as new rock compositions are formed due to melt extraction, thereby depleting the source and simultaneously creating new rocks in melt emplacement areas. Within the modeling code, we let the algorithm find a "suitable" phase diagram from the database for each chemical state. If a suitable phase diagram is not available, it must be computed. Consequently, after computing the missing phase diagrams with BRCs for Perple_X, the geodynamic simulation has to be repeated over and over again, until no further phase diagrams are required. In the following section, we discuss the extent to which our independently-created database helps to avoid such time-consuming repetitions. Moreover, we show that applying the clustering algorithm to requested rock compositions from geodynamic models, cluster their physical conditions (e.g., pressure, temperature and melt fraction) at which they were produced, as well.

4.4.1 Predictive power of the sampling techniques

The predictability of required BRCs for geodynamic simulations is tested by comparing the requested compositions with rock compositions obtained from the different sampling approaches. The sampling is based on either the unfractionated initial BRCs or the compositional clusters to demonstrate the importance of the clustering algorithm. For this, the

minimal Euclidean distances (D_{min}) are computed (eq. 4.1) between new BRCs created with the sampling methods and those requested from geodynamic simulations. For the respective geodynamic simulations, the number of available phase diagrams is equal to the number of initial BRCs (17,088) used to determine new BRCs with one of the sampling approaches. The model configurations are equivalent for geodynamic simulations which are used both for establishing the initial database and to get the composition requests presented here. The requested compositions exclusively represent bulk rock compositions that are not used already in the phase diagram database.

In the following section, results are presented from the minimal-distance-calculations in which the minimal Euclidean distances are computed starting from the newly created BRCs (Fig. 4.9A). The average D_{min} between newly created and requested BRCs increases for all sampling techniques from the cluster sampling to the sampling that is based on the unfractionated initial data ensemble. Significant differences are observed especially for the BRCs created with the M-CS and the uniform PCA-CS (Fig. 4.9A). The frequency distributions of the minimal Euclidean distances show a bimodal distribution for the clustered initial data set, with a first maximum at small distances (some of the new BRCs are similar to requested BRCs) and a second maximum at higher minimal Euclidean distances (Fig. 4.9A, left). Additionally, newly created BRCs exist that are dissimilar in chemistry to those requested from geodynamic simulations (wide scattering of the minimal Euclidean distances for each of the applied sampling methods, Fig. 4.9A). Applying the minimal-distance-calculations to a larger initial data set (27,049 initial BRCs), slightly improves the results in terms of average D_{min} values (from 3.66 to 3.60 for the M-CS; from 3.83 to 3.64 for the uniform PCA-CS; from 3.23 to 2.81 for the normal PCA-CS; from 3.39 to 3.30 for the normal-centering PCA-CS).

Similar trends are observed if the minimal Euclidean distances are computed starting from each of the requested compositions (Fig. 4.9B). In general, the average D_{min} values are smaller (Fig. 4.9B) compared to those computed the other way around starting from newly created BRCs (Fig. 4.9A). Increasing the number of initial BRCs from 17,088 to 27,049, decreases the average D_{min} for each of the applied sampling methods (from 2.98 to 1.90 for the M-CS; from 3.00 to 1.95 for the uniform PCA-CS; from 2.56 to 1.52 for the normal PCA-CS; from 3.01 to 2.02 for the normal-centering PCA-CS), perhaps as a result from the improved sampling space in which new BRCs are determined. The range in rock compositions that can be created with the sampling approaches is controlled by the initial BRCs of the database forming the sampling space. This is directly linked to the predictability of requested BRCs, as the sampling of new BRCs is guided with the

location of the initial BRCs.

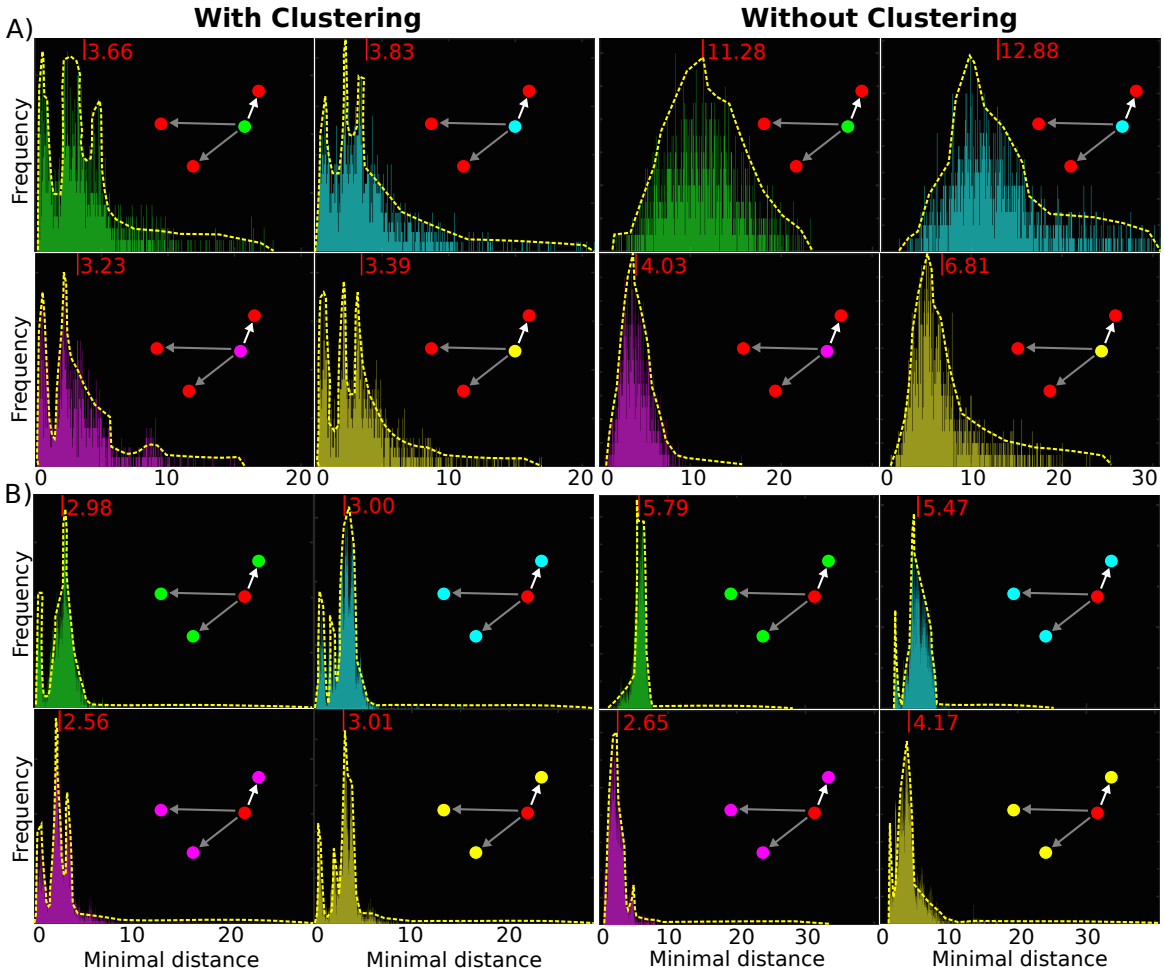

Figure 4.9: Minimal Euclidean distances computed between new BRCs obtained from sampling and requested BRCs from geodynamic simulations (eq. 4.1). Results are shown for a clustered (left) and an unfractionated initial data ensemble (right). A) the minimal Euclidean distances are computed starting from each of the newly created compositions and B) starting from each of the requested compositions. The direction is indicated by the small sketches, where red balls represent the requested compositions and the colored balls belong to the respective methods. The colors refer to the used sampling methods, with which new compositions are determined (green for M-CS, turquoise for uniform PCA-CS, pink for normal PCA-CS and yellow for normal-centering PCA-CS). The minimal Euclidean distance (D_{min}) is shown with the white arrow. Red lines, with the corresponding numbers, specify the average D_{min} for each of the applied sampling methods. The results are shown as histogram plots. 1,350 new BRCs are used from each sampling method. The requested compositions consist of 5,900 BRCs.

To evaluate the differences between both minimal-distance-calculations (starting from both directions; Fig. 4.9A,B), one has to keep in mind that the new BRCs are determined within the whole range of initial BRCs. Not all of these initial BRCs are relevant for the current geodynamic simulation. Consequently, composition requests cover most likely never the full parameter space of initial BRCs. Additionally, BRCs are only re-

quested in geodynamic models if they are not used already in the database. Therefore, large differences in the minimal Euclidean distances are expected between newly created and requested compositions. To estimate the predictive power, the minimal Euclidean distances have to be considered that were determined starting from the requested BRCs. For this, all methods show nearly identical results if the initial BRCs were clustered before (Fig. 4.9B, left). To conclude, all sampling methods are equally well suited to predict or at least to compute new compositions which are similar in chemistry to those requested in the geodynamic simulations (Fig. 4.9).

Finally, a combination of the sampling approaches may result in a most complete database to explain the resulting rocks in geodynamic models of magmatic systems. Thus, the sampling guided through the location of unfractionated initial BRCs with M-CS or uniform PCA-CS, produces BRCs with a wider range in chemistry as of those available in the database. This guarantees that even requested BRCs from geodynamic simulations with an unusual chemistry are at least estimated by the phase diagrams of the extended database. For most of the requested BRCs, the initial database might already cover all relevant rock compositions such that new BRCs can be created based on the clustered initial BRC ensemble to improve the results.

4.4.2 Evolution of requested BRCs with an increasing number of available phase diagrams

The differences between requested and available phase diagrams are investigated for a database that contains either 17,088 or 27,049 phase diagrams. Only if those differences are insignificant, the chemical evolution of magmatic systems can be tracked in detail. As rocks are tracked during geodynamic simulations only by the phase diagrams with the closest BRC, differences between requested ("Requested BRCs", Tab. 4.1) and available phase diagrams ("Initial BRCs", Tab. 4.1) become smaller the larger the database is. To quantitatively describe the evolution of requested BRCs, the average D_{min} is computed (Tab. 4.1) between the requested and the initial BRCs for both databases. The extension of the database from 17,088 to 27,049 phase diagrams is based on rock composition requests from geodynamic simulations. The results of the minimal-distance-calculations are shown in Table 4.1, where the maximal D_{min} specifies the maximal Euclidean distance that any requested rock composition can have to the closest already existing composition in the phase diagram database. The average D_{min} is nearly identical for both databases if the minimal Euclidean distances are computed starting from the initial BRCs (Tab. 4.1, top). However, to analyze the evolution of requested compositions, one must focus on the average

D_{min} computed starting from each of the requested compositions. The resulting average D_{min} values (Tab. 4.1, bottom) indicate that requested compositions from geodynamic simulations that use the extended database are more similar to the initial BRCs. The average D_{min} decreases from 1.42 to 0.59, and the maximal D_{min} between requested and existing BRCs decreases from 28.57 to 13.63 (Tab. 4.1).

Furthermore, we collected requested rock compositions from three geodynamic simulations with distinguishable initial model configurations, which were not used before to establish the database. This validates the applicability of the database to other geodynamic models. It is observed that including requested rock compositions from these three simulations does not change the overall results from the minimal-distance-calculations. Thus, we can conclude that the current database (including 27,049 phase diagrams) might cover already most of the relevant bulk rock compositions (BRCs) needed to explain the compositional evolution in crustal magmatic systems with similar model configurations as used in our study. Even if the initial model configuration slightly changes (e.g., the geothermal gradient or the intrusion depth), the BRCs of the phase diagrams cover the relevant rock compositions required in our geodynamic models. It might become critical, if the initial rock composition changes in the geodynamic model, e.g. to a more hydrous one, that may produce distinguishable magmatic rock types. However, before interpreting the rock types generated through any kind of geodynamic simulation, the differences between requested and available rock compositions in the database have to be explored. Only if these differences are negligible for most of the required phase diagrams, the evolution of the chemical and mineralogical compositions is interpretable.

The number of required phase diagrams in a database and with which accuracy the rock properties have to be tracked in geodynamic models can strongly vary depending on the problem that is addressed. Thus, if the main interest is only to estimate the different rock types, larger differences between requested and available phase diagrams may be acceptable, with minimal Euclidean distances of a few wt%. For some problems, this accuracy may not be sufficient, especially if elements with low weight percent affect the mineral assemblage. Here, we suggest that the minimal Euclidean distances should not be larger than 1 wt% on average. However, two aspects must be kept in mind, i) the Euclidean distance represents a sum of all distances between the respective oxides which compensate each other, and ii) the Euclidean distance considers all oxides equally. Oxides with a high concentration (e.g., for SiO_2) can have a major contribution to the Euclidean distance, but its change in concentration may not have a big influence on the phase stability. Thus, even though an Euclidean distance is relatively large, differences in

rock properties between requested and available phase diagrams can be small. For oxides with a low concentration, not sufficiently considering small changes in their concentration might become critical.

Table 4.1: Average and maximal D_{min} between initial BRCs already used in the database and newly requested BRCs from geodynamic simulations. Euclidean distances are computed using equation 4.1. Top: Minimal Euclidean distances are computed from the initial to the requested compositions. Bottom: Minimal Euclidean distances are computed from the requested to the initial compositions. # = number.

# Initial BRCs	# Requested BRCs	Average D_{min} (initial to requested composition)	Maximal D_{min} (initial to requested composition)
17,088	10,063	2.14	21.10
27,049	10,063	2.23	37.80

# Initial BRCs	# Requested BRCs	Average D_{min} (requested to initial composition)	Maximal D_{min} (requested to initial composition)
17,088	10,063	1.42	28.57
27,049	10,063	0.58	13.57

4.4.3 Requested rock compositions and their correlation to melt extraction conditions

During an ongoing geodynamic simulation, new BRCs are requested for residue, dikes or cumulates formed through melt extraction. Thus, each of those requested BRCs was produced under specific physical conditions, e.g. pressure, temperature and melt/crystal fraction. Depending on those conditions and the rock type that has been molten, the chemistry of the requested compositions is strongly variable. How this chemistry changes from geodynamic simulations that use a database consisting of either 17,088 or 27,049 phase diagrams, is evaluated here. In seven geodynamic simulations, a total of ∼10,000 new rock compositions were requested (orange points, Fig. 4.10A1) with an initial database consisting of 17,088 phase diagrams. These ∼10,000 BRCs are used to extend the database from 17,088 to 27,049 phase diagrams. In Figure 4.10, differences between BRCs of the initial and of the extended database are shown (grey and orange points, A1). To test the effect of this extended database on geodynamic models and thus on their rock composition requests, all seven geodynamic simulations are repeated. In this second round, ∼10,000 additional phase diagrams are requested (yellow points, Fig. 4.10A2) not used before in the database. Whereas the requested rock compositions from the first set of runs can still be distinguishable from the initial database, the new rock composition requests from the second set of runs are already quite well represented by the existing ones

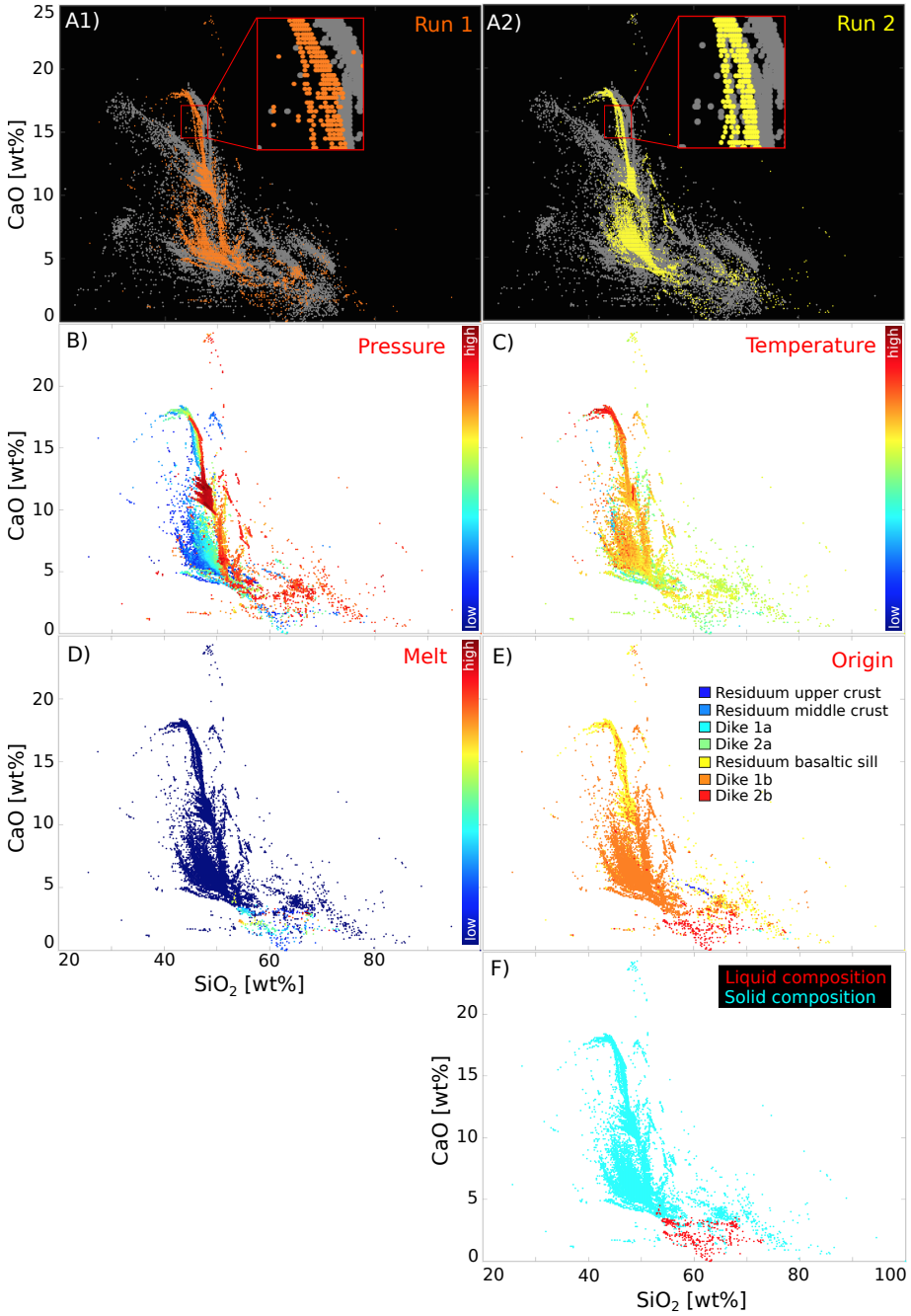

Figure 4.10: Requested BRCs and their melt extraction conditions for the oxide combination, CaO vs. SiO_2. For more oxide combinations, see Figure 4.A9 in the Appendix. A) The requested BRCs are shown for two sets of geodynamic simulations (each of them consists of seven simulations). ~10,000 requested BRCs from both the first set of runs (orange points) and from the second set of runs (yellow points). In grey, BRCs of the database (~17,000 phase diagrams are used for the first and ~27,000 ones for the second round). For each requested composition, melt extraction conditions are presented, with pressure (B), temperature (C) and stable melt fraction (D). The rock phases declaring the origin of the requested BRCs (crustal host rocks, dikes or basaltic sills) are shown in E). "Dike 1" represents the first generation of dikes (or their respective cumulates), from which a second generation ("Dike 2") can form. "a" defines dikes originating from crustal host rocks, and "b" those originating from basaltic injected sills. The information about the type of the composition (liquid or solid fraction) is provided in F).

of the extended database (Fig. 4.10A1–A2). However, it must keep in mind, that new unpredictable compositional branches of the requested BRCs can be produced, which are not even approximately considered in the phase diagram database (e.g., seen in SiO_2 vs. TiO_2, Fig. 4.A9 in the Appendix). In our case, the occurrence of new branches is strongly reduced through the repetition of the geodynamic simulations (e.g., seen in SiO_2 vs. TiO_2 of "Run 2", Fig. 4.A9 in the Appendix). Consequently, extending the database using the autonomous forecast approach is very useful once most of the compositional branches are generated. Therefore, the initial guess of the parameter space is crucial to generate all relevant rock compositions required in petro-thermo-mechanical models of magmatic systems.

To describe the origin of requested compositions (especially for newly generated compositional branches), we visualize their melt extraction conditions as well (Fig. 4.10). Here, the residuum is the leftover after melt extraction and is thus described by the solid phase, whereas the extracted melt is characterized through the liquid composition (Fig. 4.10F). For each dike, it is known at which pressure and temperature and thus melt fraction (Fig. 4.10B–D) its melt composition was stable. Additionally, the rock phase is known for which the BRCs were requested (Fig. 4.10E). The dikes originate either from a partially molten host rock, from a partially crystallized basaltic sill, or even from a previously formed dike if its residual melt fraction is sufficiently high to be extracted. The stable melt fraction and the type of the requested rock composition (liquid or solid composition) is correlated, as the residuum compositions coexist with low residual melt fractions (the non-extractable amount of 0.5 vol%) (Fig. 4.10D,F).

4.4.4 Correlation between clustering, chemistry and melt extraction conditions

The correlation between rock compositions and their formation conditions is tested by applying the clustering algorithm to requested BRCs from geodynamic simulations. If such a correlation exists, the formation conditions such as pressure, temperature, melt/crystal fraction and the type of composition (solid vs. liquid fraction) must be clustered as well, although only the chemistry is provided to the clustering algorithm.

To test this assumption, requested rock compositions are used from 14 geodynamic simulations. It is observed that the clustering algorithm not only provides groups of similar compositions but also correlates them to their formation conditions, especially for small clusters, highlighted with circles in Figure 4.11. Only if many BRCs form a continuously compositional trend, they may merge together forming one big cluster (cluster 27, Fig.

4.11A). Due to the gradual change in rock chemistry in such a big cluster, the related parameters (e.g., P and T) are more variable as well (Fig. 4.11C–D).

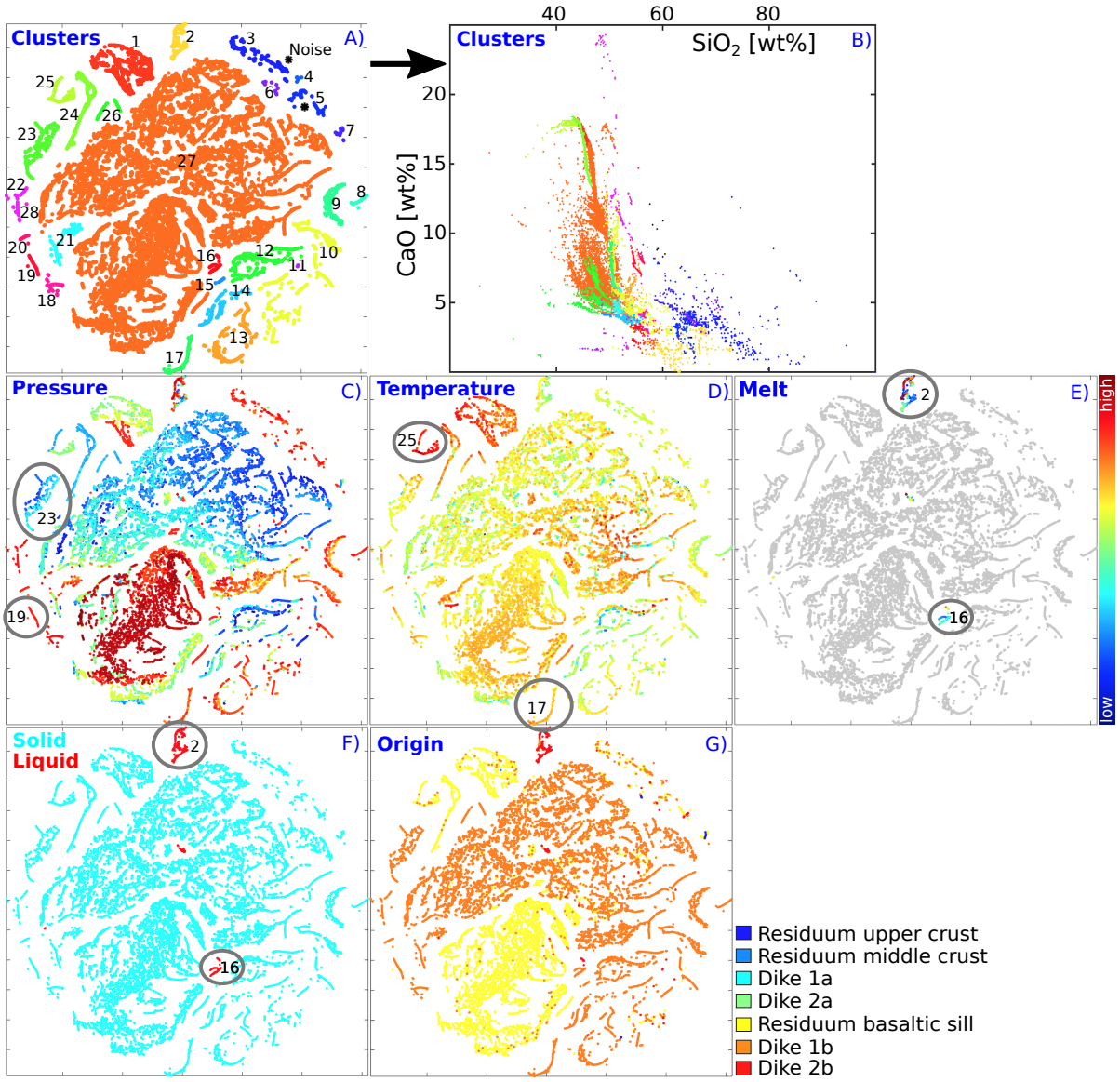

Figure 4.11: A) Requested BRCs (~22,500 in total) from 14 geodynamic simulations are clustered into 28 groups, visualized as 2D representation of the Barnes-Hut t-SNE projection showing the relative coordinates of the data points. Colors show clustering results using DBSCAN applied to the ensemble in the projection space. B) Each group contains specific BRCs, shown for the oxide combination CaO vs. SiO_2. Each BRC is related to an equilibrium pressure, temperature and melt fraction conditions (C–E) at which it was generated. The information about the type of the composition (liquid or solid fraction) is provided in F). The rock phases declaring the origin of the requested compositions (crustal host rocks, dikes or basaltic sills) are shown in G). "Dike 1" represents the first generation of dikes (or their respective cumulates), from which a second generation ("Dike 2") can form. "a" defines dikes originating from the crustal host rocks, and "b" those originating from basaltic injected sills.

4.4.5 Applicability of the phase diagram database

The applicability of the phase diagram database is visualized on a TAS (total alkali-silica) diagram for plutonic rocks (Fig. 4.12). The 27,049 BRCs of the database cover nearly all relevant igneous rock types and especially along magma differentiation trends their density is high (Fig. 4.12). Melt is extracted in our geodynamic models from a source that is basaltic in composition (gabbro) to form higher differentiated rocks such as monzonite, quartz monzonite or granite. The related cumulates form a reverse trend towards lower SiO_2 concentrations (peridotgabbro or even more depleted). The BRCs of the database originate either from requested rock compositions of the geodynamic simulations or from our autonomous forecast approach, and are well located on liquid lines of descent of natural igneous rock suites (green arrows, Fig. 4.12). The liquid line of descent describes the way the liquid composition changes as crystallization proceeds. Thus, the database is suitable to model magmatic processes with a high precision. Small changes within the same rock type can be tracked as well. Repeating geodynamic simulations with this extended database consisting of 27,049 BRCs, indicates that the new requested rock compositions are almost perfectly explained by the existing ones in the database (red and black symbols, Fig. 4.12). Therefore, although the number of new requested rock compositions is high ($>$ 10,000) they are not required to extend the database, as the evolution of rocks can be tracked already with a sufficient precision. Applying the forecast approach to this database shows that most of the new BRCs have similar compositions like the ones in the database, with a wider scattering for a few samples (Fig. 4.12). Comparing them with requested rock compositions indicates that ca. half of the new BRCs may be irrelevant for the geodynamic forward models, as requested BRCs occur in a much narrower range (Fig. 4.12). Thus, applying the sampling approaches generates new BRCs that were potentially relevant in older geodynamic simulations, but not all of them in the current ones which were based on 27,049 initial BRCs. This results from the fact that the database was initially constructed with requested rock compositions which were mostly not based on a sufficiently accurate phase diagram. With the extension of the database, the differences between requested and available phase diagrams have been decreased. Therefore, one could guide the sampling through the location of the requested BRCs to focus the sampling on the more relevant part of the oxide parameter space, but it would strongly limit the compositional range of future rock composition requests.

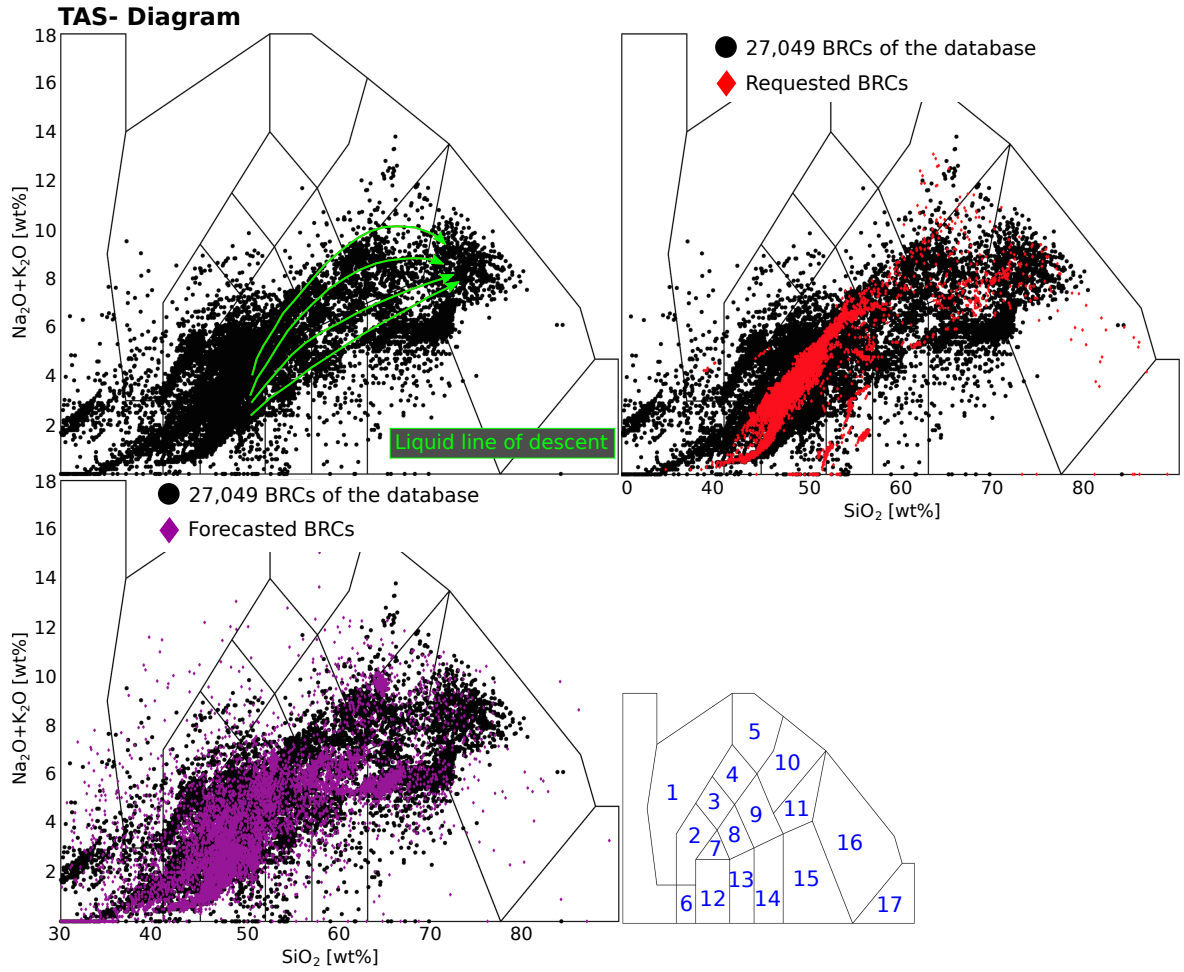

Figure 4.12: Requested, forecasted and database BRCs shown on a TAS diagram (normalized without water) for plutonic rocks (after Middlemost, 1994). 27,049 BRCs of the database (black points), requested BRCs from geodynamic simulations that use this database (red diamonds; 13,029 in total) and forecasted BRCs using the sampling approaches (purple diamonds; 9148 in total). 1: Foidolite; 2: Foid Gabbro; 3: Foid Monzodiorite; 4: Foid Monzosyenite; 5: Foid Syenite; 6: Peridotgabbro; 7: Monzogabbro; 8: Monzodiorite; 9: Monzonite; 10: Syenite; 11: Quartz Monzonite; 12: Gabbro; 13: Gabbroic Diorite; 14: Diorite; 15: Granodiorite; 16: Granite; 17: Quartzolite. Liquid lines of descent are presented as green arrows for different igneous rock suites after Middlemost (1994).

4.5 CONCLUSION

The efficient establishment of a phase diagram database is crucial to investigate the chemical evolution of magmatic systems in petro-thermo-mechanical models. To establish such a comprehensive database, bulk rock compositions (BRCs) must be collected to compute phase diagrams for each chemical state. To avoid such a collection exclusively from geodynamic simulations, a forecast approach is developed that creates new BRCs automatically. BRCs are determined using either manually constrained sampling (M-CS) or sampling

that is based on principal components (PCA-CS). To better focus the sampling on individual compositional branches of the initial data set (initial BRCs), the whole sampling space is split into smaller fractions similar rock compositions (clusters). This is done by applying Barnes-Hut t-SNE in combination with DBSCAN. Depending on the employed sampling technique and on whether a clustering algorithm is applied, the sampling results vary regarding predicting requested BRCs from geodynamic simulations. The main findings of this study are:

1) M-CS and uniform PCA-CS create new BRCs that are uniformly distributed over the sampling space considering its extreme oxide concentrations.

2) PCA-CS with a normal distribution locates most of the new BRCs in the center of mass of initial BRCs and thus gives less weight to the marginal parameter space.

3) Outliers in the initial BRC ensemble can strongly affect the sampling results, if the range for the sampling is specified by the extreme oxide concentrations and does not follow a Gaussian distribution.

4) Applying the sampling approaches to the clustered initial BRC ensemble, new BRCs are emplaced much closer to the existing data set for all sampling methods.

5) BRCs of requested phase diagrams are well explained by BRCs determined with the sampling approaches applied to the clustered initial BRC ensemble.

6) Differences between requested and available phase diagrams become smaller the more the database is extended.

Applying the clustering algorithm to the requested BRCs indicates a clear correlation between rock compositions and their formation conditions (pressure, temperature, melt fraction and solid vs. liquid origin), although only the chemistry is provided to the clustering algorithm. Thus, new BRCs represent rock compositions which were produced under specific physical conditions and they can be used to compute required phase diagrams of arc-related magmatism avoiding the time-consuming repetition of geodynamic simulations.

4.6 ACKNOWLEDGEMENTS

Funding was provided by the VAMOS Research Center, University of Mainz (Germany). We would like to thank the ZDV at the University of Mainz to provide us computational

time on MOGON I to invoke parallel computations of Perple_X. We also acknowledge funding by the ERC Consolidator Grant MAGMA (project #71143).

4.7 APPENDIX

Selected figures of the paper are extended by further oxide combinations. Figures 4.A1–4.A4 belong to Figure 4.5, in which new BRCs are determined for unfractionated initial BRCs using M-CS or PCA-CS (uniform, normal and normal-centering PCA-CS). Figures 4.A5–4.A8 are the extension of Figure 4.7 (Cluster 11) and show the distribution of new BRCs for clustered initial BRCs. Figures 4.A9 and 4.A10 show the requested rock compositions for two sets of geodynamic simulations and their melt extraction conditions, for each SiO_2-combination, as extension of Figure 4.10.

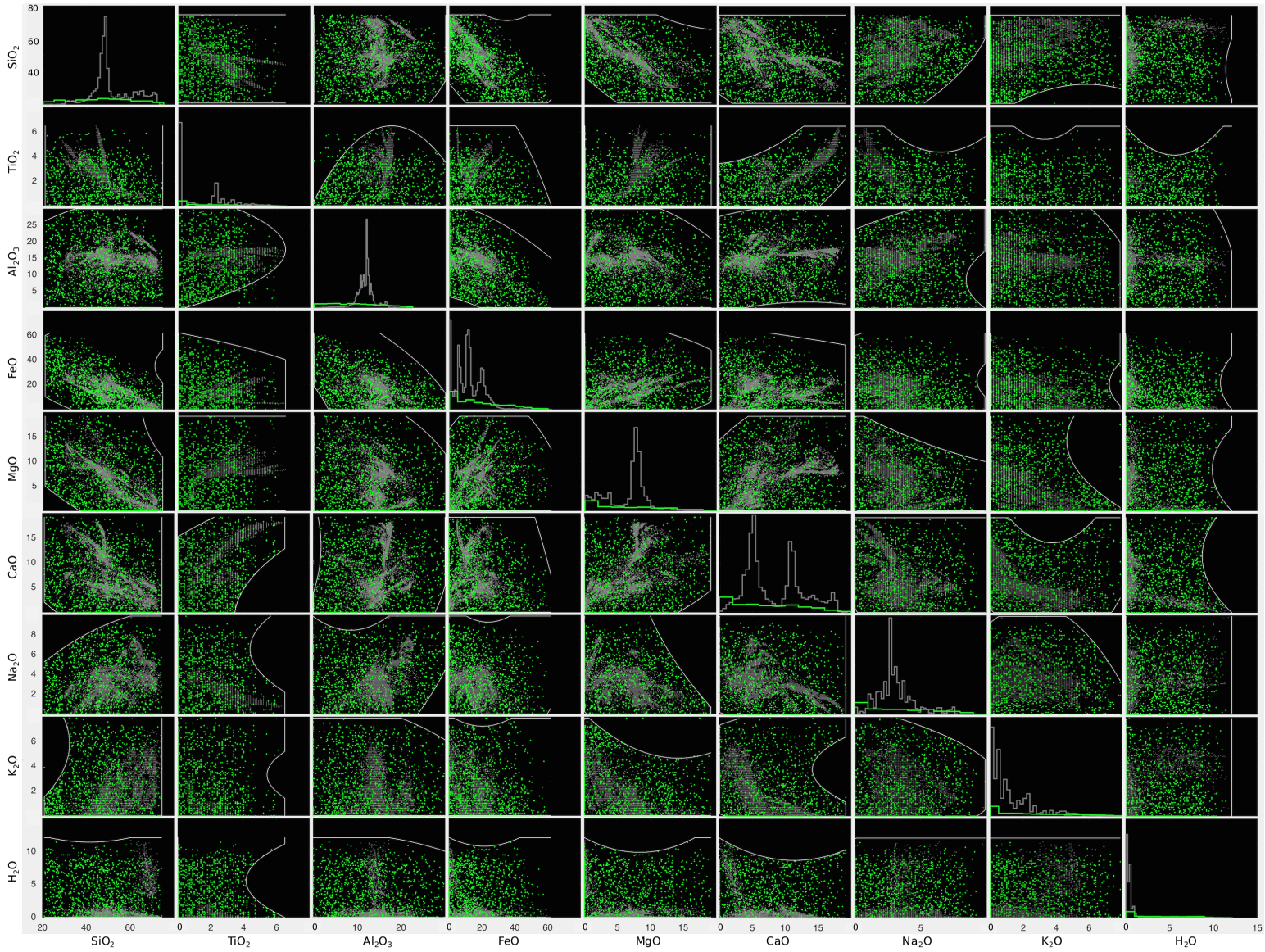

Figure 4.A1: Around 1,350 new BRCs are created between manually constrained boundaries (white lines). The initial data (grey points, 17,088 BRCs) are not clustered here. Within the manually constrained boundaries, new oxide concentrations are randomly determined, indicated as green points. Oxides are given in wt%. This is an extension of Figure 4.5.

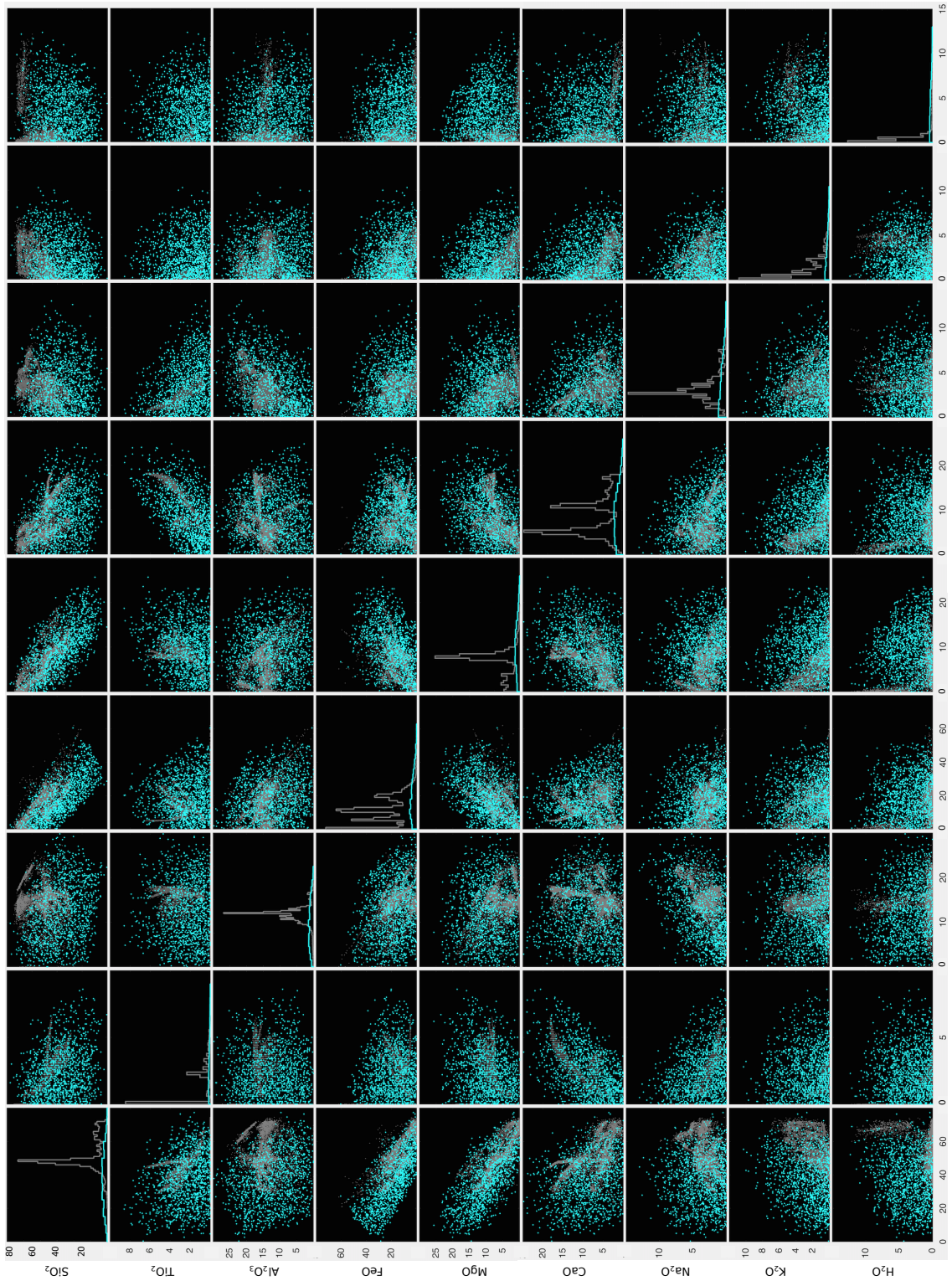

Figure 4.A2: Around 1,350 new BRCs are randomly determined using the uniform PCA-CS. The initial data (grey points, 17,088 BRCs) are not clustered here. Oxides are given in wt%. This is an extension of Figure 4.5.

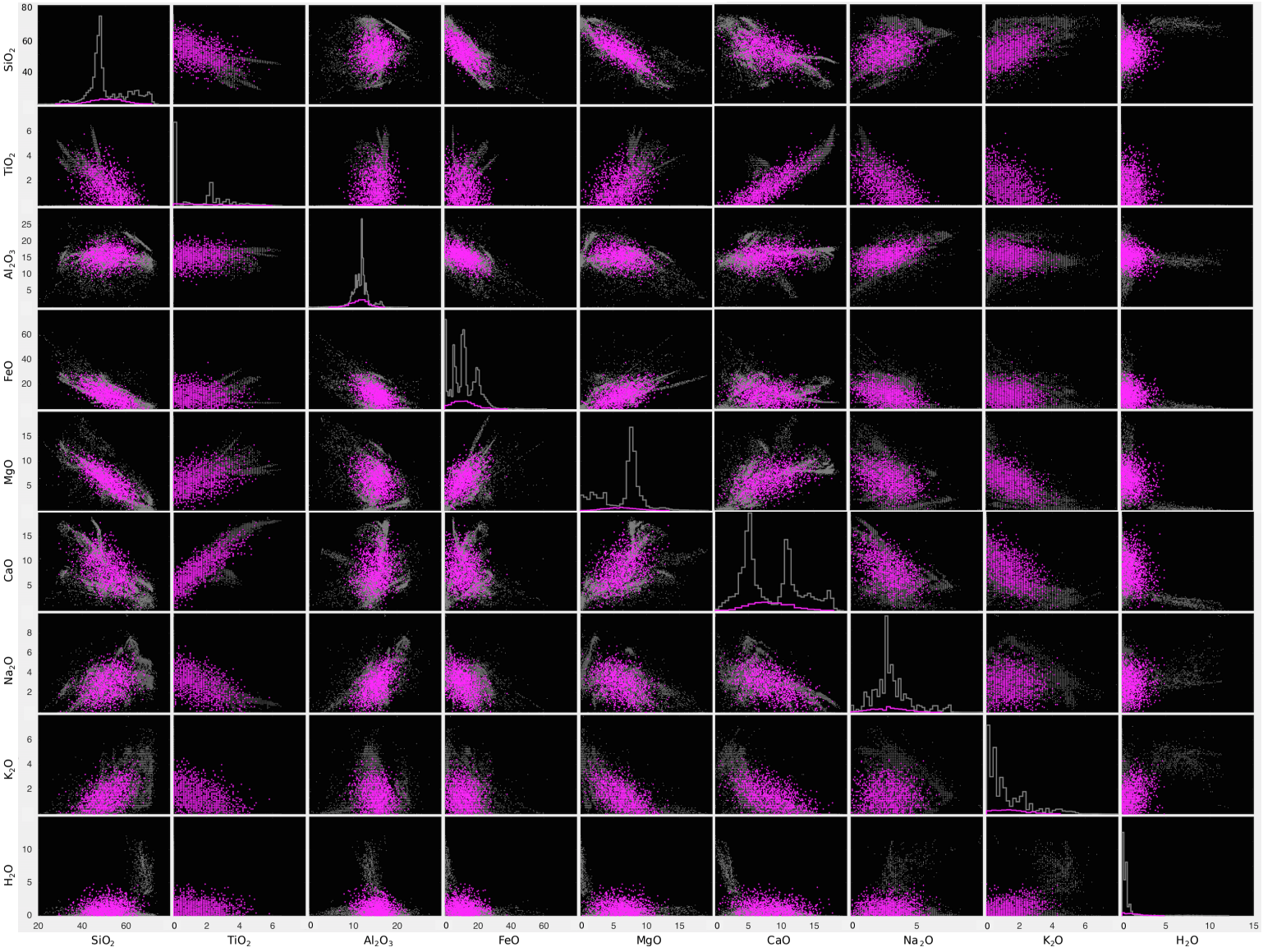

Figure 4.A3: Around 1,350 new BRCs are randomly determined using the normal PCA-CS. The initial data (grey points, 17,088 BRCs) are not clustered here. Oxides are given in wt%. This is an extension of Figure 4.5.

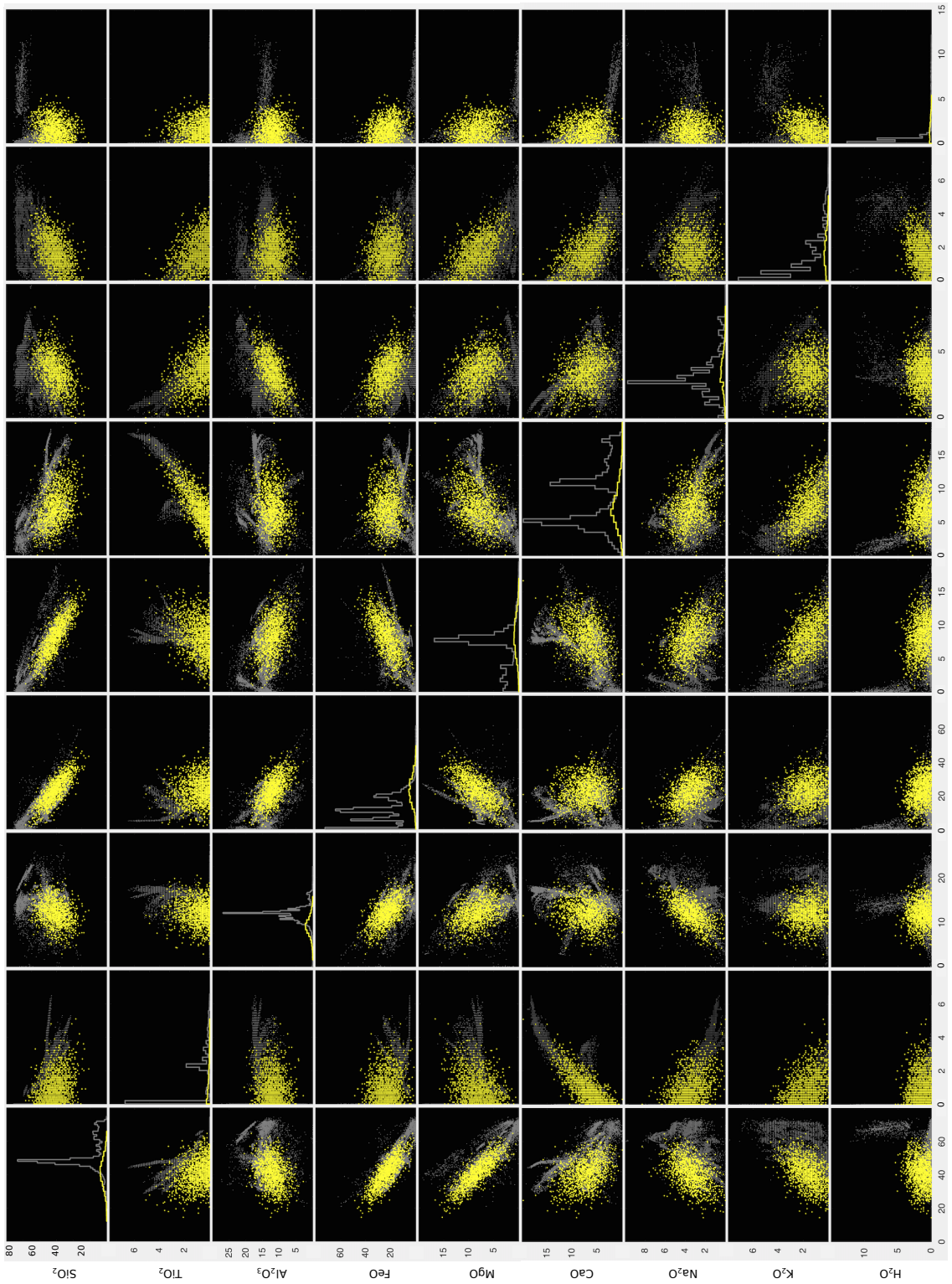

Figure 4.A4: Around 1,350 new BRCs are randomly determined using the normal-centering PCA-CS. The initial data (grey points, 17,088 BRCs) are not clustered here. Oxides are given in wt%. This is an extension of Figure 4.5.

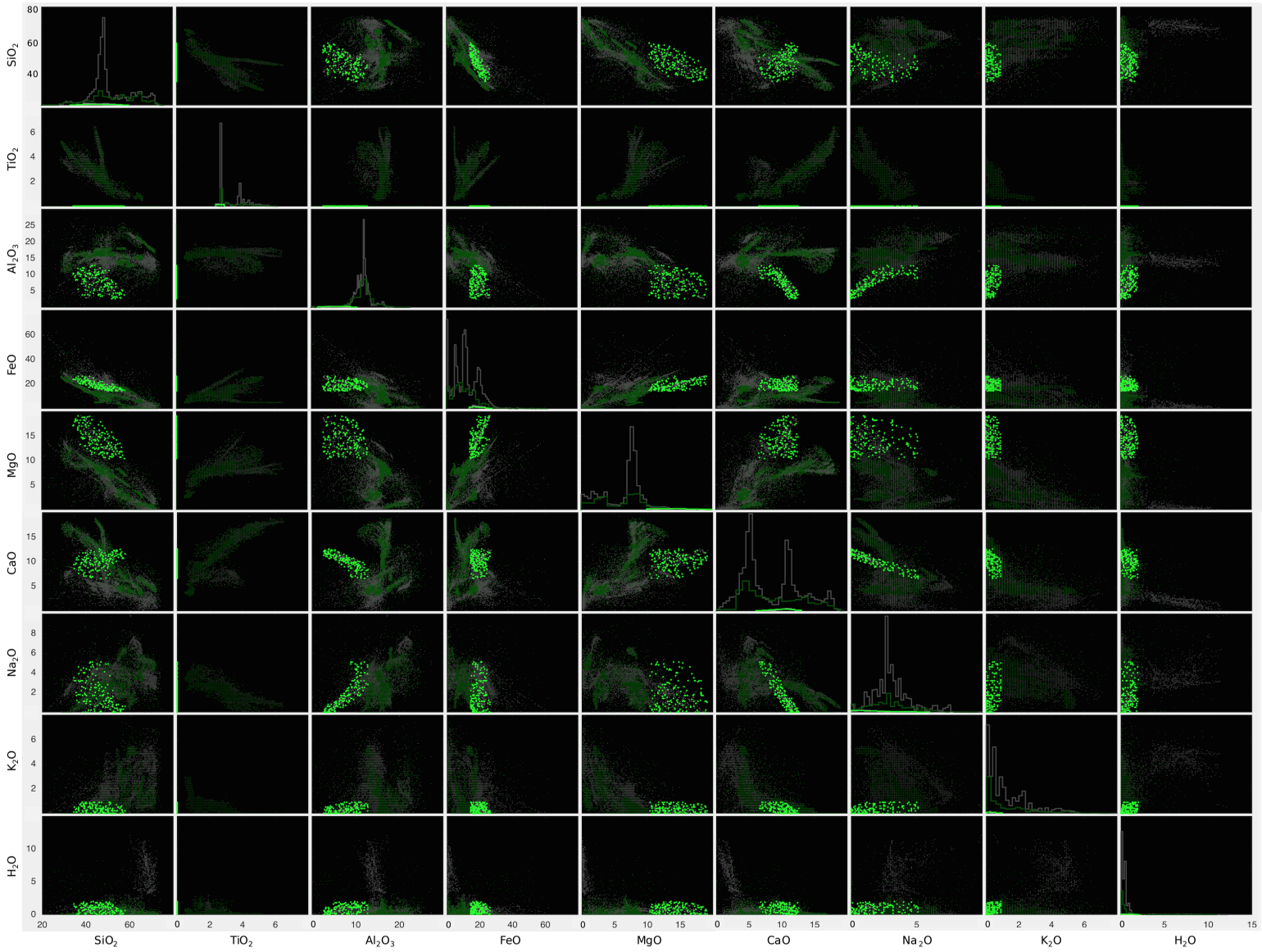

Figure 4.A5: Around 150 new BRCs are generated for cluster 11 (Fig. 4.2 and Fig. 4.6) and are highlighted here. 17,088 BRCs are used for the clustering (grey points), 226 of them are in cluster 11, the rest is allocated to other clusters (not highlighted). New oxide concentrations are randomly created (green points) within the manually constrained boundaries (white lines). The lines are the shifted polynomial fitting line through the initial data (here, 2nd degree polynomial) and are limited to the maximum and minimum concentrations of the initial BRCs. Oxides are given in wt%. This is an extension of Figure 4.7.

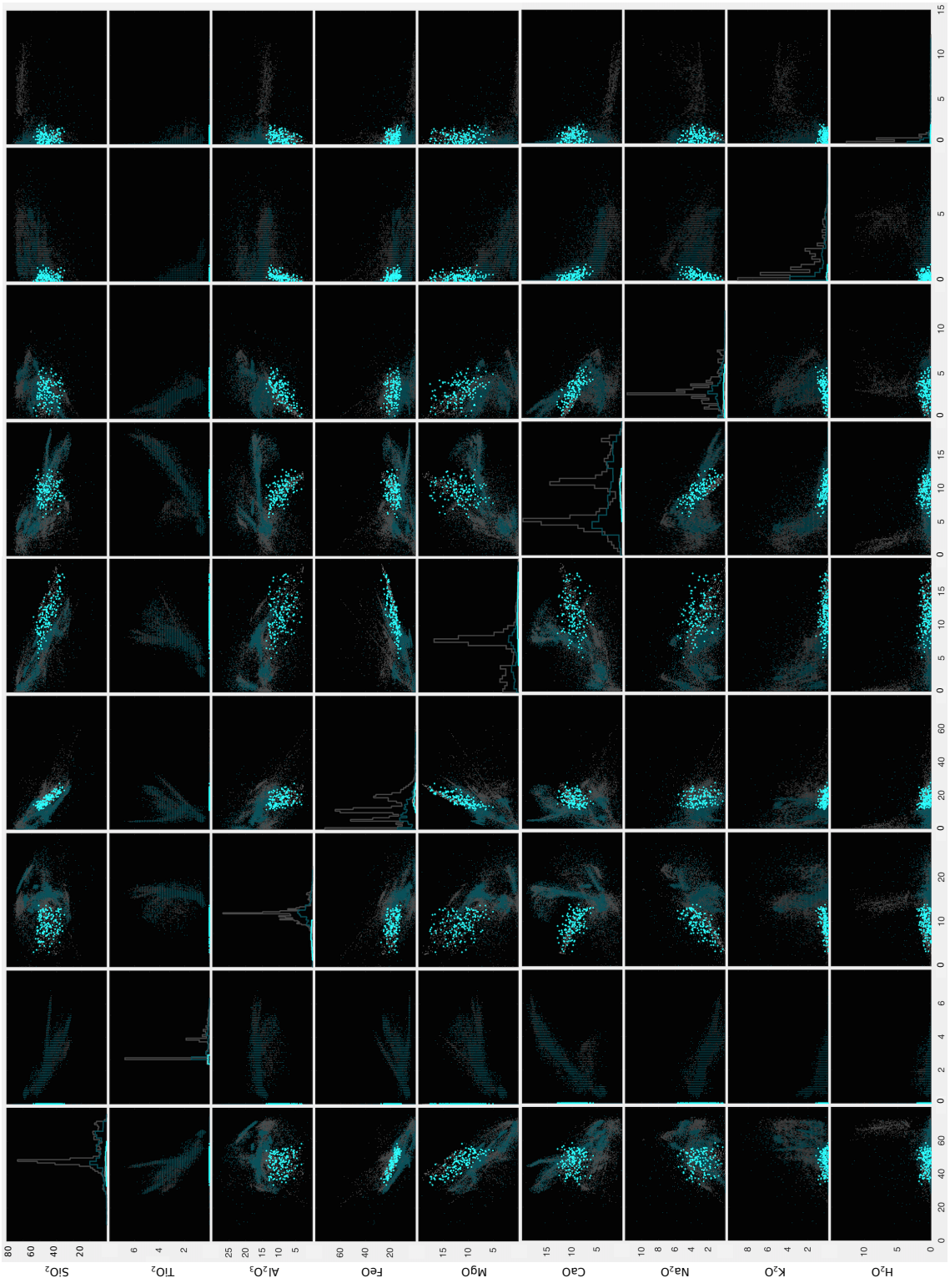

Figure 4.A6: Around 150 new BRCs are generated for cluster 11 (Fig. 4.2 and Fig. 4.6) and are highlighted here. 17,088 BRCs are used for the clustering (grey points), 226 of them are in cluster 11, the rest is allocated to other clusters (not highlighted). New oxide concentrations are randomly created using uniform PCA-CS. Oxides are given in wt%. This is an extension of Figure 4.7.

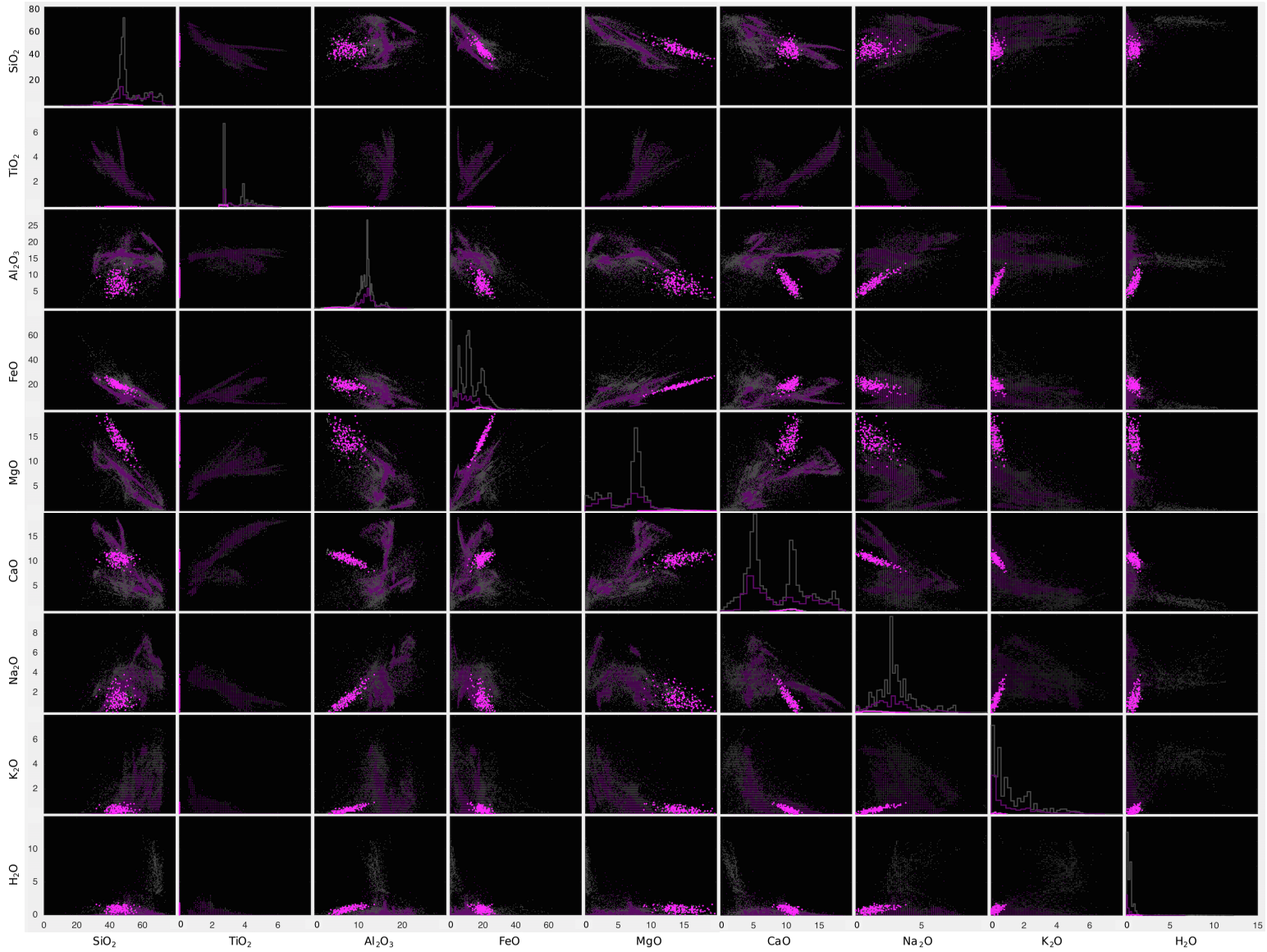

Figure 4.A7: Around 150 new BRCs are generated for cluster 11 (Fig. 4.2 and Fig. 4.6) and are highlighted here. 17,088 BRCs are used for the clustering (grey points), 226 of them are in cluster 11, the rest is allocated to other clusters (not highlighted). New oxide concentrations are randomly created using normal PCA-CS. Oxides are given in wt%. This is an extension of Figure 4.7.

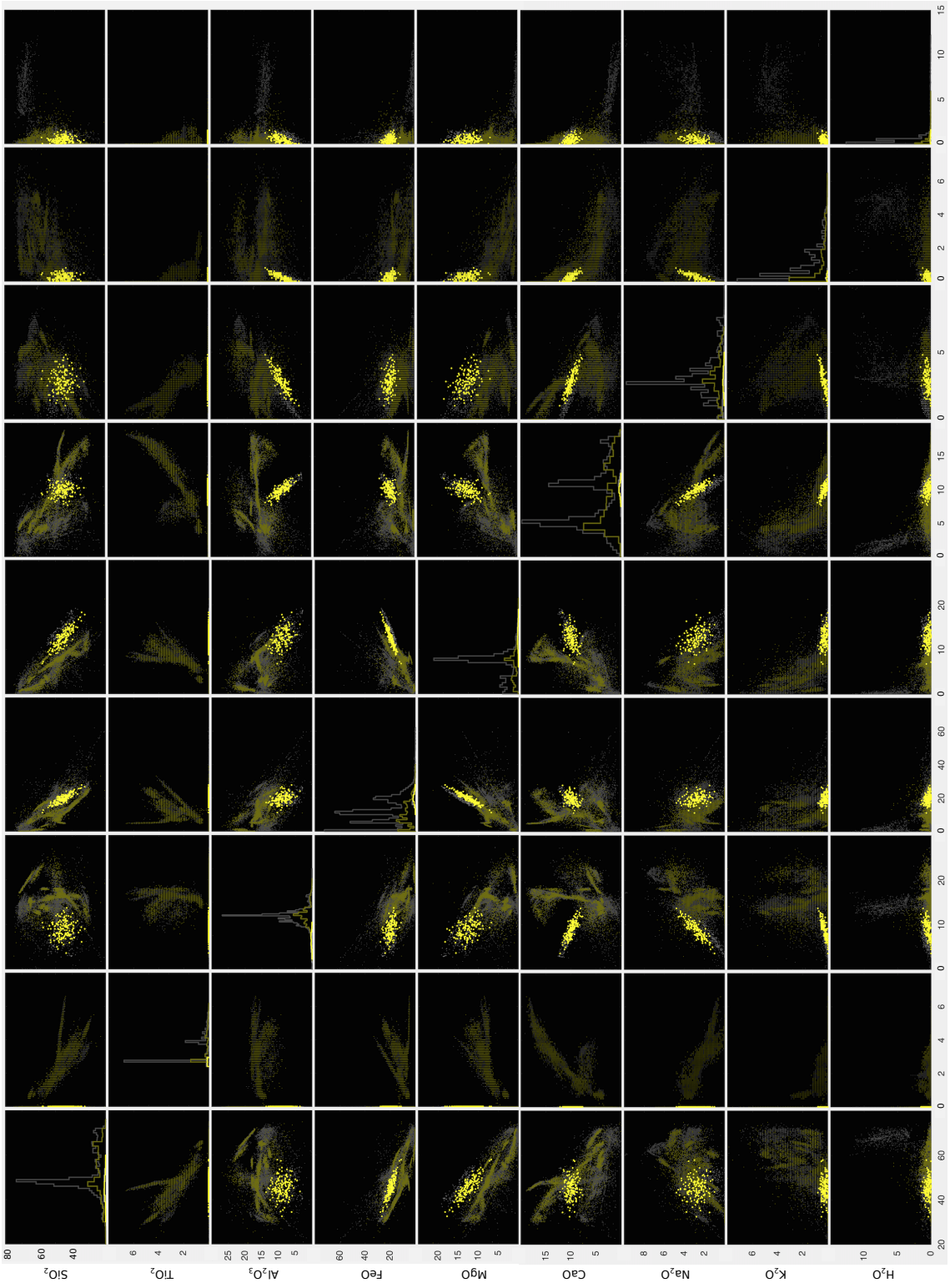

Figure 4.A8: Around 150 new BRCs are generated for cluster 11 (Fig. 4.2 and Fig. 4.6) and are highlighted here. 17,088 BRCs are used for the clustering (grey points), 226 of them are in cluster 11, the rest is allocated to other clusters (not highlighted). New oxide concentrations are randomly created using normal-centering PCA-CS. Oxides are given in wt%. This is an extension of Figure 4.7.

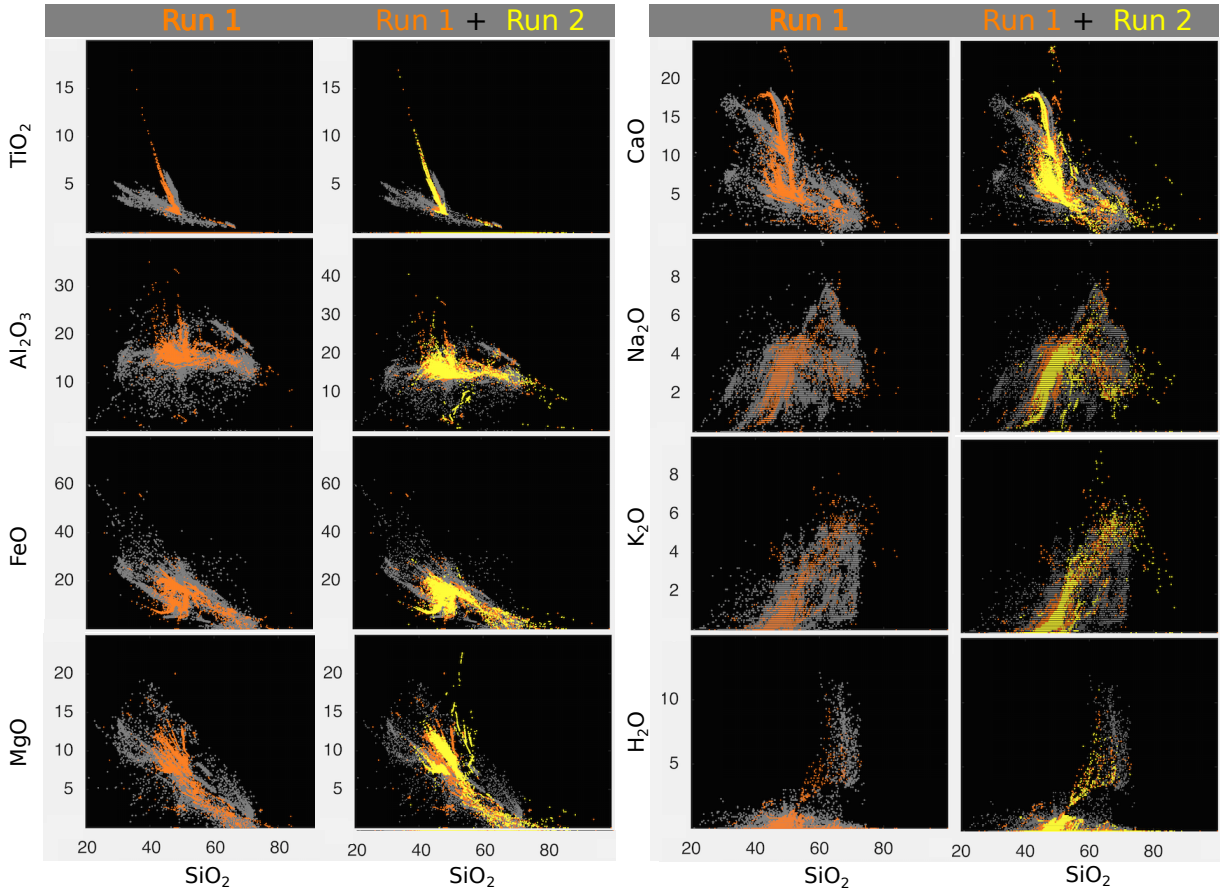

Figure 4.A9: Requested BRCs are shown for two sets of geodynamic simulations (each of them consists of seven simulations). ~10,000 requested BRCs from both the first set of runs (orange points) and from the second set of runs (yellow points). Grey points indicate the initial BRCs of the database. The compositions are shown for all SiO_2 oxide combinations. Oxides are given in wt%. This is an extension of Figure 4.10.

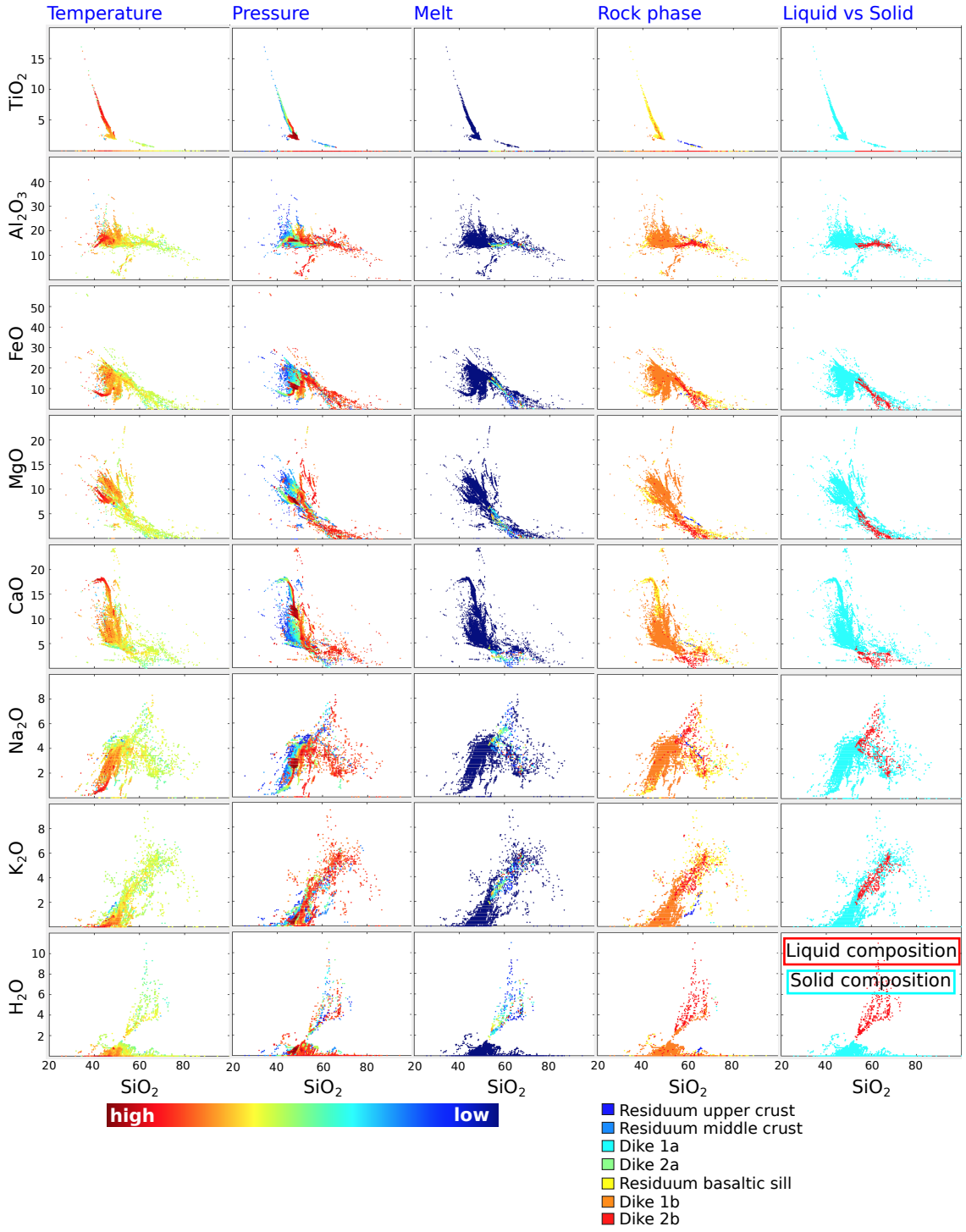

Figure 4.A10: Melt extraction conditions of requested BRCs from geodynamic simulations, for all SiO_2 oxide combinations. For each liquid (extracted melt) or solid composition (remaining residual material), the conditions are stored at which their compositions are stable, with pressure, temperature and stable melt fraction. The rock phases declaring the origin of the requested compositions (crustal host rocks, dikes or basaltic sills) are shown. "Dike 1" represents the first generation of dikes (or their respective cumulates), from which a second generation ("Dike 2") can form. "a" defines dikes originating from the crustal host rocks, and "b" those originating from basaltic injected sills. The information about the type of the composition (liquid or solid fraction) is provided in the last column. Oxides are given in wt%. This is an extension of Figure 4.10.

REFERENCES

Afonso, J., Fullea, J., Griffin, W., Yang, Y., Jones, A., D Connolly, J., O'Reilly, S., 2013. 3-D multiobservable probabilistic inversion for the compositional and thermal structure of the lithosphere and upper mantle. I: A priori petrological information and geophysical observables. Journal of Geophysical Research: Solid Earth 118 (5), 2586–2617.

Afonso, J. C., Zlotnik, S., Díez, P., 2015. An efficient and general approach for implementing thermodynamic phase equilibria information in geophysical and geodynamic studies. Geochemistry, Geophysics, Geosystems 16 (10), 3767–3777.

Barnes, J., Hut, P., 1986. A hierarchical O (N log N) force-calculation algorithm. nature 324 (6096), 446.

Connolly, J., 2009. The geodynamic equation of state: what and how. Geochemistry, Geophysics, Geosystems 10 (10).

Connolly, J. A., 2005. Computation of phase equilibria by linear programming: a tool for geodynamic modeling and its application to subduction zone decarbonation. Earth and Planetary Science Letters 236 (1), 524–541.

de Capitani, C., Petrakakis, K., 2010. The computation of equilibrium assemblage diagrams with Theriak/Domino software. American Mineralogist 95 (7), 1006–1016.

Duesterhoeft, E., Quinteros, J., Oberhaensli, R., Bousquet, R., de Capitani, C., 2014. Relative impact of mantle densification and eclogitization of slabs on subduction dynamics: A numerical thermodynamic/thermokinematic investigation of metamorphic density evolution. Tectonophysics 637, 20–29.

Ester, M., Kriegel, H.-P., Sander, J., Xu, X., et al., 1996. A density-based algorithm for discovering clusters in large spatial databases with noise. In: Kdd. Vol. 96. pp. 226–231.

Faccenda, M., Dal Zilio, L., 2017. The role of solid–solid phase transitions in mantle convection. Lithos 268, 198–224.

Gerya, T. V., Meilick, F., 2011. Geodynamic regimes of subduction under an active margin: effects of rheological weakening by fluids and melts. Journal of Metamorphic Geology 29 (1), 7–31.

Ghiorso, M. S., Hirschmann, M. M., Reiners, P. W., Kress III, V. C., 2002. The pMELTS: A revision of MELTS for improved calculation of phase relations and major element partitioning related to partial melting of the mantle to 3 GPa. Geochemistry, Geophysics, Geosystems 3 (5), 1–35.

Ghiorso, M. S., Sack, R. O., 1995. Chemical mass transfer in magmatic processes IV. A revised and internally consistent thermodynamic model for the interpolation and extrapolation of liquid-solid equilibria in magmatic systems at elevated temperatures and pressures. Contributions to Mineralogy and Petrology 119 (2-3), 197–212.

Green, E., White, R., Diener, J., Powell, R., Holland, T., Palin, R., 2016. Activity–composition relations for the calculation of partial melting equilibria in metabasic rocks. Journal of Metamorphic Geology 34 (9), 845–869.

Gropp, W. D., Gropp, W., Lusk, E., Skjellum, A., 1999. Using MPI: portable parallel programming with the message-passing interface. Vol. 1. MIT press.

Gualda, G. A., Ghiorso, M. S., Lemons, R. V., Carley, T. L., 2012. Rhyolite-MELTS: a modified calibration of MELTS optimized for silica-rich, fluid-bearing magmatic systems. Journal of Petrology 53 (5), 875–890.

Hebert, L. B., Antoshechkina, P., Asimow, P., Gurnis, M., 2009. Emergence of a low-viscosity channel in subduction zones through the coupling of mantle flow and thermodynamics. Earth and Planetary Science Letters 278 (3-4), 243–256.

Hinton, G. E., Roweis, S. T., 2003. Stochastic neighbor embedding. In: Advances in neural information processing systems. pp. 857–864.

Holland, T. J., Green, E. C., Powell, R., 2018. Melting of peridotites through to granites: a simple thermodynamic model in the system KNCFMASHTOCr. Journal of Petrology.

Hotelling, H., 1933. Analysis of a complex of statistical variables into principal components. Journal of educational psychology 24 (6), 417.

Jennings, E. S., Holland, T. J., 2015. A simple thermodynamic model for melting of peridotite in the system NCFMASOCr. Journal of Petrology 56 (5), 869–892.

Kaus, B. J., 2010. Factors that control the angle of shear bands in geodynamic numerical models of brittle deformation. Tectonophysics 484 (1), 36–47.

Kaus, B. J., Connolly, J. A., Podladchikov, Y. Y., Schmalholz, S. M., 2005. Effect of mineral phase transitions on sedimentary basin subsidence and uplift. Earth and Planetary Science Letters 233 (1-2), 213–228.

Maaten, L. v. d., Hinton, G., 2008. Visualizing data using t-SNE. Journal of machine learning research 9 (Nov), 2579–2605.

MacQueen, J., et al., 1967. Some methods for classification and analysis of multivariate observations. In: Proceedings of the fifth Berkeley symposium on mathematical statistics and probability. Vol. 1. Oakland, CA, USA, pp. 281–297.

Magni, V., Bouilhol, P., van Hunen, J., 2014. Deep water recycling through time. Geochemistry, Geophysics, Geosystems 15 (11), 4203–4216.

Middlemost, E. A., 1994. Naming materials in the magma/igneous rock system. Earth-Science Reviews 37 (3-4), 215–224.

Nakagawa, T., Tackley, P. J., Deschamps, F., Connolly, J. A., 2009. Incorporating self-consistently calculated mineral physics into thermochemical mantle convection simulations in a 3-D spherical shell and its influence on seismic anomalies in Earth's mantle. Geochemistry, Geophysics, Geosystems 10 (3).

Oliveira, B., Afonso, J. C., Zlotnik, S., Diez, P., 2017. Numerical modelling of multiphase multicomponent reactive transport in the Earths interior. Geophysical Journal International 212 (1), 345–388.

Powell, R., Holland, T., 1988. An internally consistent dataset with uncertainties and correlations: 3. Applications to geobarometry, worked examples and a computer program. Journal of metamorphic Geology 6 (2), 173–204.

Riel, N., Bouilhol, P., van Hunen, J., Cornet, J., Magni, V., Grigorova, V., Velic, M., 2018. Interaction between mantle-derived magma and lower arc crust: quantitative reactive

melt flow modelling using STyx. Geological Society, London, Special Publications 478, SP478–6.

Rummel, L., Kaus, B. J., White, R. W., Mertz, D. F., Yang, J., Baumann, T. S., 2018. Coupled petrological-geodynamical modeling of a compositionally heterogeneous mantle plume. Tectonophysics 723, 242–260.

Rüpke, L. H., Morgan, J. P., Hort, M., Connolly, J. A., 2004. Serpentine and the subduction zone water cycle. Earth and Planetary Science Letters 223 (1-2), 17–34.

Steinhaus, H., 1956. Sur la division des corp materiels en parties. Bull. Acad. Polon. Sci 1 (804), 801.

Thielmann, M., Kaus, B. J., 2012. Shear heating induced lithospheric-scale localization: Does it result in subduction? Earth and Planetary Science Letters 359, 1–13.

Tirone, M., Ganguly, J., Morgan, J., 2009. Modeling petrological geodynamics in the Earth's mantle. Geochemistry, Geophysics, Geosystems 10 (4).

Van Der Maaten, L., 2014. Accelerating t-SNE using tree-based algorithms. Journal of machine learning research 15 (1), 3221–3245.

White, R., Powell, R., Holland, T., 2001. Calculation of partial melting equilibria in the system Na2O–CaO–K2O–FeO–MgO–Al2O3–SiO2–H2O (NCKFMASH). Journal of Metamorphic Geology 19 (2), 139–153.

White, R., Powell, R., Holland, T., Johnson, T., Green, E., 2014. New mineral activity–composition relations for thermodynamic calculations in metapelitic systems. Journal of Metamorphic Geology 32 (3), 261–286.

Yamato, P., Agard, P., Burov, E., Le Pourhiet, L., Jolivet, L., Tiberi, C., 2007. Burial and exhumation in a subduction wedge: Mutual constraints from thermomechanical modeling and natural P-T-t data (Schistes Lustrés, western Alps). Journal of Geophysical Research: Solid Earth 112 (B7).

CHAPTER 5

INSIGHTS INTO THE COMPOSITIONAL EVOLUTION OF CRUSTAL MAGMATIC SYSTEMS FROM COUPLED PETROLOGICAL-GEODYNAMICAL MODELS

Abstract The evolution of crustal magmatic systems is incompletely understood, as most studies are limited either by their temporal or spatial resolution. Exposed plutonic rocks represent the final stage of a long term evolution punctuated by several magmatic events with different chemistry and generated under different mechanical conditions. Although the final state can be easily described, the nature of each magmatic pulse is hampered. This study presents a new method to investigate the compositional evolution of plutonic systems while considering thermal and mechanical processes. A thermomechanical code (MVEP2) extended by a semi-analytical dike/sill formation algorithm, is combined with a thermodynamic modeling approach (Perple_X) to investigate the feedback between petrology and mechanics. Melt is extracted to form dikes while depleting the source region. The evolving rock compositions are tracked on markers using a different phase diagram for each petrological composition. The rock compositional evolution is thus tracked with a high precision by means of a database with more than 50,000 phase diagrams. This database is able to describe how density, melt fraction, the chemical composition of melt and solid fractions and mineralogical assemblages change over crustal to uppermost mantle P–T conditions for a large range of rock compositions. Each bulk rock composition is composed of the 10 major oxides (SiO_2–TiO_2–Al_2O_3–Cr_2O_3–MgO–FeO–CaO–Na_2O–K_2O–H_2O) including an oxygen buffer. The combined modeling approach is applied to study

the chemical evolution of the crust during arc magmatism and related melt extraction and magma mixing processes. Basaltic sills are periodically injected into the crust to model heat influx from the mantle. Accumulated sills turn into long-lived mush chambers by using a lower rock cohesion or due to high intrusion depths. The resulting melts can be highly evolved and are extracted to form dikes in the overlying crust. Associated partial melting of crustal host rocks is promoted by the water amount, and occurs around dense distributed dikes and sills. High silica rocks (e.g. granites) are generated by partial melting of the host rocks, melt segregation within dikes, and from fractional crystallization of basalts. For the genesis of arc continental crust are these highly in silica enriched rocks only of minor relevance, as mafic to intermediate rocks dominate.

5.1 INTRODUCTION

The prevailing views about the existence of long-lived, liquid-dominated magma chambers, evolved drastically in the last decades. It is widely accepted that a crust-wide dike and sill network exists, with magma storage levels from the uppermost mantle to the upper crust (e.g. Cashman et al., 2017; Putirka, 2017). Different numerical and geochemical studies of exposed lower arc crust indicate that the magma reservoir is composed of several magma pulses, and thus formed incrementally (e.g. Leuthold et al., 2012; Blundy and Annen, 2016; Coleman et al., 2016). It is assumed that a magma reservoir is most of its time in a mush-like state consisting of melt within a pervasive crystalline framework (Bachmann and Bergantz, 2004; Bergantz et al., 2015), with only few percent of melt (e.g. Huang et al., 2015), forming only ephemerally eruptable, liquid-dominated bodies (e.g. Putirka, 2017; Cooper, 2017; Sparks and Cashman, 2017). The long-lived mush chambers may be formed by one of the two following mechanisms: incremental intrusion of magma into sub-solidus rocks, or melt segregation and rapid merging of melt-rich layers (e.g. Sparks and Cashman, 2017). Within the mush, several processes may take place, such as magma mixing, melt segregation and compaction, fractional crystallization, magma influx, and entrainment of older plutonic crust and/or host rocks (e.g. Hildreth and Moorbath, 1988; Annen et al., 2015). State of the art of studies related to silicic magma reservoirs are summarized in Bachmann and Huber (2016). The arc magmatism itself is highly episodic at all scales (temporal and spatial) in the production of melt, the growth of the magmatic system and the associated volcanic eruptions (e.g. Paterson and Ducea, 2015; De Silva et al., 2015). As most of the magma in arcs crystallizes before ever reaching the Earth's surface (3–4% only erupts, e.g. Paterson and Ducea, 2015), it is especially important to

look at the evolution of plutons in arcs.

Magmatic or plutonic systems can be investigated by looking at exposed plutonic bodies and volcanic rocks to study ancient magmatic systems (e.g. Paterson et al., 2011; Leuthold et al., 2012; Jagoutz, 2014; Cooper, 2017), or by directly addressing the active system through geodetic, seismic, gravity and magnetotelluric measurements (e.g. Lees, 2007; Hill et al., 2009; Pritchard and Gregg, 2016; Kiser et al., 2016; Biggs and Pritchard, 2017). Furthermore, the general dynamics of magmatic systems can be investigated with numerical simulations. Previous studies focus on thermal processes (e.g. Paterson et al., 2011; Annen et al., 2015; Karakas et al., 2017), mechanical ones as dike initiation and propagation (e.g. Gudmundsson, 2006; Rivalta et al., 2015; Gerbault et al., 2018), or processes inside the magma reservoir as crystal and bubble evolution, chemical interaction and compaction processes (e.g. Solano et al., 2012, 2014; Huber and Parmigiani, 2018; Riel et al., 2018). However, most of those models still focus on the thermomechanical aspects, do not consider the compositional variability of the system, and in case phase diagrams are employed, their number is relatively small. Phase diagrams in geodynamic models are mostly used from lookup tables, which were precomputed over a prescribed P–T range and limited bulk rock compositions (e.g. Rüpke et al., 2004; Yamato et al., 2007; Johnson et al., 2014; Magni et al., 2014; Rummel et al., 2018). These lookup tables can be used to track the chemical evolution of extracted melts, as it is shown by Rummel et al. (2018) for a rising mantle plume. However, the usage of such phase diagrams is still not standard and simplified melt parameterizations (e.g. from Katz et al., 2003) are often employed without considering the evolving chemistry of the melt and residuum. Therefore, to investigate the evolution of a crustal magmatic system and to understand the interactions between mechanical, thermal and chemical processes, a coupling between petrological (thermodynamical) and geodynamical models is unavoidable. Quantifying conditions for magma storage, magma pathways and other processes that affect the efficiency of magma transport to the surface as stress conditions, is critical to better understand the compositional evolution in the magma reservoir and its cumulates left behind after melt extraction. Although new advances have been made in coupling thermodynamics with geodynamics (e.g. Tirone et al., 2009; Hebert et al., 2009; Duesterhoeft et al., 2014; Oliveira et al., 2017; Riel et al., 2018), it is still a challenge to do this for a more complex chemical (and realistic) system with a large number of oxides that massively increases the computation time. To track both the chemical/mineralogical and the mechanical evolution with a high precision, we developed a new parallel framework to establish a phase diagram database covering the chemical range of magmatic systems. We use a suitable Gibbs free energy

minimization program to compute those phase diagrams for a broad range of rock compositions, Perple_X (Connolly, 2005, 2009). Recent advances in extending melting models from metapelitic rocks (White et al., 2001, 2014) to mantle rocks (Jennings and Holland, 2015), metabasic rocks (Green et al., 2016), or even for the whole range (Holland et al., 2018), opens new perspectives on the thermodynamic modeling over large P–T fields and diverse rock types.

In this study, we investigate both the mechanical and chemical/mineralogical evolution of a magmatic system by focusing on the dike-sill network formed by periodic mafic magma influx into the crust.

5.2 THERMODYNAMIC AND GEODYNAMIC MODELING APPROACHES

The evolution of crustal magmatic systems is strongly affected by mechanical and chemical differentiation processes that influence the lifetime of magma reservoirs. To model the evolution of those systems, we integrate thermodynamic rock properties (computed with Perple_X, Connolly, 2005, 2009) into a 2D geodynamic code (MVEP2, Kaus, 2010; Thielmann and Kaus, 2012). The geodynamic code solves the conservation equations of mass, momentum and energy for a visco-elasto-plastic rheology and is combined with a semi-analytical fracture opening algorithm (Sun, 1969) to simulate dike/sill formation (Rozhko et al., 2007). We focus here on the mechanical and chemical evolution of plutonic systems after basaltic magma from the mantle has been intruded into horizontally opened fractures at depths ranging from upper crust to uppermost mantle. We call them "sills" independent of the crystallization degree. The ascent of basaltic magma from its melting source in the mantle is not taken into account. The stress field around the intruded sills determines if and where fractures will be formed to transport magma toward shallower crustal levels. Depending on the crack propagation direction influenced by the local stress field, vertically or horizontally oriented magma filled fractures are formed. Magma filled fractures that are generated from the sills or from partially molten host rocks are called "dikes" here independent of their propagation direction and crystallization degree. These dikes are subdivided into first and second generation structures. The second generation describes dikes that are formed from those of the first generation. When the melt is extracted to form dikes, the source region becomes depleted (the term source region is used here to describe an area from which melt can be extracted). This process produces diverse new rock compositions, which are tracked on markers (marker-in-cell method) using a

different phase diagram for each chemical composition in the geodynamic model. For this, a database with more than 50,000 phase diagrams has been created. Each of those phase diagrams is computed for one specific bulk rock composition and describes the evolution of density, melt fraction as well as chemistry and mineralogy over crustal to uppermost mantle P–T conditions.

5.2.1 Thermodynamic modeling

The thermodynamic modeling is executed with the Gibbs free energy minimization program Perple_X 6.7.9 (Connolly, 2005, 2009). Perple_X uses internally-consistent thermodynamic data for endmembers (thermodynamic data file used: "hp622ver") and activity-composition models for solid-solution phases (Tab. 5.B1, see Appendix). The chemical system used is: SiO_2–TiO_2–Al_2O_3–Cr_2O_3–FeO–MgO–CaO–Na_2O–K_2O–H_2O, but is reduced depending on the chemical system for which the respective employed melting models are calibrated. Available mantle melting excludes K_2O, TiO_2 and H_2O (Jennings and Holland, 2015) and melting of more evolved mafic magmatic rocks (Green et al., 2016) excludes Cr_2O_3 from its chemical system. The mantle model (Jennings and Holland, 2015) is only used in our models to compute the initial phase diagram of the mantle, whereas for all other rock compositions the model for metabasic rocks (Green et al., 2016) is used. The system is buffered along the QFM (quartz-fayalite-magnetite) oxygen buffer. The incorporation of oxygen is required, because it strongly affects phase relations (e.g. Ulmer et al., 2018), and thus the solidus temperature. The total amount of melt and its density and chemistry are taken from both the solution phase (melt(G) or Melt(JH), Tab. 5.B1, see Appendix) and from potentially stable endmember phases (e.g., albite liquid). The solid density and composition are computed from the whole system by subtracting the melt proportion. We compute thermodynamic properties on a grid with a final resolution of 257×257 points. With a pressure range of 0.1–3000 MPa and a temperature range of 290–1900 K, thermodynamic properties are determined every 11.7 MPa and 6.3 K. The thermodynamic data files used are provided in electronic supplementary materials.

For the geodynamic simulations, we assume the continental crust to consist of an upper, middle and lower crust, using average compositions after Rudnick and Gao (2003). The magma in injected sills has a basaltic composition (Le Maitre, 1976). We add between 0.1 and 5 wt% H_2O to the crustal and 1 or 5 wt% H_2O to the basaltic composition. The chosen higher water content in the basalt is based on arc related studies (e.g. Pichavant et al., 2002; Plank et al., 2013). The mantle has a pyrolitic composition after McDonough and Sun (1995). The rock compositions outlined above (Tab. 5.1) are used to compute

the initial phase diagrams employed in the geodynamic simulations.

Table 5.1: Initial rock compositions used in Perple_X. Pyrolitic mantle (pyrolite model, McDonough and Sun, 1995), where K_2O, TiO_2, MnO, NiO and P_2O_5 are excluded. Basalt (Le Maitre, 1976), MnO, P_2O_5 and CO_2 are excluded. Upper (UC), middle (MC) and lower (LC) crust (Rudnick and Gao, 2003), MgO and P_2O_5 are excluded. H_2O is added to the crustal and basaltic compositions, respectively. Oxides are given in wt%.

Oxide	**Mantle**	**Basalt**		**LC**		**MC**		**UC**	
SiO_2	45.18	49.94	47.92	53.46	53.25	63.35	61.76	66.06	63.39
TiO_2	0.00	1.87	1.79	0.82	0.82	0.69	0.67	0.63	0.61
Al_2O_3	4.47	15.98	15.33	16.92	16.85	14.96	14.59	15.27	14.65
Cr_2O_3	0.39	0.00	0.00	0.00	0.00	0.00	0.00	0.00	0.00
FeO	8.08	10.70	10.27	8.58	8.55	6.01	5.85	5.00	4.80
MgO	37.95	6.83	6.56	7.25	7.22	3.58	3.49	2.46	2.36
CaO	3.56	9.61	9.22	9.60	9.56	5.24	5.11	3.56	3.42
Na_2O	0.36	2.95	2.83	2.65	2.64	3.38	3.30	3.24	3.11
K_2O	0.00	1.12	1.07	0.61	0.61	2.29	2.24	2.78	2.66
H_2O	0.00	1.00	5.00	0.10	0.50	0.50	3.00	1.00	5.00

As soon as melt is extracted from a partially molten/crystallized region in the geodynamic simulation, the bulk rock chemistry of the initial stage changes and new phase diagrams are required to track the rock evolution onwards. The extracted melt fills an opened tensile fracture with an average bulk rock chemistry assuming homogeneous mixing of melts. Depending on the P–T condition at which melt is extracted, the amount of extracted melt and the melt chemistry is different. The remaining solid (residuum) composition is directly related to the extracted melt, and thus may vary strongly between markers depending on the amount and composition of extracted melt. Therefore, a single generated dike (thermodynamically described with one phase diagram) leaves behind a depleted source with strongly variable composition. For all these chemically different stages, a different phase diagram is needed that describes how solid and liquid compositions as well as density, melt fraction and stable mineral assemblage will evolve over a prescribed P–T range. All computed phase diagrams are stored in a database (more than 50,000 in total) that is used in the geodynamic simulations. To establish such a large database, the computation of phase diagrams is executed in parallel. The bulk rock compositions used in the phase diagrams, are either compositions requested from previously executed geodynamic simulations or were randomly determined within the relevant compositional parameter space. The procedure of how to establish and to extend the database efficiently is beyond the scope of this paper (Chapter 4). Here, it is only important, that the phase diagrams available in the database cover all relevant rock compositions to track all the

possible source, residue, cumulate and melt compositions of the magmatic system. How the phase diagrams are incorporated into the geodynamic models is described in Section 5.2.2.4.

5.2.2 Geodynamic modeling

5.2.2.1 General method

The geodynamic modeling utilised the finite element code MVEP2[1] (Kaus, 2010; Thielmann and Kaus, 2012), in which tracers (marker-in-cell-technique) are used to track evolving rock properties (melt fraction, density, chemistry and mineralogy). The geodynamic model employs a computational mesh of around 400×350 finite elements with a resolution of ∼125 m horizontal and ∼115 m vertical. The compositions are tracked on markers of which there are initially ∼1.3 million, but the number of markers increases during the simulations as new dikes/sills are generated. A semi-analytical algorithm for fracture opening and thus dike/sill formation is incorporated into the 2D visco-elasto-plastic thermo-mechanical models. The 2D code solves the governing conservation equations of mass, momentum and energy of slowly creeping fluids on geological timescales (Kaus, 2010; Thielmann and Kaus, 2012). The effect of melt on the viscosity is taken into account using laboratory-constrained creep laws (used values are listed in Tabs. 5.B2–5.B3 in the Appendix). The numerical code, employed here, has been described in detail elsewhere (Kaus, 2010; Thielmann and Kaus, 2012; Johnson et al., 2014; Rummel et al., 2018) and is only briefly summarized here.

5.2.2.1.1 Governing equations:

The conservation of mass and momentum for slowly creeping incompressible rocks are described by:

$$\frac{\partial v_i}{\partial x_i} = 0 \tag{5.1}$$

$$-\frac{\partial P}{\partial x_i} + \frac{\partial \tau_{ij}}{\partial x_j} = -\rho g_i, \tag{5.2}$$

where v is velocity, $P = -0.5(\sigma_{xx} + \sigma_{zz})$ is pressure, τ the deviatoric stress tensor, g is the gravitational acceleration, ρ is the density and $i = (x, z)$ denotes spatial directions, and we employ a Boussinesq approximation.

[1] code is provided at: https://bitbucket.org/bkaus/mvep2

The rheology is Maxwell visco-elasto-plastic:

$$\dot{\varepsilon}_{ij} = \dot{\varepsilon}_{ij}^{elastic} + \dot{\varepsilon}_{ij}^{viscous} + \dot{\varepsilon}_{ij}^{plastic} = \frac{1}{2G}\frac{D\tau_{ij}}{Dt} + \frac{1}{2\eta_{eff}}\tau_{ij} + \dot{\lambda}\frac{\partial Q}{\partial \sigma_{ij}}, \tag{5.3}$$

where $\dot{\varepsilon}_{ij}$ is the (deviatoric) strain rate tensor, G the elastic shear modulus, $\frac{D\tau_{ij}}{Dt}$ the Jaumann objective derivative, $\dot{\lambda}$ the plastic multiplier and Q the plastic flow potential. η_{eff} is the effective creep viscosity, which is computed from dislocation and diffusion creep laws:

$$\eta_{eff}^{dis} = FA^{-\frac{1}{n}}((C_{OH})^r)^{-\frac{1}{n}}\ \dot{\varepsilon}_{II}^{\frac{1}{n}-1}\exp\left(\tfrac{E+PV}{nRT}\right)\exp\left(-\tfrac{\beta}{n}M\right) \tag{5.4}$$

$$\eta_{eff}^{diff} = FA^{-1}d^p((C_{OH})^r)^{-1}\exp\left(\tfrac{E+PV}{RT}\right)\exp(-\beta M), \tag{5.5}$$

with F as prefactor for tensorial form, prefactor A, powerlaw exponent n, water fugacity in $H/10^6Si$ (C_{OH}), exponent of C_{OH}-term r, grain size d, exponent of the grain size p, second invariant of the strain rate tensor $\dot{\varepsilon}_{II}$, activation energy E, pressure P, activation volume V, gas constant R, temperature T, melt fraction prefactor β and M as current melt fraction. To avoid numerical instabilities, a lower and upper viscosity cutoff of 10^{17} and 10^{25} Pas is used.

The solved energy equation is given by:

$$\rho c_p\left(\frac{\partial T}{\partial t} + v_i\frac{\partial T}{\partial x_i}\right) = \frac{\partial}{\partial x_i}\left(k\frac{\partial T}{\partial x_i}\right) + H_r + H_a + H_d + H_l, \tag{5.6}$$

where ρ is density, c_p heat capacity, $v_i\frac{\partial T}{\partial x_i}$ the advection term with v_i as spatial velocity and k is the thermal conductivity. H_r, H_a and H_d are the heat sources with radioactive (H_r), adiabatic (H_a) and dissipative or shear heating (H_d). Additionally, latent heat (H_l) induced by melting (heat consumption) or crystallization (heat production) processes is taken into account, by increasing the effective heat capacity (C_{Peff}) and the effective thermal expansion (α_{eff}) of the partially molten/crystallized source, calculated following Burg and Gerya (2005) as:

$$C_{Peff} = C_P + Q_L\left(\frac{\partial M}{\partial T}\right)_{P=const.} \tag{5.7}$$

$$\alpha_{eff} = \alpha + \rho\frac{Q_L}{T}\left(\frac{\partial M}{\partial P}\right)_{T=const.}, \tag{5.8}$$

with Q_L as latent heat of fusion. α_{eff} is considered in the adiabatic heating term H_a.

The density in the models is a function of rock composition (X), melt fraction (M), pressure (P) and temperature (T), with $\rho = f(X, M, P, T)$ and computed as follows:

$$\rho = \rho_{liquid}\ M + \rho_{solid}(1 - M), \tag{5.9}$$

where M is the current melt fraction and ρ_{liquid} and ρ_{solid} are the densities of the liquid and solid phase in equilibrium with the corresponding melt fraction.

In the following Sections 5.2.2.2–5.2.2.4, we describe how the semi-analytical dike/sill formation algorithm and the phase diagrams are incorporated into the geodynamic code described above.

5.2.2.2 Mafic sill injection

During the ongoing geodynamic simulation, basaltic magma is periodically injected (every 10–80 ka) as sills into different crustal levels. The intrusion depth and temperature are prescribed for each sill which is several km long. In addition to the predefined dimension of the sill (length and height), the elastic behavior (Young's modulus and Poisson's ratio) of the surrounding host rocks is a crucial aspect for calculating the spatial extension and thus the final shape of the sill. To describe how a fracture opens horizontally in an elastically deformable host rock, we use the analytical solution of Sun (1969):

$$W = \frac{2iP_{sill}(1-\nu^2)}{\pi E_{ym}} \Bigg\{ z\ ln\left(\frac{R_2+z+ia}{R_1+z-ia}\right) - (R_2-R_1) - \frac{1}{2(1-\nu)} \cdot \left[z\ ln\left(\frac{R_2+z+ia}{R_1+z-ia}\right) - iaz\left(\frac{1}{R_2}+\frac{1}{R_1}\right)\right]\Bigg\}, \tag{5.10}$$

where P_{sill} is the pressure within the injected sill, ν the Poisson's ratio, E_{ym} is the Young's modulus, a is the radius of the fracture (half of the sill length), R_1 and R_2 are complex distances and z represents the z-coordinate. $R_1 = \sqrt{r^2+(z-ia)^2}$ and $R_2 = \sqrt{r^2+(z+ia)^2}$, where r represents the radius of the polar coordinate system. i is the imaginary number $\sqrt{-1}$.

$$P_{sill} = \frac{3E_{ym}V_{sill}}{16(1-\nu^2)a^3}, \tag{5.11}$$

with V_{sill} as sill volume.

This fracture opening results in an elastic deformation of the surrounding rocks that is taken into account by moving markers. Within the horizontally-opened fracture, new markers are randomly inserted to mimic magma injection. These markers carry the information (temperature, density, melt fraction, chemistry etc.) of the basaltic magma pulse by using a precomputed phase diagram. The injected sills provide a partially crystallized region as a source for further fracture generation (see Section 5.2.2.3) to transport magma into shallower crustal depths.

5.2.2.3 Formation of dikes

The initiation and propagation of dikes are controlled by the interaction between mechanical stress-related processes and those that affect the magma behavior (e.g., temperature and pressure). The stress field in the surrounding host rocks controls the propagation direction of a dike which moves in the direction of the maximum principal stress, σ_1. Moreover, the efficiency of magma transport through a fracture depends on the fracture mode. Here, we apply a semi-analytical algorithm for crack initiation and propagation. The algorithm determines whether tensile fractures or shear bands would form around a partially molten/crystallized region, under the assumption that the magma pressure continuously increases in the source (see Section 5.2.2.3.1). Only if tensile failure is favored, melt is extracted from the source to fill the crack. We predefine the propagation direction of the crack using the local stress field (see Section 5.2.2.3.2). The dimension of the dikes is computed using the amount of extracted melt, under consideration of the numerical resolution. Apart from the mechanical evolution of the magmatic system, we track the chemical evolution in the deflated magma reservoir (after melt extraction) and in dikes by including changeable phase diagrams on the markers (see Section 5.2.2.4). We extract pure melt from the partially molten/crystallized region assuming a total decoupling between melt and crystals either by forming local melt lenses in the mush system or by density-driven crystal sedimentation (melt segregation). Although the melt fraction on each individual marker may be relatively small and thus normally not eruptable (Cashman et al., 2017), assuming perfect melt-solid separation allows us to extract melt as long the amount is numerical resolvable on the mesh (see Section 5.2.2.3.2). After a sill is injected (Section 5.2.2.2), dikes can only form in a subsequent numerical time step allowing melt accumulation through crystal-liquid separation.

The connected melt accumulations that trigger fracture initiation, consist of melts originating from either one or several melt sources. These sources are not different rock types in the proper sense but are defined by the rock phase (e.g., crustal host rock, basaltic injected sill or dike). We tested two extreme scenarios, in which we assume i) full homogenization of all melts in the source region as long as these melts are connected, or ii) fully separated systems for melts from different sources, even if they physically coexist (immiscible melts). The markers within the partially molten/crystallized (source) region and thus the magma compositions are randomly mixed to mimic magma mixing (4. Magma mixing, Fig. 5.1).

From each generated dike of the first generation (formed from basaltic sills or from partially molten crustal host rocks), melt can be extracted again if either the material

remains molten or enough heat is provided to partially remelt those rocks. These extracted melts form dikes of the second generation. Further continuation of melt extraction from dikes of the second generation is not possible in our models.

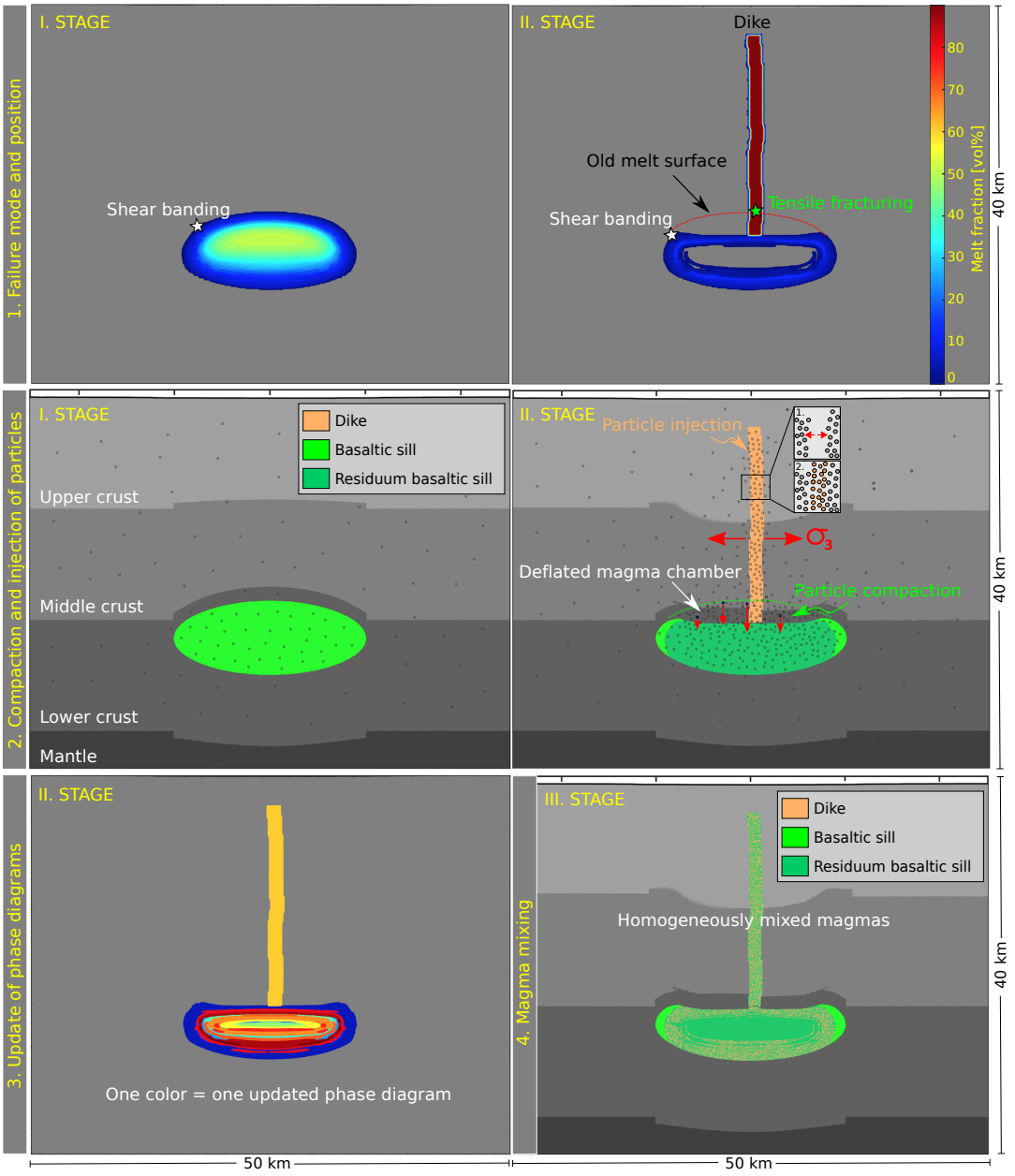

Figure 5.1: Methodological procedure of melt extraction 1–3, with magma mixing (4) as a potential additional step. Stages I to III represent the temporal sequence. Stage I: Magma reservoir is stable and the stress field only favors shear band formation above the partially crystallized region. Stage II: magma reservoir becomes unstable and a tensile fracture is formed. Melt is extracted from the magma reservoir into the fracture to form a dike. Subsequently, the markers are compacted in the deflating magma reservoir and around the fracture. Injection of markers into the newly formed fracture that carry the information of the melt phase. The phase diagrams used are updated based on the cumulate and melt chemistry. Stage III: Magma is mixed if melt accumulations are connected from different sources.

5.2.2.3.1 Determination of the failure mode above each melt accumulation

The stress field and the critical pore fluid pressure (P_{crit}) above which the rock will fail, are determined for each element of the computational grid along the interface between the partially molten/crystallized source and the surrounded solid host rock. An analytical solution of the critical pore fluid pressure in a porous elasto-plastic medium is given by Rozhko et al. (2007) as follows:

$$P_{crit} = \frac{k_b(\sigma_v - \sigma_h) + k_\tau + k_\sigma(\sigma_v + \sigma_h)}{k_f}, \tag{5.12}$$

with σ_v as vertical effective stress (dynamic pressure (P) + deviatoric stress in z-direction (σ_{zz})) and σ_h as horizontal effective stress (dynamic pressure (P) + deviatoric stress in x-direction (σ_{xx})). The effect of fluid in the pore space is assumed to be negligible for the total stress in the host rocks. As soon as P_{crit} is exceeded, supposing an increase of the fluid pressure in the magma reservoir on top of the existing overpressure caused by the buoyancy of the magma, the rock will fail either by forming shear bands or tensile fractures (dikes). Four failure modes (FM 1 – FM 4) are defined by Rozhko et al. (2007), for which different equations are valid (see Tab. 5.2). Which of those modes are theoretically possible, depends on the local stress field (extensional vs. compressional conditions) along the melt interface. The minimal difference between the fluid pressure (P_{fluid}, dynamic pressure as a first approximation) and the critical pore fluid pressure (P_{crit}) indicates the failure position and the mode of failure (shear banding vs. tensile fracturing; 1. Failure mode and position, Fig. 5.1). Thus, only if P_{crit} is lower for the tensile fracturing than for the shear banding mode, a dike is formed. For a localized overpressure source, as applied here, equations of failure are extended by γ_σ and γ_τ, which affects both the shift of the Mohr's circle towards lower pressures and the size of the circle (Fig. 5.2). This increases, in our case, the critical pore-fluid pressure (P_{crit}) that has to be exceeded to initiate failure.

$$\gamma_\sigma = 1 - \frac{\psi}{2}\frac{1-2\nu}{1-\nu}\left(1 - \frac{0.5}{ln(\frac{4h}{w})}\right) \tag{5.13}$$

$$\gamma_\tau = \frac{\psi}{4}\frac{1-2\nu}{1-\nu}\frac{1}{ln(\frac{4h}{w})}, \tag{5.14}$$

with w as the width of the overpressure source (here, one element wide in order to numerical resolve it), h is the distance from the melt interface to the model surface, ν is the Poisson's ratio, ψ is the Biot-Willis poro-elastic coupling constant. C is the rock cohesion, ϕ is the

friction angle and σ_T defines the tensile strength of the rock. If $\gamma_\sigma = 1$ and $\gamma_\tau = 0$, for incompressible rocks, with $\nu = 0.5$, or if ψ is set to zero, equations 5.13–5.14 recovers the expected Terzaghi's limit.

Table 5.2: Parameters used to compute P_{crit} for the four different failure modes (FM 1 – FM 4). FM 1: Shear banding under extensional conditions; FM 2: Shear banding under compressional conditions; FM 3: Tensile fracturing under extensional conditions; FM 4: Tensile fracturing under compressional conditions. After Rozhko et al. (2007).

Parameter	**FM 1** $\sigma_v > \sigma_h$ Shear banding	**FM 2** $\sigma_v < \sigma_h$ Shear banding	**FM 3** $\sigma_v > \sigma_h$ Tensile fracturing	**FM 4** $\sigma_v < \sigma_h$ Tensile fracturing
k_f	$2(\gamma_\tau + \sin(\phi)\ \gamma_\sigma)$	$2(\gamma_\tau - \sin(\phi)\ \gamma_\sigma)$	$2(\gamma_\tau+\gamma_\sigma)$	$2(\gamma_\tau-\gamma_\sigma)$
k_τ	$2\ C\ \cos(\phi)$	$-2\ C\ \cos(\phi)$	$2\ \sigma_T$	$-2\ \sigma_T$
k_σ	$\sin(\phi)$	$-\sin(\phi)$	1	-1
k_b	1	1	1	1

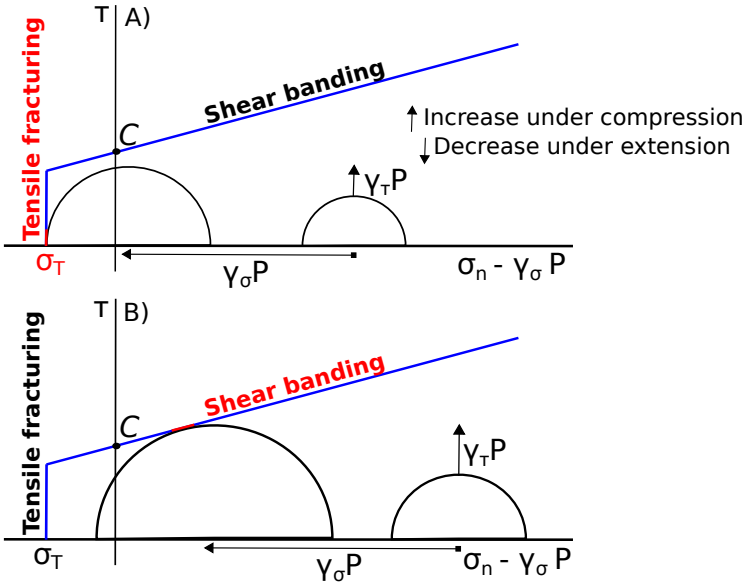

Figure 5.2: Rock failure for A) tensile fracturing and B) shear banding. C = cohesion; σ_T = tensile strength; σ_n = normal stress, P = fluid pressure and τ = shear stress. The shift of the Mohr circle is controlled by P and γ_σ (eq. 5.13). The radius is controlled by the ratio of the normal stresses σ_1 and σ_3 (here as σ_h and σ_v), P and γ_τ (eq. 5.14) and increases under compressional and decreases under extensional conditions. The cohesion defines the intercept.

5.2.2.3.2 Size and orientation of dikes

To generate a dike in our model, not only does the failure mode have to be favorable (tensile fracturing) above the partially molten/crystallized source (1. Failure mode and position, Fig. 5.1), but also the amount of melt has to exceed a critical value. The volume

of magma (here assumed to be 100% melt) has to cover at least the dimension of two elements in x- and y-direction (ca. 200 m $\times$ 200 m) in order to be numerically resolved. However, only melt above the non-extractable amount (here set to 0.5 vol%) is extracted from the partially molten/crystallized region. The length of the resulting dike is computed from the extracted melt volume divided by the width of the dike, with a minimum width of two elements. As soon as the dike length exceeds the model dimension, the width increases by one element width. The orientation of the dike during its propagation is computed from the stress field in the model domain, such that it opens perpendicular to σ_1. To track the fracture propagation direction, fracture increments with a length of two elements are put on top of each other, under consideration of the local stress field, until the maximum length of the dike is reached, which depends on the available melt. The formation of each dike is accompanied by an elastic deformation of the surrounded host rocks, as described for the injected sills (see Section 5.2.2.2).

5.2.2.3.3 Injection and compaction of markers caused by melt extraction

After melt is extracted, markers are moved downward accordingly above the melt extraction zone to mimic the compaction of the deflated magma reservoir in a volume-conservative manner. This is a numerically simple manner to mimic volumetric processes within a Boussinesq model approximation. Other approaches are possible, which involve adding sink/source terms in the conservation of mass equation (e.g. Gerya and Yuen, 2007; Vogt et al., 2012; Schmeling and Arndt, 2017), but are not considered here. The formation of dikes causes an elastic deformation of the surrounding rocks. With the fracture opening, old markers are moved aside while new markers are randomly inserted which carry the information about the rock properties (chemistry, density, etc.) of the newly generated dike (2. Compaction and injection of markers, Fig. 5.1). The temperature within the newly formed dike is specified by the average temperature of the partially molten/crystallized source from which its melt was originated.

The procedure described in Section 5.2.2.3 is individually applied for each melt pocket. Parameters used for the geodynamic simulations including those for the dike/sill algorithm are listed in Table 5.B4 in the Appendix.

5.2.2.4 Phase diagrams employed in the geodynamic simulation

The computation of the phase diagrams used during the geodynamic simulation, can be done in two ways (i) by a direct call within the geodynamic simulation, or (ii) before the simulation for all previously requested rock compositions during compositional space

investigation.

i) The computation of phase diagrams simultaneously with the geodynamic simulation allows us to reduce the number of computed phase diagrams of the database to a minimum, as all phase diagrams are based on the correct requested bulk rock compositions. After each melt extraction event, the residuum, cumulate or melt compositions are directly used to compute new phase relationships. The phase diagram would be immediately updated on the marker, from which melt was extracted, and the chemical system develops accordingly. However, the disadvantage of this method is, that the geodynamic simulation has to wait until all phase diagrams are computed for each computational time step. The computation of each of those phase diagrams for a wide range in P and T takes in our case around 10 hours. Thus, even if the computation of the phase diagrams is executed in parallel, and only a single P–T point is considered, direct coupling is very inefficient, unless major improvements are made to speed up the internal calculation time of the phase diagrams.

ii) To use precomputed diagrams requires a method to check whether a required phase diagram is already available. During an ongoing geodynamic simulation, the phase diagrams on the markers must be updated after the bulk rock compositions have been changed due to melt extraction (3. Update of phase diagrams, Fig. 5.1). The affected bulk rock composition changes by splitting into a liquid part describing the extracted melt, and into a solid part to describe the remaining residuum. To find the most appropriate phase diagram, we discretize the rock compositions with offsets of $\Delta_{\mathrm{Ox.}} = 0.1$ wt%. Thus, the chemistry of each marker is compared with an accuracy of one decimal to the already existing phase diagrams in the database. The phase diagram of the database, which has the closest bulk rock composition, replaces the previous one on the marker. Density, melt fraction and compositions are interpolated from the phase diagram to the markers. As soon as the phase diagrams are updated in the deflated magma reservoir, the rocks become depleted and thus have a higher solidus temperature. If a phase diagram with the requested bulk rock composition does not exist yet in the database, the rock composition is stored and will only be used after the geodynamic simulation has been completed to calculate a further phase diagram. The computation of those phase diagrams is executed in parallel to reduce the overall computation time. However, updating marker compositions with the most similar bulk rock compositions during the geodynamic simulation may produce results that are chemically incorrect. Therefore, each geodynamic simulation has to be repeated, while computing new phase diagrams for the database, until the

differences between requested and existing rock compositions in the phase diagram database are negligible. This can be verified by calculating a similarity index, D_{min}, which is a distance-based measure with units of wt% and denotes the Euclidean distance between every requested bulk rock composition ($\mathrm{BRC}^{request}$) and its closest neighbor among all already existing bulk rock compositions used in the database (BRC^{dabase}).

$$D_{min,i} = \min_{j=1,\ldots,N_{dabase}} \left(\sqrt{\sum_{ox=1}^{9} \left(\mathrm{BRC}_{i,ox}^{request} - \mathrm{BRC}_{j,ox}^{dabase} \right)^2} \right), i = 1, \ldots, N_{request}, \tag{5.15}$$

where ox represents the respective oxide and N is the number of rock compositions.

To avoid too many repetitions, the database is extended independently from the geodynamic simulation by defining new possibly needed rock compositions within the already existing compositional range. Even if not all of the phase diagrams are used in one specific geodynamic simulation, the large compositional range used in the database (with more than 50,000 bulk rock compositions) allows us to change the model setup without necessarily having to compute new phase diagrams.

The evolution of both the chemical composition and the melt fraction on the markers, which depends on temperature, magma mixing, and melt extraction, is graphically illustrated in Figure 5.3.

The source code including the semi-analytical dike/sill formation algorithm and the way how phase diagrams are incorporated into the geodynamic code is provided as MATLAB library in electronic supplementary materials.

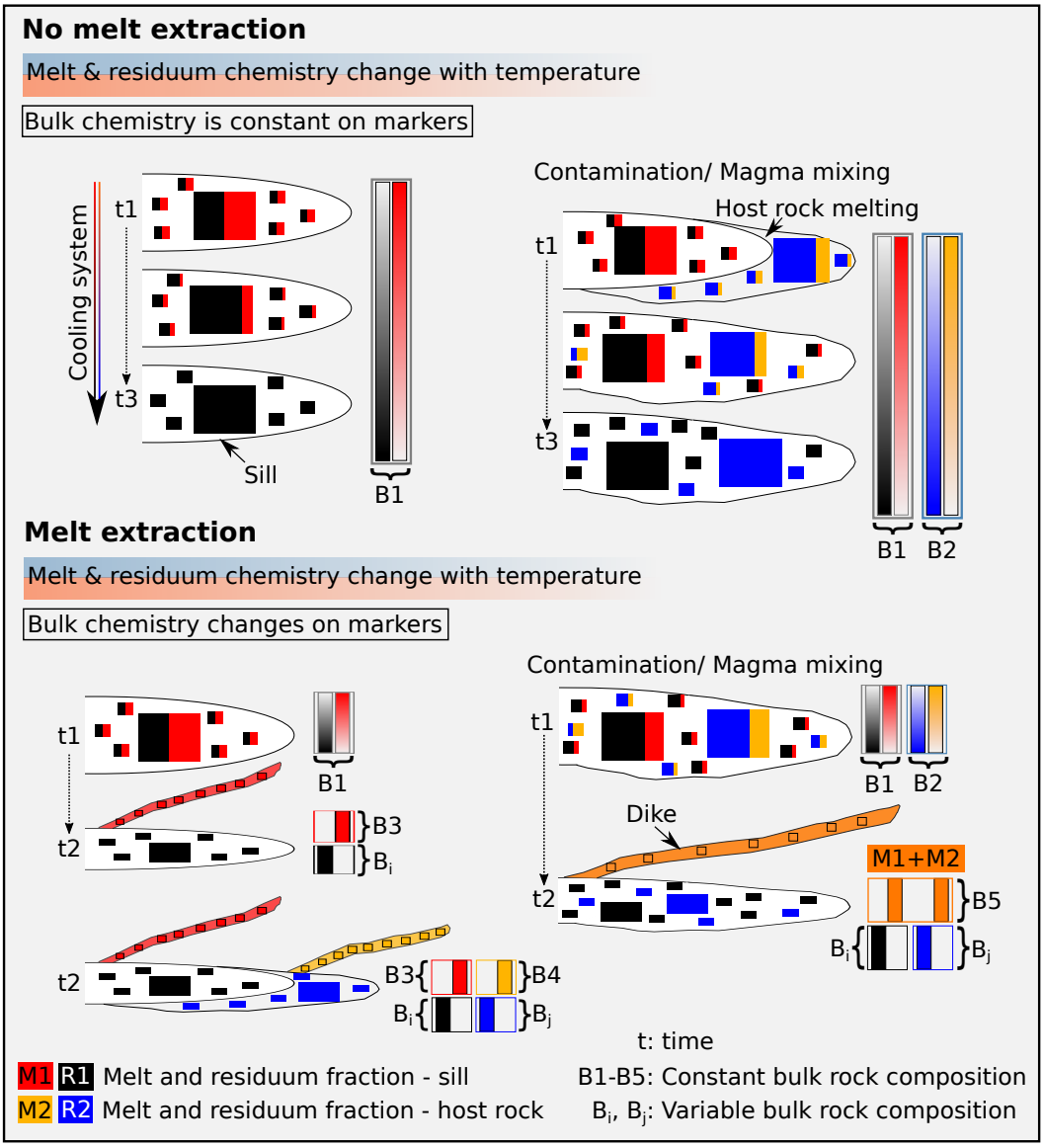

Figure 5.3: Scheme describing the evolution of chemistry and melt fraction. Top: melt is not extracted from a sill and thus the bulk rock composition ("B") remains constant on the markers (rectangles). Melt to residuum ratio changes with decreasing temperature (with progressing time, t1–t3) and thus their chemical compositions as well. Through magma mixing, host rock melts can be incorporated by mixing markers. Bottom: Melt extraction changes the bulk rock compositions on the markers. The dike is described with one new bulk rock composition, whereas the residuum has different bulk rock compositions (i, j) depending on the amount and composition of extracted melt. Through magma mixing, host rock melts and residual melts from a sill form a common dike, with a bulk rock composition averaged from all extracted melts.

5.2.3 Model setup

To better understand the dynamics and chemical differentiation of arc magmatic systems, we model a 50 km wide and 40–50 km deep 2D cross-section over ∼1 million years (Fig. 5.4). The 2D model box consists of an upper, middle and lower crust, which are underlain by a pyrolitic mantle. We use a dry olivine rheology for the mantle and usually a quartzite rheology for the upper crust and a plagioclase (An75) rheology for middle and lower crust as well as for the sills and dikes. We vary the rheology of the crustal host rocks in a few simulations to test the control of rheology on tensile fracture formation (Tab. 5.B2, see Appendix).

Mechanical boundary conditions are kinematic prescribed velocities on both model sides and on the bottom, where the velocity is chosen such that a constant extensional or compressional background strain rate of 10^{-15} s^{-1} is obtained. For comparison, we also perform a simulation with no background deformation using free-slip boundary conditions. The top boundary is a free surface (stress-free). Thermal boundary conditions are isothermal at the top and bottom and flux-free at the side boundaries.

The initial geotherm has a surface temperature of 20 °C and increases linearly up to 600–800 °C at 40 km depth or up to 900 °C at 50 km depth. New basaltic magma pulses are periodically injected as sills (every 10–80 ka) into the continental crust or uppermost mantle at varying depth levels and lateral extensions (Fig. 5.4), with thicknesses between 0.5–3 km. Their injection conditions are prescribed. The intrusion depths are chosen such that different possible scenarios are investigated. We consider three different cases for basaltic magma intrusion: 1) sills are injected at constant depth into one main zone (single magmatic system), 2) sills are injected at constant depth into two main zones (double magmatic system, reference simulation), or 3) they are injected at variable depths (non-connected). The intrusion temperature is set between 900 and 1200 °C, with 1050 °C as the most common one to simulate a mush-like starting system (with ∼45 vol% crystals). The injection temperature of the basalt is constant during the geodynamic simulation for all sills. After ca. 400–500 ka, the heat and material influx from the mantle comes to an end and the magmatic system cools down.

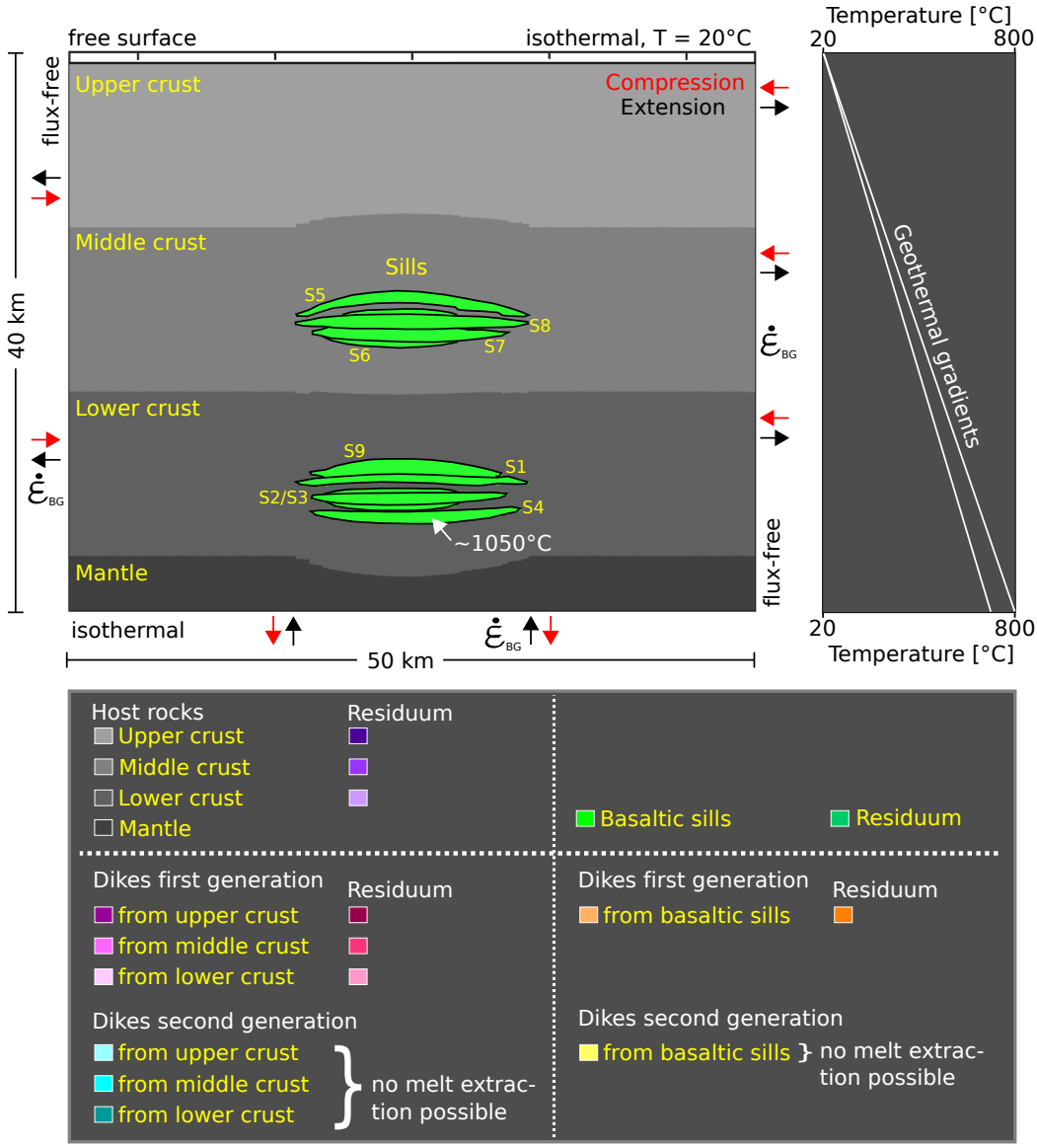

Figure 5.4: Initial 2D numerical model configuration. The thermal and mechanical boundary conditions used are described in the main text. The range of depth-dependent temperature distribution is shown with the two employed geothermal gradients. Basaltic sills are periodically injected at varying depth levels (here, S1–S9) with constant temperatures of 900–1200 °C for each individual sill. After melt extraction, residual material (cumulate rocks) remains. Melt can be extracted from dikes of the first generation, but not from those of the second generation, whose melts originate from dikes of the first generation.

5.3 RESULTS

We developed a coupled petrological-geodynamical method to investigate the compositional evolution of crustal magmatic systems affected by melt extraction through dikes. The interactions between mechanically and thermodynamically controlled processes are studied, which strongly affect the longevity of magma reservoirs. For this, we systematically change magma fluxes (sill injection frequency and the number of injections), sill-related parameters (such as size and temperature) and intrusion depths (upper, middle, lower crust or mantle; connected vs. unconnected sills). Moreover, the effects of the initial state of the crust, such as geothermal gradient, mechanical boundary conditions (background strain rate) and the rheology of the host rocks, are additionally tested. Two different rock cohesion values (5 and 10 MPa) are used, as cohesion controls the fracture mechanism (tensile fractures vs. shear bands). Several hydration states of the initial crustal host rocks and injected basaltic sills are used (Tab. 5.1). The contamination of the mush system through assimilated host rocks is tested by including magma mixing in a simplified manner. Employed parameters used in the presented models are summarized in Table 5.3. The evolution of the magmatic system is shown for a reference simulation in Section 5.3.1.

5.3.1 Reference simulation

Basaltic magma is periodically injected (36 times in total) into the middle and lower crust producing a new sill every 10 ka (Fig. 5.5). The sills are injected in an extensional environment and have an initial thickness of ∼0.5 km each and an intrusion temperature of 1050 °C. In Figure 5.7, the reference model is slightly modified, with 18 injected sills that have an initial thickness of ∼1 km each. A rock cohesion of 10 MPa is employed, which causes dike formation as a direct consequence of a newly injected sill (no shear band formation). Under these conditions, the cumulate fraction is ∼50 vol% in the sill, too low to produce rocks through fractional crystallization that exceed an intermediate rock composition. However, if further fractionation occurs by extracting residual melts from those dikes, high silica rocks can be generated. To the end, dikes and sills form a complex and interacting network of differentiated rocks from crystallized melts, and their counterparts, the cumulates (Fig. 5.5). Through this dense network, heat is continuously released to the surrounding host rocks and triggers their melting (Fig. 5.5). However, some partially crystallized rocks maintain their original chemical composition, if the system cools

Table 5.3: Employed parameters used in the presented models. The background strain rate ($\dot{\varepsilon}_{BG}$) is 10^{-15} s^{-1} and can either be compressional or extensional. Basaltic sills are injected with a prescribed initial temperature ($T_{SillIntrusion}$) and thickness (*Sill thickness*). They are injected at chosen depths (*Injection depths*) with a frequency defined in *Injection frequency*. LC = lower crust, MC = middle crust and UM = uppermost mantle. If two injection depths are listed (e.g., LC and MC), sills are injected into both of those depth levels. Variable: Sills are distributed over middle to lower crustal depths. The total number of injections is described in *Number of injections*. T_{bottom} is the geotherm at the model bottom. *Wet crust/basalt*: Initial rock compositions with a higher water content are employed (Tab. 5.1).

Model	$T_{SillIntrusion}$ [°C]	*Cohesion* [MPa]	$\dot{\varepsilon}_{BG}$	*Number of injections*	*Injection frequency* [ka]	*Injection depths*	*Sill thickness* [km]	T_{bottom} [°C]	*Wet crust*	*Wet basalt*	*Magma mixing*
6	1050	10	exten.	9	40	LC	∼1.0	800	no	no	no
7	1050	5	exten.	18	20	LC and MC	∼1.0	800	no	no	no
10*	1050	10	exten.	18	20	LC and MC	∼1.0	800	no	no	no
12	900	10	exten.	9	40	LC	∼1.0	800	no	no	no
16	1050	10	exten.	9	40	UM	∼1.0	900	no	no	no
18	1050	10	compr.	36	10	LC and MC	∼0.5	800	no	no	no
19*	1050	10	exten.	36	10	LC and MC	∼0.5	800	no	no	no
20	1050	10	compr.	23	20	variable	∼1.0	800	no	no	no
21	1050	10	exten.	23	20	variable	∼1.0	800	no	no	no
26	1050	5	compr.	18	20	LC and MC	∼1.0	800	no	no	no
28	1200	10	exten.	9	40	LC	∼1.0	800	no	no	no
36	1050	10	exten.	18	20	LC and MC	∼1.0	800	yes	no	no
38	1050	10	exten.	24	20	variable	∼1.0	800	yes	no	no
39	1050	10	exten.	18	20	LC and MC	∼1.0	800	no	yes	no
43	1050	10	exten.	24	20	variable	∼1.0	800	yes	no	yes
44	1050	5	exten.	18	20	LC and MC	∼1.0	800	yes	no	yes
45	1050	5	exten.	24	20	variable	∼1.0	800	yes	no	yes

*reference model

down below the solidus temperature before the melt could be extracted (Fig. 5.5).

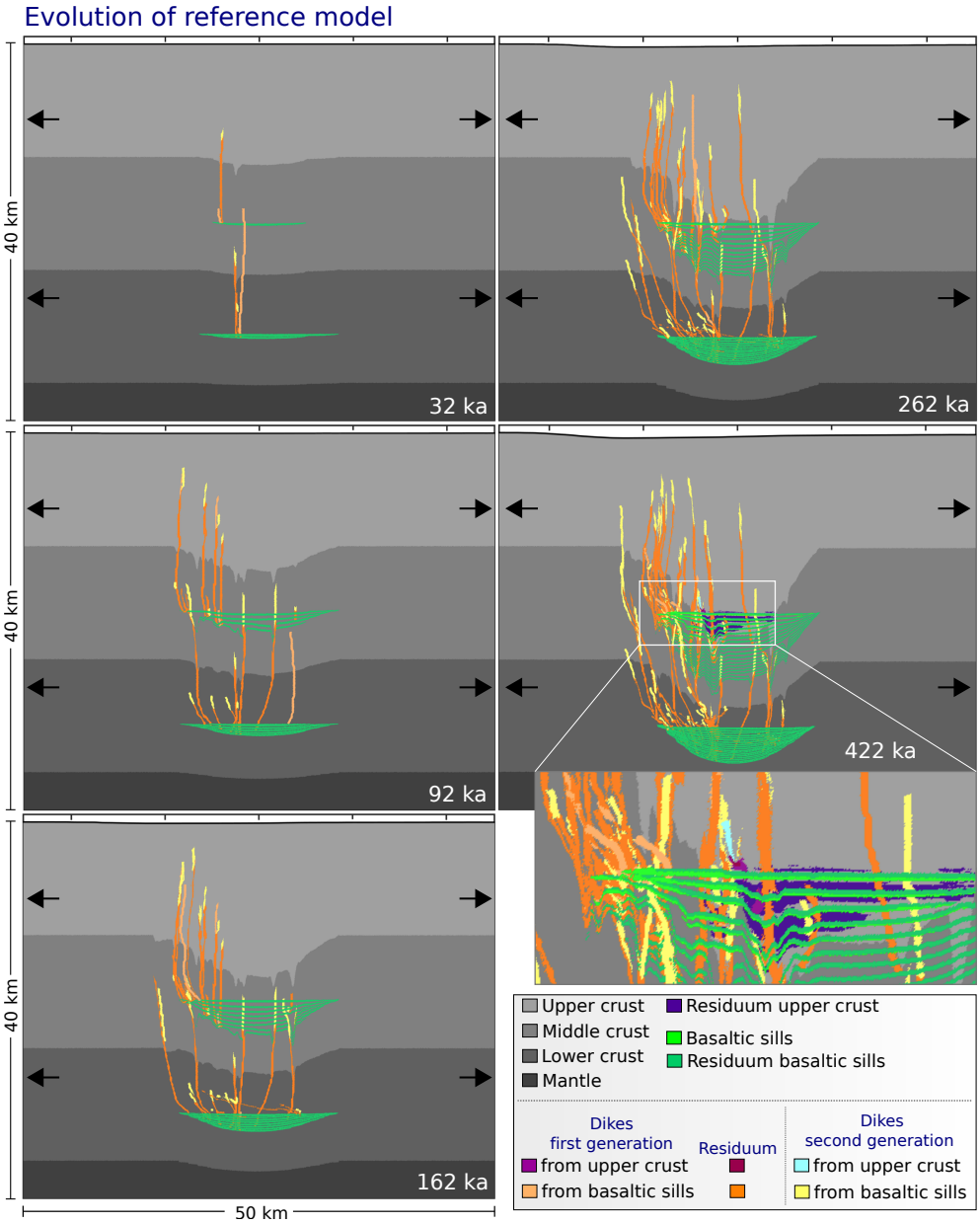

Figure 5.5: Evolution of the reference simulation (model 19, Tab. 5.3). Sills are periodically injected every 10 ka (36 in total) into either the middle or the lower crust at prescribed depths. Employed extensional background strain rate = 10^{-15} s^{-1} and rock cohesion = 10 MPa. Intrusion temperature of the basaltic sills = 1050 °C and bottom temperature of the model domain (T_{bottom}) is set to 800 °C (initial geotherm at 40 km depth). The sills are injected with an initial thickness of ∼0.5 km.

5.3.2 Dike generation and propagation and longevity of partially molten/crystallized regions

The extraction of melts depends on the stress field, as it controls the failure mechanism and the dike propagation. The global stress field in the model domain is controlled by the chosen background strain rate, which dominantly produces horizontally propagating fractures under compressional and vertically propagating fractures under extensional conditions, as the fractures follow the local stress field and open perpendicularly to σ_1 (Fig. 5.6). Locally, the far-field stress is disturbed by the generated dikes, injected basaltic sills, or by descending overlying crust due to source rock compaction, through which uncommon fracture orientations may be produced. If there is no imposed tectonic deformation, the fracture propagation direction is usually between those observed under extensional and under compressional background strain rates. Furthermore, the rheology of the surrounding host rock influences the stress field and thus the propagation direction of dikes, e.g. a weak lower crust (wet quartzite, Tab. 5.B2 in the Appendix) accommodates the stresses generated through background strain rates, which results in non-vertically oriented dikes even under extensional conditions. For deeply rooted source regions in the uppermost mantle, efficient melt transport to shallower crustal levels is hampered due to a horizontal σ_1 orientation (model 16, Fig. 5.6).

We assume a pressure in the partially molten/crystallized region that is sufficiently high to exceed the critical overpressure (P_{crit}, eq. 5.12) to break the rocks. As long as sufficient melt is present, magma can be extracted to fill the opening tensile fractures. In most of the cases, after a sill is injected into the continental crust, the stress field above this partially crystallized region allows tensile fracturing and thus magma transport (see reference model, 10, Fig. 5.7). The main controlling parameters on the failure mechanism, are the rock cohesion and the depth of the partially crystallized region. Using a smaller rock cohesion (5 MPa instead of 10 MPa) preferentially results in shear band formation. Consequently, dikes are not necessarily generated as a direct consequence of an injected sill (models 7 and 26, Fig. 5.7). This may result in the ongoing generation of late dikes from the early sills in a partially crystallized region which was not previously depleted by melt extraction. Therefore, even after the sill injection process is over (∼400–500 ka), melt can still be present in a sill.

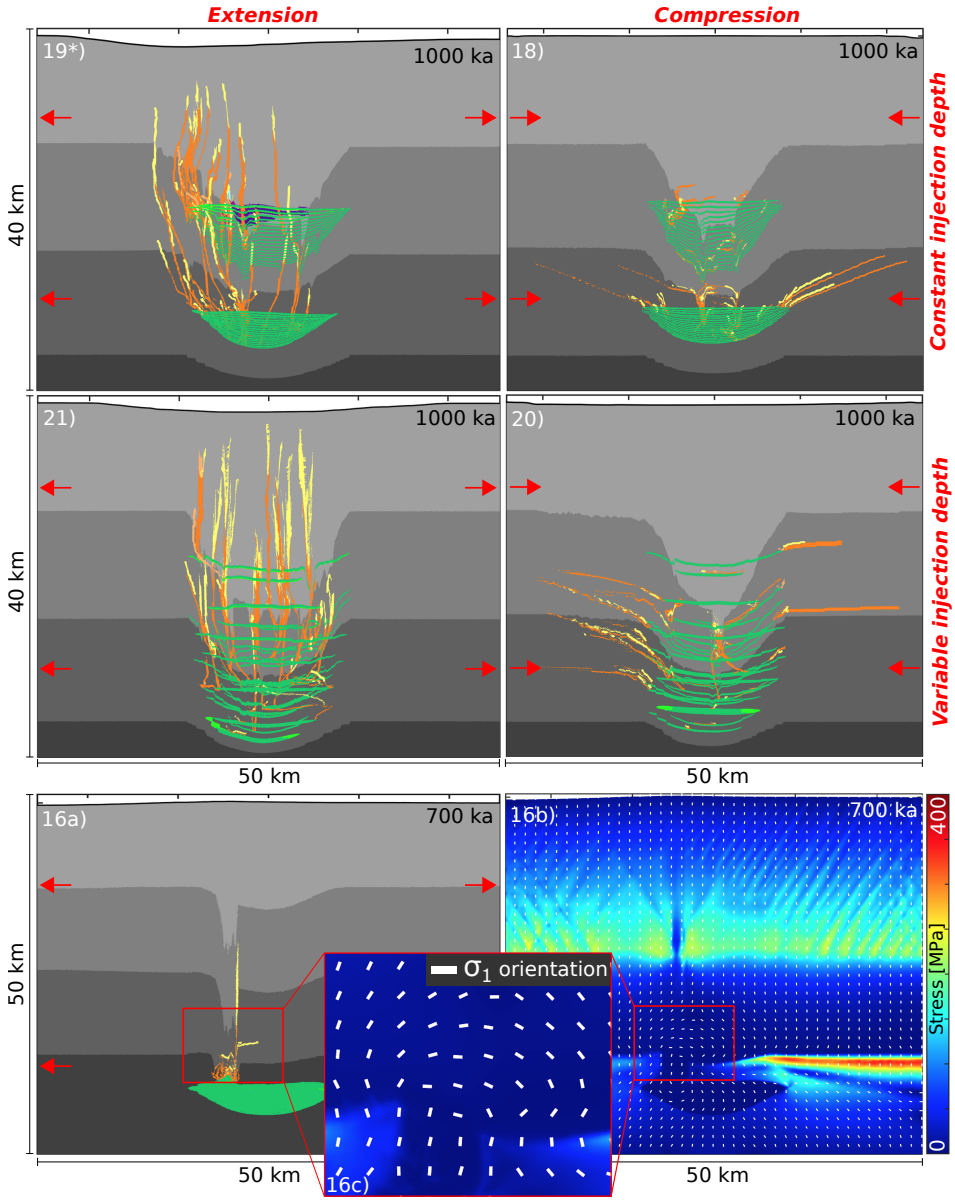

Figure 5.6: Snapshots (after 1000 or 700 ka) of the magmatic systems with differently oriented dikes. The parameters used are described in Table 5.3. Models 19, 21 and 16 are under extensional background strain rates and produce mainly vertically orientated dikes; Models 18 and 20 are under compressional conditions and produce mainly horizontally orientated dikes. Sill injection depths are constant for the respective zones (models 19, 18 and 16) and variable for models 21 and 20. The produced stress field (stress invariant, 16b) hampers the magma transport from the uppermost mantle into shallower crustal levels by inducing a horizontal σ_1 orientation (16c).

In addition, the chosen depth of the injected sills influences the longevity of their partially crystallized regions (model 16, Fig. 5.7). The deeper the partially crystallized source, the less efficiently dikes are generated from it. Consequently, a magma reservoir in the lower crust (> 32 km depth) remains an active system by generating a stress field

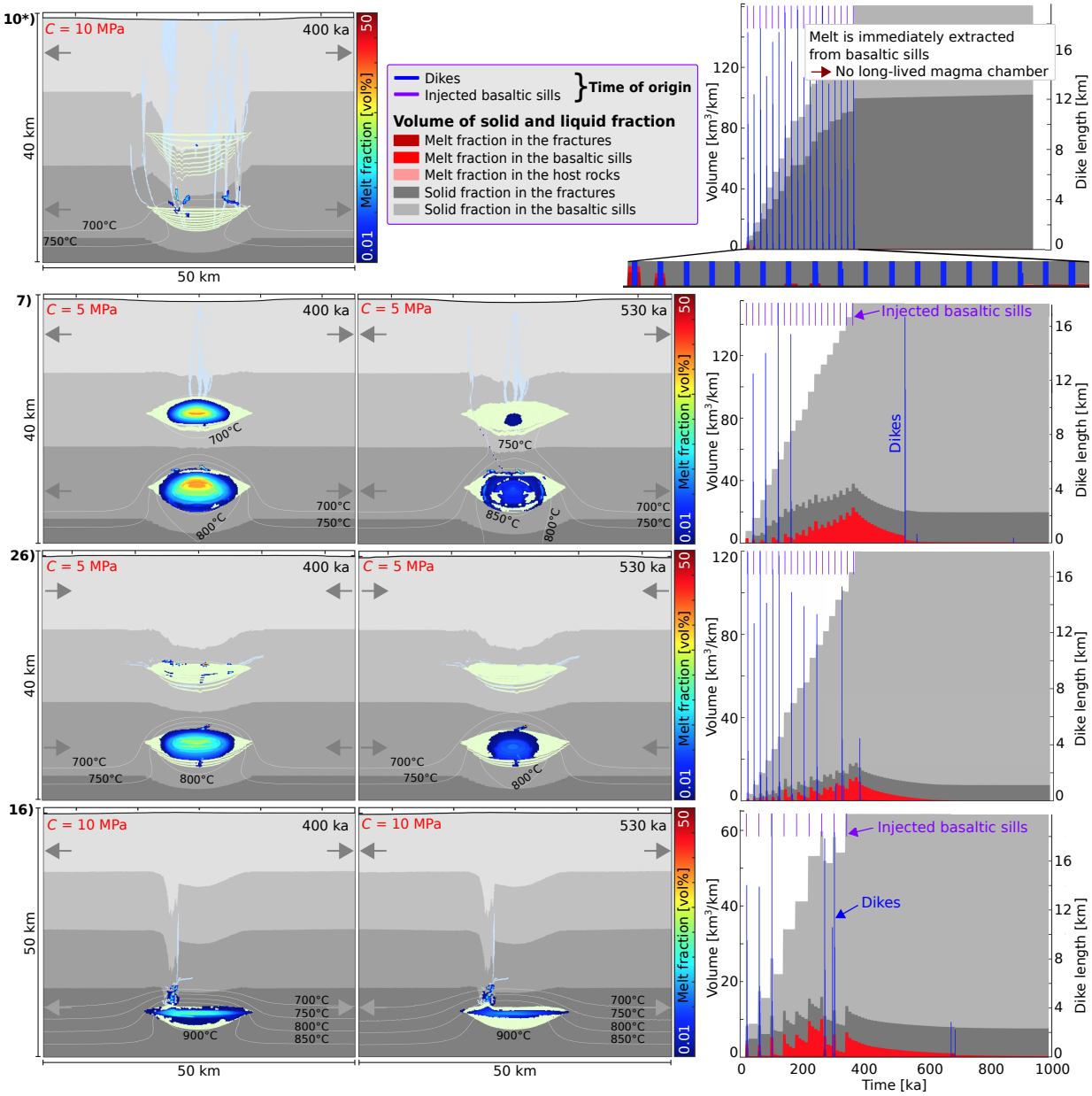

Figure 5.7: Melt retention as a function of rock cohesion and injection depth. The parameters used are described in Table 5.3. Left: Evolution of melt fraction, shown for 400 and 530 ka. Grey arrows pointing out the background strain rate directions (extension vs. compression). Right: Volume evolution of liquid and cumulate fractions with time. The blue lines show the length of the respective dikes. The purple ones indicate only the sill injection time. 10) Reference model, melt is extracted from basaltic sills immediately after it is injected. Models 7 and 26: Decreasing the rock cohesion (from 10 MPa to 5 MPa) stabilizes the melt fraction in the source by suppressing diking. Model 16: A deeper magma reservoir remains partially crystallized longer and keeps melt in the source.

above the currently injected sills that results in preferred shear band formation. Using the modified failure equations (see eq. 5.13 and eq. 5.14) allows shear band formation even under very low stresses in the lower crust. Dikes can be generated after the magma influx from the mantle has ceased due to the changing stress field, provided that sufficient melt is present. Changing the intrusion temperature only has a minor effect on that result. Other parameters, such as the initial thermal and mechanical state of the crust (rheology of host rocks, geothermal gradient, extensional vs. compressional environment), the number of injected sills (less thicker or more thinner ones) or their injection times, have no considerable control on the tensile fracture initiation. Even between single and double magmatic systems (one or two sill injection zones), or between connected (one injection depth) and non-connected sills (distribution of sills over a larger depth interval), there are no significant differences in terms of dike formation. Of course, partial melting of the host rocks may be influenced by those parameters as well, as e.g. a higher intrusion temperature heats up the surrounding material more efficiently, or specific dike/sill arrangements triggers host rock partial melting and thus potentially new dike formation. As long as melt is not extracted and the source region remains partially molten/crystallized, the amount of melt decreases slowly due to diffusive cooling. This process is more pronounced for shallower magma reservoirs than for deeper ones, given the geothermal gradient in the host rocks (models 7 and 26, Fig. 5.7). To conclude, the first generation of dikes is normally triggered by the sill injection and only a lower rock cohesion or a deeper sill injection zone influences the fracturation mechanism in such a way, that the basaltic magma source remains partially crystallized despite waning magma influx from the mantle. Thus, a deep-seated partially crystallized region(s) with a lower rock cohesion is thus the most efficient way to keep the source region in a non-fully crystallized state (Fig. 5.7).

5.3.3 Chemical evolution of the magmatic system

We investigate the compositional evolution of crustal magmatic systems by tracking the rock composition on each individual marker. Mafic to felsic rocks are generated, with high-silica enriched rocks formed either directly from basaltic injected sills by fractional crystallization, from partial melting of crustal host rocks, or from two-stage dike formation. For the two-stage procedure, residual melts are extracted from dikes of the first generation and crystallize in fractures of the second generation to mimic fractional crystallization.

We visualize the rock compositional results on a TAS (total alkali-silica) diagram, on which the different types of rocks are classified depending on their SiO_2, Na_2O and K_2O

concentrations. Here, we use the classification of plutonic rocks after Middlemost (1994), in order to keep the rock names consistent over the whole modeled time independently of the melting/crystallization degree. Thus, the injected basaltic sills have a gabbroic composition, the upper and middle crust consist of granodiorite and the lower crust of gabbroic diorite. Starting from this gabbroic composition, the magmatic system evolves by fractionation as melt is extracted from the sill to fill tensile fractures (Fig. 5.8). The composition of these dikes is strongly affected by the degree of crystallization of the sill, from which the melt is extracted. Consequently, the elapsed time between a new mafic injection pulse and the extraction of melt is a crucial aspect. If the injected sills have an intrusion temperature of 1050 °C (∼55 vol% of the material is initially liquid) and trigger directly the formation of tensile fractures, the generated dikes have a monzo-dioritic to monzonitic composition. Extracting melts from those dikes produces dikes of the second generation with monzonitic, syenitic/quartz-monzonitic or even granitic (with high $Na_2O + K_2O$ concentrations) compositions (model 19, Fig. 5.8). Moreover, a deep-seated magma reservoir in the lower crust (∼35 km depth) or in the uppermost mantle may also generate such high-silica enriched rocks (quartz-monzonite, granite, granodiorite; model 6, Fig. 5.8). This is because it is more difficult to generate tensile fractures at these depths, which leads to melt retention in the partially crystallized region. Within this partially crystallized region, the temperature slowly decreases which results in an increase of the solid fraction, a related decrease of the melt fraction (Fig. 5.7), and thus an enrichment of the melt in both incompatible elements and silica content. Highly differentiated rocks can then be produced, if these melts are later extracted, even though their source is basaltic in composition, leaving behind a mafic to ultramafic residue. Changing the rock cohesion from 10 MPa to 5 MPa has the same effect (model 26, Fig. 5.8). The remaining cumulates have a wide spectrum in their depleted rock chemistry and are characterized by lower SiO_2 and lower $Na_2O + K_2O$ concentrations. Decreasing the intrusion temperature from 1050 °C to 900 °C decreases the initial amount of stable melt from ∼55 vol% to ∼16 vol% in the injected sills, which results in the formation of exclusively silicic rocks from crystallized melts (granites; model 12, Fig. 5.8). To conclude, highly silica-enriched rocks can be produced in the models in different ways: 1) By retaining the melt in the sill, where it continuously crystallizes due to cooling (> 90% crystallizes), before being lately extracted; 2) By starting the mush-like system at lower initial temperatures, which reduces the amount of extractable melt; 3) By extracting residual melts from dikes; or 4) By melt extraction from partially molten host rocks. In all cases, the ratio between cumulates or residue and extracted melts controls the enrichment of the rocks, particularly

the SiO_2 content.

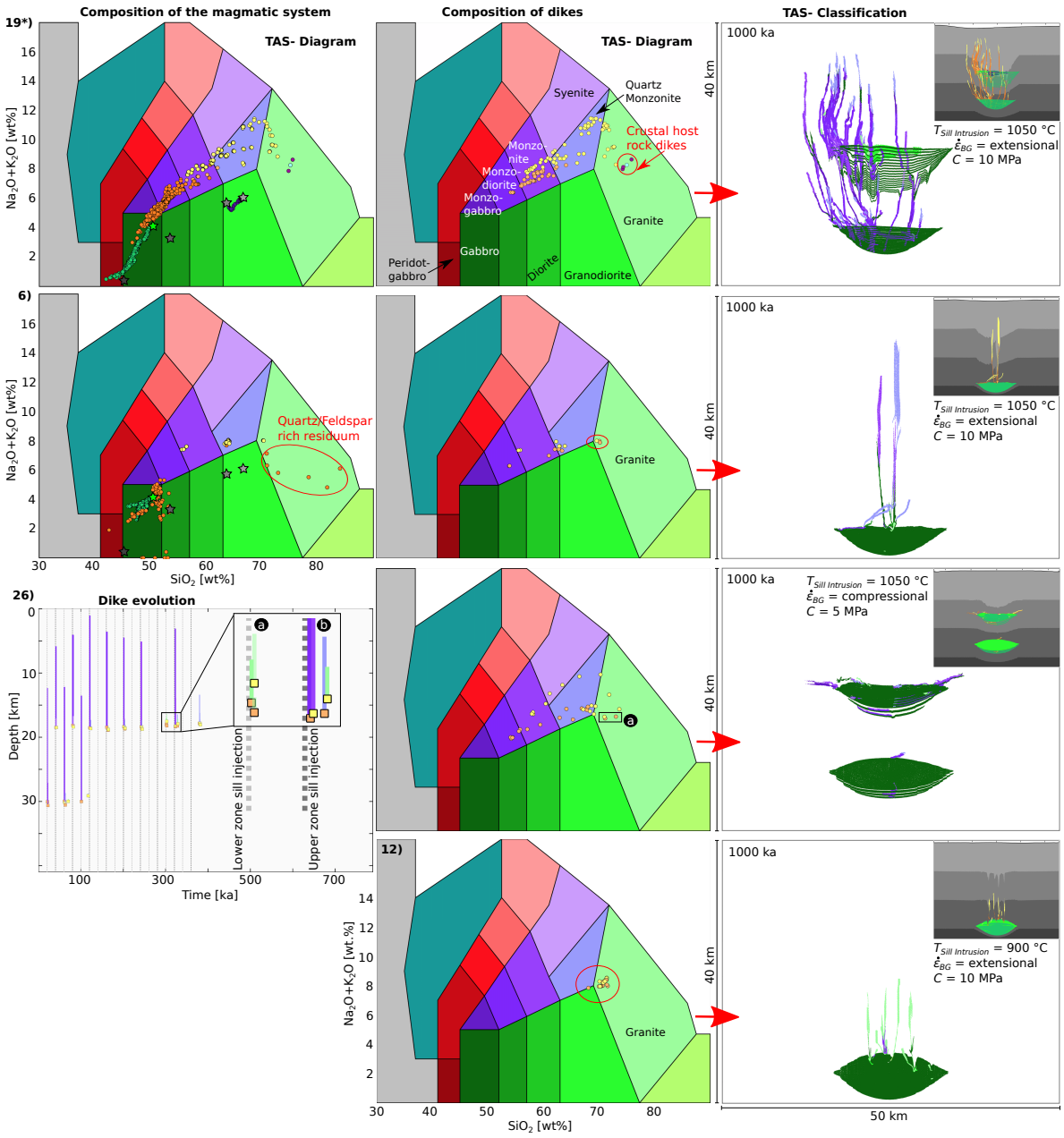

Figure 5.8: Compositional evolution of the magmatic system (after 1000 ka) shown on a TAS diagram (normalized without water) for plutonic rocks (after Middlemost, 1994). The parameters used are described in Table 5.3. The colors of the circles represent the respective rock phases (Fig. 5.4). Initial rock compositions are shown as stars. On the right side, rock types are shown with regard to the magmatic system using the TAS-classification. Here, also the configurations of the four models are presented ($T_{SillIntrusion}$, $\dot{\varepsilon}_{BG}$ and cohesion). Model 26: With a lower rock cohesion (5 MPa), dikes may be generated delayed after the sill was injected into the middle crust (a), which produces higher in silica enriched rocks (melt/cumulate ratio decreases from ~1 to ~0.05). In the dike evolution image, squares indicate the fracture source (orange for first-generation and yellow ones for second-generation dikes originating from basaltic sills). The color of the respective dikes shows the rock type (after TAS diagram). In case the sill triggers directly tensile fracturing, the generated magmatic rocks are less enriched in silica (b).

If the temperature of intrusion is increased from 1050 °C to 1200 °C for deep crustal sills (initial melt fraction increases from ∼55 vol% to ∼82 vol%), the dikes formed from the extracted melts have similar compositions to those observed in models with a lower intrusion temperature (Fig. 5.8 and Fig 5.A1, see Appendix). The generated dikes show a wide spectrum in rock compositions, from monzodiorite through monzonite to quartz monzonite and granite. Due to the higher intrusion temperature, a larger amount of heat is provided to the surrounding, which produces granodioritic dikes from partially molten host rocks. Since higher amounts of melt are extracted from the injected sills, their cumulates are slightly more depleted in SiO_2 (down to ∼35 wt% in the TAS diagram) (Fig. 5.A1, see Appendix).

5.3.4 Mineralogical evolution of the magmatic system

In addition to the chemical composition, also the minerals are tracked on markers throughout the geodynamic simulation. This allows us to visualize the evolution of the mineral assemblages in time and space over the model domain. In order to visualize the mineral distribution within the magmatic system, we average the mineral concentrations over small domains. In these domains, the average mineral concentrations are shown on markers by allocating the respective mineral percentage to a number of markers with a specific color. Thus, for example, if 60% consists of olivine and 40% of garnet, 60% of the markers have a green color (for olivine) and 40% of them a red one (for garnet). The domains are defined for each coherent rock phase (e.g., crustal host rocks, basaltic injected sills or evolved dikes) and melt pocket. How such a mineral distribution can look like is shown in Figure 5.9 for a geodynamic simulation after 450 ka. Exemplary mineral assemblages of that model are presented for different rock phases, dikes and cumulates below. The mineral assemblages are taken from the cooling magmatic system at subsolidus conditions. Dikes of the second generation, originating from the basaltic injected sills, are composed of mainly feldspar (∼60%), chlorite (∼17%), amphibole (∼15%), pyroxene (∼6%) and minor Fe-stilpnomelane, quartz, biotite and spinel. Whereas, the cumulates of the first generation of dikes show a characteristic mineral assemblage consisting of: feldspar (∼40%), amphibole (∼30%), garnet (∼15%), pyroxene (∼10%) and minor olivine, biotite and spinel. Dikes of the second generation, but originating from the partially molten host rocks, have a higher proportion of felsic minerals, with: feldspar (∼66%), quartz (∼29%), amphibole (∼2%) and minor mica and other accessory phases. Cumulates of the basaltic sills have mainly the following composition: feldspar (∼42%), pyroxene (∼30%), garnet (∼14%), amphibole (∼10%), ilmenite (∼3%) and minor rutile. All these mentioned mineral assem-

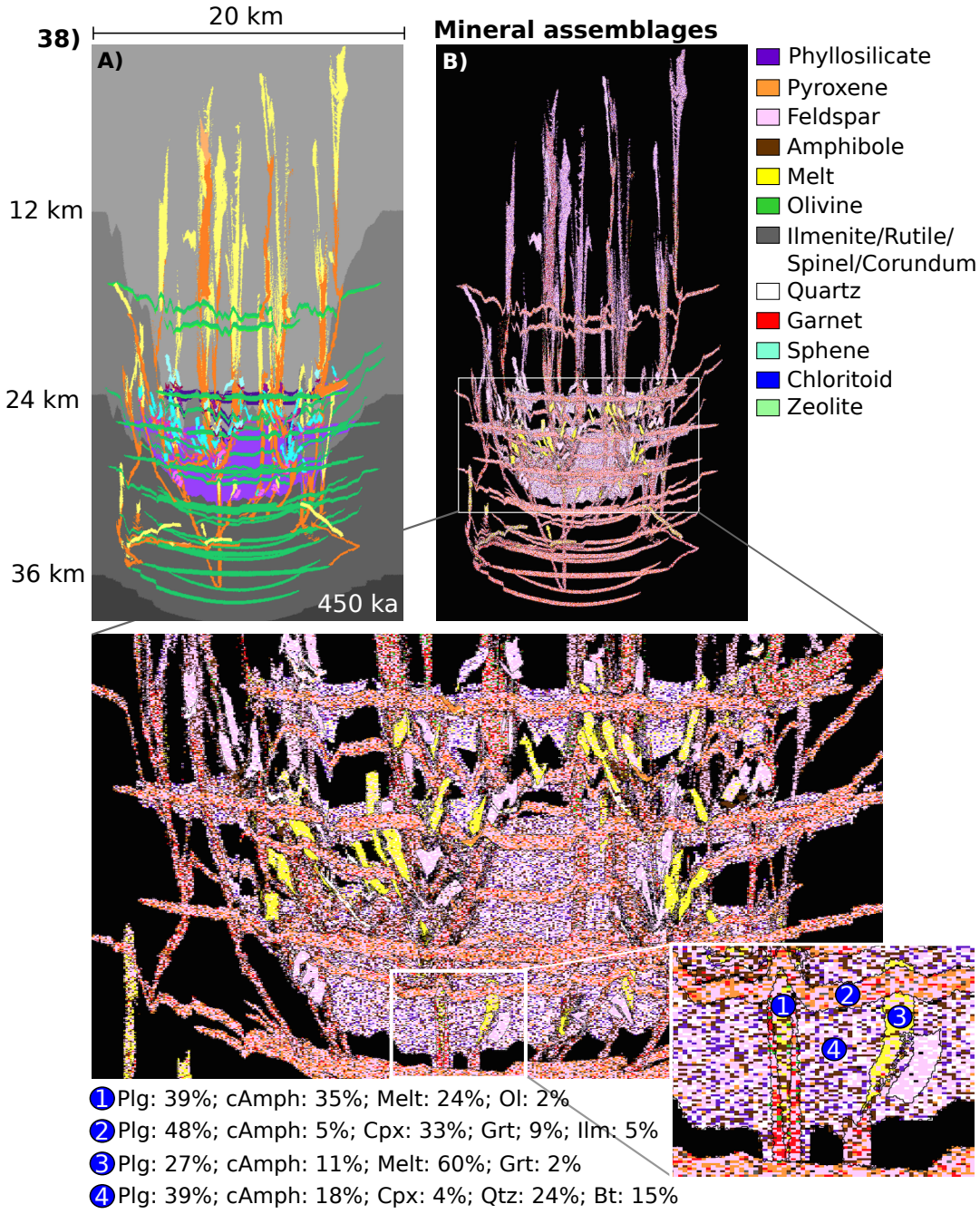

Figure 5.9: Snapshot of the magmatic system after 450 ka (rock phases, A) and corresponding mineral assemblages (B) of the model 38 (used parameters, Tab. 5.3). Sills are injected under extensional conditions. The crust has a higher water content (0.5, 3 and 5 wt% H_2O for the lower, middle and upper crust, Tab. 2.1). The higher water content increases the amount of extracted melt from the host rocks (residue, dikes and cumulates from host rocks are presented with purple-pink and turquoise colors, top left). The phase assemblages are listed for selected domains (1–4). Plagioclase (Plg), clinoamphibole (cAmph), olivine (Ol), clinopyroxene (Cpx), garnet (Grt), ilmenite (Ilm), quartz (Qtz) and biotite (Bt). Proportions are given in vol%.

blages are only examples from that specific geodynamic model presented in Figure 5.9 and may vary over the model domain and with time.

5.3.5 Effect of magma mixing on fracture formation and chemistry

In order to test the effect of magma mixing on the evolution of the system, we perform simulations in which we employ a simplified magma mixing algorithm. This algorithm allows us to mix magmas from different rock phases if they are contiguous. Thus, the magmas from the sills, dikes and partially molten host rocks can be mixed. This process reduces the total number of generated dikes but does not change the general mechanical behavior. Nevertheless, through magma mixing, small liquid accumulations (e.g., from the crustal host rocks) can easier be incorporated into the active magmatic system, from which melt is continuously extracted.

Magma mixing processes produce rock compositions with a wider chemical spectrum, especially for the cumulates left behind after melt extraction. The dikes follow the general trend as observed already for non-mixed magmas, from monzodiorite through monzonite to syenite/quartz monzonite or granite. Due to the mixing process, dikes from the first and second generation become indistinguishable and the main phase determines the main source (e.g., crustal host rocks, basaltic injected sills or evolved dikes). All minor phases are here considered to be contamination phases. Contamination from the surrounding host rocks takes place at all crustal levels and is affected by their water content. Under some conditions, more heat is provided to the host rocks through a dense dike and sill network. This allows a higher amount of newly-formed melt to be incorporated into the parental melts, or even to form separate dikes of predominantly locally-derived partial melt towards the end of the active magmatic system.

5.3.6 Influence of water content on melting, host rock assimilation and dike formation

Low quantities of melt are extracted even from less hydrated crustal host rocks if the heat provided from the intruded dikes and sills is high enough (model 19, Fig. 5.10). Therefore, the intrusion temperature is an especially crucial aspect controlling the melting process of surrounding crustal material. However, the dikes derived from crustal host rocks are rare and generally limited to late extraction events (unless the intrusion temperature is increased). However, the fact that melt was not extracted from the host rocks, does not

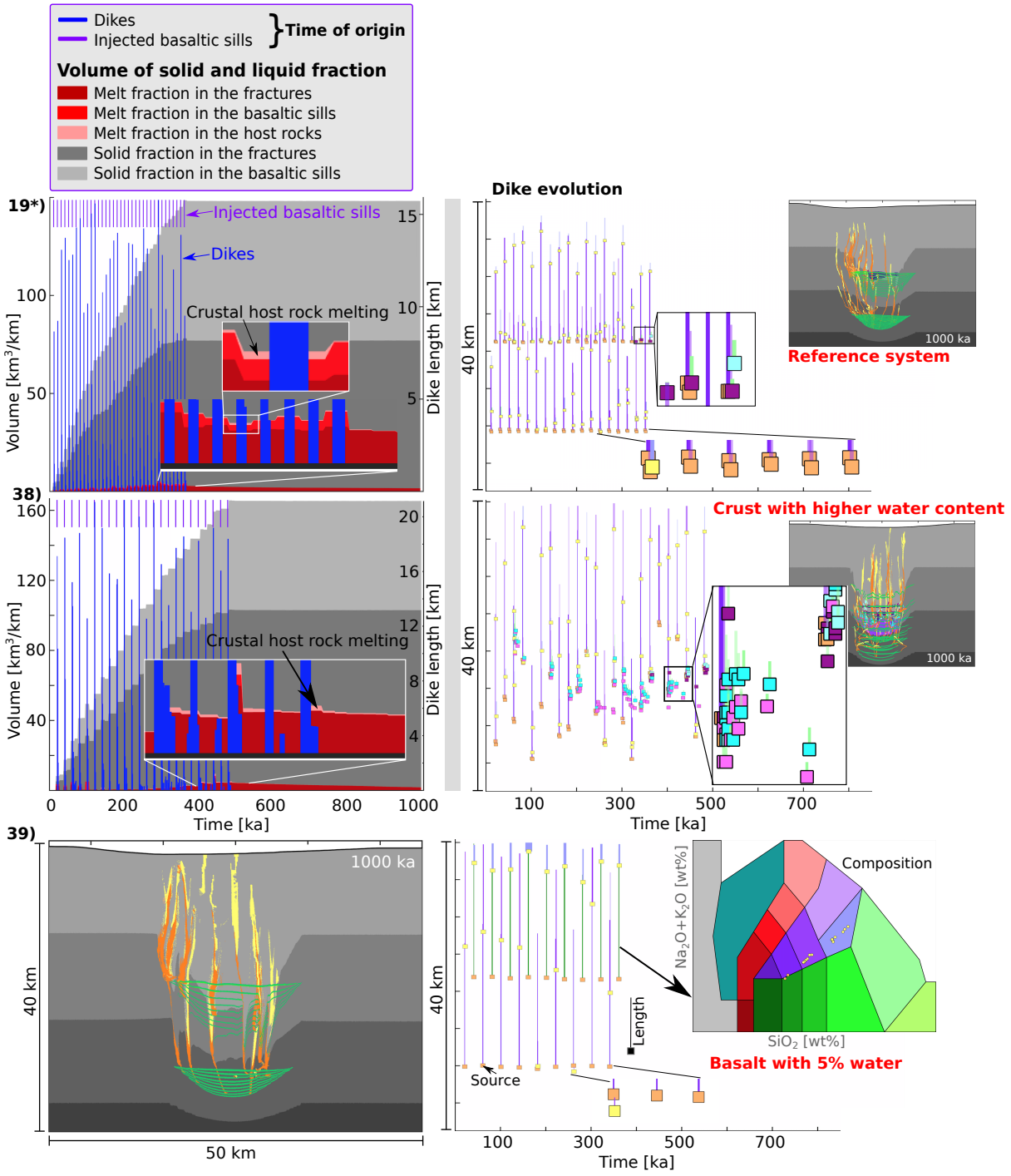

Figure 5.10: Influence of water content on melting and fracture formation. Initiation times of dikes, their types (source, Fig. 5.4), lengths and compositions are shown for each model on the right side. Left: Volume evolution of liquid and cumulate fractions with time (models 19 and 38) and snapshot of the system after 1000 ka for model 39. The length of the blue lines shows the length of the respective dikes. The purple ones indicate only the sill injection time. Zoomed in areas illustrate partial melting of host rocks. The parameters used are described in Table 5.3. The water content of the injected basalt increases from 1 wt% for the models 19 and 38 to 5 wt% for the model 39. The crust in model 38 is enriched in water (upper crust: 5 wt%; middle crust: 3 wt%; lower crust: 0.5 wt% H_2O, Tab. 5.1).

necessarily imply that these rocks were not partially molten during the early stage of the magmatic system. Thus, either the amount of melt was insufficient to be extracted or the fracture mechanism did not result in mode-1 dikes. Dikes from more hydrated host rocks are much more common and occur soon after the first sills were injected (model 38, Fig. 5.10). In these hydrous host rocks, the initial water content is increased from 1 wt% to 5 wt% for the upper, from 0.5 wt% to 3 wt% for the middle and from 0.1 wt% to 0.5 wt% for the lower crust. The dikes generated under these conditions are granitic or granodioritic in composition (Fig. 5.11). The compositions of the remaining depleted host rocks (or cumulates in dikes) range from peridotgabbro through gabbroic diorite/diorite to granite (Fig. 5.11). The partial melting of hydrated host rocks occurs throughout the modeled crust. A significant amount of melts can be accumulated, especially close to the cross-cutting network of sills and dikes, which provides a heat source to the surrounding material (Fig. 5.11). However, as long as the rock cohesion is $\geq$ 10 MPa, melt is nearly continuously extracted from the partially molten host rocks, limiting the lifetime of each melt-rich area (model 38, Fig. 5.10).

As the melt-content increases in the host rock with increasing water content, mixing between melts from basaltic sills or dikes with melts produced by partial melting of host rock, is enhanced. However, melt extraction from the basaltic sills is normally faster than heat diffusion, which does not allow significant host rock contamination. Therefore only at the sill margin, where melt was not previously extracted, small melt fractions remain and small-scale magma mixing leads to the formation of diverse rock compositions (model 43, Fig. 5.12). The residual melts from non-solidified dikes can be mixed to variable degrees with melts from newly injected sills and partially molten host rocks. The resulting dike compositions have a continuous mixing trend from monzodiorite to granite depending on the proportions of the respective melt phases.

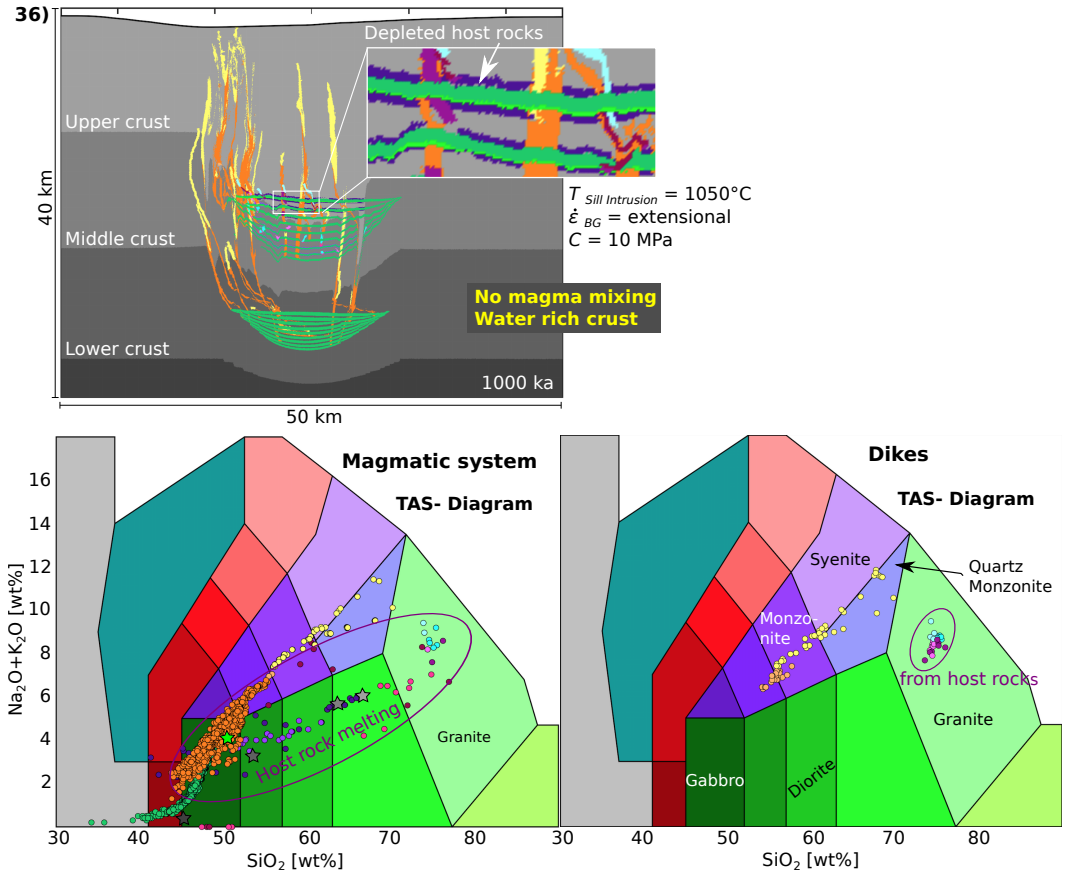

Figure 5.11: Evolution of the magmatic system (after 1000 ka) with a water-rich upper (5 wt% H_2O), middle (3 wt% H_2O) and lower crust (0.5 wt% H_2O). Melts from the host rocks are extracted mostly from areas around the heat providing sills (top). Compositions of the system (bottom left) and of the generated dikes (bottom right) are shown on a TAS diagram for plutonic rocks (after Middlemost, 1994). The colors of the circles represent the respective rock phases (Fig. 5.4). In blueish-purple those from host rock partial melting. Initial rock compositions are shown as stars. The parameters used for the model 36 are described in Table 5.3.

Changing the water content in the basaltic injected sills (from 1 to 5 wt% H_2O), increases the amount of initial melt from ∼55 vol% to ∼83 vol% with an intrusion temperature of 1050 °C. Dikes are generated as a direct consequence of a newly injected sill using a rock cohesion of 10 MPa. However, instead of producing multiple dikes from one injected sill, as it is observed for most of the other models (e.g., model 19, Fig. 5.10), each injected sill generates only one dike by injecting a large amount of melt into the fracture (model 39, Fig. 5.10). Thus, less dikes are generated from the sills. The amount of injected melt per tensile fracture increases from ∼ 8 km^2 to ∼ 11.5 km^2 (maximal amount), or ∼3.9 km^2 to ∼8.8 km^2 on average, from an injected basalt with 1 wt% H_2O to an injected basalt with 5 wt% H_2O. Moreover, due to the higher amount of extracted melt, the residual rocks (cumulates) are more depleted and dikes are less enriched with slightly

lower SiO_2 and Na_2O+K_2O concentrations.

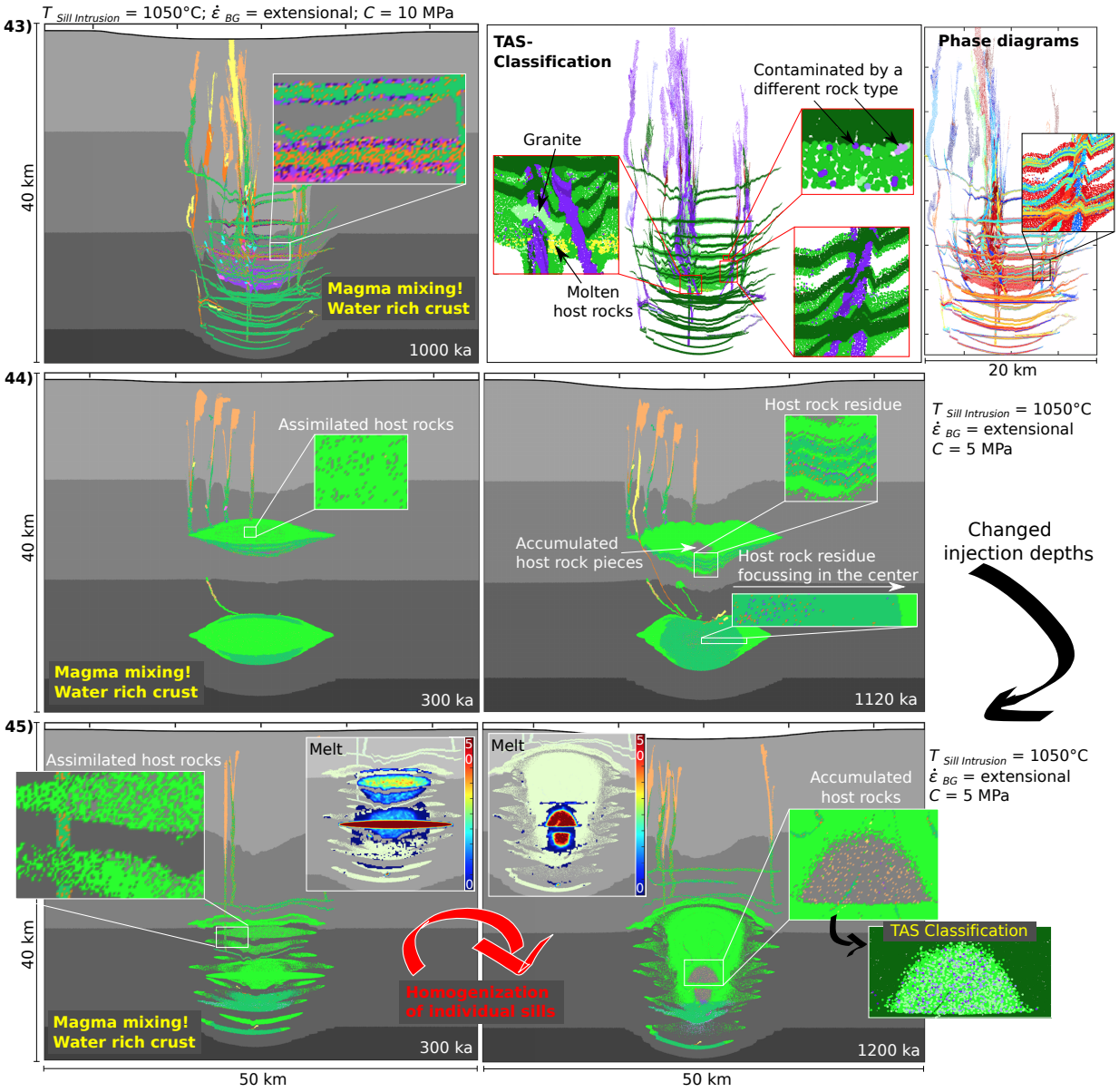

Figure 5.12: Assimilation of hydrated crustal host rocks due to mixing or mingling processes at different times. Markers are randomly mixed in connected partially molten/crystallized regions. The initial crustal host rocks have a higher water content (upper crust 5 wt%, middle crust 3 wt% and lower crust 0.5 wt% H_2O). Used parameters are described in Table 5.3. The rock cohesion decreases from 10 MPa (model 43) to 5 MPa (models 44 and 45). Model 43: Assimilation of host rocks is limited due to the immediate melt extraction after sill injection. The updated phase diagrams are shown (top right), with each color representing a different employed phase diagram (4951 in total). Models 44 and 45: Crustal host rocks are assimilated into the long-lived mush chamber (partially crystallized region of the injected sills). The TAS diagram is used to classify the rock types (top middle), see colors Figure 5.8.

Decreasing the rock cohesion to 5 MPa, stabilizes the melt containing reservoir, as discussed already in Section 5.3.2. Through this long-lived magma reservoir, a high amount

of hydrated crustal host rocks can be assimilated. Solid host rocks are incorporated through convection and partially molten ones through magma mixing or mingling. If melt is not extracted, these pieces of assimilated host rocks accumulate in the magma reservoir (models 44–45, Fig. 5.12) due to density-driven convection. The accumulated partially molten host rocks consist predominantly of silicic rocks, which are surrounded by basaltic material of the injected sills (model 45, Fig. 5.12). Injecting basaltic sills at variable depth (deep middle and lower crust), with a surrounding rock cohesion of 5 MPa, is most efficient in keeping the melt in the source (independently of the crustal water content) by connecting the separated sills through melt driven convection (model 45, Fig. 5.12).

5.3.7 Number of employed phase diagrams

The total number of phase diagrams in the database is ∼58,000. However, the actual number of phase diagrams employed in a particular geodynamic simulation is much lower, with up to ∼5,000, or on average with ∼1,700. The number of employed phase diagrams increases significantly through magma mixing, strongest under more hydrous host rock conditions. Due to the diversity of our executed models, a wide spectrum of the precomputed phase diagrams was required, with ∼25,000 phase diagrams used in total for all 45 executed simulations.

5.4 DISCUSSION

5.4.1 Model limitations and assumptions

We couple thermodynamic and geodynamic models by building a large database of precomputed phase diagrams that are used during geodynamic simulations. As soon as the rock chemistry changes on a marker due to melt extraction, the phase diagram with the closest bulk rock composition replaces the previous one. However, even with $>$ 50,000 phase diagrams, rock compositions can still be produced during geodynamic simulations that are not closely represented by the bulk rock compositions included in the phase diagram database, particularly very variable cumulate compositions. As long as the required rock compositions and the existing bulk rock compositions of the database are very similar, the use of the compositionally-closest phase diagram is acceptable given the possible thermodynamic and geodynamic inaccuracies and uncertainties caused by e.g., interpolation, resolution, and calibration. Only if all differences are relatively small, the updated

phase diagrams are able to describe the rock evolution onwards. If this is not the case, the phase diagram database has to be extended and the geodynamic simulation must be repeated. Consequently, even if the pre-computation of the phase diagrams speeds up the geodynamic simulation itself, the required number of repetitions may slow down the whole process. Moreover, computing such a large number of phase diagrams automatically and in parallel does not allow us to visually inspect the results of all computed ones. Therefore, compositional artifacts in some phase diagrams are possible. Additionally, we use the solution models of Green et al. (2016) in Perple_X for the whole compositional range observed from the modeled sills, dikes and their residuum, yet the solution models are not perfectly calibrated for this full compositional range. The use of the more generalized model of Holland et al. (2018) may alleviate this issue. Using only simplified melt parameterizations, on the other hand, is also not advisable. The non-linear relationship between temperature and melt fraction shown on simple binary systems suggests that modeling of magmatic systems should be based on appropriate phase diagrams, which should account for different starting compositions (Caricchi and Blundy, 2015).

The evolution of a magmatic system is controlled by the interaction between chemical and mechanical processes, which is only incorporated in a simplified manner in our model. Ideally, a fully compressible code including three-phase flow and reaction kinetics, that takes the change in magma properties during its propagation into account, is needed to solve everything in an internally-consistent way. We extract exclusively melt and assume full melt segregation, even though this melt is still in equilibrium with the surrounding crystals until it is extracted. In nature, the fracture initiation and length scale of the dike is controlled by the change in magma overpressure, density contrast and magma composition, which are not considered in our model. The reason for this is that our numerical time step is much larger (hundreds of thousands of years) than the average crustal transport rates for mantle magmas (80 m per day, Ruprecht and Plank, 2013). As it is widely recognized that fractures can efficiently transport granitic magmas through the crust (e.g. Clemens and Mawer, 1992; Petford et al., 1993), we exclusively allow our melt to be transported through tensile fractures. At shallower crustal levels, non-solidified felsic dikes/sills may interact in our models, or even coalesce to form larger plutonic bodies (Clemens and Mawer, 1992). Stress release through either melt flow along grain boundaries into the surrounding crustal rocks, shear band formation, or volume change due to crystallizing magma, are not taking into account. Thus, we assume, that the pressure in the partially molten/crystallized source is sufficiently high to break the rocks locally due to melt accumulation processes (e.g., melt segregation through compaction) that push highly

molten material upward, or through mafic refill from below. Furthermore, the solidification of the modeled dikes is slowed down due to their thickness defined by the numerical resolution. In nature, thin dikes/sills cool much faster. However, if several thin dikes are emplaced in a narrow zone, the temperature is kept high, preserving them in a partially crystallized state. Therefore, within dike swarms in the lower crust, partial melting of crustal material and magma mixing and mingling processes are most efficient (Dufek and Bergantz, 2005). This is consistent with our models, in which the temperature supply from dense distributed dikes/sills leads to intensive crustal partial melting, especially for hydrated host rocks, and contamination from them. Even though different magmas may not mix due to their viscosity contrast, which is not considered in our simplified mixing model, magma mingling may potentially take place. Considering our numerical resolution, the magma compositions can be averaged independently of the dominant magmatic process (magma mixing or mingling). Another simplification is that we inject sills as opening fractures in elastically deformable host rocks, even though viscous behavior could play an important role as well, especially for the deep injection zones. Here, mafic influx warms up the surrounding continental crust, which may influence the storage behavior (Karlstrom et al., 2017). Independently of the viscous behavior, fractures are formed in our model assuming a sufficiently high overpressure inside the magma reservoir to break the rocks, even though the fluid overpressure has to be much higher in a regime, in which the stresses are relaxed by viscous creep. However, in general, the viscosity contrast between the injected basalt and solid rocks is sufficiently high, and timescale of emplacement sufficiently short to promote elasto-plastic fracture formation (Rubin, 1993). Furthermore, due to the mostly continuous melt extraction from the source region, which increases the density through the melt loss, diapiric rising in a viscous environment is effectively suppressed in our simulations.

Eruptable, liquid-dominated bodies, can form within a mush through fractional crystallization. The melt fraction window of 30–50 vol% is most favorable for liquid-crystal separation (Dufek and Bachmann, 2010). This may rapidly localize melt lenses in our model after a new sill is injected with ∼55 vol% melt with an intrusion temperature of 1050 °C. Furthermore, melt can be accumulated due to compaction-driven melt segregation, which under low melt fractions is strongly controlled by the melt viscosity and matrix properties (McKenzie, 1984). For the spatial dimension of our modeled single sill (usually ∼1 km thick), compaction seems to be a powerful mechanism to accumulate a high amount of melt within a short time, comparable with our employed numerical time step of few hundreds of years (Tegner et al., 2009). This justifies the assumption of the extraction of

pure liquid in our model. In case of higher melt fractions, segregation processes may be strongly affected by convection in the magma reservoir. This is particularly relevant in our models for a deep magma reservoir, stabilized by a low rock cohesion. Here, depending on the amount of assimilated colder host rocks, the overall temperature is decreased within the magma reservoir, which affects magma differentiation processes.

Within the assumptions or simplifications we made, our results show some first order mechanical effects on the chemical evolution of magmatic systems and illustrate that we can track the evolving chemistry in time and space with a high degree of precision.

5.4.2 Applicability of model results

Liquid compositions generated during a geodynamic simulation are compared with liquid lines of descent of igneous rock suites to show the applicability of the model results to natural systems (Fig. 5.13A). The liquid line of descent describes the way the liquid composition changes as crystallization proceeds. Starting with a partially crystallized zone composed of injected sills, with up to 50 vol% melt fraction, the composition of the melts evolves with decreasing temperature in the cooling magma reservoirs (blue points, Fig. 5.13A). The melt compositions range from monzodiorite to granite. From different cooling stages and thus crystallization degrees, melts are extracted to form dikes during the geodynamic simulation. The compositions during their extraction (orange points, Fig. 5.13A) are located on the respective liquid line of descent of the cooling basalt, as they were generated from it (Fig. 5.13A). The modeled liquid compositions are well located on the trajectories of the liquid lines of descent of natural igneous rock suites.

Understanding the processes that lead to highly differentiated melts is crucial to understand eruption behavior on Earth. The transition between the generation of intermediate and acid rocks is controlled in our models by the amount of extracted melt and thus the melting/crystallization degree in the source. Investigating the compositions of dikes formed within all executed geodynamic simulations suggests a clear trend between the SiO_2 content and the melting/crystallization degree. The SiO_2 concentration in the dikes is correlated with the crystallization degree, or inversely correlated with the melting degree, of the source (Fig. 5.13B). Exceptions are dikes originating from partially molten host rocks, which already have a high SiO_2 concentration independent of the melting degree.

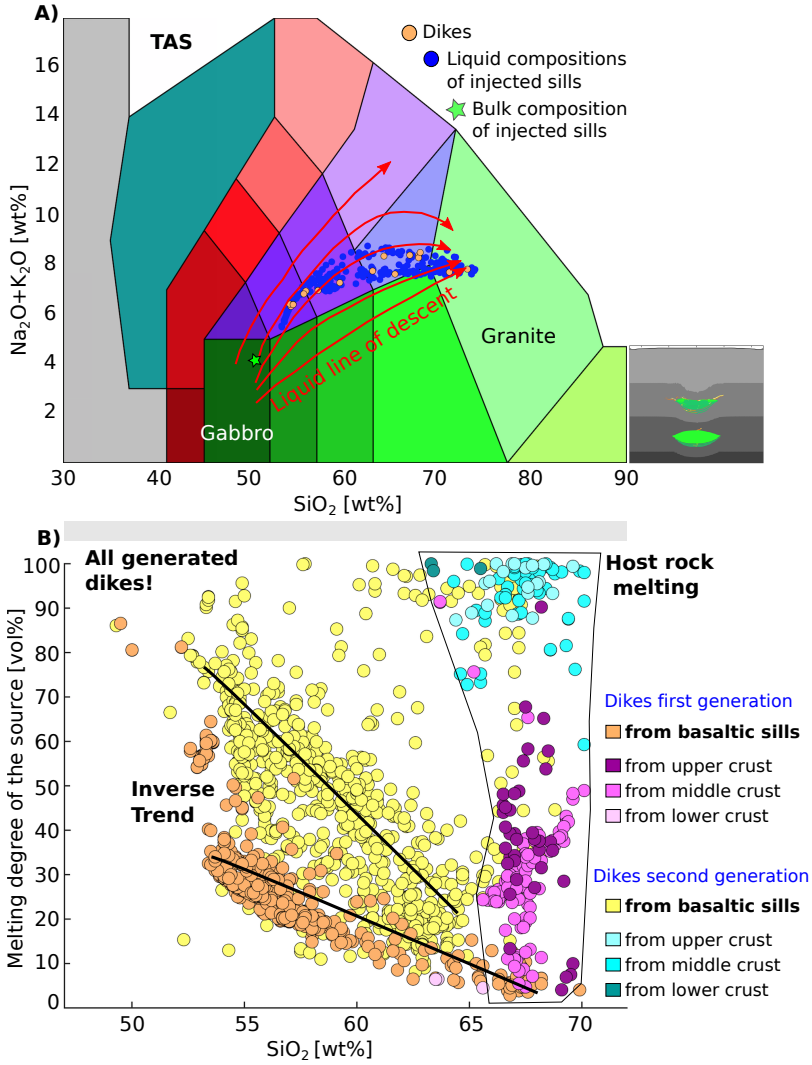

Figure 5.13: A) TAS diagram (normalized without water) for plutonic rocks (after Middlemost, 1994). Evolving liquid compositions generated from the cooling modeled magma reservoirs (blue points). For the magma reservoirs, basaltic sills (bulk rock composition as a green star) are injected at two different crustal levels under compressional background conditions and a rock cohesion of 5 MPa (model 26, Fig. 5.7 and Fig. 5.8). Melt is extracted from the system to form dikes, and their compositions (orange points) are located on the respective liquid line of descent. Red lines show liquid lines of descent for several rock suites (after Middlemost, 1994). B) Melting degree of the source [in vol%] vs. SiO_2 concentration of dikes from all executed geodynamic simulations. The SiO_2 concentrations are correlated with the crystallization degree, or inversely correlated with the melting degree, of the source from which the dikes were generated. This is the case for all dikes, which have their origin in the basaltic injected sills and not in the crustal host rocks.

Large silicic (rhyolitic) ignimbrites commonly erupt from compositionally variable magma reservoirs. For example, for the Snake River Plain magmatic system, observations indicate that hot refractory margins within a mush system insulate melt-rich lenses and maintain their high temperature (Ellis et al., 2014) (Fig. 5.14C). This process may also be relevant in our models, in which the refractory material can either be the solid

part of the newly injected sill accumulated towards the rim (not modeled here), or cumulates of previously drained sills in which new mantle-derived magma is intruded. These cumulates may isolate the newly injected sill from the colder surrounding host rocks (Fig. 5.14A) and thus prevent host rock contamination. Within a cooling magmatic system, melt becomes enriched in silica depending on the liquid-solid ratio (e.g., ~ 68 wt% SiO_2 in liquids equilibrated with ~92 vol% crystals, Fig. 5.14A) and can be mobilized in case of effective melt segregation. If this is the case, rhyolites can be formed in our models comparable with those observed in the Snake River Plain (Fig. 5.14B).

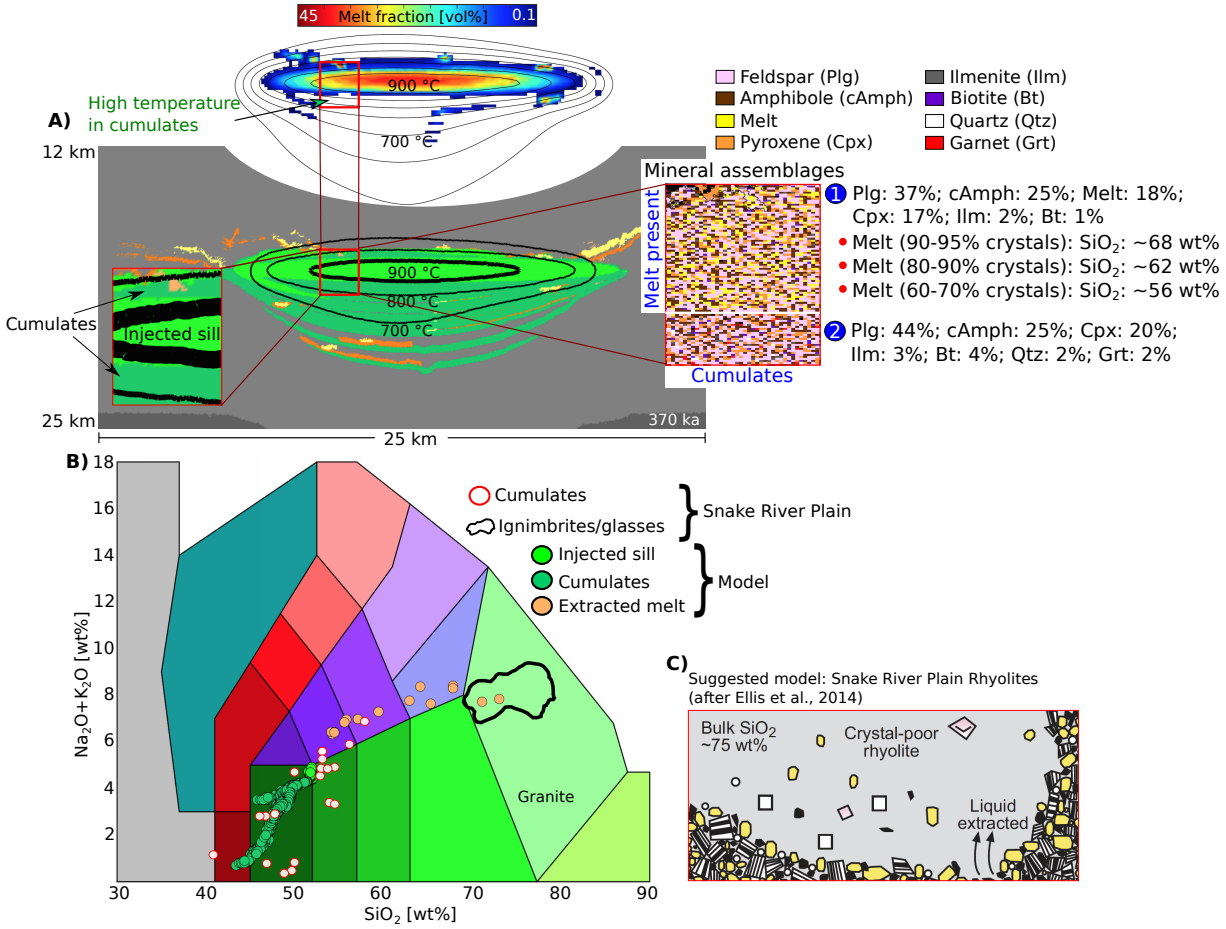

Figure 5.14: Model results compared with a suggested model for the generation of rhyolites from the Snake River Plain. A) Snapshot of the modeled system after 370 ka (see parameters, model 26, Fig. 5.8, Tab. 5.3) with zoom in into melt fraction and mineral assemblages of a section, in which heat is preserved through surrounding hot refractory material. B) TAS diagram (normalized without water) for plutonic rocks (after Middlemost, 1994) for the modeled injected sills (and their cumulates) and the corresponding compositions of extracted melt. Cumulates and volcanic rocks from the Snake River Plain are added (Ellis et al., 2014). The suggested process generating Snake River Plain Rhyolites is shown in C).

Experimental studies show that in order to produce rocks with a rhyolitic composition, the parental magma of basaltic composition has to be crystallized by at least 80%, whereas

the formation of andesitic-dacitic melts requires only a crystallization degree of 40–60% (Sisson et al., 2005; Scaillet et al., 2016). A rhyolitic liquid can form at near-solidus conditions either by advanced crystallization-differentiation or by high-degree crystallization of a mantle-derived basaltic source (e.g. Sisson et al., 2005; Ulmer et al., 2018; Müntener and Ulmer, 2018; Jagoutz and Klein, 2018). Other authors suggest that the crystallization of basaltic magmas in combination with host rock melting generates silicic magmas, forming a mobile magma through melt segregation in the mush (Solano et al., 2012, 2014; Riel et al., 2018). Our model results show that a relatively cool mush system (high crystallization degree) may form silicic rocks from a primary basaltic bulk rock composition, but also magma mixing can shift the melt compositions towards rhyolites/granites, as host rock melts have a rhyolitic to granodioritic composition. Additionally, rhyolites may also form in dikes of the second generation through fractionation of basaltic magma. Although, only two fractionation steps have been carried out in our models (from basaltic sills to second generation dikes), this already roughly illustrates the influence of fractionation on the liquid line of descent and on the phase relations. In our models, most of the melt extraction is triggered by mafic influx from below, producing only relatively small eruption volumes proportional to the volume of the previously injected basaltic sill. Under particular model conditions (deep sill injection zone or low rock cohesion), the melt may stay in the magma reservoir, where it can fractionate and differentiate to more highly evolved rocks (e.g. Annen et al., 2015). Magma reservoirs in the lower crust maintain activity for a long time, forming a zone in which melting, assimilation, storage (fractionation), and homogenization (magma mixing) (MASH, after Hildreth and Moorbath, 1988) take place. In addition to those processes, remelting, recharge and magma eruption are further aspects that control the chemical and the mechanical evolution of magmatic systems. Our models indicate that the evolving chemistry is the main controlling parameter in maintaining the system in a partially molten/crystallized state, instead of the temperature as suggested in previous studies. Successive melt extraction depletes the source region. Therefore, even if the temperature is relatively high, the melting/crystallization degree is strongly affected by the composition of the rocks that controls the solidus temperature, and which changes as soon as melt is extracted. The efficiency of melt extraction from the reservoir is a crucial factor in maintaining a larger mush zone. This partially crystallized zone is formed either through a merging of formerly separated partially crystallized sills or through a reduced heat loss due to the injection of fresh basaltic magma into the already existing mush zone. Older undepleted material (injected before as basaltic sills, now crystallized) can even be reactivated through the heat supply of a new basaltic influx. Younger magma pulses may

be efficient in recycling of older plutonic material (e.g. Paterson et al., 2008) that results in extensive mixing of crystals and melts. However, the total amount of eruptable melt is not necessarily correlated with the size of the magma reservoir, because it is controlled by the crystallization degree that increases with decreasing temperature. Thus, if melts accumulate over a large area, a large eruptable melt volume can be produced, despite a high average crystallization degree. This may, on the long term, result in episodic events of eruption of highly differentiated liquids. This is consistent with geophysical observations suggesting that the failure to find large bodies of fully molten magmas likely requires the existence of large mush bodies with only small melt fractions (e.g. Pritchard and Gregg, 2016).

The total volume of the modeled continental crust increases with each basaltic magma intrusion from the mantle. Melt extraction and partial melting of host rocks result in dike formation leaving behind diverse cumulate and residual rocks. The total amount of newly-created crust is dominated by the injected basaltic sills, followed by dikes which were generated from them. The volume ratio between injected sills and dikes of the first and the second generation is influenced by the melt extraction efficiency that controls the ratio between the remaining cumulates and the amount of extracted melt. The newly-created crust can nearly exclusively consist of basalts using a low rock cohesion of 5 MPa (model 26, Fig. 5.15). Partial melting of host rocks modifies the crustal composition only to a minor extent and is only relevant for a strongly hydrated primary crust (model 38, Fig. 5.15). Using this hydrated crust (upper crust: 5 wt%; middle crust: 3 wt%; lower crust: 0.5 wt% H_2O, Tab. 5.1), the volume of highly in silica enriched rocks (> 70 wt% SiO_2) increases, which is small under lower crustal water contents and normally dominated by the fractionated magma from the sills (dikes of the second generation). The silica concentration of the sill-cumulates changes with intrusion depth, temperature, and composition. Low SiO_2 concentrations are produced either under shallow injection depths assuming constant intrusion temperatures, with high intrusion temperatures, or with a hydrated initial basaltic composition (Fig. 5.15 and Fig. 5.A2, see Appendix). Whereas, a high SiO_2 concentration in the cumulates requires a deep sill injection zone (model 6, Fig. 5.15) or lower intrusion temperatures. All these parameters influence the crystallization degree, such that a lower silica concentration implies a higher amount of extracted melt. The modeled dikes become more enriched in silica through melt retention in the source by using a low rock cohesion (5 MPa) or by choosing a deep intrusion depth as discussed in Section 5.3.3. Furthermore, the silica concentration is often slightly increased for dikes triggered by shallower sill intrusions at middle or even upper crustal levels. However, the

chemistry of dikes of the second generation is especially affected by the liquid/solid ratio in the source from which their melt was extracted. Thus, not only the melt extraction efficiency but also the temperature that keeps the system in a partially molten/crystallized state and the pressure conditions are crucial for the evolution of the dike chemistry.

The density decreases in general with increasing silica content in our models (Fig. 5.15). The basalt injected as sills into the crust, has, in a fully crystallized state, a higher density (3035 kg/m^3 with 1 wt% H_2O or 2960 kg/m^3 with 5 wt% H_2O) than both the upper (2823 kg/m^3 with 1 wt% H_2O or 2639 kg/m^3 with 5 wt% H_2O) and the middle crust (2849 kg/m^3 with 0.5 wt% H_2O or 2791 kg/m^3 with 3 wt% H_2O), and a lower density than the lower crust (3127 kg/m^3 with 0.1 wt% H_2O or 3071 kg/m^3 with 0.5 wt% H_2O). Consequently, delamination of basaltic material into the lower crust or mantle is not possible using the chosen basaltic and crustal rock compositions. However, if melt is extracted, the remaining cumulates can have a lower density with respect to the surrounding crust and the underlying mantle (Fig. 5.15 and Fig. 5.A2, see Appendix). This can lead to delamination of dense cumulitic material into the deep lower crust (lingering at the Moho) or even into the mantle, on the long term, and may explain the paradox between the volume of silicic magma and that of the remaining cumulates. The observed volume of mafic-ultramafic cumulates in exposed crustal arc sections is far too low to explain large granitic bodies through fractional crystallization of a parental mafic melt. Therefore, delamination of dense cumulitic material is suggested (e.g. Jagoutz and Kelemen, 2015; Jagoutz and Klein, 2018). Using a hydrated mantle (not modeled here) and a more hydrated lower crust may also support this process by lowering both the density and the viscosity.

An arc system is dominated by igneous rocks and their cumulates. Exposed crustal sections show a continuum from mafic cumulates (indicating mineral accumulation and residual melt loss) to felsic intrusives (frozen liquids) in the upper crust, and indicate that most magmatic differentiation is restricted to the lower crust (Jagoutz, 2014). With the change in rock compositions from mafic to felsic the intrusion shape also changes, from more horizontally oriented structures in the lower crust to more vertically oriented ones in the upper arc crust (Jagoutz, 2014). These observations are in agreement with modeling results, in which differentiation and the variable amount of extracted melt lead to diverse cumulate chemistries. Their depletion degree can increase with depth due to the higher amount of extracted melt with increasing magma temperatures. Melts were extracted from horizontally oriented structures (basaltic sills) to form frozen liquids as dikes in the overlying crust.

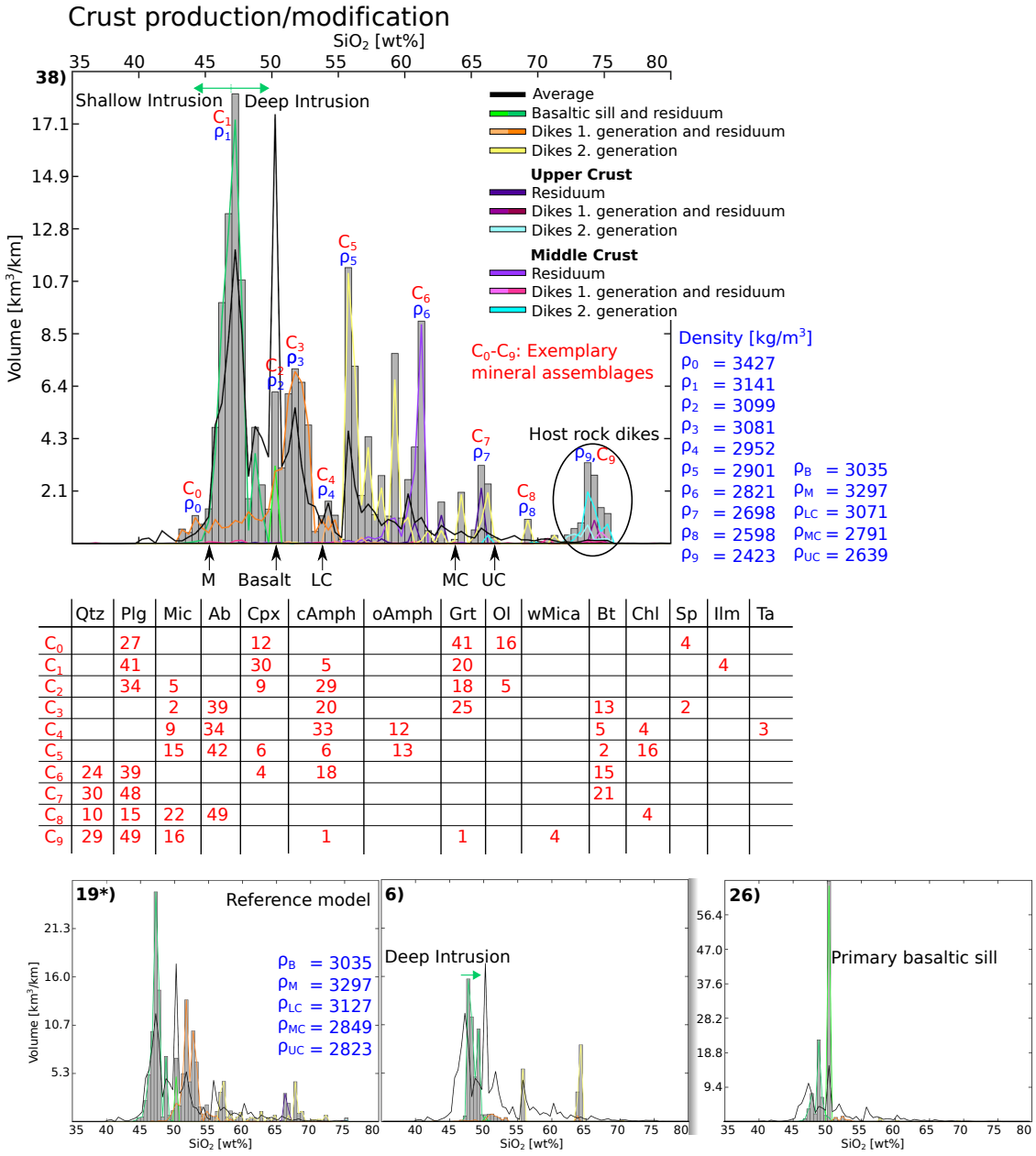

	Qtz	Plg	Mic	Ab	Cpx	cAmph	oAmph	Grt	Ol	wMica	Bt	Chl	Sp	Ilm	Ta
C_0		27			12			41	16				4		
C_1		41			30	5		20						4	
C_2		34	5		9	29		18	5						
C_3			2	39		20		25			13		2		
C_4			9	34		33	12				5	4			3
C_5			15	42	6	6	13				2	16			
C_6	24	39			4	18					15				
C_7	30	48									21				
C_8	10	15	22	49								4			
C_9	29	49	16			1		1		4					

Figure 5.15: Volume of different crust contributions from sills, cumulates, dikes, and modified crustal host rocks, and their SiO_2 concentrations (normalized without water). For the histogram, 90 bins are used, each with a width of 0.5 wt% SiO_2. The total amount of newly-created or -modified crust is presented as grey bars. The colored lines represent the contributions of the respective rock phases. The black line is the average from all executed geodynamic simulations. The parameters used are described in Table 5.3. SiO_2 concentrations of the basalt (B) and of the initial mantle (M), upper (UC), middle (MC) and lower crust (LC) are provided. Densities are given for selected bins (ρ_0–ρ_9) and for the initial injected (now crystallized) basalt as well as for the mantle and for the upper, middle and lower crust. Exemplary mineral assemblages are specified for the selected bins (C_0–C_9). Qtz (quartz), Plg (plagioclase), Mic (microcline), Ab (albite), Cpx (clinopyroxene), cAmph (clinoamphibole), oAmph (orthoamphibole), Grt (garnet), Ol (olivine), wMica (white mica), Bt (biotite), Chl (chlorite), Sp (spinel), Ilm (ilmenite), Ta (talc), given in vol%. The endmembers of the solution models can be stable as well, possibly due to the constraints of the solution models.

Magmatic rocks generated in our models are compared with igneous rocks from the Kohistan and Famatinian arc. The Kohistan arc is located in NW Pakistan and represents a fossil Jurassic to Cretaceous island arc that was wedged between the Indian and the Asian plates during their collision. It consists of the Southern Plutonic Complex (SPC), the Chilas- and the Gilgit Complex (e.g. Jagoutz et al., 2011). The SPC represents the upper mantle and the lower to middle crust of this island arc and shows a cumulate sequence formed by "hydrous" medium- to high-pressure fractionation (Jagoutz et al., 2011). The Chilas Complex is a large ultramafic-mafic intrusion and its magmatic sequence is suggested to result from "dry" lower crustal fractionation (Jagoutz et al., 2011). The Sierra Valle Fértil represents a lower to middle crustal section of the Early Ordovician active margin of West Gondwana, the Famatinian arc, which is located in central-western Argentina (e.g. Otamendi et al., 2010a, 2012; Walker Jr et al., 2015). Our modeled compositions are similar to the igneous rocks observed in the Kohistan and Famatinian arc (Fig. 5.16). Differences are mainly observed for the MgO- and TiO_2 content. The MgO concentration is higher for some samples of the Kohistan arc compared to the modeled rock compositions and the TiO_2 concentration can be higher in the modeled cumulates (Fig. 5.16). The thermodynamic melting model does not incorporate Ti that is why all Ti can be stored in ilmenite and rutile. Differences between modeled and natural igneous rocks are potentially a consequence of the chosen initial basaltic composition, the oxygen fugacity that controls the Fe^{2+} to Fe^{3+} ratio, intrusion and melt extraction conditions and constraints of the thermodynamic model. Furthermore, the composition of partially molten and thus assimilated host rock may influence magma compositions as well.

Finally, comparing model results with natural observations remains challenging, as each of the neglected processes may have a large influence on the whole evolution of the magmatic system. More work is required to study their relative importance.

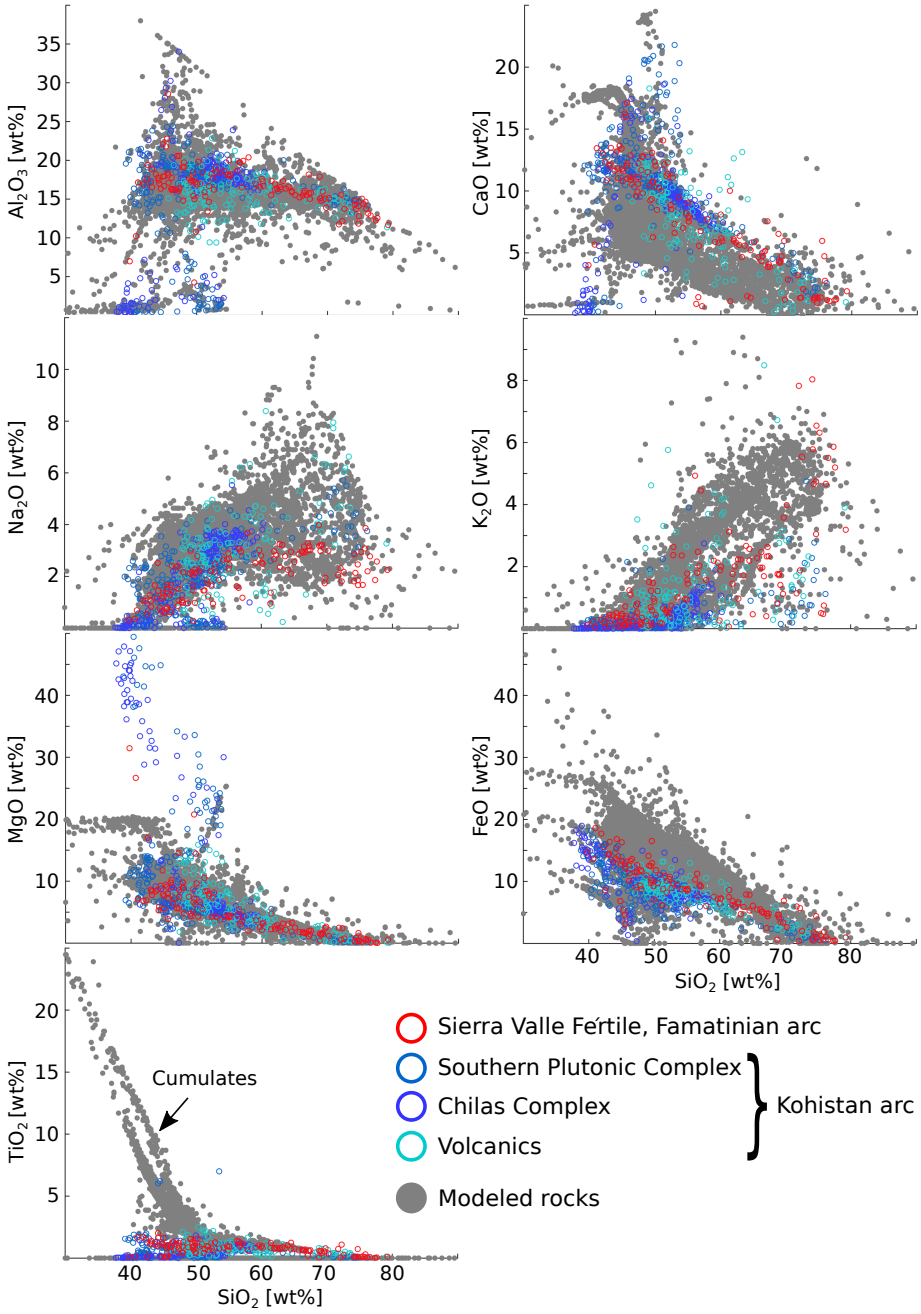

Figure 5.16: Comparison of igneous rocks generated in the petro-thermo-mechanical models with exposed rocks from the Famatinian and Kohistan arc. Rock compositions are on a LOI (loss on ignition) free basis. Magmatic rock compositions of the Famatinian arc are from Otamendi et al. (2009a,b, 2010a,b, 2012) and Walker Jr et al. (2015). Rock compositions of the Kohistan arc are summarized in Jagoutz et al. (2011) and are based on the works of Jan and Howie (1981), Khan (1988), Miller and Christensen (1994), Yamamoto and Yoshino (1998), Shah and Shervais (1999), Mikoshiba et al. (1999), Rolland et al. (2002), Bignold and Treloar (2003), Garrido et al. (2006), Jagoutz et al. (2006, 2011), Takahashi et al. (2007) and Dhuime et al. (2007, 2009).

5.5 CONCLUSION

We study the chemical and mineralogical evolution of arc-related crustal magmatism by integrating thermodynamic models into a visco-elasto-plastic geodynamic code. The compositional evolution consisting of 10 major oxides, is tracked on more than a million markers, while recently developed thermodynamic models for metabasic rocks (Green et al., 2016) are employed to simulate melting and crystallization. As the chemistry continuously changes as a result of melt extraction, new thermodynamic computations are continuously required. To make this computational tractable, we developed a system which links geodynamic models with over 50,000 precomputed phase diagrams that allows tracking the temporal evolution of the evolving rock chemistry and mineralogy as well as its feedback on the mechanics. Magma mixing and the effect of host rock contamination can be included in a simplified manner as well. The geodynamic simulations are linked with a simplified parameterized semi-analytical dike and sill formation algorithm, which tracks whether mode-1 cracks (fluid-filled dikes) or mode-2 shear zones may develop as a result of melt pressure and local stress state. Dikes drain the partially crystallized mush chambers and propagate perpendicular to the main compressive stresses, with a size that depends on the amount of available melt.

With this modeling approach, we can test the chemical, mechanical and thermal evolution of a crustal-scale magmatic system, as a function of tectonic deformation, magma fluxes and sill-related parameters (such as size and temperature). We performed systematic numerical simulations to better understand the physics of this system and the main findings are:

1) Sill injection can often immediately trigger dike formation, unless the cohesion of the host rocks is sufficient low (< 10 MPa) and/or the sills are emplaced sufficiently deep (> 32 km). In those cases, longer-lived mush bodies are formed that are much larger than a single sill increment.

2) Partial melting of crustal host rocks occurs in areas with densely distributed dikes and sills. A higher sill intrusion temperature or a higher water content in the host rocks promote partial melting of the host rock and contamination of mantle-derived magmatic sills.

3) The composition of the newly-created igneous rocks varies between peridotgabbro (or even more depleted) for cumulates and highly differentiated rocks like syenite, quartz monzonite or granite for dikes. Fractionation trends of the modeled magmatic rocks are consistent with those observed in the Kohistan and Famatinian arc.

4) Highly-differentiated rocks such as granites can be formed by i) continuous melt extraction from previously generated dikes, ii) crustal host rock melting, or iii) high-degree crystallization of basaltic sills. To increase the crystallization degree, either the intrusion temperature has to be decreased (starting with a colder mush system) or the magma reservoir has to live longer, by having a low rock cohesion or by being in a deeper part of the crust.

5) Magma mixing generates a wider spectrum of rock compositions, especially for cumulates. Partially molten (wet) host rocks can be assimilated by mixing or mingling processes into the magma reservoir.

These results thus show that mechanical and chemical processes interact and that both of them must be considered to model natural magmatic systems. To a first order, our results are consistent with existing models of deep magma reservoirs that maintain active for a long time forming a zone in which fractionation, assimilation, and magma mixing occur. However, it is not temperature variations that primarily controls the maintenance of the partially molten/crystallized region, but the change in solidus temperature as a function of rock chemistry change driven by open system processes.

5.6 ACKNOWLEDGEMENTS

Funding was provided by the VAMOS Research Center, University of Mainz (Germany). We would like to thank the ZDV at the University of Mainz to provide us computational time on MOGON I cluster to run Perple_X in parallel. We also acknowledge funding by the ERC Consolidator Grant MAGMA (project #71143).

5.7 APPENDIX

5.A Models

To test the effect of a higher intrusion temperature, basaltic sills are injected into the lower crust with 1200 °C. Due to the higher intrusion temperature, the surrounding host rocks of the lower crust become partially molten (Fig. 5.A1). Additionally, the melt fraction in the newly injected sill increases by 27 vol%, from 55 vol% at 1050 °C for the reference model to 82 vol% at 1200 °C. If these melts are extracted, the remaining cumulates are more depleted than cumulates formed in the reference model (model 19, Fig. 5.8; Fig. 5.A1). Whereas, the rock compositions of the resulting dikes have a similar chemistry to those observed in the reference model (model 19, Fig. 5.8; Fig. 5.A1).

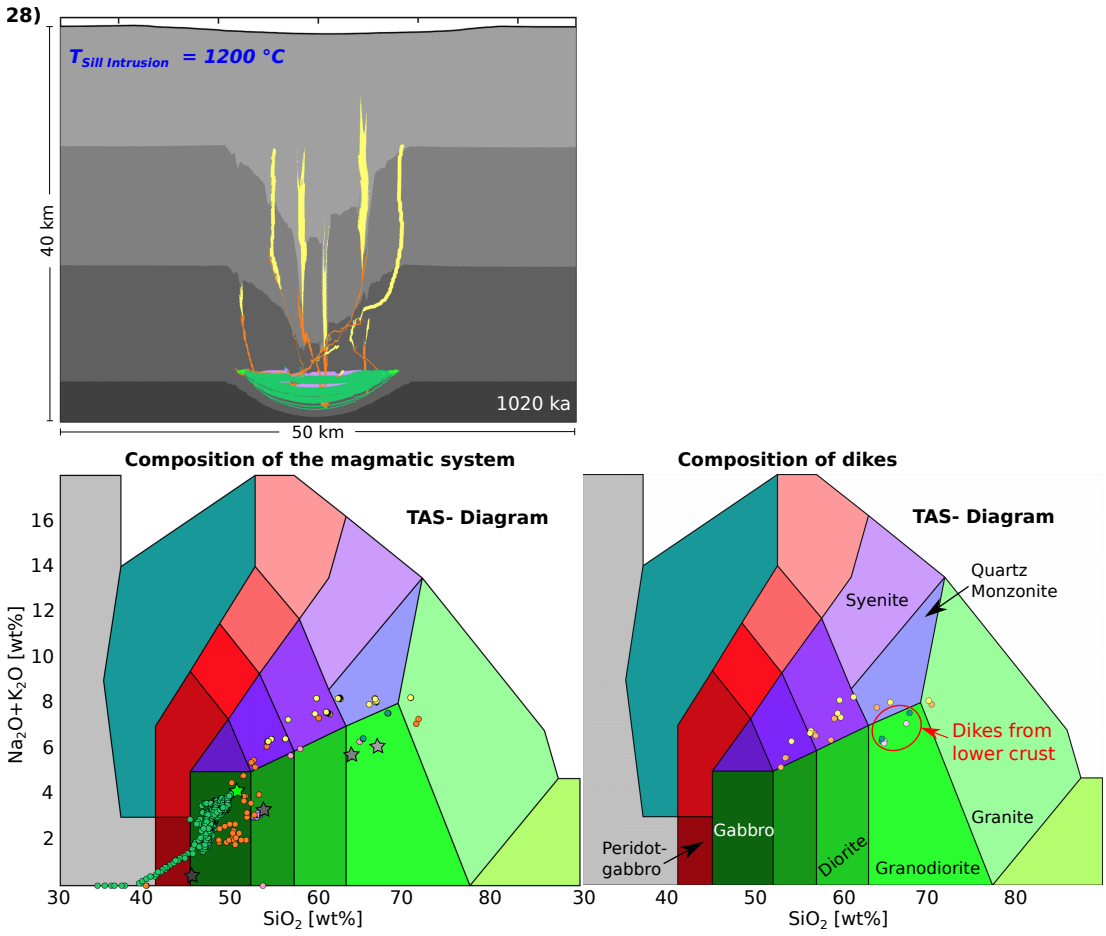

Figure 5.A1: Snapshot of the magmatic system after 1020 ka with a higher basaltic intrusion temperature (top). Rock compositions are shown on a TAS diagram (normalized without water) for plutonic rocks (after Middlemost, 1994), bottom. The colors of the circles represent the respective rock phases (Fig. 5.4). Initial rock compositions are shown as stars. The sills are injected with a temperature of 1200 °C into the lower crust. Employed parameters of the model 28 are described in Table 5.3.

The contribution of the different rock phases (sills, dikes, cumulates or residue) to the crust genesis or modification is presented for two special cases in Figure 5.A2, with a more hydrous basaltic initial composition (5 wt% H_2O) and with a higher sill intrusion temperature (1200 °C). In both models, a higher melt fraction is stable in the injected sill and its extraction produces ultramafic cumulates (Fig. 5.A2). The magmatic products produced through the fractionation of hydrous basaltic magma, are highly enriched in silica for dikes and strongly depleted for cumulates (model 39, Fig. 5.A2).

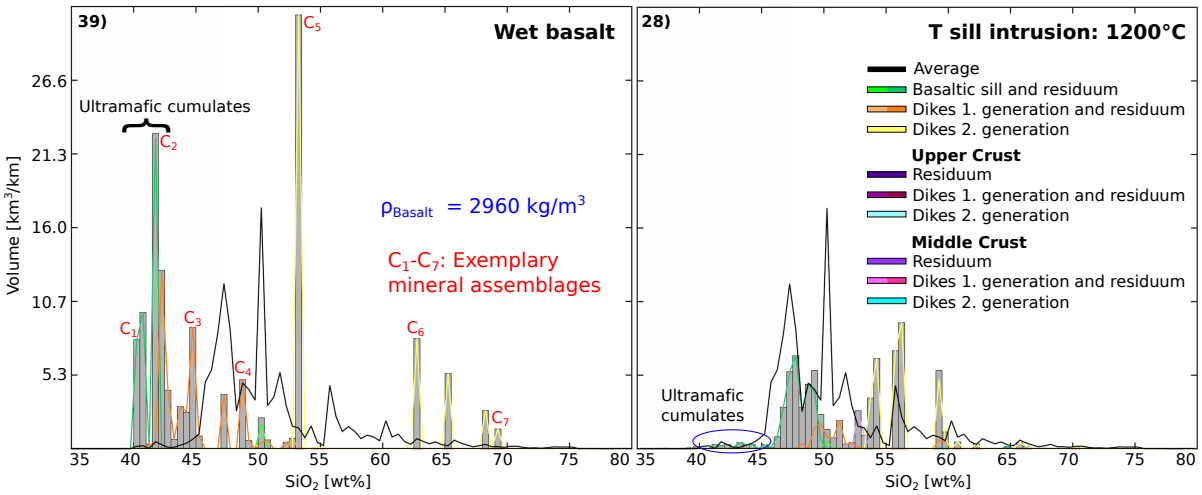

	Qtz	Mic	Ab	Cpx	cAmph	wMica	Grt	Ol	Fstp	Chl	Zo	Sp	Ilm	Ky	Heu	Stlb
C_1				76			4	2				3	15			
C_2				59	21		8						11			
C_3			23	19	20		31					7				
C_4		1	30	7	29		30							2		
C_5	6	10	35	7						26	17					
C_6		18	45	3					7	8					18	
C_7	10	18	47			2			6	3						14

Figure 5.A2: Volume of different crust contributions from sills, cumulates, dikes and modified crustal host rocks, and their SiO_2 concentrations (normalized without water). For the histogram, 90 bins are used, each with a width of 0.5 wt% SiO_2. The total amount of newly-created or -modified crust is presented as grey bars. The colored lines represent the contributions of the respective rock phases. The black line is the average from all executed geodynamic simulations. The parameters used are described in Table 5.3. ρ_{Basalt}: density of the hydrous fully crystallized basalt (bulk rock composition with 5 wt% H_2O). Exemplary mineral assemblages are specified for the selected bins (C_1–C_7) for the model 39. Qtz (quartz), Mic (microcline), Ab (albite), Cpx (clinopyroxene), cAmph (clinoamphibole), wMica (white mica), Grt (garnet), Ol (olivine), Fstp (Fe-stilpnomelane), Chl (chlorite), Zo (zoesite), Sp (spinel), Ilm (ilmenite), Ky (kyanite), Heu (heulandite), Stlb (stilbite), given in vol%. The endmembers of the solution models can be stable as well, possibly due to the constraints of the solution models.

5.B Modeling parameters

Perple_X is used to compute stable phase assemblages for a specific bulk rock composition at prescribed P–T conditions. Different thermodynamic databases are used to compute those phase relationships either for the mantle or for the evolved magmatic rocks. The

employed activity-composition models for solid-solution phases, the melting models and the excluded endmembers are provided in Table 5.B1.

Table 5.B1: Excluded and solution phases (with activity-composition models and references) used in Perple_X for mantle and evolved magmatic rocks (basalt, initial and depleted crusts, cumulates and dikes). 1: Activity-composition model, 2: Mineral name, 3: Reference

Mantle	**Evolved magmatic rocks**		
Excluded phases			
1	**1**	**2**	**3**
fo8L, foTL, foL	fo8L, fojL, foL	forsterite liquid	
fa8L, faTL, faL	fa8L, fajL, faL	fayalite liquid	
q8L, qL	qjL, qL	quartz liquid	
sil8L, silL	sil8L	sillimanite liquid	
anL, abL, kspL	anL	anorthite-, albite-, K-feldspar liquid	
diL, woL, enL	diL, dijL, enL	diopside-, wollastonite-, enstatite liquid	
	ctjL, jdjL	Ca-Ts (kushiroite)-, jadeite liquid	
eskL, hemL, oanL	eskL, ekjL, hemL, hmjL	eskolaite-, hematite liquid	
fliq	fliq	Fe-liquid	
hliq, h2oL	hliq	H_2O-liquid	
mliq	mliq	Mg-liquid	
	ma, andr, ilm, ilm_nol	margarite, andradite, ilmenite	
H_2, O_2	H_2, O_2	hydrogen, oxygen	
Solution phases			
Melt(JH)	melt(G)	melt	[1], [2]
O(JH)	O(HP)	olivine	[1], [7]
Sp(JH)	Sp(WPC)	spinel	[1], [5]
Grt(JH)	Gt(W)	garnet	[1], [3]
Opx(JH), Cpx(JH)	Augite(G)	pyroxene	[1], [2]
	cAmph(G), Ilm(WPH)	clino-amphibole, ilmenite	[2], [6]
	St(W), Crd(W), Ctd(W)	staurolite, cordierite, chloritoid	[3]
	Bi(W), Mica(W), Chl(W)	biotite, mica, chlorite	[3]
Pl(JH)	Fsp(C1), Pl(I1,HP)	feldspar	[1], [4]

[1] Jennings and Holland (2015); [2] Green et al. (2016); [3] White et al. (2014); [4] Holland and Powell (2003); [5] White et al. (2002); [6] White et al. (2000); [7] Holland and Powell (1998)

A visco-elasto-plastic rheology is considered in our geodynamic models. Rheology parameters used for the laboratory-constrained dislocation and diffusion creep laws are provided in Tables 5.B2 and 5.B3. Constant parameters employed in the geodynamic simulations are listed in Table 5.B4.

Table 5.B2: Rheology parameters used for the dislocation creep in the crust and mantle. Dry olivine (Hirth and Kohlstedt, 2003); quartzite, wet quartzite and plagioclase (An75) (Ranalli, 1995); quartz diorite (Carter and Tsenn, 1987); granite (Tirel et al., 2008).

Symbol	**Meaning**	**Unit**	**Quartzite**	**Plagioclase (An75)**	**Dry Olivine**	**Quartz Diorite**	**Granite**	**Wet Quartzite**
A	Prefactor	$\mathrm{Pa}^{-n}s^{-1}$	$2.6673{\cdot}10^{-20}$	$2.0822{\cdot}10^{-23}$	$1.1000{\cdot}10^{-16}$	$1.2589\cdot10^{-16}$	$7.8870\cdot10^{-29}$	$5.0717\cdot10^{-18}$
n	Stress exponent		2.4	3.2	3.5	2.4	3.2	2.3
E	Activation energy	kJ/mol	156	238	530	212	123	154
V	Activation volume	m^3/mol	0	0	$1.5{\cdot}10^{-5}$	0	0	0
F	Prefactor for tensorial form		0.3065	0.3019	0.3048	0.3337	0.3105	0.3073
C_{OH}	Water fugacity	$H/10^6Si$	1	1	1	1	1	1
r	C_{OH}-exponent		0	0	0	0	0	0
β*	Melt fraction prefactor		40	40	40	40	40	40

*β as melt fraction prefactor is only valid for small melt fractions ($\lesssim$ 12 vol%; Hirth and Kohlstedt, 2003).
However, higher melt fractions forces the viscosity to reach the lower cutoff value of 10^{17} Pas.

Table 5.B3: Diffusion creep rheology parameters (Hirth and Kohlstedt, 2003) used for the pyrolitic mantle.

Symbol	Meaning	Unit	Dry Olivine
A	Prefactor	$Pa^{-1}s^{-1}$	1500
E	Activation energy	kJ/mol	375
V	Activation volume	m^3/mol	$5{\cdot}10^{-6}$
F	Prefactor for tensorial form		0.5
d	Grain size	m	0.01
p	Grain size exponent		3
C_{OH}	Water fugacity	$H/10^6 Si$	1
r	C_{OH}-exponent		0
β*	Melt fraction prefactor		30

*see footnote Table 5.B2

Table 5.B4: Constant parameters used in the geodynamic models.

Symbol	Meaning	Unit	Value
η_{LC}	Viscosity lower cutoff	Pas	10^{17}
η_{UC}	Viscosity upper cutoff	Pas	10^{25}
g	Gravity value	m/s^2	9.8
	Gravity angle	°	90
α	Thermal expansivity	K^{-1}	$3{\cdot}10^{-5}$
k	Thermal conductivity	W/(mK)	3
C_p	Heat capacity	J/(kgK)	1050
	Radioactive heat crust	$\mu W/m^3$	1
	Radioactive heat mantle	$\mu W/m^3$	0.022
Q_L	Latent heat of fusion	kJ/kg	400
ϕ	Friction angle	°	30
C	Cohesion	Pa	$5{\cdot}10^6$–$10{\cdot}10^6$
G	Shear modulus	Pa	$3.6{\cdot}10^{10}$ for crust
			$7.4{\cdot}10^{10}$ for mantle
σ_T	Tensile strength	Pa	$5{\cdot}10^6$
E_{ym}	Young's modulus	Pa	$5{\cdot}10^{10}$
ν	Poisson's ratio		0.25
ψ*	Biot-Willis poro-elastic coupling constant		0.47

*Paterson and Wong (2005). σ_T, E_{ym}, ν and ψ are only used for the fracture algorithm to generate dikes and sills.

REFERENCES

Annen, C., Blundy, J. D., Leuthold, J., Sparks, R. S. J., 2015. Construction and evolution of igneous bodies: Towards an integrated perspective of crustal magmatism. Lithos 230, 206–221.

Bachmann, O., Bergantz, G. W., 2004. On the origin of crystal-poor rhyolites: extracted from batholithic crystal mushes. Journal of Petrology 45 (8), 1565–1582.

Bachmann, O., Huber, C., 2016. Silicic magma reservoirs in the Earths crust. American Mineralogist 101 (11), 2377–2404.

Bergantz, G., Schleicher, J., Burgisser, A., 2015. Open-system dynamics and mixing in magma mushes. Nature Geoscience 8 (10), 793.

Biggs, J., Pritchard, M. E., 2017. Global volcano monitoring: what does it mean when volcanoes deform? Elements 13 (1), 17–22.

Bignold, S., Treloar, P., 2003. Northward subduction of the Indian Plate beneath the Kohistan island arc, Pakistan Himalaya: new evidence from isotopic data. Journal of the Geological Society 160 (3), 377–384.

Blundy, J. D., Annen, C. J., 2016. Crustal magmatic systems from the perspective of heat transfer. Elements 12 (2), 115–120.

Burg, J.-P., Gerya, T., 2005. The role of viscous heating in Barrovian metamorphism of collisional orogens: thermomechanical models and application to the Lepontine Dome in the Central Alps. Journal of Metamorphic Geology 23 (2), 75–95.

Caricchi, L., Blundy, J., 2015. The temporal evolution of chemical and physical properties of magmatic systems. Geological Society, London, Special Publications 422, SP422–11.

Carter, N. L., Tsenn, M. C., 1987. Flow properties of continental lithosphere. Tectonophysics 136 (1-2), 27–63.

Cashman, K. V., Sparks, R. S. J., Blundy, J. D., 2017. Vertically extensive and unstable magmatic systems: a unified view of igneous processes. Science 355 (6331), eaag3055.

Clemens, J., Mawer, C., 1992. Granitic magma transport by fracture propagation. Tectonophysics 204 (3-4), 339–360.

Coleman, D. S., Mills, R. D., Zimmerer, M. J., 2016. The pace of plutonism. Elements 12 (2), 97–102.

Connolly, J., 2009. The geodynamic equation of state: what and how. Geochemistry, Geophysics, Geosystems 10 (10).

Connolly, J. A., 2005. Computation of phase equilibria by linear programming: a tool for geodynamic modeling and its application to subduction zone decarbonation. Earth and Planetary Science Letters 236 (1), 524–541.

Cooper, K. M., 2017. What Does a Magma Reservoir Look Like? The Crystal's-Eye View. Elements 13 (1), 23–28.

De Silva, S. L., Riggs, N. R., Barth, A. P., 2015. Quickening the pulse: Fractal tempos in continental arc magmatism. Elements 11 (2), 113–118.

Dhuime, B., Bosch, D., Bodinier, J.-L., Garrido, C., Bruguier, O., Hussain, S. S., Dawood, H., 2007. Multistage evolution of the Jijal ultramafic–mafic complex (Kohistan, N Pakistan): implications for building the roots of island arcs. Earth and Planetary Science Letters 261 (1-2), 179–200.

Dhuime, B., Bosch, D., Garrido, C. J., Bodinier, J.-L., Bruguier, O., Hussain, S. S., Dawood, H., 2009. Geochemical architecture of the lower-to middle-crustal section of a paleo-island arc (Kohistan Complex, Jijal–Kamila area, northern Pakistan): implications for the evolution of an oceanic subduction zone. Journal of Petrology 50 (3), 531–569.

Duesterhoeft, E., Quinteros, J., Oberhaensli, R., Bousquet, R., de Capitani, C., 2014. Relative impact of mantle densification and eclogitization of slabs on subduction dynamics: A numerical thermodynamic/thermokinematic investigation of metamorphic density evolution. Tectonophysics 637, 20–29.

Dufek, J., Bachmann, O., 2010. Quantum magmatism: Magmatic compositional gaps generated by melt-crystal dynamics. Geology 38 (8), 687–690.

Dufek, J., Bergantz, G., 2005. Lower crustal magma genesis and preservation: a stochastic framework for the evaluation of basalt–crust interaction. Journal of Petrology 46 (11), 2167–2195.

Ellis, B. S., Bachmann, O., Wolff, J. A., 2014. Cumulate fragments in silicic ignimbrites: The case of the Snake River Plain. Geology 42 (5), 431–434.

Garrido, C. J., Bodinier, J.-L., Burg, J.-P., Zeilinger, G., Hussain, S. S., Dawood, H., Chaudhry, M. N., Gervilla, F., 2006. Petrogenesis of mafic garnet granulite in the lower crust of the Kohistan paleo-arc complex (northern Pakistan): Implications for intracrustal differentiation of island arcs and generation of continental crust. Journal of Petrology 47 (10), 1873–1914.

Gerbault, M., Hassani, R., Novoa Lizama, C., Souche, A., 2018. Three-Dimensional Failure Patterns Around an Inflating Magmatic Chamber. Geochemistry, Geophysics, Geosystems 19 (3), 749–771.

Gerya, T. V., Yuen, D. A., 2007. Robust characteristics method for modelling multiphase visco-elasto-plastic thermo-mechanical problems. Physics of the Earth and Planetary Interiors 163 (1), 83–105.

Green, E., White, R., Diener, J., Powell, R., Holland, T., Palin, R., 2016. Activity–composition relations for the calculation of partial melting equilibria in metabasic rocks. Journal of Metamorphic Geology 34 (9), 845–869.

Gudmundsson, A., 2006. How local stresses control magma-chamber ruptures, dyke injections, and eruptions in composite volcanoes. Earth-Science Reviews 79 (1-2), 1–31.

Hebert, L. B., Antoshechkina, P., Asimow, P., Gurnis, M., 2009. Emergence of a low-viscosity channel in subduction zones through the coupling of mantle flow and thermodynamics. Earth and Planetary Science Letters 278 (3-4), 243–256.

Hildreth, W., Moorbath, S., 1988. Crustal contributions to arc magmatism in the Andes of central Chile. Contributions to mineralogy and petrology 98 (4), 455–489.

Hill, G. J., Caldwell, T. G., Heise, W., Chertkoff, D. G., Bibby, H. M., Burgess, M. K., Cull, J. P., Cas, R. A., 2009. Distribution of melt beneath Mount St Helens and Mount Adams inferred from magnetotelluric data. Nature Geoscience 2 (11), 785.

Hirth, G., Kohlstedt, D., 2003. Rheology of the upper mantle and the mantle wedge: A view from the experimentalists. Inside the subduction Factory, 83–105.

Holland, T., Powell, R., 1998. An internally consistent thermodynamic data set for phases of petrological interest. Journal of metamorphic Geology 16 (3), 309–343.

Holland, T., Powell, R., 2003. Activity–composition relations for phases in petrological calculations: an asymmetric multicomponent formulation. Contributions to Mineralogy and Petrology 145 (4), 492–501.

Holland, T. J., Green, E. C., Powell, R., 2018. Melting of peridotites through to granites: a simple thermodynamic model in the system KNCFMASHTOCr. Journal of Petrology.

Huang, H.-H., Lin, F.-C., Schmandt, B., Farrell, J., Smith, R. B., Tsai, V. C., 2015. The Yellowstone magmatic system from the mantle plume to the upper crust. Science 348 (6236), 773–776.

Huber, C., Parmigiani, A., 2018. A Physical Model for Three-Phase Compaction in Silicic Magma Reservoirs. Journal of Geophysical Research: Solid Earth 123 (4), 2685–2705.

Jagoutz, O., 2014. Arc crustal differentiation mechanisms. Earth and Planetary Science Letters 396, 267–277.

Jagoutz, O., Kelemen, P. B., 2015. Role of arc processes in the formation of continental crust. Annual Review of Earth and Planetary Sciences 43, 363–404.

Jagoutz, O., Klein, B., 2018. On the importance of crystallization-differentiation for the generation of SiO2-rich melts and the compositional build-up of arc (and continental) crust. American Journal of Science 318 (1), 29–63.

Jagoutz, O., Müntener, O., Burg, J.-P., Ulmer, P., Jagoutz, E., 2006. Lower continental crust formation through focused flow in km-scale melt conduits: The zoned ultramafic bodies of the Chilas Complex in the Kohistan island arc (NW Pakistan). Earth and Planetary Science Letters 242 (3-4), 320–342.

Jagoutz, O., Müntener, O., Schmidt, M. W., Burg, J.-P., 2011. The roles of flux-and decompression melting and their respective fractionation lines for continental crust formation: Evidence from the Kohistan arc. Earth and Planetary Science Letters 303 (1-2), 25–36.

Jan, M. Q., Howie, R., 1981. The mineralogy and geochemistry of the metamorphosed basic and ultrabasic rocks of the Jijal complex, Kohistan, NW Pakistan. Journal of Petrology 22 (1), 85–126.

Jennings, E. S., Holland, T. J., 2015. A simple thermodynamic model for melting of peridotite in the system NCFMASOCr. Journal of Petrology 56 (5), 869–892.

Johnson, T. E., Brown, M., Kaus, B. J., VanTongeren, J. A., 2014. Delamination and recycling of Archaean crust caused by gravitational instabilities. Nature Geoscience 7 (1), 47–52.

Karakas, O., Dufek, J., Mangan, M. T., Wright, H. M., Bachmann, O., 2017. Thermal and petrologic constraints on lower crustal melt accumulation under the Salton Sea Geothermal Field. Earth and Planetary Science Letters 467, 10–17.

Karlstrom, L., Paterson, S. R., Jellinek, A. M., 2017. A reverse energy cascade for crustal magma transport. Nature Geoscience 10 (8), 604.

Katz, R. F., Spiegelman, M., Langmuir, C. H., 2003. A new parameterization of hydrous mantle melting. Geochemistry, Geophysics, Geosystems 4 (9).

Kaus, B. J., 2010. Factors that control the angle of shear bands in geodynamic numerical models of brittle deformation. Tectonophysics 484 (1), 36–47.

Khan, M., 1988. Petrology and structure of the Chilas ultramafic^ mafic complex, Kohistan Arc, NW Himalayas. Unpublished PhD Thesis, University of London.

Kiser, E., Palomeras, I., Levander, A., Zelt, C., Harder, S., Schmandt, B., Hansen, S., Creager, K., Ulberg, C., 2016. Magma reservoirs from the upper crust to the Moho inferred from high-resolution Vp and Vs models beneath Mount St. Helens, Washington State, USA. Geology 44 (6), 411–414.

Le Maitre, R., 1976. The chemical variability of some common igneous rocks. Journal of petrology 17 (4), 589–598.

Lees, J. M., 2007. Seismic tomography of magmatic systems. Journal of Volcanology and Geothermal Research 167 (1-4), 37–56.

Leuthold, J., Müntener, O., Baumgartner, L. P., Putlitz, B., Ovtcharova, M., Schaltegger, U., 2012. Time resolved construction of a bimodal laccolith (Torres del Paine, Patagonia). Earth and Planetary Science Letters 325, 85–92.

Magni, V., Bouilhol, P., van Hunen, J., 2014. Deep water recycling through time. Geochemistry, Geophysics, Geosystems 15 (11), 4203–4216.

McDonough, W. F., Sun, S.-S., 1995. The composition of the Earth. Chemical geology 120 (3), 223–253.

McKenzie, D., 1984. The generation and compaction of partially molten rock. Journal of petrology 25 (3), 713–765.

Middlemost, E. A., 1994. Naming materials in the magma/igneous rock system. Earth-Science Reviews 37 (3-4), 215–224.

Mikoshiba, M., Takahashi, Y., Takahashi, Y., Kausar, A. B., Khan, T., Kubo, K., Shirahase, T., 1999. Rb-Sr isotopic study of the Chilas igneous complex, Kohistan, northern Pakistan. SPECIAL PAPERS-GEOLOGICAL SOCIETY OF AMERICA, 47–58.

Miller, D. J., Christensen, N. L., 1994. Seismic signature and geochemistry of an island arc: A multidisciplinary study of the Kohistan accreted terrane, northern Pakistan. Journal of Geophysical Research: Solid Earth 99 (B6), 11623–11642.

Müntener, O., Ulmer, P., 2018. Arc crust formation and differentiation constrained by experimental petrology. American Journal of Science 318 (1), 64–89.

Oliveira, B., Afonso, J. C., Zlotnik, S., Diez, P., 2017. Numerical modelling of multiphase multicomponent reactive transport in the Earths interior. Geophysical Journal International 212 (1), 345–388.

Otamendi, J., Cristofolini, E., Tibaldi, A., Quevedo, F., Baliani, I., 2010a. Petrology of mafic and ultramafic layered rocks from the Jaboncillo Valley, Sierra de Valle Fértil, Argentina: implications for the evolution of magmas in the lower crust of the Famatinian arc. Journal of South American Earth Sciences 29 (3), 685–704.

Otamendi, J., Pinotti, L., Basei, M. A. S., Tibaldi, A., 2010b. Evaluation of petrogenetic models for intermediate and silicic plutonic rocks from the Sierra de Valle Fértil-La

Huerta, Argentina: Petrologic constraints on the origin of igneous rocks in the Ordovician Famatinian-Puna paleoarc. Journal of South American Earth Sciences 30 (1), 29–45.

Otamendi, J. E., Ducea, M. N., Bergantz, G. W., 2012. Geological, petrological and geochemical evidence for progressive construction of an arc crustal section, Sierra de Valle Fertil, Famatinian Arc, Argentina. Journal of Petrology 53 (4), 761–800.

Otamendi, J. E., Ducea, M. N., Tibaldi, A. M., Bergantz, G. W., de la Rosa, J. D., Vujovich, G. I., 2009a. Generation of tonalitic and dioritic magmas by coupled partial melting of gabbroic and metasedimentary rocks within the deep crust of the Famatinian magmatic arc, Argentina. Journal of Petrology 50 (5), 841–873.

Otamendi, J. E., Vujovich, G. I., de la Rosa, J. D., Tibaldi, A. M., Castro, A., Martino, R. D., Pinotti, L. P., 2009b. Geology and petrology of a deep crustal zone from the Famatinian paleo-arc, Sierras de Valle Fértil and La Huerta, San Juan, Argentina. Journal of South American Earth Sciences 27 (4), 258–279.

Paterson, M. S., Wong, T.-f., 2005. Experimental rock deformation-the brittle field. Springer Science & Business Media.

Paterson, S. R., Ducea, M. N., 2015. Arc magmatic tempos: gathering the evidence. Elements 11 (2), 91–98.

Paterson, S. R., Okaya, D., Memeti, V., Economos, R., Miller, R. B., 2011. Magma addition and flux calculations of incrementally constructed magma chambers in continental margin arcs: Combined field, geochronologic, and thermal modeling studies. Geosphere 7 (6), 1439–1468.

Paterson, S. R., Žák, J., Janoušek, V., 2008. Growth of complex sheeted zones during recycling of older magmatic units into younger: Sawmill Canyon area, Tuolumne batholith, Sierra Nevada, California. Journal of Volcanology and Geothermal Research 177 (2), 457–484.

Petford, N., Kerr, R. C., Lister, J. R., 1993. Dike transport of granitoid magmas. Geology 21 (9), 845–848.

Pichavant, M., Mysen, B., Macdonald, R., 2002. Source and H 2 O content of high-MgO magmas in island arc settings: an experimental study of a primitive calc-alkaline basalt

from St. Vincent, Lesser Antilles arc. Geochimica et Cosmochimica Acta 66 (12), 2193–2209.

Plank, T., Kelley, K. A., Zimmer, M. M., Hauri, E. H., Wallace, P. J., 2013. Why do mafic arc magmas contain 4 wt% water on average? Earth and Planetary Science Letters 364, 168–179.

Pritchard, M. E., Gregg, P. M., 2016. Geophysical evidence for silicic crustal melt in the continents: where, what kind, and how much? Elements 12 (2), 121–127.

Putirka, K. D., 2017. Down the crater: where magmas are stored and why they erupt. Elements 13 (1), 11–16.

Ranalli, G., 1995. Rheology of the Earth. Springer Science & Business Media.

Riel, N., Bouilhol, P., van Hunen, J., Cornet, J., Magni, V., Grigorova, V., Velic, M., 2018. Interaction between mantle-derived magma and lower arc crust: quantitative reactive melt flow modelling using STyx. Geological Society, London, Special Publications 478, SP478–6.

Rivalta, E., Taisne, B., Bunger, A., Katz, R., 2015. A review of mechanical models of dike propagation: Schools of thought, results and future directions. Tectonophysics 638, 1–42.

Rolland, Y., Picard, C., Pecher, A., Lapierre, H., Bosch, D., Keller, F., 2002. The cretaceous Ladakh arc of NW himalayaslab melting and melt–mantle interaction during fast northward drift of Indian Plate. Chemical Geology 182 (2-4), 139–178.

Rozhko, A., Podladchikov, Y., Renard, F., 2007. Failure patterns caused by localized rise in pore-fluid overpressure and effective strength of rocks. Geophysical Research Letters 34 (22).

Rubin, A. M., 1993. Dikes vs. diapirs in viscoelastic rock. Earth and Planetary Science Letters 119 (4), 641–659.

Rudnick, R., Gao, S., 2003. Composition of the continental crust. Treatise on geochemistry 3, 659.

Rummel, L., Kaus, B. J., White, R. W., Mertz, D. F., Yang, J., Baumann, T. S., 2018. Coupled petrological-geodynamical modeling of a compositionally heterogeneous mantle plume. Tectonophysics 723, 242–260.

Rüpke, L. H., Morgan, J. P., Hort, M., Connolly, J. A., 2004. Serpentine and the subduction zone water cycle. Earth and Planetary Science Letters 223 (1-2), 17–34.

Ruprecht, P., Plank, T., 2013. Feeding andesitic eruptions with a high-speed connection from the mantle. Nature 500 (7460), 68.

Scaillet, B., Holtz, F., Pichavant, M., 2016. Experimental constraints on the formation of silicic magmas. Elements 12 (2), 109–114.

Schmeling, H., Arndt, N., 2017. Modelling komatiitic melt accumulation and segregation in the transition zone. Earth and Planetary Science Letters 472, 95–106.

Shah, M. T., Shervais, J. W., 1999. The Dir-Utror metavolcanic sequence, Kohistan arc terrane, northern Pakistan. Journal of Asian Earth Sciences 17 (4), 459–475.

Sisson, T., Ratajeski, K., Hankins, W., Glazner, A., 2005. Voluminous granitic magmas from common basaltic sources. Contributions to Mineralogy and Petrology 148 (6), 635–661.

Solano, J., Jackson, M., Sparks, R., Blundy, J., 2014. Evolution of major and trace element composition during melt migration through crystalline mush: implications for chemical differentiation in the crust. American Journal of Science 314 (5), 895–939.

Solano, J., Jackson, M., Sparks, R., Blundy, J., Annen, C., 2012. Melt segregation in deep crustal hot zones: a mechanism for chemical differentiation, crustal assimilation and the formation of evolved magmas. Journal of Petrology 53 (10), 1999–2026.

Sparks, R. S. J., Cashman, K. V., 2017. Dynamic magma systems: Implications for forecasting volcanic activity. Elements 13 (1), 35–40.

Sun, R. J., 1969. Theoretical size of hydraulically induced horizontal fractures and corresponding surface uplift in an idealized medium. Journal of Geophysical Research 74 (25), 5995–6011.

Takahashi, Y., Mikoshiba, M. U., Takahashi, Y., Kausar, A. B., Khan, T., Kubo, K., 2007. Geochemical modelling of the Chilas Complex in the Kohistan Terrane, northern Pakistan. Journal of Asian Earth Sciences 29 (2-3), 336–349.

Tegner, C., Thy, P., Holness, M. B., Jakobsen, J. K., Lesher, C. E., 2009. Differentiation and compaction in the Skaergaard intrusion. Journal of Petrology 50 (5), 813–840.

Thielmann, M., Kaus, B. J., 2012. Shear heating induced lithospheric-scale localization: Does it result in subduction? Earth and Planetary Science Letters 359, 1–13.

Tirel, C., Brun, J.-P., Burov, E., 2008. Dynamics and structural development of metamorphic core complexes. Journal of Geophysical Research: Solid Earth 113 (B4).

Tirone, M., Ganguly, J., Morgan, J., 2009. Modeling petrological geodynamics in the Earth's mantle. Geochemistry, Geophysics, Geosystems 10 (4).

Ulmer, P., Kaegi, R., Müntener, O., 2018. Experimentally Derived Intermediate to Silica-rich Arc Magmas by Fractional and Equilibrium Crystallization at 1· 0 GPa: an Evaluation of Phase Relationships, Compositions, Liquid Lines of Descent and Oxygen Fugacity. Journal of Petrology 59 (1), 11–58.

Vogt, K., Gerya, T. V., Castro, A., 2012. Crustal growth at active continental margins: numerical modeling. Physics of the Earth and Planetary Interiors 192, 1–20.

Walker Jr, B. A., Bergantz, G. W., Otamendi, J. E., Ducea, M. N., Cristofolini, E. A., 2015. A MASH zone revealed: the mafic complex of the Sierra Valle Fértil. Journal of Petrology 56 (9), 1863–1896.

White, R., Powell, R., Clarke, G., 2002. The interpretation of reaction textures in Fe-rich metapelitic granulites of the Musgrave Block, central Australia: constraints from mineral equilibria calculations in the system K2O–FeO–MgO–Al2O3–SiO2–H2O–TiO2–Fe2O3. Journal of metamorphic Geology 20 (1), 41–55.

White, R., Powell, R., Holland, T., 2001. Calculation of partial melting equilibria in the system Na2O–CaO–K2O–FeO–MgO–Al2O3–SiO2–H2O (NCKFMASH). Journal of Metamorphic Geology 19 (2), 139–153.

White, R., Powell, R., Holland, T., Johnson, T., Green, E., 2014. New mineral activity–composition relations for thermodynamic calculations in metapelitic systems. Journal of Metamorphic Geology 32 (3), 261–286.

White, R., Powell, R., Holland, T., Worley, B., 2000. The effect of TiO2 and Fe2O3 on metapelitic assemblages at greenschist and amphibolite facies conditions: mineral equilibria calculations in the system K2O-FeO-MgO-Al2O3-SiO2-H2O-TiO2-Fe2O3. Journal of Metamorphic Geology 18 (5), 497–511.

Yamamoto, H., Yoshino, T., 1998. Superposition of replacements in the mafic granulites of the Jijal complex of the Kohistan arc, northern Pakistan: dehydration and rehydration within deep arc crust. Lithos 43 (4), 219–234.

Yamato, P., Agard, P., Burov, E., Le Pourhiet, L., Jolivet, L., Tiberi, C., 2007. Burial and exhumation in a subduction wedge: Mutual constraints from thermomechanical modeling and natural P-T-t data (Schistes Lustrés, western Alps). Journal of Geophysical Research: Solid Earth 112 (B7).

CHAPTER 6

EMPLOYED PHASE DIAGRAMS AND THEIR BULK ROCK COMPOSITIONS

A database was established with more than 58,000 phase diagrams (Chapter 4) for studying crustal magmatic systems (Chapter 5). Each marker used to track rock properties during a geodynamic simulation has potential access to all these phase diagrams. Which of those phase diagrams are finally used depends on the model evolution. After melt is extracted, the phase diagrams are updated based on their closest bulk rock chemistries either to the residual solid compositions for the depleted magma source, or to the liquid chemistry for a newly generated dike. In case the right phase diagram does not exist yet (with an accuracy of one decimal place), the respective requested rock composition is stored. After the completion of a geodynamic simulation, it is verified that each of the updated phase diagrams was accurate enough to describe the ongoing rock evolution. This can be verified by comparing the chemical differences between each of the requested compositions (not used in the database) and the closest bulk rock compositions of the database using Euclidean distances, equation 5.15. We decided for our geodynamic simulations that an average minimal Euclidean distance of $\sim$0.5 wt% is acceptable, as significantly higher distances are rare and only observed for very few cumulate/residuum chemistries. In Figure 6.1, new requested compositions of an exemplary geodynamic simulation are visualized together with bulk rock compositions of the phase diagram database for all oxides. It is observed that the requested compositions are very similar to already existing bulk rock compositions used in the phase diagram database. Therefore, we decided for this specific simulation that the available phase diagrams are good enough to describe the ongoing rock evolution. For other geodynamic simulations this might not be the case and additional phase diagrams are required.

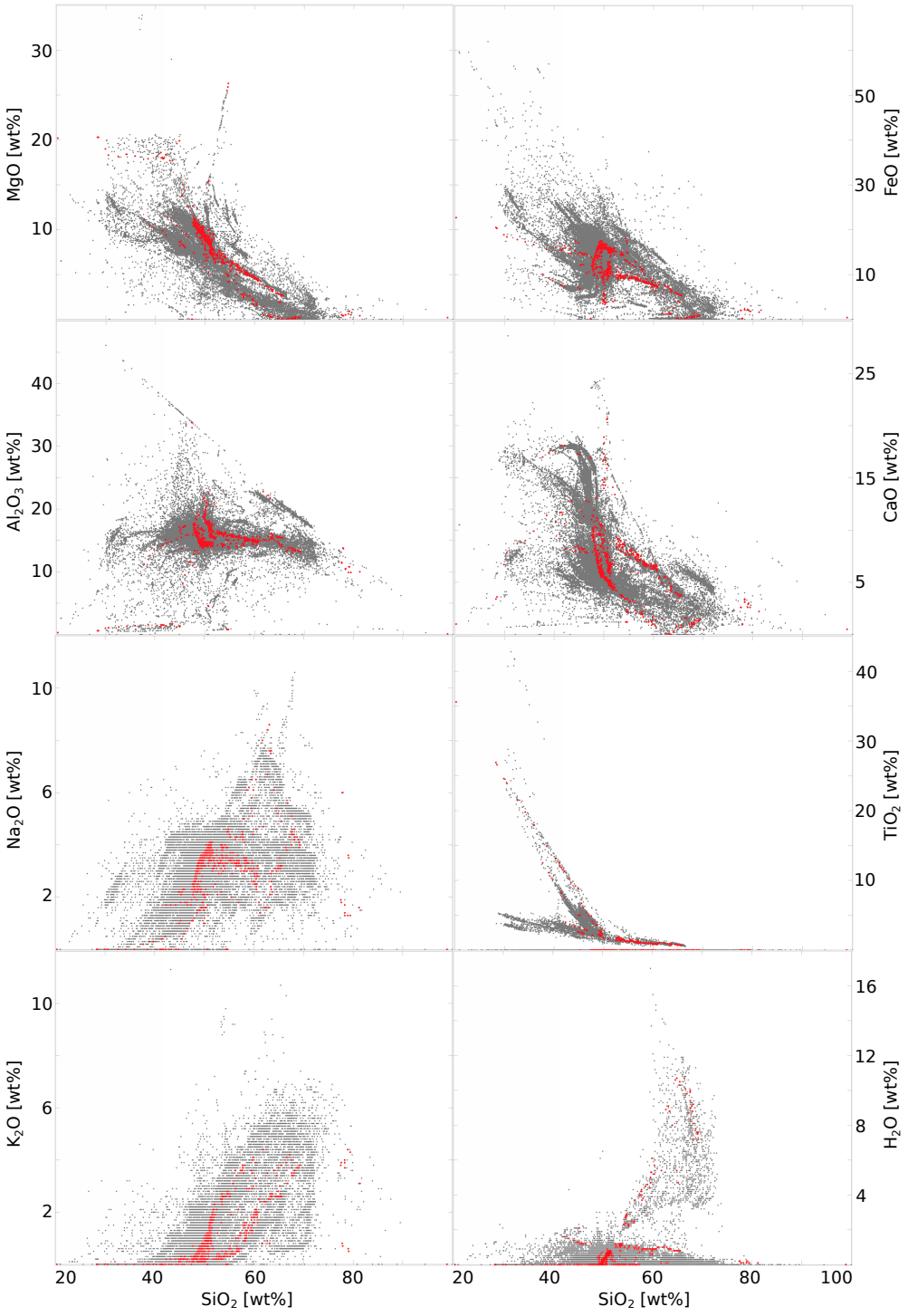

Figure 6.1: Requested rock compositions and bulk rock compositions used in the phase diagram database. Shown here for different oxide combinations. Red points indicate requested rock compositions from an exemplary geodynamic simulation and grey points show the bulk rock compositions of the 58,173 precomputed phase diagrams of the database. The requested compositions are located close to already existing ones of the database. The average minimal Euclidean distance is 0.5 wt% between requested and bulk rock compositions of the database. This allows us to interpret the outcome of the geodynamic simulation in terms of rock chemistry.

The phase diagrams vary strongly in their bulk rock compositions if they are either used for a dike, or for describing the ongoing evolution of cumulitic or residual material in a geodynamic simulation. However, dikes are generated from different kinds of sources and thus even a wider range in phase diagrams with distinguishable rock chemistries are required. Melts can originate from injected basaltic sills, already depleted materials, partially molten host rocks, or from previously generated dikes of the first generation. The more the chemistry of the dikes varies, the larger is the variety of different bulk rock compositions produced in the locally depleted magma sources. All these effects become even stronger in case magma mixing is involved.

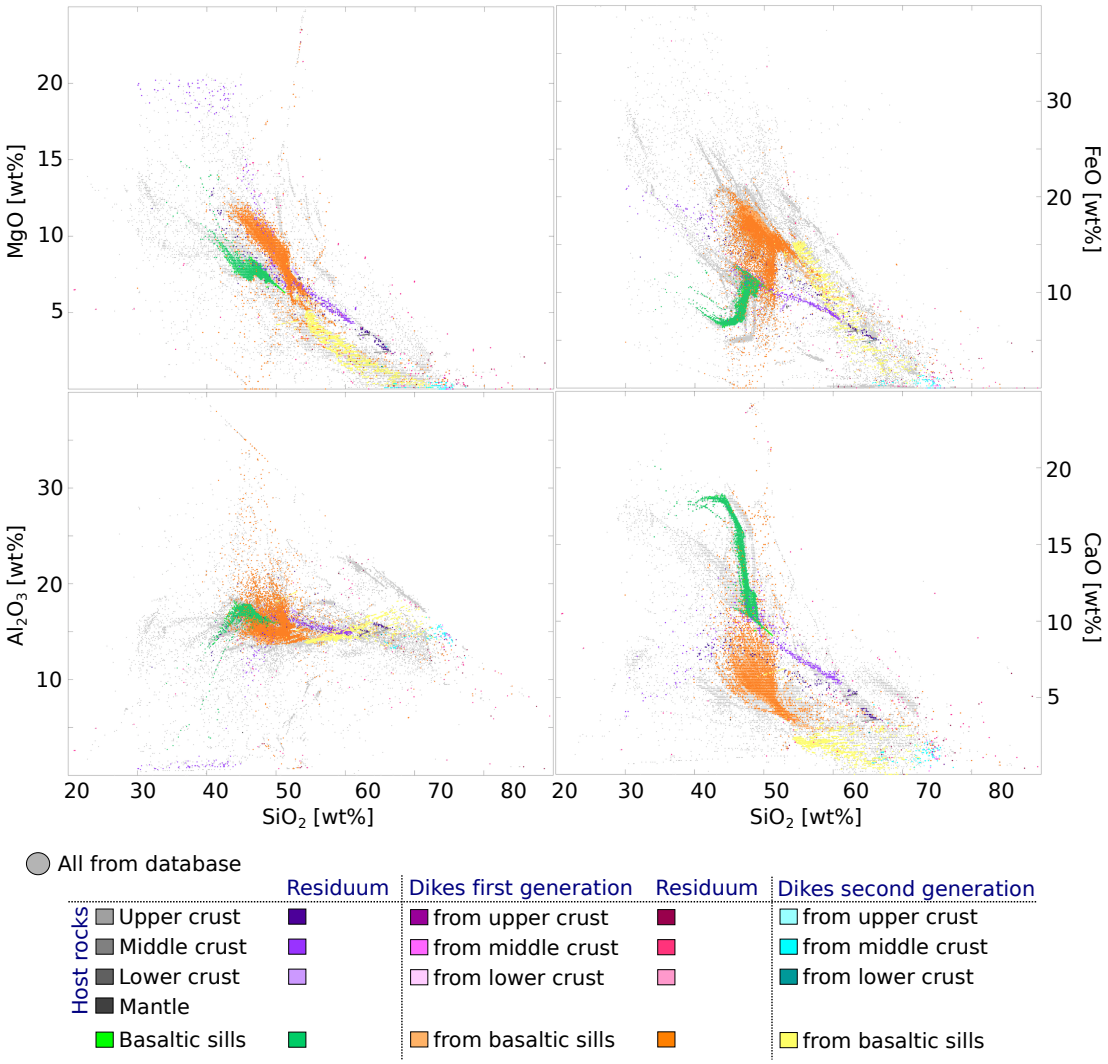

Figure 6.2: Bulk rock compositions of employed phase diagrams of all executed geodynamic simulations, shown here for different oxide combinations (excluded are models in which magma mixing is active). The colors of the points are related to the rock phases, with light grey ones representing all phase diagrams in the database (58,173 in total). Different rock phases use phase diagrams with distinguishable bulk rock compositions.

We analyze the bulk rock compositions of employed phase diagrams for different rock phases regarding their oxide concentrations. Which of the precomputed phase diagrams are required during an ongoing geodynamic simulation depends on the model. In our case, for example, employing a more hydrous crust in the model increases the number of required phase diagrams, as partial melting of the crust opens a completely new branch of requested bulk rock compositions (for residuum and dikes) in the oxide parameter space. Therefore, the total number of required phase diagrams in a database is correlated with the model complexity. How the bulk rock compositions of employed phase diagrams change for different rock phases is shown in Figures 6.2–6.3 for several oxide combinations. Despite small overlaps, the bulk rock compositions of the employed phase diagrams are distinct for different rock phases (e.g., CaO decreases with increasing SiO_2 concentration from injected basaltic sills, over first generation to second generation dikes, Fig. 6.3). As the different rock phases represent different stages of basaltic magma differentiation, these trends show how the basaltic magma and the associated cumulates evolve due to fractional crystallization.

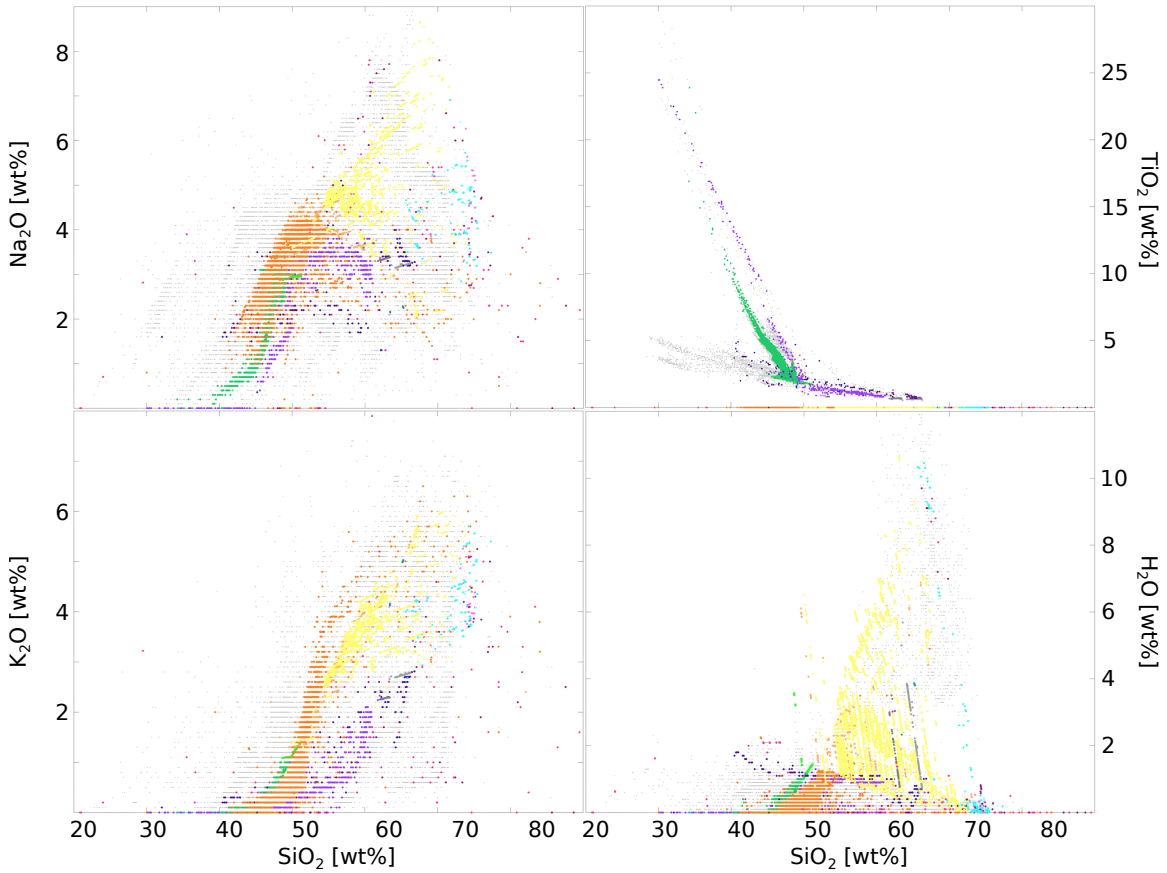

Figure 6.3: Continuation of Figure 6.2.

Although we established our phase diagram database in such a way that it covers most of the rock compositions required during a geodynamic simulation of a crustal arc system, it is never guaranteed, that by changing the model configuration no further phase diagrams are required. Therefore, if our database is applied to another geological setting, it has to be ensured that the residuum and liquid compositions are covered by the oxide ranges of bulk rock compositions used in the database.

CHAPTER 7

FINAL REMARKS AND OUTLOOK

Geodynamic with thermodynamic modeling were combined to investigate the complex evolution of rock compositions in magmatic systems. Two application fields were chosen, a rising compositionally heterogeneous mantle plume, and a crustal-scale arc-like system.

The modeled rising mantle plume partially melts due to decompression, or through the supply of fluids in one of the mantle components. The evolution of extracted melts was analyzed, by focusing on the K_2O/Na_2O ratio as an indicator for the mantle rock type that has been molten. To track the compositional evolution and to investigate the influence of source rock depletion on e.g. strain rate and buoyancy, phase diagrams were precomputed for different depletion stages using pMELTS. The total number of precomputed phase diagrams was limited to a few hundred for evolving mantle rock compositions, because of random crashes and hangups in the pMELTS software, which does not allow the computation of those phase diagrams efficiently in an automatized way. Due to this limited number, the composition of extracted melts shows trends rather than the exact chemistry. Additionally, it has to be kept in mind, that the actual number of employed phase diagrams during a geodynamic simulation may be much lower than the number of available ones. We constructed our bulk rock compositions used in pMELTS from potential melt extraction events at discrete P and T of the respective phase diagrams rather than from requested compositions of the geodynamic simulations. Which of the precomputed phase diagrams are finally used and updated on the markers, from which melt was extracted before in the model, is described by the closest match in composition between the solid chemistry of the marker and the bulk rock chemistry of a precomputed phase diagram. Furthermore, as we describe our initial mantle only through two endmember compositions (an anhydrous pyrolitic and a strongly enriched metasomatized mantle), it is challenging to compare our results in detail with field observations, e.g. from the West

Eifel volcanic field, beneath which a much more complex mantle structure is suggested. Nevertheless, our results are crucial to better understand general trends in melt chemistry caused through melting of a compositionally heterogeneous mantle plume.

Due to the arising problems related to the computation of phase diagrams using pMELTS, we switched to another geological field area, for which the thermodynamic software package Perple_X is suitable. We focused on the evolution of crustal-scale magmatic systems in an arc-like environment. For this, we incorporated a semi-analytical fracture opening algorithm into a 2D geodynamic code, which forms dikes and sills depending on the local stress field. To track the compositional evolution with a very high precision, we precompute a significantly larger number of phase diagrams (tens of thousands). This guaranteed that the differences between the bulk rock compositions of available phase diagrams and the requested compositions of the geodynamic simulations were negligible. To establish such a comprehensive phase diagram database, the computation time for Perple_X has to be minimized without losing data quality. To obtain this, Perple_X option parameters were systematically varied, until a sufficient phase resolution was produced with an acceptable computation time. The computation of phase diagrams was executed in parallel to compute thousands of them within a few days. As a slight change in the initial conditions of our geodynamic model may influence the bulk rock compositions of required phase diagrams, we developed a method through which the database can be extended nearly independently from a geodynamic simulation. For this, new bulk rock compositions are determined within boundaries that are constrained manually or through principal components. With more than 58,000 phase diagrams in the database, the results from all executed geodynamic simulations were interpretable. To study an arc-like setting, we injected basaltic sills within the crust/uppermost mantle with variable temperatures, thicknesses, and spatial dimensions. The diversity of employed phase diagrams varies depending on the model evolution and complexity. Consequently, the number of employed phase diagrams increases if the melt is lately extracted from the source through, e.g. a lower rock cohesion or a deeper sill injection zone, or if magma mixing, especially under water-rich host rock conditions, is included. Thus, to the end, $\sim$25,000 phase diagrams were actually used in total within all executed geodynamic simulations to study the compositional evolution in an arc-like environment. The bulk rock compositions of the employed phase diagrams were distinguishable for different rock phases (injected basaltic sills, residuals, dikes, host rocks). The results show that it is possible to track the chemical and mineralogical evolution in a continuously changing magmatic system with a sufficiently large number of available phase diagrams optimally computed.

For future projects, the compositional evolution has to be coupled more consistently with mechanics, including three-phase flow, reaction kinetics, melt segregation, and self-propagating dikes/sills with a temporal and spatial evolving magma composition. However, including all these mechanisms in one fully coupled code remains a very challenging problem.

The computation of phase diagrams for a large P–T range is very time-consuming and therefore not recommendable to do contemporaneously with a geodynamic simulation. By using only precomputed phase diagrams, a geodynamic simulation must be repeated, while extending the database, until the employed phase diagrams are able to describe the rock evolution. One way to circumvent this and to speed up the thermodynamic computation is to compute missing phase relationships "on the fly" with the geodynamic simulation, but only for required P–T conditions. This dynamic approach is free from P–T–X discretization errors, which results in a more accurate track of the chemical and mineralogical compositions. It has to be tested if a combination of both approaches is computationally feasible. Using precomputed phase diagrams constructed for crustal to uppermost mantle P–T conditions, in combination with phase relationships that are computed for single P–T points.

To study the evolution of melt compositions in a rising mantle plume, the plume initiation and rise from the mantle transition zone, or even from deeper levels, should be incorporated into the model as well. However, thermodynamic melting models for high P–T conditions for diverse mantle compositions and potentially other deep subducted materials are rare, as most thermodynamic models are simplified or restricted to a quite narrow range in P and T. As primary melts from the plume may interact with the shallower mantle or continental crust, rising velocities, reaction kinetics, host rock assimilation or magma mixing and mingling have to be taken into account. In case all these processes are considered, it still remains challenging to compare modeling results with natural rocks, as the exact composition of the continental lithosphere with all its heterogeneity is still unknown.

For studying arc magmatism, large scale processes, which are related to the subducting plate, have to be included. All processes (mechanical and chemical ones) in an arc setting may interact and should not be considered separately from each other. The subduction dynamics are influenced by the properties of both the subducting and the overriding plate and their relation to each other. Triggered by fluid release from the subducting oceanic plate, hydrous mantle melting occurs in the mantle wedge. It remains to be investigated how this magma may change its composition with time and space, and how the magma

migrates, gets stuck, differentiates and finally erupts.

Declaration

I hereby declare that the contents of this dissertation are original and have not been submitted for any other degree or qualifications. This dissertation is the result of my own work, except where specifically indicated in the text.

Erklärung

Ich versichere hiermit gemäß §10 Abs. 3d der Promotionsordnung des Fachbereichs 09 (Chemie, Pharmazie und Geowissenschaften) der Johannes Gutenberg-Universität Mainz vom 24.07.2007, die als Dissertation vorgelegte Arbeit selbständig und nur unter Verwendung der in der Arbeit angegebenen Hilfsmittel verfasst zu haben. Ich habe oder hatte die hier als Dissertation vorgelegte Arbeit nicht als Prüfungsarbeit für eine staatliche oder andere wissenschaftliche Prüfung eingereicht. Ich hatte weder die jetzt als Dissertation vorgelegte Arbeit noch Teile davon bei einer anderen Fakultät bzw. einem anderen Fachbereich als Dissertation eingereicht.

(Lisa Rummel)
Mainz, 19.02.2019